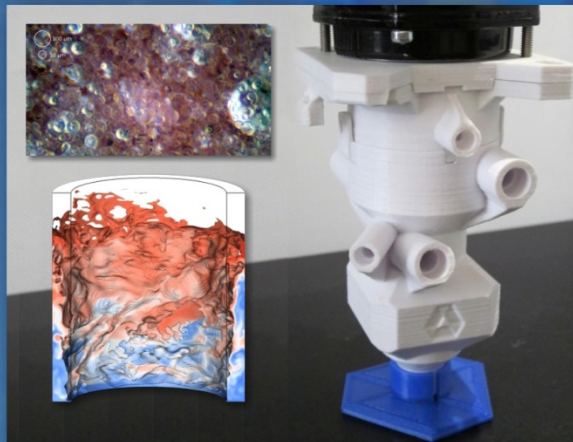
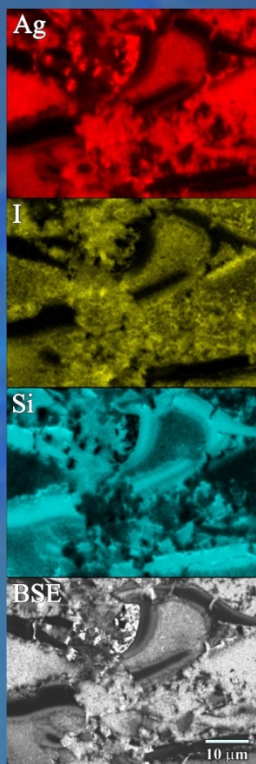
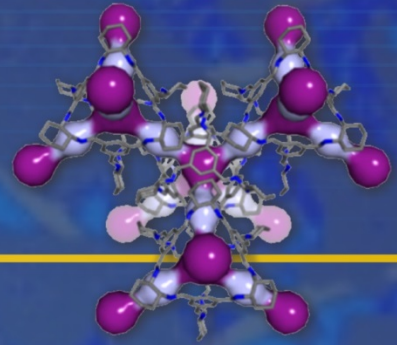


Material Recovery and Waste Form Development



FY 2014 Accomplishments Report

November 2014



DISCLAIMER

This information was prepared as an account of work sponsored by an agency of the U.S. Government. Neither the U.S. Government nor any agency thereof, nor any of their employees, makes any warranty, expressed or implied, or assumes any legal liability or responsibility for the accuracy, completeness, or usefulness, of any information, apparatus, product, or process disclosed, or represents that its use would not infringe privately owned rights. References herein to any specific commercial product, process, or service by trade name, trade mark, manufacturer, or otherwise, does not necessarily constitute or imply its endorsement, recommendation, or favoring by the U.S. Government or any agency thereof. The views and opinions of authors expressed herein do not necessarily state or reflect those of the U.S. Government or any agency thereof.

Material Recovery and Waste Form Development FY 2014 Accomplishments Report

November 2014

**Idaho National Laboratory
Idaho Falls, Idaho 83415**

<http://www.inl.gov>

**Prepared for the
U.S. Department of Energy
Office of Nuclear Energy
Under DOE Idaho Operations Office
Contract DE-AC07-05ID14517**

This page intentionally left blank.

Material Recovery and Waste Form Development FY 2014 Accomplishments Report

**FCRD-MRWFD-2015-00004
INL/EXT-14-33548**

November 2014

Compiled and Edited by:

Lori Braase (lori.braase@inl.gov)
W. Edgar May (ed.may@inl.gov)
INL Systems Analyses

Approved by:



Terry Todd
Material Recovery and Waste Form Development
National Technical Director

November 3, 2014

Date

This page intentionally left blank.

CONTENTS

FIGURES	vii
TABLES	xii
1. MRWFD CAMPAIGN MANAGEMENT AND INTEGRATION	2
1.1 Introduction.....	2
1.2 Major Research and Development Activities.....	3
1.3 Campaign Structure.....	6
1.4 Collaborations	6
2. REFERENCE TECHNOLOGIES AND ALTERNATIVES	14
2.1 Solvent Degradation Mechanisms.....	14
2.2 Tritium Pretreatment	16
2.3 Online Sampling & Monitoring at PNNL	18
2.4 Baseline H-Canyon Accountability.....	24
2.5 Lab-Scale Testing of Reference Processes: ANL	26
2.6 Lab-Scale Testing of Reference Processes: INL.....	28
2.7 Lab-Scale Testing of Reference Processes: ORNL.....	29
2.8 Lab-Scale Testing of Reference Processes: PNNL	32
2.9 Define and Document Reference Flowsheet.....	36
3. SIGMA TEAM FOR MINOR ACTINIDES	42
3.1 Successful Demonstration of Tandem Americium Oxidation and Solvent Extraction Using Process Equipment	42
3.2 Catalyzed Oxidation of Am(III) to Am(VI) Using Ozone.....	43
3.3 Electrochemical Oxidation of Americium	44
3.4 ALSEP Process Development for An/Ln Separation.....	46
3.5 Batch Testing and Proof of Concept	47
3.6 First Contactor Testing of ALSEP	48
3.7 Aqueous Complexes for Americium-Curium Separation	49
3.8 Fundamental Chemistry of TALSPEAK-Like Systems.....	50
3.9 Mixed-Donor Extractants.....	52
3.10 Separation of Minor Actinides from Trivalent lanthanides Using Bis-triazinyl Pyridine Derivatives.....	53
3.11 Dithiophosphinic Acid Extractants for Minor Actinide Extraction	54
4. SIGMA TEAM FOR OFF-GAS CAPTURE AND IMMOBILIZATION	60
4.1 Control of Tritium/Iodine Coadsorption onto Ag0Z and 3A MS	60
4.2 Effects of Aging Conditions on Iodine Adsorption	62
4.3 Determining the Mechanisms of Methyl Iodide Adsorption on Ag0Z through Deep Bed Testing	63
4.4 Improved Xe/Kr capacity and selectivity in advanced materials	65

**Material Recovery and Waste Form Development
2014 Accomplishments Report**

4.5	Behavior of Radioactive Semivolatile Species during Nuclear Fuel Reprocessing.....	67
4.6	Optimization Studies on GCM for Iodine Waste Forms.....	69
4.7	Consolidation of Iodine-Loaded Silver Sorbents.....	70
4.8	Silver-Functionalized Silica Aerogel for Iodine Adsorption and Immobilization.....	71
4.9	Results of Economic Evaluation of MOFs for Kr Capture.....	72
5.	FUNDAMENTAL SCIENCE AND METHODS DEVELOPMENT / MODELING AND SIMULATION.....	76
5.1	Contactors Modeling.....	76
5.2	Fundamental Radiation Chemistry.....	78
5.3	Separation Process Thermodynamics and Kinetics: Development of Microfluidic Devices for Solvent Extraction Studies and Radioanalytical Applications.....	80
5.4	Thermodynamics and Kinetics of Advanced Separations Systems.....	82
5.5	Thermodynamics and Kinetics.....	85
5.6	Computational and Spectroscopic Investigations of DTPA Complexes.....	88
5.7	Non-Ideality in Solvent Extraction Systems.....	93
5.8	Extractant Design by Covalency.....	94
6.	ADVANCED WASTE FORM CHARACTERIZATION.....	98
6.1	Metal Waste Forms.....	98
6.2	Oxide Waste Forms: Glass Waste Form Characterization.....	102
7.	ADVANCED WASTE FORMS AND PROCESSES.....	118
7.1	Advanced Waste Forms (Ceramics).....	118
7.2	Summary of INL CCIM Pilot Plant Test with a Low Temperature Ceramic HLW Waste Form Surrogate –Fe-MP.....	123
7.3	Advanced Waste Forms-Zirconium Recycle.....	126
8.	DOMESTIC ELECTROCHEMICAL SEPARATIONS.....	130
8.1	Salt Waste Management Trade Study.....	130
8.2	Ion-Selective Ceramics for Mixed Waste Separations.....	133
9.	FUEL RESOURCES.....	138
9.1	Adsorbent Development, Ligand Design, Nanosynthesis, and Sorption Kinetics/Evaluation at Oak Ridge National Laboratory.....	138
9.2	Thermodynamic, Kinetic, Coordination and Structure Characterization at the Lawrence Berkeley National Laboratory.....	144
9.3	Adsorbent Characterization, Durability, Toxicity, and Deployment Studies at the Pacific Northwest National Laboratory.....	146
	Appendix: Acronyms.....	152

FIGURES

1.	Structures of compounds used in the Advanced TALSPEAK process.....	14
2.	Laboratory system components housed in a radiochemical hood. 1: furnace with reactor and 2: six of the UO ₃ batches generated by the process.....	17
3.	Organic and aqueous phase reagents used in the Advanced TALSPEAK extraction system. The extraction of neodymium is highly favored at low pH values (pH ~ 3), and is less favored at higher pH values (pH ~4).	19
4.	Real-time Raman spectroscopic measurements of the aqueous raffinate phase. A) The Raman spectra are shown over the entire experiment from time = 0 to 340 min, the addition of NaOH and HNO ₃ are indicated on the figure. B) Overhead view of spectra; the relative Raman band intensity is specified by color as indicated in the legend. The pH of the solution at various time intervals is labeled on the figure.	20
5.	A) Prediction of pH for raffinate phase as a function of run time during continuous centrifugal contactor test, and compared with grab sample measurements. B) Comparison of pH measured by on-line process monitoring vs grab sample pH measured values for feed and raffinate contactor test solutions. Fit of data, $Y = 1.0364X - 0.1258$, $r^2 = 0.9866$	21
6.	Real-time UV-vis-NIR spectroscopic measurements of the A) aqueous feed, B) organic feed, C) raffinate, and D) organic product phases. The spectra are shown over the entire experiment from time = 0 to 340 min, the addition of NaOH and HNO ₃ are indicated on the figure at 135 min and 255 min respectively.....	22
7.	A) Measurement of Nd ³⁺ concentration by spectroscopic method, for aqueous feed, aqueous raffinate, organic feed and organic product phases as a function of run time during continuous centrifugal contactor test. B) Distribution ratio for Nd ³⁺ as a function of run time.....	23
8.	Extraction section of the Codecontamination flowsheet for testing.....	27
9.	a) Baseline extraction, scrub (SC), and strip (ST) flowsheet test using feed simulant, without U present. B) Extraction flowsheet with one extraction and three strip phases.....	28
10.	Iodine loading curves for 75% NO ₂ -aged silver-functionalized silica aerogel.....	30
11.	Schematic of experimental test system.....	31
12.	Chemical structures of the TALSPEAK (HDEHP) and Advanced TALSPEAK (HEH[EHP]) extractants.....	33
13.	Chemical structures of the aqueous-phase complexant and buffers used in the Advanced TALSPEAK system.....	33
14.	Overlay of the batch extraction results of lanthanides and ²⁴¹ Am with the data obtained during the dynamic flow extraction. The times for the flow data were obtained from interpolating the measured contactor D-values between the kinetic data points.	34
15.	Radiochemical hood showing the three-stage centrifugal contactor test bed, simulant feed reservoir, and bismuthate filter. Note: The system was photographed prior to introducing radioactivity, and therefore there are no Contamination Area postings on the hood.....	43
16.	Stability of Am(VI) in 10 mM AgNO ₃ /1 M HNO ₃ after ozonation. Left: Residual Am(III) with ingrowth of Am(V) as the initial reduction product of Am(VI). Right: Decrease of Am(VI) concentration over time.....	44

17.	A terpyridine ligand bound to an indium tin oxide electrode surface via a phosphonic acid linker.	45
18.	Left: Concentration of Am species in solution as measured by visible spectroscopy over time during a controlled-potential electrolysis at 1.8 V vs. Ag/AgCl using a ligand-modified high-surface-area working electrode, a Pt foil counter, and a Ag/AgCl wire as a reference electrode. The aqueous electrolyte was 0.1 M nitric acid and 0.95 M sodium nitrate. The working- and counter-electrode areas were separated by a fine glass frit. Right: Initial and final electronic spectra measured in a 1 cm path-length cuvette and modeled with Gaussian functions.	45
19.	Component chemicals used in FY 2014 testing of ALSEP.	46
20.	Distribution ratios as a function of pH for the back-extraction of various elements from the loaded ALSEP solvent into aqueous 0.125 mol/L HEDTA + 0.2 mol/L citrate; a) as-received HEH[EHP] used, b) purified HEH[EHP] used; contacting method: 60-min vortex mixing.	48
21.	Fission product, lanthanide, and ²⁴¹ Am extraction from 3 HNO ₃ with 50mM T2EHDGA and 1 M HEH[EHP] in <i>n</i> -dodecane in a 2-cm centrifugal contactor. Red: equilibrium batch distribution ratios at an O:A ratio of 1:1.6. Blue: effective distribution ratios at contactor flow rates 10.6 mL/min organic and 16 mL/min aqueous.	49
22.	Structures of candidate sterically constrained macrocyclic ligands under study: <i>N,N'</i> -bis[(6-carboxy-2-pyridyl)methyl]-4,13-diaza-18-crown-6 (bp18c6) and two new derivatives with longer picolinic acid arms.	50
23.	(a) Distribution ratios of Ln, Am, and Cm for loading of modified ALSEP solvent, 0.05 M TEHDGA/0.3 M HEDH[EHP] in dodecane from nitric acid. (b) Stripping stage distribution ratios for the modified ALSEP solvent contacted with 0.05 M bp18c6/0.4 M lactate at pH 3 show good separation of Am from Cm and lanthanides heavier than Pr.	51
24.	Advanced TALSPEAK from malonate buffer media with 0.02 M HEDTA. Organic phase: 0.2 M HEH(EHP) in <i>n</i> -dodecane.	52
25.	Plots of the distribution ratios for Am(III) and Eu(III) vs ligand concentration for 1a and 2a. Distribution measurements were made after contacting the organic phases (1,2-dichloromethane with variable concentration of ligand) with the aqueous phases (7 M LiNO ₃ , 10 ⁻⁴ M HNO ₃) at 1:1 v/v phase ratios at 25 °C.	53
26.	Camphor-BTP.	53
27.	Extraction of Am(III) and Eu(III) from nitric acid using 50 mM CA-BTP in FS-13. O:A = 1:1, <i>T</i> = 25°C. Left: 0.1 mM Ln Eu(NO ₃) ₃ . Right: 0.2 M Ln (La, Nd, Ce, Eu)(NO ₃) ₃	54
28.	Continuous-variation plot of Am(III) (open diamonds) and Eu(III) (open squares) distribution ratios for TOPO and bis-(<i>o,o</i> -trifluoromethylphenyl)dithiophosphinic acid dissolved in FS-13. Aqueous phase: 0.1 M HNO ₃	55
29.	Segregation of iodine and tritium through the use of sorbent beds.	61
30.	Deep bed adsorption test system.	64
31.	A schematic portraying the dual catalytic CH ₃ I decomposition and I confinement reaction pathway over the Ag [°] Z zeolite framework (-Si-O(-H)-Al-). The SMS unit is identified. Note: the fate of the charge balancing proton is not fully elucidated.	65
32.	New porous organic cage molecule (CC3) with 2X and 3X improved capacity and selectivity compared to NiDOBDC MOF. The perfect size to accommodate a single	

	xenon atom (cyan sphere). Two pore cavities exist in the 3D pore structure, a cage cavity inside the molecule itself (dark purple) and a window cavity between adjacent cage windows (light purple).....	66
33.	Elemental dot map of the HIP-consolidated iodine-loaded Ag ⁰ -functionalized silica aerogel.....	71
34.	(a) Snapshot from multiphase CFD simulation using multiphaseEulerFoam (Wardle & Weller 2013). (b) Image of a liquid-liquid dispersion taken <i>in situ</i> in an operating centrifugal contactor. (c) Redesigned and 3D printed ANL-2cm centrifugal contactor.....	77
35.	Structures of the two diglycolamides studied here: a. N,N,N',N'-tetraoctyldiglycolamide (TODGA) and b. N,N,N',N'-tetra-2-ethylhexyldiglycolamide (T(EH)DGA).....	78
36.	DGA concentration vs. absorbed dose. The solid squares are 0.05 M TODGA, the open diamonds are 0.05 M T(EH)DGA, the solid upward-facing triangles are 0.05 M TODGA contacted with 0.1 M HNO ₃ , the open inverted triangles are 0.05 M T(EH)DGA contacted with 0.1 M HNO ₃ , and the solid circles are 0.05 M TODGA contacted with 2.5 M HNO ₃	79
37.	Absolute organic to aqueous interfacial mass transfer constants.....	81
38.	Neodymium/Americium separation factor dependency on aqueous phase, pH and contact time.	81
39.	Sample absorption growth kinetics trace from the stopped flow spectrophotometer measuring the rate of reaction of Np(V) with AAIII at 650 nm. [Np] = 5x10 ⁻⁵ M, [AAIII] = 1x10 ⁻⁵ M I = 0.1 M, pH= 4.0, T = 21 ± 1°C. Open circles represent the measured data the red line represents the fit.	82
40.	Temperature dependence for the extraction of Eu, Cm, Am by TODGA. Organic phase: 0.0035 M TODGA in dodecane. Aqueous phase: 3.0 M HNO ₃	84
41.	Calorimetric titrations of the protonation of HEDTA, I = 1 mol/L NaClO ₄ , t = 25°C. (Top) a representative thermogram. (Bottom) A plot of Q _{partial} vs. the volume of titrant, Symbols of the bottom: ■ - experimental Q, lines – fit. Initial cup solutions: HEDTA, C _H ⁰ /C _L ⁰ (mmol/L) = 29.88/9.96; titrant: 99.83mmol/L NaOH, 5.0 μL/addition.	86
42.	Speciation of HEDTA as a function of acidity (-log[H ⁺]) at different temperatures. I = 1 mol/L NaClO ₄	86
43.	Fluorescence spectra (left) and lifetime (right) of Eu(III)/HEDTA at 25 °C. I= 1 M NaClO ₄ . Excitation. 395 nm, I ⁰ = 5.04 mL, C _{Eu} /C _L /C _H (mM) = 36.26/37.30/80.0. Titrant: 0.1 mM NaOH.	87
44.	Structural information for the lowest energy QM/MM optimized solution with coordinating water molecules. Only structurally significant water molecules are included in the figure. The bond distances are shown in Angstroms.	88
45.	Comparison of experimental Raman spectra of La-DTPA solutions from pH = 3 – 8, 11 and calculated Raman spectra of [La ^{III} (DTPA)-H ₂ O] ²⁻ (pink) and [La ^{III} (HDTA)-H ₂ O] ⁻ (green). The values were offset to show discernable differences between spectra.....	89
46.	Optimized structure of H ₃ DTPA ²⁻ and HLac in water.	89
47.	Molecular orbital diagram for [Eu(dtpa)(H ₂ O)] ²⁻	90
48.	MO diagram and associated spin-orbit splittings of UOCl ₅ ⁻ . The vertical axis is in Hartrees.....	92

**Material Recovery and Waste Form Development
2014 Accomplishments Report**

49.	Calculated scalar and spin-orbit TDDFT spectra for UOCl_5^- . Values are scaled for comparison with experiment.....	92
50.	The P K-edge XAS data from $[\text{AsPh}_4]\text{S}_2\text{P}(\text{C}_{12}\text{H}_8)$ (green trace), $[\text{AsPh}_4]\text{S}_2\text{P}(\text{o-CF}_3\text{C}_6\text{H}_4)_2$ (pink trace), $[\text{AsPh}_4]\text{S}_2\text{P}(\text{m-CF}_3\text{C}_6\text{H}_4)_2$ (black trace), $[\text{AsPh}_4]\text{S}_2\text{P}(\text{p-CF}_3\text{C}_6\text{H}_4)_2$ (gray trace), and $[\text{AsPh}_4]\text{S}_2\text{P}(\text{C}_6\text{H}_4)_2$ (blue trace).....	95
51.	Solution phase S K-edge XAS spectrum from $[\text{AsPh}_4][\text{Nd}(\text{S}_2\text{PPh}_2)_4]$ (3 M) in CH_2Cl_2	95
52.	Optimized synthetic steps for the preparation of new extractant design 1 in gram quantities.....	96
53.	Results of electrochemical tests with RAW-5 showing: (a) corrosion current, (b) Nyquist plot of EIS results showing decrease in corrosion resistance, (c) cumulative releases of U and alloy constituents, and (d) SEM image showing depletion of U-bearing phases at alloy electrode surface (black voids). (scale bar = 100 μm)	100
54.	Images of cross sectioned RAW-1 electrode after corrosion at 700 mV: (a) Optical micrograph showing corroded layer penetrating about 3 mm and SEM images (b) showing outer layer (A), inner layer (B), and uncorroded alloy (C) (scale bar = 500 μm), (c) region of outer layer A (scale bar = 500 μm), and (d) interface of regions B/C (scale bar = 100 μm).....	101
55.	Schematic reaction progress plot for glass corrosion.....	103
56.	Plot of the silicon isotopic ration with depth in ISG glass corroded in a ^{29}Si enriched solution. The miniscule ratio change in the amorphous alteration layer shows that only one atom in every thousand from that layer originated in the solution.....	105
57.	Interdiffusion profiles for labeled ions, including both fits (thin lines) and data (thick lines) for 10 day, 30 day, and 89 day measurements.	106
58.	Total alkali metal (M) concentration vs. pH for glasses that entered Stage 3 (solid symbols) or did not enter Stage 3 (open symbols) in long-term PCTs conducted at 90 $^\circ\text{C}$. Red symbols for HLW glasses and black symbols for LAW glasses.....	110
59.	Boron concentrations for PCTs with glasses (a) that do show Stage III behavior and (b) that do not show Stage III behavior: WV glasses (black), DWPF glasses (red), AFCI glass (blue), and SON68 (green). Solid symbols are for PCTs at $\sim 2000\text{ m}^{-1}$ and open symbols are for PCTs at $\sim 20,000\text{ m}^{-1}$	111
60.	Total alkali metal (M) concentration vs. pH for glasses that entered Stage 3 (solid symbols) or did not enter Stage 3 (open symbols) in long-term PCTs conducted at 90 $^\circ\text{C}$. Red symbols for HLW glasses and black symbols for LAW glasses.....	113
61.	Boron concentrations for PCTs with glasses (a) that do show Stage III behavior and (b) that do not show Stage III behavior: WV glasses (black), DWPF glasses (red), AFCI glass (blue), and SON68 (green). Solid symbols are for PCTs at $\sim 2000\text{ m}^{-1}$ and open symbols are for PCTs at $\sim 20,000\text{ m}^{-1}$	115
62.	Digital images of pour patties form laboratory scale melting of the (A) Fe-MP and (B) CAF-5%TM-MP compositions.....	120
63.	SEM micrograph and corresponding area map of CAF-5%TM-MP sample after cooling showing phase assemblage.	121
64.	Viscosity relationship of (\blacklozenge/\lozenge) Fe-MP and (\bullet/\circ) CAF-5%TM-MP compositions.....	121
65.	Pre-test fill of the Fe-MP surrogate charge into the crucible. Total crucible height is 14 in.	123

66.	Right Side: As observed through the south view port, the induced glowing of the second heaviest titanium ring (8.5"OD X 7.5"ID X 1/16H) just prior to the salt junction. Unlike the last ring, the second ring was only partially insulated with ~ 200 grams of Fe-MP surrogate from the hopper, as such allowing this visual. The left side shows the remaining segment of the second ring after its dissolution and removal from the crucible.....	124
67.	Left Side: The bridge at the top of the bed of the partial melt after initiation with the last heaviest titanium ring. The bridge was formed as anticipated since ~1kg of Fe-MP surrogate was added to the bed as insulation after the placement of the last ring. The partially melted ~8.5" diameter core (Right Side) resided about 1 inch below the bridge. Note the complete melt of the outer surface as the ring melted down the length of the crucible.....	125
68.	Shard of cold melt removed just below the core section shown in Figure 65 .The thin dark rim is consistent with high temperature melting in the annulus location of the third titanium ring. The yellow region indicates the extent of insufficient (for coupling) radial heat conduction in one location as a result of the ring being mobile. The remaining reddish area is the compacted original Fe-MP surrogate that is possibly only partially sintered.....	125
69.	Four shards of melted material taken from the marsh that possess sufficient dark melt volume for follow on analysis to determine if SynRoc phase(s) were made.....	125
70.	Chlorination Reactor.....	127
71.	Difference in cost as a function of salt impurity metal chloride loading for disposal in (a) salt repository and (b) clay repository	131
72.	(Left) VCR-fitting schematic containing a ceramic pellet. (Middle) Scheme to use VCR-fitting with ceramic pellets for volumetric salt purification. (Right) Photograph of assembled VCR-device in molten salt (after cooling test device to room temperature).....	134
73.	(Left) Potentiostatic discharge through and LLTO ceramic pellet. Constant applied potential was -200mV across the cell. Charge balance was maintained with Cu-chemistry.....	135
74.	Flume studies of the AF1 adsorbent showing color changes over time. The flume in use is shown in the bottom right.	139
75.	Time series marine testing of the AF1 series adsorbent	140
76.	RIGP-ATRP hybrid method (A), direct ATRP method (B)	140
77.	Calculated binding energies of some uranyl chelators.....	141
78.	Performance comparison of adsorbent treated with KOH at different conditions and tested with uranium screening solution.....	142
79.	U(VI) speciation under seawater conditions in the absence (upper figure) and presence of 0.01 M Ca(II) and 0.053 M Mg(II) (lower figure). $C_U = 1.4 \times 10^{-8} \text{ M}$, $C_{\text{carbonate}} = 0.0023 \text{ M}$. 1 - UO_2^{2+} , 2 - $\text{UO}_2(\text{CO}_3)(\text{aq})$, 3 - $\text{UO}_2(\text{CO}_3)_2^{2-}$, 4 - $\text{UO}_2(\text{CO}_3)_3^{4-}$, 5 - $\text{CaUO}_2(\text{CO}_3)_3^{2-}$, 6 - $\text{MgUO}_2(\text{CO}_3)_3^{2-}$, 7 - $\text{Ca}_2\text{UO}_2(\text{CO}_3)_3(\text{aq})$	144
80.	Time-series measurements of uranium adsorption capacity determined using flume exposure studies for 4 different formulations of the amidoxime-based adsorbent AF1 produced by ORNL. Data have been normalized to a salinity of 35 psu.....	146
81.	Time series measurements of adsorbent capacity for three different temperatures with the ORNL adsorbent AI8. Lines drawn through the data points were generated with a one-site ligand saturation model. Data were normalized to a salinity of 35 psu.....	147

82.	Temperature dependence on adsorption capacity. For experiments 1 and 2, the adsorption capacity represents 56 days of exposure. The data points for experiment 3 represent 35 days of exposure. The 32 degree point capacity for experiment 2 was taken from a separate biofouling experiment run concurrently with the temperature experiment. Data were normalized to a salinity of 35 psu.	148
83.	Model domain of the unstructured grid hydrodynamic model (FVCOM) adapted to the Coastal Waters off Washington State.	150

TABLES

1.	Tritium in Surry-2 cladding	32
2.	<i>D</i> values of lanthanides and ²⁴¹ Am and minimum SF in the dynamic flow extraction.....	35
3.	Summary of Projected Waste Form Masses and Volumes	38
4.	Aging studies completed at ORNL	62
5.	Maximum required DFs for the semi-volatile isotopes with the potential to yield 0.025 mRem to the MEL.....	68
6.	Comparative Criteria for MOF and Cryogenic Process Evaluations	73
7.	Complete set of thermodynamic parameters for Eu, Cm, Am extraction with TODGA from 3.0 M HNO ₃ . The thermodynamic data reported in Ref. 4 for Am extraction with TODGA from 1.0 M HNO ₃ is shown for comparison.	84
8.	Heats of extraction for Eu and Am extraction by 0.0035 M TODGA/0.0053 M HEH[EHP. The extractant ratios were scaled down to reflect the original ALSEP formulation.....	84
9.	Thermodynamic parameters for the protonation of HEDTA. <i>I</i> = 1.0 M NaClO ₄ and log $\beta_{H,M}$ represents the protonation constants in molarity.	85
10.	Thermodynamic parameters for the Nd(III)/HEDTA complexes at different temperatures. <i>I</i> = 1 M NaClO ₄ . log β_M represents the complex formation constants in molarity.	87
11.	Projected and re-normalized waste composition targeted in this study.	118
12.	Target Oxide Concentrations (wt. %) in Ceramic Waste Form.	119
13.	Equilibrium constants and enthalpy of Ca/Mg complexation with UO ₂ (CO ₃) ₃ ⁴⁻	144
14.	Stability constants of calcium, magnesium, and uranium complexes with glutarimidedioxime (denoted as H ₂ L in the table)	145
15.	Comparison of the stability constants of V(V) and U(VI) complexes with glutarimide-dioxime (denoted as H ₂ L in the table)	145
16.	Comparison of 56-day adsorption capacity (μg U/g adsorbent) ¹ for the ORNL AF1 adsorbent determined using both column and flume exposure methods	147
17.	Effect of temperature on adsorbent kinetics for three adsorbent materials. Values in the table represent the half-saturation time in days	148
18.	ORNL AF1 adsorbent characterization – elemental specificity	149

CAMPAIGN MANAGEMENT AND INTEGRATION

SECTION 1

1. MRWFD CAMPAIGN MANAGEMENT AND INTEGRATION

T. Todd, Idaho National Laboratory

1.1 Introduction

The Material Recovery and Waste Form Development (MRWFD) Campaign under the U.S. Department of Energy (DOE) Fuel Cycle Technologies (FCT) Program is responsible for developing advanced separation and waste form technologies to support the various fuel cycle options defined in the *DOE Nuclear Energy Research and Development Roadmap, Report to Congress, April 2010*. The fiscal year (FY) 2014 Accomplishments Report provides a highlight of the results of the research and development (R&D) efforts performed within the MRWFD Campaign in FY 2014. Each section contains a high-level overview of the activities, results, technical point of contact, applicable references, and documents produced during the fiscal year.

This report briefly outlines campaign management and integration activities, but primarily focuses on the many technical accomplishments made during FY 2014. The campaign continued to utilize an engineering driven-science-based approach to maintain relevance and focus. There was increased emphasis on development of technologies that support near-term applications that are relevant to the current once-through fuel cycle.

The MRWFD Campaign management and integration activities included international collaboration activities (France, China, Russia, Japan, European Union, and the International Atomic Energy Agency [IAEA]), integration of MRWFD Campaign activities with other FCRD campaigns, (Advanced Fuels, Used Fuel Disposition, Fuel Cycle Options, and Material Protection, Accountancy and Control Technology), and integration with DOE Office of Environmental Management (EM).

Technical accomplishments are reported under the following R&D categories:

- Reference Technologies and Alternatives
- Sigma Team for Minor Actinide Separations
- Sigma Team for Off-Gas Capture and Immobilization
- Fundamental Science and Methods, Modeling and Simulation
- Advanced Waste Form Characterization
- Advanced Waste Forms and Processes
- Domestic Electrochemical Separation Technologies
- Fuel Resources

Mission

Develop advanced fuel cycle separation and waste management technologies that improve current fuel cycle performance and enable a sustainable fuel cycle, with reduced processing, waste generation, and potential for material diversion.

Mission

Material Recovery and Waste Form Development, formerly Separations and Waste Forms, applies expertise and technical capabilities to a wide array of applications. This campaign now also leverages its expertise by working with others in areas such as environmental remediation, national security missions, as well as civilian nuclear applications. The mission of MRWFD is to

Develop advanced fuel cycle separation and waste management technologies that improve current fuel cycle performance and enable a sustainable fuel cycle, with minimal processing, waste generation, and potential for material diversion.

Mission implementation is outlined in the *Campaign Implementation Plan*, issued in November 2012. A revision will be made following issuance of a new Nuclear Energy Roadmap, expected in FY 2015.

Objectives

- Develop technologies that support the current once-through fuel cycle and have near-term potential application.
- Develop a fundamental and practical understanding of methods for the separation of uranium and transuranic elements from used fuel.
- Develop a fundamental and practical understanding of the factors affecting performance of advanced waste forms.
- Develop and demonstrate enabling technologies to separate and immobilize gaseous fission products from used nuclear fuel.
- Demonstrate predictable performance of advanced waste forms with greatly improved durability and waste loadings.

Challenges

- Separation of minor actinides from lanthanides.
- Capture and immobilization of off-gas constituents of used fuel, including iodine, krypton, tritium and potentially carbon in a cost-effective manner.
- Development of separation technologies and waste forms is very interrelated to the types of fuels being processed, the types of fuels being fabricated, and the reactors used to burn recycled fuels.
- Achievement of advanced separation and immobilization processes in a cost effective manner.

1.2 Major Research and Development Activities

Reference Technologies and Alternatives is developing and evaluating mass balances to enable objective comparison of technology performance for new separation technologies. Additionally, this activity supports development of on-line monitoring tools, evaluation of solvent degradation mechanisms, and development of tritium removal technologies (for open and closed fuel cycle applications). The focus in FY 2014 was on demonstrating the use of on-line monitors to measure the pH evolution during Trivalent Actinide - Lanthanide Separation by Phosphorous reagent Extraction from Aqueous Komplexes (TALSPEAK) and the closed loop NO₂ oxidation of sim-fuel at low temperature. In addition, the closed fuel cycle case study was updated and the closed fuel cycle waste management strategy was developed.

Sigma Team for Minor Actinide Separations is developing more robust and simplified approaches for separating minor actinides to enable future fuel cycles that transmute minor actinides for improved resource and waste management. There is a large international effort in nearly every fuel cycle country working on this difficult chemical separation and the Fuel Cycle Research and Development (FCRD) program is making significant progress on the development of cost-effective methods of separating the

Material Recovery and Waste Form Development 2014 Accomplishments Report

minor actinides from used fuel. In FY 2014, the first ever bench-scale demonstration was completed of tandem oxidation of Am and solvent extraction. A catalyst was developed for effective Am oxidation. A conceptual flowsheet of Actinide-Lanthanide Separation (ALSEP) and a fundamental understanding of TALSPEAK-like processes were developed.

Sigma Team for Off-Gas Capture and Immobilization is needed to enable licensing of any new fuel treatment facility to meet current regulations. The capture of iodine at very high decontamination factors is required and iodine has a very long half-life, so immobilization is important to reducing the source term in a geologic repository. Krypton (Kr) capture will be needed if processing fuel less than 30 years old. Tritium may also require capture. It is very important to understand the behavior of the entire off-gas system, to avoid cross-contamination of sorbents (e.g., iodine on tritium or krypton sorbent). For FY 2014, a process was developed to mitigate coadsorption of tritium and iodine, the Kr capacity was increased in capture materials, research was initiated on organic iodide capture, and the economics were evaluated of metal-organic-frameworks (MOF) for near room-temperature capture of Kr.

Fundamental Science and Methods Development Modeling and Simulation are utilizing new tools and research methods to understand the fundamental properties of extraction systems. These fundamental properties are the basis for understanding any separation process from a science-based approach rather than an empirical approach, which has been the typical approach used in the past. A greater understanding of the fundamental properties (such as thermodynamics, kinetics, effects of radiation on chemistry) will enable the development of more robust processes and also support future models that allow for a predictive capability of process performance. In FY 2014, the structure of phosphorous bonding sites was measured using X-ray absorption spectroscopy (XAS). The effects of alpha radiation were assessed on the stability of solvent extraction ligands. In addition, an initial model was developed for non-ideal mixing in the TALSPEAK system.

Advanced Waste Form Characterization is used to develop sufficient understanding of waste form degradation behavior to predict radionuclide release over geologic timescales. This fundamental understanding is required to optimize waste form chemistry and support disposal system performance assessment. In 2014, a database was created of glass corrosion characteristics that lead to accelerated corrosion. An expression for coupled glass corrosion and alteration product precipitation was developed, as well as an initial alloy waste form corrosion rate model. The performance characteristics of ancient analog glasses, was measured.

Advanced Waste Forms and Processes are necessary for the immobilization of waste streams from the advanced separation processes, including advanced aqueous and electrochemical processes. These waste forms are designed to improve the performance over current waste forms, such as borosilicate glass, over geologic time frames. Higher performance can be achieved by utilizing glass ceramic or ceramic waste forms. Any new waste form must be processed in production-scale continuous processing equipment. Ceramic containing waste forms must be processed at higher temperatures than glass waste forms; therefore standard joule-heated melters are not adequate. Investigation of cold crucible induction melters for processing advanced waste forms is in progress. The goal of this work is to significantly reduce the cost of waste treatment, storage, transportation and disposal, while improving performance. In FY 2014, a first-of-a-kind proof-of-principle melter test was performed with ceramic waste forms and a reference ceramic waste form was developed that immobilizes high level waste (HLW). An analysis was completed on the impact of oxide layer formation on cladding recycle kinetics. A composition variation study was initiated for glass ceramic HLW forms.

Domestic Electrochemical Separations Technologies is developing technologies to enhance performance and reduce waste volumes in the treatment of fast reactor fuels. This technology is ideally suited to treatment of metallic fuels for recycle of transuranics. In FY 2014, a trade study was performed on salt waste management and a proof-of-principle test was performed on selective ceramic membrane separations of CsCl . In addition a kg-scale unit for uranium/transuranic (U/TRU) codeposition studies was designed and constructed.

The Fuel Resources Program seeks to identify and implement actions to ensure that economic nuclear fuel resources remain available. The program will evaluate nuclear fuel resources and develop recovery technologies to enable a sustainable fuel cycle through increasing the fuel resources. Priority attention in the near term will focus on developing the technology for extraction of uranium from seawater.

Key Fiscal Year 2014 Deliverables

- Updated case study, including mass balances, on a set of potential fuel cycle technologies. This report forms a complete reference flowsheet for use in directing research. The current state-of-the-art technologies are shown in the context of an integrated flowsheet along with near-term target technologies for improved performance.
- Completed demonstration of pH monitoring of a TALSPEAK-like process using spectroscopic on-line monitoring of a flow extraction system. This activity has demonstrated the application of on-line monitoring in a prototypic unit operation at laboratory scale.
- Completed an optimization study for the use of MOF materials for Kr capture. This report documents the cost competitiveness of MOFs for near room-temperature Kr separation from fuel treatment off-gas.
- Completed a multi-kg simfuel dry tritium pretreatment process test with recycled gas. The demonstration showed the feasibility of recycling gas used in a low-temperature head end pretreatment of oxide fuel for tritium removal.
- Completed an analysis of the behavior of semi-volatiles under anticipated fuel processing plant conditions. This report summarizes the anticipated semi-volatiles and the associated mitigation requirements for successful fuel treatment.
- Demonstrated the ability to control of co-absorption of iodine and tritium. This test has quantified the challenge of iodine and tritium co-adsorption on capture media. The researchers propose a method to mitigate this challenge for successful off-gas treatment.
- Demonstrated the ability to extract americium (VI) in centrifugal contactor equipment.
- Demonstrated a process and associated equipment for the separation of hexavalent Am, which is effective in performing actinide recycle if a suitably stable species can be developed and process equipment capable of withstanding the highly oxidizing environment is developed. The demonstration shows promise of achieving the separation.
- Issued the “Closed Fuel Cycle Waste Treatment Strategy,” which updated the previous waste management studies performed during Global Nuclear Energy Partnership with more current philosophies on separations and summarizes and accounts for the considerable research performed over the last 5 years.

1.3 Campaign Structure

The campaign is organized in a flat structure to facilitate cross-campaign integration. Federal Project Directors are responsible for oversight and approval of all MRWFD work activities. The National Technical Director (NTD) and Deputy NTDs are responsible for work prioritization, integration, and management. Control account managers are responsible for integration of work packages within the control account, as well as monthly progress and budget status reporting.

Campaign leadership consists of:

- National Technical Director, Dr. Terry Todd, Idaho National Laboratory (INL)
- Deputy National Technical Director, Dr. John Vienna, Pacific Northwest National Laboratory (PNNL)
- Federal Project Director, Dr. James Bresee, Department of Energy Office of Nuclear Energy (DOE-NE)
- Federal Project Director, Fuel Resources and Domestic Electrochemical Separations Technology, NTD Fuel Resources, Dr. Stephen Kung, DOE-NE
- Federal Project Director, Waste Forms, Kimberly Gray, DOE-NE

1.4 Collaborations

T. Todd, Idaho National Laboratory, J. D. Vienna, Pacific Northwest National Laboratory

DOE Office of Environmental Management (EM) Collaboration

A long-standing interaction exists between the DOE Office of Nuclear Energy (NE) and the DOE Office of Environmental Management (EM), particularly in the areas of separations, waste forms, and disposal research. Many laboratory researchers work jointly for NE and EM, and many of the program objectives are similar. This close collaboration was formalized in 2011 by an MOU entitled, *Memorandum of Understanding between The Department of Energy Office of Environmental Management and The Department of Energy Office of Nuclear Energy for Used Nuclear Fuel and Radioactive Waste Management and Processing Research and Development*. The MOU, signed by Assistant Secretaries P. Lyons and I. Triay in March 2011, describes a policy of collaborative research and highlights several collaborative research tasks.

Three joint DOE NE-EM-National Nuclear Security Administration nuclear separations technologies workshops were held to identify common needs and requirements in separations as well as opportunities for partnerships between the three offices. The first such workshop was held in July 2011, the second in September 2012, and the third in December 2012. The outcome of these workshops were documented in meeting reports (the first published in 2012, the second in 2013, and the third in early 2014) and in a joint roadmap that describes the individual and collaborative research areas that will be pursued as part of this joint effort. The roadmap was drafted in 2014 and is due to be issued in the first quarter of fiscal year 2015.

A joint EM-NE-International glass corrosion study that started in 2010 was continued through 2014 (as described above).

IAEA-DOE Collaboration

The United States has a long history of nuclear energy research and development (R&D) collaboration with the international community through the International Atomic Energy Agency (IAEA). Specific areas of MRWFD collaboration in FY 2014 include:

- Participation in an international workshop titled “Advanced Actinide Recycle Technologies”
- Development of a technical handbook of “Treatment of Radioactive Gaseous Waste,” IAEA-TECDOC-1744, July 2014
- Participation in the Coordinated Research Project, “Processing Technologies for High-Level Waste, Formulation of Matrices, and Characterization of Waste Forms.”
- Participation in the preliminary study, “Waste from Innovative Types of Reactors and Fuel Cycles.”

These collaborations share methods, technologies, and research among practitioners from the member states. As such, there is a distinct advantage to campaign participation in that researchers gain valuable insight into the results from a wide range of member states that can be leveraged in conducting campaign R&D.

EU-DOE Collaboration

The European Union (EU) Framework Safety of Actinide Separation ProceSses (SACSESS) program is a 3-year effort that follows the very successful EU Actinide reCycling by SEParaTion (ACSEPT) program that ran for the four previous years and developed and demonstrated a number of new minor actinide separation processes. This program includes most of the leading European separation experts from the Commissariat à l’Énergie Atomique (CEA) in France; National Nuclear Laboratory (NNL) in the United Kingdom (UK); Forschungszentrum Juelich, Karlsruhe Institute of Technology, and the Institute for Transuranium Elements in Germany; Chalmers University in Sweden; and Czech Technical University and the Nuclear Research Institute in the Czech Republic, along with about 15 other European Universities.

The SACSESS program and the U.S. Fuel Cycle Research and Development (FCRD) MRWFD campaign are both interested in collaborating in this field. Scientists from the United States have been asked to participate in a number of ACSEPT and SACSESS meetings, but there is a mutual desire to have a more formal collaboration.

CEA-DOE Collaboration

The United States and France share a long history of nuclear energy R&D collaboration, particularly in the area of separations and waste management. In particular, DOE and CEA have had a very successful nuclear technology interchange for several decades. A *Nuclear Energy Cooperative Action Plan* was drafted in 2012, and a joint planning meeting was held in October 2012 at Argonne National Laboratory (ANL).

A technical meeting was held in Paris on May 2014, and progress was reported at the annual Steering Committee meeting on May 15, 2014. Plans for Waste Forms in FY 2015 are to contribute together on an international consensus on a source-term model for radionuclide release from glass.

**Material Recovery and Waste Form Development
2014 Accomplishments Report**

- CEA and PNNL have co-organized a broad international collaboration in the field of glass corrosion (7 countries involved).
- Significant achievement: The first time Atom Probe Tomography was successfully applied to the characterization of the passivating layer on a French R7T7-type glass, completed in 2012 during the 1year visit of French national expert S. Gin at PNNL.
- Future objectives: joint publications, further studies on the coupling of near-field conditions (effect of groundwater composition, effect of Fe and Fe-corrosion products) to the understanding gained in the first phase, and student exchanges (Lindsey Neill to CEA-Marcoule and Benjamin Parruzot to Washington State University).

DOE and CEA have both invested heavily for more than 30 years in the development of nuclear waste glass technology. Sharing of data, methods and models will benefit both nations in order to still improve the science and technology of waste vitrification. Initial efforts in FY 2015 will focus on:

- Sharing of glass property data and glass property-composition models for composition regions of mutual interest
- Building on the success of the collaboration in a number of these subjects, such as round-robin tests of common glasses or improving modeling and formulation approaches. Initial meetings were held to determine the appropriate first steps, describe the databases and methods from both organizations; further meeting will be organized in order to agree upon next steps to expand collaboration.

Iodine Waste Form Performance Assessment is a new topic with the objective to obtain a reliable calculation of the source term for iodine release from corroding waste forms. A common roadmap towards this outcome has been jointly established.

DOE and CEA are collaborating on joint research projects in areas related to separations, on benchmarking of minor actinide separation processes, and on discussion for possibly performing separation flowsheet tests on used nuclear fuel in the ATALANTE facility at Marcoule. Separations collaborative research is ongoing on:

- Degradation mechanisms of extraction molecules
- On-line process monitoring
- Capture of volatile off-gas constituents
- Better understanding of the mechanisms of extraction molecule selectivity for minor actinides.

Technical meetings on degradation took place between national experts in 2013 and 2014 (06/2014 in CEA/Marcoule) and it is planned that an US Postdoc (Jessica Drader) will work at CEA/Marcoule in 2015 on radiolysis and complexation of degradation products. About extraction molecule selectivity for minor actinides, a common publication is in progress, and next step is to plan a new workshop.

The benchmarking of minor actinide separation processes is a new collaboration topic, and it is planned to begin in US FY 2014 with a meeting to initiate this benchmarking activity (planning meeting held in Wurzburg, Germany during 2014 International Solvent Extraction Conference, September 2014)

The ATALANTE facility is a unique research facility capable of testing advanced flowsheets with multi-kg batches of fuel. The US program is currently planning to test minor actinide separation processes in the 2017-2018 time frame and to discuss the possibility of flowsheet testing at ATALANTE. Before an

active test, validation of a minor actinide separation process on simulated raffinate could be possibly performed with a test at Jülich Research Center (SACSESS European Project) in 2015 or 2016, depending on CEA and US support.

JAEA-DOE Collaboration

Collaboration with Japan on separations technology is carried out by the Civil Nuclear Working Group (CNWG), chartered under the *United States – Japan Bilateral Commission on Civil Nuclear Cooperation*. Japanese technical participation in the activities of the working group is primarily from the Japan Atomic Energy Agency (JAEA), with occasional involvement of the Central Research Institute of the Electric Power Industry (CRIEPI). The responsible Japanese agency is the Ministry of Education, Culture, Sports, Science and Technology.

The second meeting of the CNWG as well as a Steering Committee meeting was held in Japan, in February 2014 to review action plans and initiate discussions on detailed collaboration topics. Two areas relative to the Separations and Waste Forms Campaign are part of the collaboration: Aqueous separation from oxide fuels and uranium extraction from seawater.

The objective of the aqueous separation from oxide fuels activity is to share technical results and perform joint research activities on methods to separate minor actinides from lanthanides and select fission products (e.g. cesium) from used nuclear fuel. The first technical discussions were held in Oarai, Japan in February 2014. Japanese researchers visited ANL and INL in August 2014 to share technical results and discuss possible follow-on collaborative activities. Another technical workshop on the development of new minor actinide extractants is planned in October 2014, prior to the Separation Science and Technology Symposium, to be held at Oak Ridge National Laboratory (ORNL).

The objective of the uranium extraction from seawater activity is to jointly pursue the development of uranium extraction from unconventional resources, with a focus on harvesting uranium from seawater. This collaboration has been ongoing for a few years and has been very productive. Three collaborative tasks were identified: 1) Seawater uranium extraction technology cost analysis, 2) Adsorbent materials development by radiation induced graft polymerization, and 3) Marine testing of uranium recovery systems.

ROSATOM-DOE Collaboration

The “United States – Russia Civil Nuclear Energy Cooperation Action Plan” provides a framework with agreed upon areas of joint civil nuclear energy R&D cooperation for possible future collaborative activities. The “Action Plan” identifies specific technical activity areas of mutual interest within each of following technical elements:

- Reactor Demonstration Projects
- R&D for Innovative Nuclear Energy Technology Options
- Global Civil Nuclear Energy Framework Development
- Modeling and Simulation.

The long-term objectives are to leverage U.S. and Russian scientific and engineering resources and facilities to advance the growth of clean, safe, secure, and affordable nuclear energy through the development of innovative nuclear energy technologies, systems, and services. Both parties understand that the initial collaborative activities will be limited to those that do not require entry into force of the

“Agreement between the Government of the United States of America and the Government of the Russian Federation for Cooperation in the Field of Peaceful Uses of Nuclear Energy.” Collaboration activities with Russia were suspended early in FY-14 and it is unclear when they may resume again.

Russian scientists met at INL in October 2013, following the Global 2013 International Fuel Cycle Conference in Salt Lake City. A number of technical presentations were given by both Russian and U.S. researchers; many of the US participants were not able to travel due to the government slowdown. This meeting represented the fourth technical workshop on MRWFD Technologies.

Six Nation Collaboration on Long-Term Performance of Glass

The U.S. DOE is co-leading a six-nation collaborative effort to develop the technical basis for an international consensus nuclear waste glass corrosion rate model along with CEA (France) and JAEA (Japan). Belgium (SCK-CEN), France (CEA, Subatech), Germany (University of Bonn), Japan (JAEA, Kyushu University, Tokyo University), the United Kingdom (NNL, Sheffield University, Serco), and the United States (ANL, Alfred University, Lawrence Berkeley National Laboratory [LBNL], ORNL, PNNL, Pennsylvania State University [PSU], Savannah River National Laboratory [SRNL], University of North Texas, [UNT], Washington State University [WSU]) are participating in the collaboration.

Although the international community agrees on which phenomena occur during glass alteration, insufficient data is available on their rates to understand which control long-term performance under which disposal conditions. These processes include:

- Ion exchange between solid glass and solution
- Surface-controlled reaction
- Transport of ions to and from reacting glass surface
- Impact of alteration product formation.

A joint paper summarizing the current state of understanding and remaining challenges was issued by the study co-leads in fiscal year 2014 [1]. This article and a previous one [2] describe the focus of the collaborative efforts. In addition there are specific detailed bilateral agreements describing scope and milestones with CEA and JAEA.

Representatives from nine countries (six major partners plus Switzerland, China, and Turkey) shared data, techniques, and theories at an international workshop associated with a major conference in May in Aachen, Germany. A special issue of the International Journal of Applied Glass Science (*Glass Corrosion and General Glass Science*) containing 12 research articles from the international team summarizing their most recent results was compiled by the team.

An international workshop to compare potential analytical models of long-term performance of glass and outline a method to develop consensus on those models is scheduled for November 2014 in Tokyo.

References

1. Vienna, J.D., J.V. Ryan, S. Gin, and Y. Inagaki. 2013, “Current Understanding and Remaining Challenges in Modeling Long-Term Degradation of Borosilicate Nuclear Waste Glasses,” *International Journal of Applied Glass Science*, 4(4), 283-294.
2. Gin, S., A. Abdelouas, L.J. Criscenti, W.L. Ebert, K. Ferrand, T. Geisler, M.T. Harrison, Y. Inagaki, S. Mitsui, K.T. Mueller, J.C. Marra, C.G. Pantano, E.M. Pierce, J.V. Ryan, J.M. Schofield, C.I.

Steeffel, and J.D. Vienna. 2013. “An International Initiative on Long-Term Behavior of High-Level Nuclear Waste Glass,” *Materials Today*, 16(6), 243-248.

AREVA-JNFL-DOE Collaboration on Iodine Management

DOE, AREVA and Laboratory personnel have continued to explore several ideas for follow-on collaborations as a result of the site visits facilitated by AREVA to Rokkasho Japan and La Hague that would draw upon AREVA’s experience and could possibly be accomplished under the existing Advisory and Assistance Contract [A&AC DE NE 0000291 (IDIQ Task 10)] or similar mechanism. One of the areas of mutual interest is to examine in greater detail the release of volatile iodine species from operating facilities. The study of iodine pathways that was completed in FY13 was shared and reviewed by AREVA. An Excel model of the pathway for the four primary volatile radionuclides was developed and shared. This tool provides a means to evaluate the “critical” releases pathways that are thought to control the overall plant emissions. AREVA will be populating the spreadsheet with available data from LaHague and from Japan Nuclear Fuel Limited (JNFL) for review in early FY15.

Based on the anticipated results that will stem from the analysis, follow-on discussions are planned into identifying means to gain a better understanding of the iodine pathways through the reprocessing plants, the speciation of the iodine, and how the speciation is related to the iodine emitted from the facility. Initial discussions with AREVA indicate it may be possible to install a sampling system to specifically allow the determination of iodine species, i.e., elemental, organic (and specific organic iodide compounds), and/or particulate released at the main stack. Such studies would potentially lead to the installation of additional monitoring and sampling equipment on the main stack as well as reviewing historic stack data.

Comparable data requests directed to JNFL, a partner of AREVA and from Energy Solutions would be equally valuable and might be accomplished under a similar approach.

China-DOE Collaboration

As the two largest energy consumers in the world, the United States and the People's Republic of China share the view that nuclear energy is indispensable as an energy source for combating climate change as well as ensuring energy security. Further cooperation between both countries in the peaceful uses of nuclear energy will advance our shared objectives of nuclear non-proliferation, safety, and security. The *China–United States Bilateral Civil Nuclear Energy Cooperation Action Plan*, signed in Vienna, Austria on September 18, 2007, is a programmatic commitment for both countries to further facilitate joint long term R&D collaborative activities in advanced civilian nuclear technologies. Presently, seven technical working groups have been established and organized under the U.S.-China Nuclear Energy Action Plan cooperation framework. They are: (1) Advanced Separation Technologies, (2) Fast Reactor Technologies, (3) Advanced Fuels and Materials Development, (4) Safeguards and Physical Protection Technologies, (5) Nuclear Safety Enhancement, (6) Spent Fuel Storage and Repository Sciences, and (7) High Temperature Reactor Technologies.

The Advanced Separations Technologies Working Group’s mission is the collaborative development of advanced reprocessing and waste form production methods that enhance proliferation risk reduction, provide economic benefits, and reduce environmental impacts. The group seeks to achieve a mutually beneficial and equitable program of technological collaboration on the back end of the nuclear fuel cycle. Collaborative activities have been focused on:

- Management of tritium and iodine for advanced reprocessing
- Development of advanced aqueous product conversion methods

**Material Recovery and Waste Form Development
2014 Accomplishments Report**

- Development of pyrochemical recycling research facilities and technology
- Development of advanced on-line process monitoring and control instrumentation

Major Accomplishments, Ongoing and Future Activities. The co-chairs and technical experts met several times in the past two years to discuss topics related to head-end tritium capture, including requirements and regulatory issues, and iodine waste forms. The Steering Committee of the United States–China Bilateral Civil Nuclear Energy Cooperative Action Plan met on April 24, 2014, in Arlington, Virginia. The meeting reaffirmed the two sides’ commitment to cooperative research and development in civil nuclear energy. Future information exchange meetings will continue to focus on iodine and tritium management. Topics to be discussed are near- and long-term separations approaches, lab test protocols, data requirements to support future collaboration, and updates on recent developments. Potential topics for joint projects include iodine capture from dilute off-gas streams, iodine distribution and speciation, iodine waste forms, and tritium management for aqueous-based processes. The accomplishments since the last Steering Committee meeting are listed below:

- Completed an exchange of tritium and iodine management requirements for advanced reprocessing facilities
- Reviewed iodine pathways within reprocessing facilities and anticipated iodine speciation
- Drafted a detailed Multiyear Collaboration Outline.

The scope of the collaboration plan is broken down into near-term, mid-term, and long-term activities, and is further divided into primary topics: tritium management, tritium waste forms, iodine management, iodine capture, and iodine waste forms. The long-term goals of these activities are joint tests to be conducted within hot cell facilities in China.

REFERENCE TECHNOLOGIES AND ALTERNATIVES

SECTION 2

2. REFERENCE TECHNOLOGIES AND ALTERNATIVES

Reference and Alternative Technologies develops and evaluates mass balances to enable objective comparison of technology performance for new separation technologies. Additionally, this activity supports development of on-line monitoring tools, evaluation of solvent degradation mechanisms, and development of tritium removal technologies (for open and closed fuel cycle applications).

2.1 Solvent Degradation Mechanisms

D. R. Peterman, J. D. Law, Idaho National Laboratory

The INL is studying the impacts of gamma radiolysis on the Advanced TALSPEAK flowsheet. In the Advanced TALSPEAK process, the bis(2-ethylhexyl)phosphoric acid (HDEHP) extractant used in the traditional TALSPEAK process is replaced by the extractant 2-ethylhexylphosphonic acid mono-2-ethylhexyl ester (HEH[[EHP]]). In addition, the aqueous phase complexant and buffer used in traditional TALSPEAK is replaced with the combination of N-(2-hydroxyethyl)ethylenediamine-N,N',N'-triacetic acid (HEDTA) and citric acid. The structures of these compounds are shown in Figure 1.

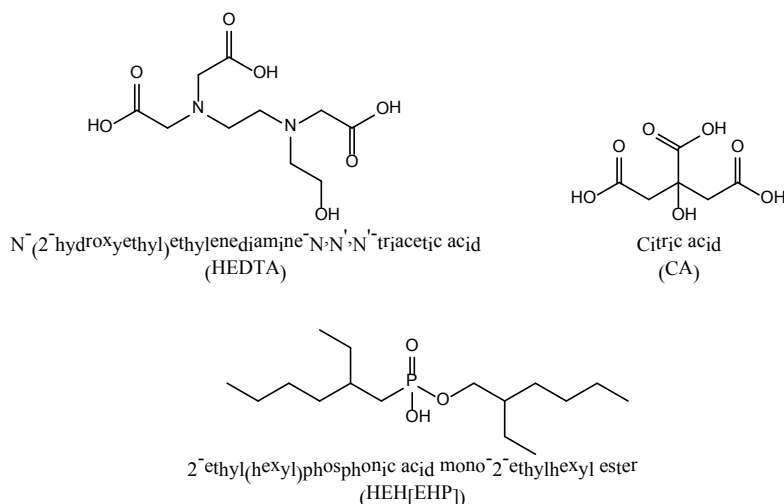


Figure 1. Structures of compounds used in the Advanced TALSPEAK process.

Separating the minor actinide elements (americium and curium) from the fission product lanthanides is an important step in closing the nuclear fuel cycle. Isolating the minor actinides will allow transmuting them to short-lived or stable isotopes, thereby reducing the long-term hazard associated with these elements. A two-step method has been studied by FCRD to separate the minor actinides from acidic high-level waste. The first step involves co-extracting the lanthanides and minor actinides using the transuranic extraction (TRUEX) process. The second step uses the Trivalent Actinide-Lanthanide Separations by Phosphorus-reagent Extraction from Aqueous Complexes (TALSPEAK) process to separate the minor actinides from the lanthanides. The tandem TRUEX-TALSPEAK approach has been demonstrated on irradiated fuel at a laboratory scale. However, the TALSPEAK process suffers the disadvantages of slow extraction kinetics and high sensitivity to the aqueous phase pH. To overcome these disadvantages, a variation of the TALSPEAK process has been proposed which replaces the traditionally used bis(2-ethylhexyl)phosphoric acid (HDEHP) extractant with 2-ethylhexylphosphonic acid mono-2-ethylhexyl ester (HEH[[EHP]]). [1] This is referred to as an Advanced TALSPEAK process. The key advantages of

switching to the HEH[EHP] extractant are reported to be: less dependence of the process performance on the aqueous solution pH, more predictable extraction behavior, and more rapid extraction kinetics. The Advanced TALSPEAK process is being considered as a candidate to replace conventional TALSPEAK in the FCRD full recycle case study.

The Advanced TALSPEAK solvent is comprised of 1 M HEH[EHP] dissolved in n-dodecane. The impacts of gamma radiolysis were investigated using two aqueous phase compositions, 0.125 M N-(2-hydroxyethyl)ethylenediamine-N,N',N'-triacetic acid (HEDTA) and 0.2 M citric acid ("normal citrate") and 0.125 M HEDTA and 1.5 M citric acid ("high citrate"). In the case of the "normal citrate" aqueous composition, the distribution ratios for americium and europium increased dramatically with increasing absorbed dose. While the separation factors for europium from americium ($SF_{Eu/Am}$) vary from $SF_{Eu/Am} \sim 84$ at 0 kGy absorbed dose to $SF_{Eu/Am} \sim 26$ at 1130 kGy absorbed dose, the value of D_{Am} increases from $D_{Am} = 0.78$ at 0 kGy absorbed dose to $D_{Am} = 1.4$ at 271 kGy. For comparison, gamma irradiation of 1 M HEH[EHP] in contact with 1.5 M lactic acid and 0.05 M diethylenetriaminepentaacetic acid (DTPA) up to 200 kGy absorbed dose yielded $SF_{Eu/Am} \sim 74$ with $D_{Am} = 0.05$ and $D_{Eu} = 3.7$. The significant increase in the value of D_{Am} with increasing absorbed dose was attributed to the slower rate of reaction of citric acid (relative to lactic acid) with radiolytically produced hydroxyl radical.

For the γ -radiolysis of acidic aqueous and organic mixtures, the hydroxyl radical is the predominate radical species present in solution.[2] The variation in the rate constants for the reaction of hydroxyl radical with different polyaminopolycarboxylates and carboxylic acids can explain the differences observed for the irradiation of the TALSPEAK and Advanced TALSPEAK solvent systems. The primary mode of interaction between hydroxyl radical and polyaminopolycarboxylic and carboxylic acids is H-atom abstraction.[3] In order to confirm the importance of hydroxyl radical chemistry, static irradiations were performed using a "high citrate" aqueous concentration of 1.5 M and 0.125 M HEDTA. The data for the "high citrate" composition are strikingly different than what was observed for the "normal citrate" irradiations. The americium and europium distribution ratios increase in both experiments, but the magnitudes of the increases were significantly smaller when the "high citrate" concentration was used. The value of D_{Am} increases from $D_{Am} = 0.087$ at 0 kGy absorbed dose to $D_{Am} = 0.86$ at 570 kGy and the corresponding separation factors for the "high citrate" system vary from $SF_{Eu/Am} \sim 50$ to $SF_{Eu/Am} \sim 13$ at 0 kGy and 570 kGy absorbed dose, respectively.

The extent of radiolytic degradation of HEH[EHP] and HEDTA in the "high citrate" Advanced TALSPEAK composition are significantly smaller than observed using the "normal citrate" composition. The reduction in radiolytic degradation observed for the "high citrate" composition is consistent with the higher citrate concentration being able to effectively scavenge more hydroxyl radical which leads to less degradation of HEH[EHP], HEDTA, or citric acid. The main radiolytic degradation product of HEH[EHP] is thought to be monoethylhexylphosphonic acid (or a degradation product of that species) and the main radiolytic degradation product of HEDTA is glycolic acid.

Continuing work will include determination of the minimum concentration citric acid required to ensure effective operation of the Advanced TALSPEAK flowsheet. These studies would be performed using the INL Test Loop. In addition, the impact of radiolysis on the remaining sections of the Advanced TALSPEAK flowsheet will be evaluated with the INL Test Loop.

References

1. Braley, J. C.; Grimes, T. S.; Nash, K. L. "Alternatives to HDEHP and DTPA for Simplified TALSPEAK Separations," *Industrial & Engineering Chemistry Research*, 2011, 51, 629.

2. Mincher, B.J.; Mezyk, S.P. "Radiation chemical effects on radiochemistry: A review of examples important to nuclear power." *Radiochimica Acta*, 2009, 97, 519.
3. Bxton, G. V., Greenstock, C. L.; Helman, W. P.; Ross, A. B. "Critical review of rate constants for reactions of hydrated electrons, hydrogen atoms and hydroxyl radicals ($\cdot\text{OH}/\cdot\text{O}$ -) in aqueous solution." *Journal of Physical and Chemical Reference Data*, 1988, 17, 513.

Publications

1. Peterman, D. R.; Olson, L. G., McDowell, R. G., Groenewold, G. S., Zarzana, C. A., Bauer, W. F., Morgan, S. J. *Investigation of the Impacts of Gamma Radiolysis on an Advanced TALSPEAK Separation*, Idaho National Laboratory, FCRD-SWF-2014-000205, August 15, 2014.
2. Peterman, D. R.; Olson, L. G., McDowell, R. G. *Initiate test loop irradiations of ALSEP process solvent*, Idaho National Laboratory, FCRD-SWF-2014-000206, September 30, 2014.

2.2 Tritium Pretreatment

G. D. Delcul, B. B. Spencer and R. D. Hunt, Oak Ridge National Laboratory

A dry pretreatment process based on the oxidation of used nuclear fuel is being studied for the removal and capture of tritium and iodine prior to the fuel dissolution step. The process converts oxide fuel into a fine powder at low temperature using oxygen and nitrogen dioxide (NO_2) as a gas catalyst. The powder product can be selected to be triuranium octoxide (U_3O_8), uranium trioxide (UO_3), or a nitrated form of uranium by adjusting the processing conditions. The UO_3 dissolves readily in HNO_3 without gas evolution, allowing for a very fast "fumeless" dissolution that can produce higher concentrations of uranyl nitrate at lower acidities than may be obtained from direct dissolution of uranium dioxide (UO_2). Therefore, the dissolution time can be shortened from several hours to minutes while also reducing the volume and acid concentration of the dissolver solution and generating a dissolver product with higher actinide concentration. The latter advantage potentially translates into smaller tankage and less volume of residual raffinate waste, decreased facility footprint, and reduced facility cost. The nitrated form can be readily dissolved by an organic solvent (e.g., TBP), leaving behind most of the fission products that remain insoluble, thus completely eliminating the high-acid raffinate waste stream.

An instrumented recirculation system based on the catalytic oxidation of UO_2 pellets using NO_2/O_2 mixtures was built (see Figure 2) and tested to determine the behavior and stability of such a system during the consecutive treatment of several batches of UO_2 pellets. Eight 0.5-kg batches of unirradiated UO_2 pellets were successfully reacted with NO_2 to produce fine UO_3 powders. The product from each test displayed the typical brick-red color of $\epsilon\text{-UO}_3$ that is produced by NO_2 , and the weight gained matched the UO_3 stoichiometry.

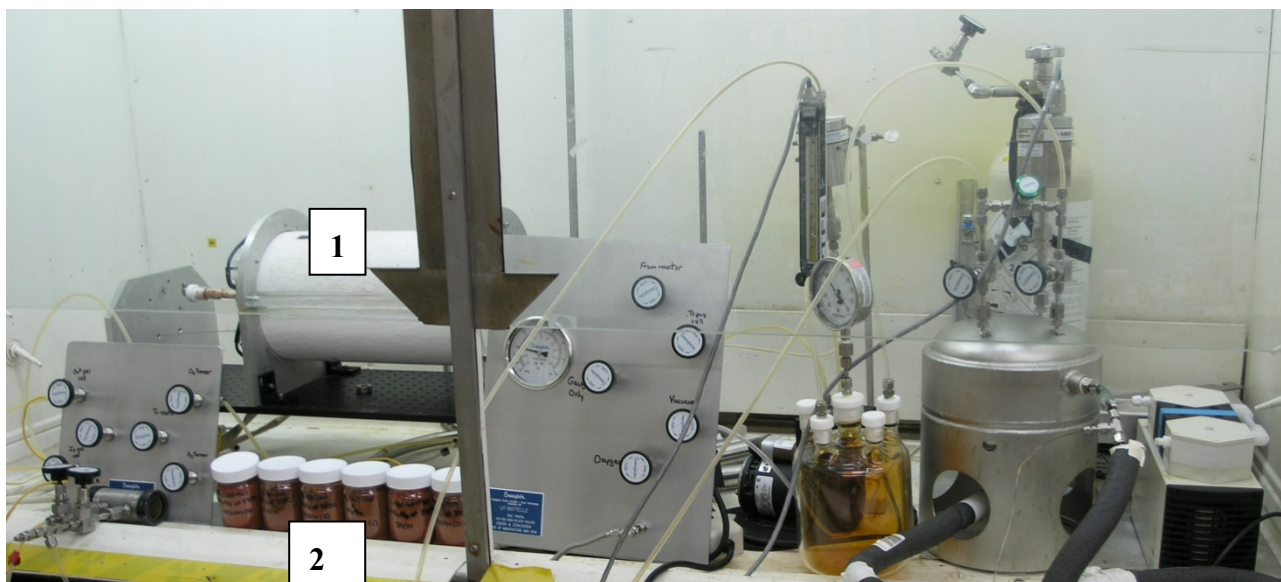


Figure 2. Laboratory system components housed in a radiochemical hood. 1: furnace with reactor and 2: six of the UO_3 batches generated by the process

To ascertain the actual behavior of hydrogen (tritium) in the NO_2 recirculation loop, hydrogen, water, and nitric acid were introduced into the system and composition of the recirculating gas mixture analyzed using Fourier transform infrared spectroscopy (FTIRS). The experimental results confirmed the equilibrium calculations. At room temperature HNO_3 was observed but at the operating temperature only water was observed. In fact, when HNO_3 was injected into the system it rapidly decomposed into $\text{NO}_2/\text{N}_2\text{O}_4$ and water.

Hydrogen added into the system without any sample in the reactor chamber very slowly transformed into water. However in the presence of uranium oxide powder or copper oxide it rapidly reacted into water.

In standard air or oxygen oxidation, a copper oxide catalyst is usually used to ensure conversion of hydrogen (tritium) into water followed by water trapping using a molecular sieve. The uranium oxide powder generated by NO_2 catalyzed oxidation appears to be as effective as copper oxide to catalyzed the conversation of hydrogen (tritium) into water. Accordingly, there is no need for a copper oxide catalyst to be added to the system.

Three trapping materials were tested for the removal of water. They included molecular sieve 3A provided by the sigma team, Sorbead WS® and silica gel 60®. All three sorbents removed and trapped the water from the NO_x gas mixture; however, the Sorbead and silica gel 60 also trapped a significant amount of NO_x . All three materials appear to be stable under NO_x when exposed for a few days. Long-term stability (months) needs to be evaluated.

From this preliminary scoping tests, it appears molecular sieve 3A is a suitable material for trapping water from the NO_2 catalyzed oxidation process. The total amount of hydrogen (tritium) in used fuel is of the order of parts per billion. The resulting amount of water is too small for the molecular sieve to be effective. In practice, some level of humidity will have to be introduced into the recirculation system with the reagent oxygen. The optimum level of humidity required for an efficient tritium removal is one of the variables that need to be investigated.

To present, all of the major tenants of the process has been tested and successfully corroborated at kilogram scale with surrogate materials and at gram scale with actual fuel.

Patents

1. Two provisional U.S. patents were awarded for the “Advanced Dry Head-End Reprocessing of Light Water Reactor Spent Nuclear Fuel”
2. Patent US 8,747,790 B2 was awarded on June 10, 2014 and the Patent No. 8,574,523 was issued on November 5, 2013

2.3 Online Sampling & Monitoring at PNNL

S.A. Bryan and Amanda J. Casella, Pacific Northwest National Laboratory

Significant effort has been focused on the back end of the nuclear fuel cycle, including treatment and reuse of irradiated fuel. Solvent extraction reprocessing methods that have been developed often contain various steps, with each one tailored to the separation of specific radionuclides, which are highly dependent upon solution properties. Acid strength/pH is of critical importance for process quality and control, as it affects speciation of the target fuel components and thus their extraction efficiency and selectivity. In a full-scale nuclear fuel reprocessing facility, classic potentiometric pH measurements are not suitable for obtaining real-time continuous data due to their requirements of frequent calibration and maintenance and poor long-term stability in aggressive chemical and radiation environments. Towards addressing this need, this work aimed to develop a general method for determining pH by spectroscopic methods, which provides real-time remote on-line monitoring capability. Solution chemistry relevant to the TALSPEAK process was utilized to develop this method.

In FY 2013, we demonstrated process monitoring of pH and Nd concentration using a traditional TALSPEAK flowsheet. The aqueous phase of the TALSPEAK process consisted of a lactic acid buffer and diethylenetriamine-N,N,N',N'',N''-pentaacetic acid (DTPA) as the actinide hold back reagent while the organic phase contained the extractant di(2-ethylhexyl)phosphoric acid (HEDHP)[1]. To demonstrate the utility of our process monitoring technique across various flowsheet applications, we have extended this work in FY 2014 for use with the Advanced TALSPEAK system.

The objective of this experiment was to demonstrate the utility of optical process monitoring methods, with the goal of being able to simultaneously measure pH and metal ion concentration using Raman and visible (vis) near infra-red (NIR) spectroscopic methods, respectively. The pH was monitored using Raman spectroscopy for all aqueous streams, while the Nd³⁺ concentration was monitored by vis-NIR for all inlet and outlet streams. Multiple sample locations were measured simultaneously using optical-multiplexers connected to both the Raman and vis-NIR spectroscopic systems, for the direct and simultaneous measurement of the feed inlet, aqueous raffinate outlet, organic solvent inlet, and organic product outlet. The following sections contain the results of Raman and vis-NIR measurements using solutions mimicking the Advanced TALSPEAK streams.

The concentrations for the aqueous and organic phases simulated those used in the Advanced TALSPEAK system. This lanthanide/actinide separation system was chosen for demonstration purposes to compare with data currently being obtained by other researchers under the MRWFD Campaign. Figure 3 (left) shows the organic and aqueous phase reagents used in the Advanced TALSPEAK extraction system. The extraction of neodymium is favored at low pH values (pH ~3; right panel), and is less favored at higher pH values (pH ~4; right panel) [2, 3].

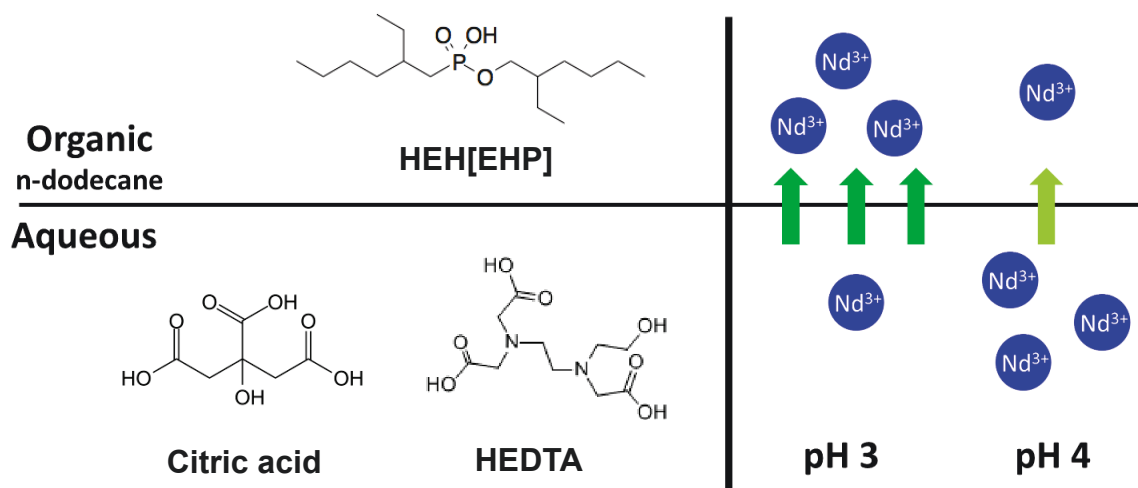


Figure 3. Organic and aqueous phase reagents used in the Advanced TALSPEAK extraction system. The extraction of neodymium is highly favored at low pH values (pH ~ 3), and is less favored at higher pH values (pH ~4).

The experimental design for performing spectroscopic monitoring on Advanced TALSPEAK separation process included on-line measurements of the process during a pH change of the process feed. At the beginning of the experiment, the pH of the feed was set at ~3, a value chosen for optimal extraction of neodymium. At a predetermined time, the pH was increased to ~4 by adding a base (NaOH), at which neodymium extraction would be less favored. Time was allowed for steady state extraction conditions to be reestablished, and then the pH was reduced by the addition of nitric acid to the original pH value to reestablish conditions more favorable to the extraction of neodymium. The contactor experiment was carried out using a single stage in a 2-cm centrifugal contactor bank. The aqueous inlet and outlet streams were monitoring for pH using Raman in-line probes, while the inlets and outlets of both aqueous and organic streams were monitored for Nd using vis-NIR probes.

The centrifugal contactor system test was initially started with an aqueous feed composed of 20 mM $\text{Nd}(\text{NO}_3)_3$ at pH 3.1. The other components in the aqueous phase include the Advanced TALSPEAK system components (0.125 M HEDTA, and pH buffering by a 0.2 M citrate/citric acid buffer); the organic phase was composed of 1.0 M HEH[EHP] in *n*-dodecane. The aqueous phase and organic phase flow rates were set at approximately 10 mL/min each. After approximately 135 minutes of stable flow through the system, the feed solution was adjusted by the addition of NaOH pellets to induce a pH change to achieve a final solution pH of 4.2. At approximately 255 minutes, the feed solution was adjusted to a lower pH by the addition of nitric acid, resulting in a final feed pH of 3.2. This pH 3.2 solution was used as the feed for the remainder of the test (~340 minutes).

Raman and vis-NIR spectroscopic monitoring of the feed, raffinate, solvent, and organic product streams were recorded during the entire flow test. The real-time Raman spectroscopic measurement of the aqueous raffinate phase is shown in Figure 4. The Raman band located at approximately 830 cm^{-1} associated with the protonated lactic acid (vC-COOH) is the most intense band in this region at the beginning of the flow experiment (times 0 to approximately 135 minutes). The pH of the raffinate stream is slightly lower than the feed, due to the transfer of H^+ into the aqueous stream when Nd^{3+} is extracted into the organic phase. When the pH is increased by the addition of NaOH to the feed at time 135 minutes, the Raman band associated with lactic acid decreases in intensity, and a new band associated with the deprotonated lactate (vC-CO_2^- at approximately 860 cm^{-1}) becomes the prominent Raman band. The pH of the raffinate after NaOH addition to the feed was measured independently to be 4.1, again

lower than the feed pH owing to the transfer of H^+ into the raffinate upon extraction of Nd^{3+} . When the pH of the feed was decreased upon addition of nitric acid at 255 minutes, the lactate band in the raffinate diminishes and the lactic acid band is once again the most prominent band in this region, with a resulting measured pH of 3.2.

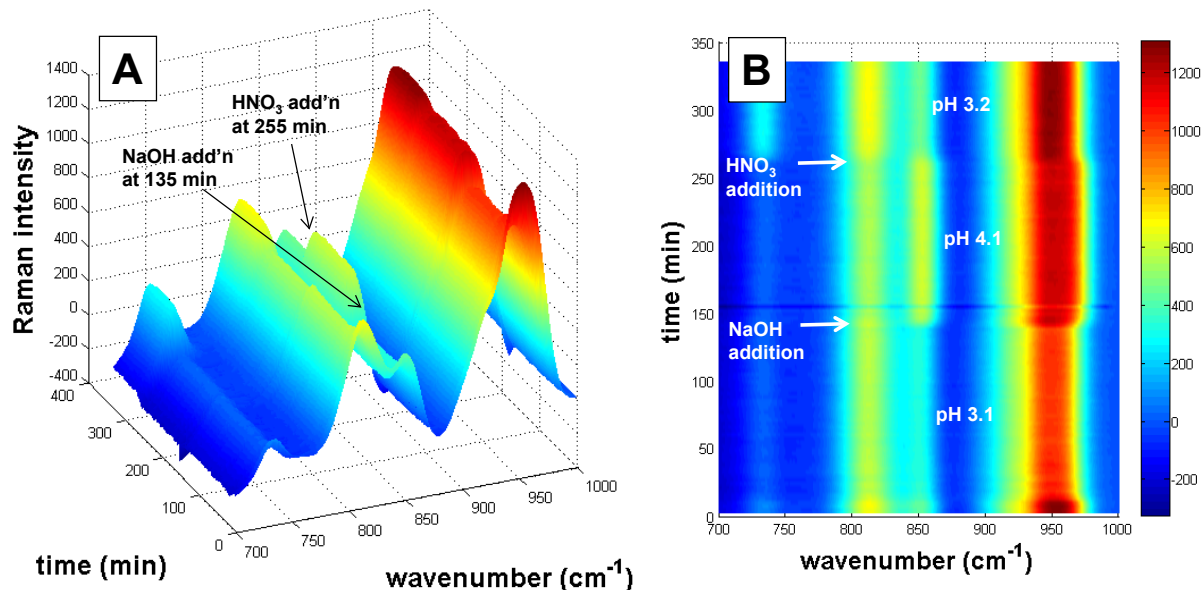


Figure 4. Real-time Raman spectroscopic measurements of the aqueous raffinate phase. A) The Raman spectra are shown over the entire experiment from time = 0 to 340 min, the addition of NaOH and HNO_3 are indicated on the figure. B) Overhead view of spectra; the relative Raman band intensity is specified by color as indicated in the legend. The pH of the solution at various time intervals is labeled on the figure.

The feed and raffinate Raman measurements from the flow test were analyzed using the chemometric model, using a training set specifically for the Advanced TALSPEAK flow experiment. The training set allows for the variation in citrate, HEDTA, $Nd(NO_3)_3$, and pH. The pH was predicted for the feed and raffinate phases; results of the raffinate phase measurements are shown in Figure 5A and are compared with grab sample measurements. Figure 5B shows a comparison of pH measured by on-line process monitoring vs grab sample pH measured values for feed and raffinate contactor test solutions, showing excellent agreement between on-line method and grab sample measurements.

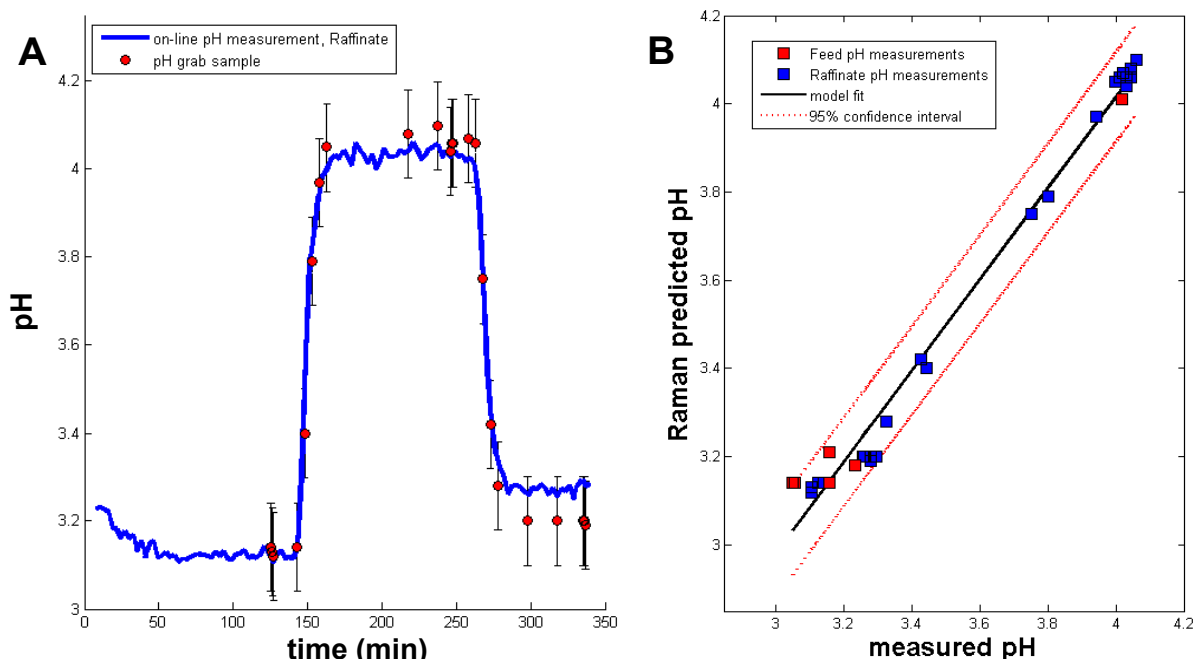


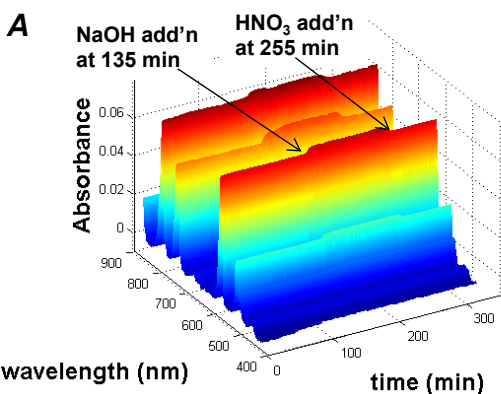
Figure 5. A) Prediction of pH for raffinate phase as a function of run time during continuous centrifugal contactor test, and compared with grab sample measurements. B) Comparison of pH measured by on-line process monitoring vs grab sample pH measured values for feed and raffinate contactor test solutions. Fit of data, $Y = 1.0364X - 0.1258$, $r^2 = 0.9866$.

All feed and product streams were measured for the amount of neodymium using vis-NIR spectroscopy during the Advanced TALSPEAK contactor experiment. Figure 6 shows the vis-NIR spectra of the A) aqueous feed, B) raffinate, C) organic solvent and D) organic product phases. These spectra were recorded during the continuous-flow centrifugal contactor experiment measuring the effect of pH on Nd^{3+} extraction using real-time spectroscopic process monitoring techniques.

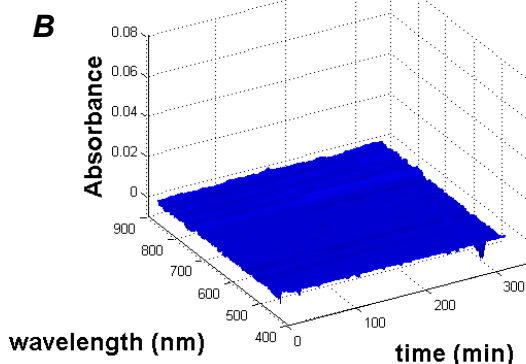
For the aqueous feed (Figure 6A), the vis-NIR bands are relatively constant throughout the entire experiment timeframe (0 to 340 minutes). There is minimal perceptible change in band intensity when solid NaOH was added (at time = 135 minutes), and a slight decrease in band intensity due to dilution when the 16 M HNO_3 was added (at time = 255 minutes). The organic feed stream, shown in Figure 6C, contains only HEH[EHP] in *n*-dodecane, and shows no observable change in the vis-NIR region throughout the entire experiment.

For the aqueous raffinate stream, minimal Nd^{3+} is observed in the vis-NIR spectra (shown in Figure 6B) prior to the addition of NaOH to the feed (time = 0 to 135 minutes). This initial period corresponds to the feed with pH of 3.1, which, under the Advanced TALSPEAK extraction conditions, favors the extraction of Nd^{3+} into the organic phase. After NaOH is added to the feed (at time = 135 to 255 minutes), the measured pH of the feed was 4.1, and concurrently the vis-NIR bands for Nd^{3+} increased in the raffinate stream. The period during which pH of the feed was elevated to 4.2 (135 to 255 minutes) corresponds to advanced TALSPEAK extraction conditions not favoring the extraction of Nd^{3+} into the organic phase; therefore, it is expected that the neodymium would be retained in the aqueous raffinate phase. Upon addition of nitric acid to the feed at 255 minutes, the pH of the feed was adjusted to 3.2, nearly the same value as the initial feed composition. After this pH adjustment, the vis-NIR bands for Nd^{3+} in the raffinate stream decreased, an indication of the increased extraction into the organic phase, as predicted based on the Advanced TALSPEAK extraction conditions favoring extraction of Nd^{3+} at lower pH values.

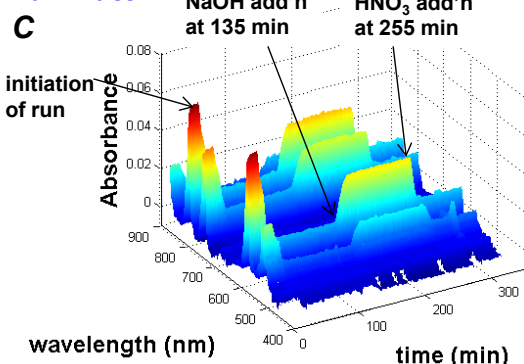
Aqueous feed



Organic feed



Raffinate



Organic product

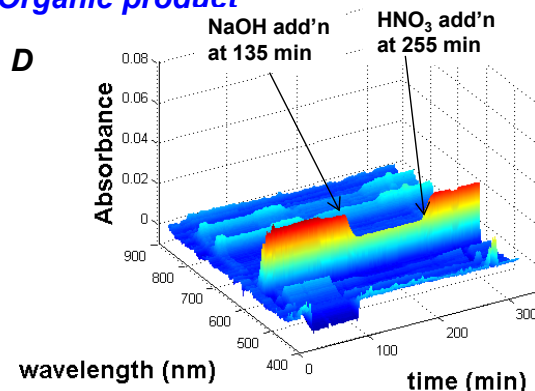


Figure 6. Real-time UV-vis-NIR spectroscopic measurements of the A) aqueous feed, B) organic feed, C) raffinate, and D) organic product phases. The spectra are shown over the entire experiment from time = 0 to 340 min, the addition of NaOH and HNO₃ are indicated on the figure at 135 min and 255 min respectively.

The vis-NIR spectra measured for the organic product stream mirrors conditions shown in the raffinate stream. Figure 6D shows the UV-vis-NIR spectra measured for organic product. During the initial period of the experiment (time = 0 to 135 minutes), the vis-NIR bands due to the presence of Nd³⁺ in the organic phase are prevalent, indicating a relatively high concentration of Nd³⁺ in the organic phase during this experimental period during which the feed pH was maintained at 3.1. This is consistent with the expectation of preferential extraction of Nd³⁺ with the Advanced TALSPEAK system at low pH values. When the pH is increased by the addition of NaOH at the 135 minute mark, the vis-NIR bands decrease in intensity, again consistent with the expectation of reduced Nd³⁺ extraction in TALSPEAK solvent at higher pH values. When the pH is decreased to 3.2 by the addition of HNO₃ in the feed (at time = 255 min and later), the Nd³⁺ bands increase again in the organic phase, consistent with the expectation of higher extraction rates of Nd³⁺ in Advanced TALSPEAK solvent system at low pH values.

The vis-NIR solution spectra shown in Figure 6 were analyzed for Nd³⁺ concentration using the chemometric model described previously [4-6]. The predicted Nd³⁺ for the aqueous feed, raffinate, organic feed, and organic product of each solution are shown in Figure 7A.

The time for addition of NaOH to the feed solution is marked on Figure 7A and coincides with the decrease in extraction of Nd³⁺ in the TALSPEAK organic phase solvent. The addition of nitric acid is also marked in this figure and coincides with the decreased extraction of Nd³⁺ into the organic product phase. Several samples were taken from the aqueous feed and aqueous raffinate streams during the process for traditional Inductively Coupled Plasma-Optical Emission Spectroscopy (ICP-OES) analysis,

the results of which are also shown on this figure. In all instances, the ICP confirmation agrees well with model prediction.

Neodymium D values obtained in this experiment are much lower than is expected based on equilibrium D values of this system [1]. According to Figure 7B, the lower end of the Nd D pH range is ~3; but the equilibrium D value data indicate it should be ~10. Likewise at the higher end of the pH range, the D value drops to approximately 0.7; but equilibrium values suggest it should be ~7. This can be attributed to the residence time in the contactor being too short to achieve the equilibrium D value [7-9]. In general, the extraction of Nd^{3+} follows the pH swing in the system. In all cases, the neodymium measured by ICP in the grab samples aligns well with the spectroscopically determined neodymium concentrations.

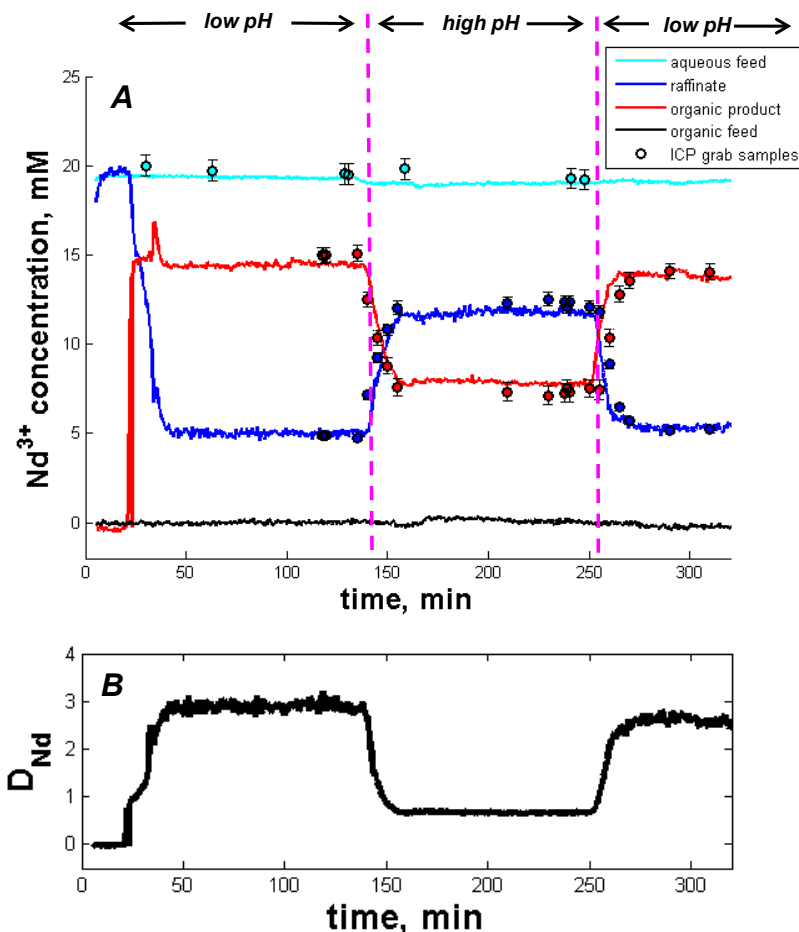


Figure 7. A) Measurement of Nd^{3+} concentration by spectroscopic method, for aqueous feed, aqueous raffinate, organic feed and organic product phases as a function of run time during continuous centrifugal contactor test. **B)** Distribution ratio for Nd^{3+} as a function of run time.

References

1. Nilsson, M. and K. L. Nash, Review article: "A review of the development and operational characteristics of the TALSPEAK process." *Solvent Extraction and Ion Exchange*, 2007, 25(6), 665-701.
2. Braley, J. C., T. S. Grimes, and K. L. Nash, Alternatives to HDEHP and DTPA for Simplified TALSPEAK Separations. *Industrial & Engineering Chemistry Research*, 2012, 51(2), 629-638.

3. G. J. Lumetta, S. I. Sinkov, C. M. Niver, and M. R. Smoot, *Advanced TALSPEAK Process Development: FY 2014 Results*, 2014, Pacific Northwest National Laboratory.
4. Bryan, S. A., T. G. Levitskaia, A. M. Johnsen, C. R. Orton, and J. M. Peterson, "Spectroscopic Monitoring of Nuclear Spent Fuel Reprocessing Streams: An Evaluation of Spent Fuel Solutions via Raman, Visible, and Near-Infrared Spectroscopy," *Radiochimica Acta*, 2011, 99, 563-571.
5. Bryan, S. A., T. G. Levitskaia, A. J. Casella, J. M. Peterson, A. M. Johnsen, A. M. Lines, E. M. Thomas, and C. Orton, "Spectroscopic On-Line Monitoring for Process Control and Safeguarding of Radiochemical Streams," in *Advanced Separation Techniques for Nuclear Fuel Reprocessing and Radioactive Waste Treatment*, K.L. Nash and G.J. Lumetta, Editors. 2011, Woodhead Publishing Ltd; CRC Press LLC.: Cornwall, UK.
6. Bryan, S. A., T. G. Levitskaia, J. M. Schwantes, C. R. Orton, J. M. Peterson, and A. J. Casella, "Monitoring, Controlling and Safeguarding Radiochemical Streams at Spent Fuel Reprocessing Facilities, Part 1: Optical Spectroscopic Methods," *International Journal on Nuclear Energy Management and Safety*, 2012.
7. Casella, A. J., L. R. Hylden, E. L. Valerio, J. M. Peterson, G. J. Lumetta, T. G. Levitskaia, and S. A. Bryan. "Advances in On-Line Monitoring for Weak Acid Based Nuclear Fuel Reprocessing Schemes," in *American Nuclear Society, Winter Meeting*, 2013.
8. Casella, A. J., T. G. Levitskaia, G. J. Lumetta, C. M. Niver, and N. K. Pence, "Single-Stage 2-cm Contactor Tests of the Advanced TALSPEAK Process," 2014, Pacific Northwest National Laboratory.
9. Bryan, S. A., A. J. Casella, T. G. Levitskaia, L. R. Hylden, and G. J. Lumetta, "Advances in On-Line Monitoring for Weak Acid Measurement within Nuclear Fuel Reprocessing Streams," in *38th Actinide Separations Conference*, 2014.

2.4 Baseline H-Canyon Accountability

T. F. Severynse, Savannah River National Laboratory

Effective protection of nuclear material requires both physical security and material accountability to deter, detect, and respond to loss, theft or diversion of the materials from the host facilities. Special nuclear materials (SNM), primarily uranium-233 (^{233}U), uranium-235 (^{235}U), and plutonium-239 (^{239}Pu) are of particular concern because these fissile isotopes can be used for proliferation of nuclear weapons. In the United States, the current nuclear fuel cycle includes uranium mining, enrichment and conversion followed by fabrication of fuel for light water reactors (LWRs). After irradiation, the used fuel is stored in pools or dry storage casks, pending final disposition. Although current policy defines that disposition as emplacement in a geologic repository, advanced fuel cycles are being investigated that would provide processing of the used fuel to recover and purify uranium, plutonium, and potentially other radionuclides for recycle. Implementation of a "closed" fuel cycle could recover the residual energy content of the used fuel, and potentially reduce the environmental impacts of repository disposal of waste.

SNM accountability in a fuel processing facility presents unique challenges due to the large quantities, various chemical and physical forms, and radiological properties of the materials. A typical separations plant can recover ten kilograms (kg) of plutonium for every metric ton of uranium (MTU) processed, or ten MT plutonium for a 1,000 MTU capacity plant. In preparation for development of the H Canyon Accountability Model in FY15, the generic attributes for an accountability program were defined and the key measurement points, including attributes and uncertainties, were documented for the H Canyon process nuclear material accountability.

The following are three key elements of a nuclear material accountability (NMA) program.

- *Physical inventory* typically involves sampling and destructive analysis of process materials to determine special nuclear material content at each key measurement point. It requires interruption of process activities, and potential radiation exposure from obtaining, transporting, and analyzing the samples.
- *Measurement and measurement control.* The physical inventory is determined by a series of activities and measurements based on calibrations linking the observed signal and the actual value. The objective of measurement control is to ensure the effectiveness of the measurement systems, and that the uncertainty of the measured data is quantified and reproducible.
- *Measurement error and propagation.* Because the actual material balance can never be measured with total certainty, statistical techniques must be invoked to determine whether an out-of-line material balance result indicates actual diversion of material. The measurement error contributes to the quantity of SNM that is actually assessed to be in the physical inventory. The actual measurement is described by a probability distribution. Each measurement has a central value that defines the actual measured value and an associated uncertainty that describes the deviation of the measured value from the true value due to various factors that may affect the measurement. Taken together, the measurement function and the probability density function define the error model. The total error (from all sources) is a combination of all the individual errors. To overcome the obscuring effect of errors in the material balance (MB) determination, statistical induction is used to draw conclusions about material diversion.

H Canyon Accountability Measurement. H Canyon was constructed in the early 1950s, and began operation in 1955. Its original mission was to separate plutonium-239 from natural uranium target materials, but the process was subsequently reconfigured in the late 1950s to allow recovery of uranium-235 and by-product neptunium-237 from enriched uranium fuels used in the site's reactors for plutonium and tritium production.

The H Canyon process for high enriched uranium (HEU) recovery uses a modified version of the plutonium uranium reduction extraction (PUREX) process, developed for plutonium (Pu) recovery. Aluminum-clad used nuclear fuel (UNF) is chemically dissolved in boiling nitric acid. The resultant solution is chemically adjusted for feeding to solvent extraction, which separates the uranium from fission products and minor actinides. The purified uranium stream can be down blended to low enriched uranium (LEU) for commercial use. Because of the throughput and in-process inventory of the HEU material, frequent inventories are required to ensure that significant quantities of material have not been diverted.

A computer model is being developed to model the H Canyon process, and the baseline data identifying key measurement points, associated process variables, measurement methods, and the sources and magnitude of uncertainty of each measurement has been assembled for input to the model. Application of the model with the H Canyon data will quantify the overall inventory uncertainty, and determine what kind of measurement data could be provided by process monitoring to significantly reduce the "limit-of-error inventory difference" between actual and measured values. The identified measurement data will then be used as a recommendation for an implementation plan to link process monitoring with NMA.

Publications

1. T. F. Severynse, “*Generic Methodology for Quantification of SNM Accountability in a Separations Plant*,” FCRD-SWF-2014-000207, Savannah River National Laboratory, June 2014.
2. T. F. Severynse, “*Baseline Accountability Measurement Error and Uncertainty for H Canyon Operations*,” FCRD-SWF-2014-000599, Savannah River National Laboratory, September 2014.

2.5 Lab-Scale Testing of Reference Processes: ANL

Candido Pereira, Argonne National Laboratory

The reference U/Pu/Np recovery process, or Co-decontamination, is based on a co-extraction of U, Pu, and Np from dissolved spent fuel, followed by selective stripping to recover product streams containing U/Pu/Np and a second product stream containing the remaining U. The Co-decontamination is based on well-understood solvent extraction using tributyl phosphate (TBP). Consequently, the process hinges on predictably controlling the behavior of the key species involved in the separations rather than on major new advances in the process. In terms of flowsheet design, the major factors include controlling the U:TRU ratio in the U/Pu/Np product, directing the majority of the Np to the U/Pu/Np product, minimizing the extraction of fission products (Mo, Ru, and Zr), and controlling Tc behavior.

Although the case study flowsheet is intended to be equipment independent, the flowsheets developed using the Argonne Model for Universal Solvent extraction (AMUSE) assume ideal behavior, i.e. high efficiency and low dispersion. Multistage tests with a lab-scale 2-cm contactor are being run to validate the flowsheet as designed. High efficiency and low dispersion are approached by the centrifugal contactors used for testing, and deviations from expected behavior should be readily evident.

Due to the extended shutdown of the contactor laboratory in 2013 and early 2014, a significant amount of time was devoted to ensuring that the contactor was operating properly. Zero points were measured for all of the motor-rotor assemblies and all of the stage housings. As a result of these measurements, several of the rotors originally on the unit were found to have significantly lower zero points than others in the unit. These were replaced to assure performance consistency across the bank. In addition, rotors placed in an order that matches the largest zero points with the highest throughput. Pumps and balances were recalibrated and tested, and in some cases replaced. As the system is currently used for two different projects, a number of modifications were also made to improve functionality (raising the contactor to increase floor space, upgrades to the data acquisition system) and in-line instrumentation (thermocouples, UV-vis microprobes) was added to the contactor, replacing the existing instrumentation. All of these changes delayed start of testing until August.

Lab-scale flowsheet testing is divided into three components: (1) demonstrating that extraction of the key fission products, Ru, Mo and Zr is controlled as predicted by AMUSE, (2) characterizing the extraction of Np as a function of redox chemistry, and (3) demonstrating the partial stripping of U in the second segment of the case study flowsheet. The first and third components require a full flowsheet, while the second component is being done using single stage tests.

The initial flowsheet used for lab-scale tests (Figure 8) was based on extraction of a feed containing U, Mo, Ru, and Zr as the first segment of the case study flowsheet was designed specifically to regulate the behavior of these species. In order to accommodate the 20-stage limit, the case study flowsheet was redesigned for the bench-scale unit but the formal structure was maintained identical to the reference sheet. The separation efficiencies were tailored to a 2-cm contactor. To maintain chemistry as close as

possible to the reference case, the initial changes to the flowsheet were limited solely to the number of stages per section. Several tests were run using cold acid feeds and process solvent to assure the hydraulic stability of the contactor with the flowsheet. These tests turned up flooding problems at test conditions. After a number of additional tests, the flooding problems were mostly alleviated by changing motor drives at several stages and leveling the contactor. It appears that several of the motors had degraded sufficiently to reduce their performance, though this was not evident in zero point tests. On-line tachometers will be added to the motors to measure rpm under process conditions as an indicator of motor function and additional motors will be procured as necessary in FY 2014.

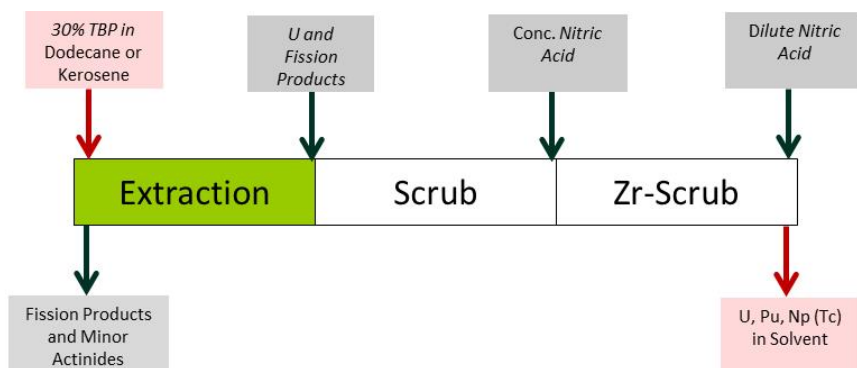


Figure 8. Extraction section of the Codecontamination flowsheet for testing

In order to develop a more stable hydraulic profile before testing with the hot feed, the flowsheet was further reworked to flatten O:A across the bank by diluting the feed and increasing scrub flow rates. The hydraulics were improved with the revised flowsheet as flooding was not evident with the cold feeds. The initial test with the hot feed was successful from a chemical viewpoint but significant flooding was again evident. It appears that the heavier solvent resulting from extraction of uranium was sufficient to impact motor function and disrupt the contactor hydraulics. Consequently analytical results from this test will only be indicative of the process behavior and not confirmatory.

The aqueous phase of the extraction section had a strong brownish tinge while the aqueous phases in both scrub stages were clear to slightly yellow. These solution color results indicate that Ru reports primarily to the raffinate. The solvent was bright yellow across the entire bank, consistent with uranium extraction. In a number of stages the amount of aqueous phase was very small. Stage samples were collected, with the aqueous solutions submitted for chemical analysis by Inductively Coupled Plasma-Mass Spectrometry (ICP-MS). The organic phases were collected and stored for eventual analysis using X-ray Fluorescence but the instrument will not be available until early FY 2014.

Because of the flooding issues, a second test of the first segment of the Codecontamination flowsheet will be run to confirm expected behavior without flooding. Testing of the second segment will use the loaded solvent from the first segment as feed once the expected fission product behavior is confirmed. The feed will not contain Pu or Np, so partial stripping of uranium from the solid at the desired ratio of ~1:9 raffinate: solvent will be the desired outcome. This test will be run once the analyses of the solutions from the first segment are complete.

To supplement the flowsheet testing, small-scale single stage tests were run to characterize the behavior of Np under the flowsheet conditions. Single stage tests allow more control of the flowsheet conditions that lead to specific outcomes. Under the conditions typical of co-decontamination processes, and absent oxidation or reduction, Np is present in nitric acid solution in multiple oxidation states and predominantly

as inextractable Np(V). The AMUSE flowsheet was based on suitable acid conditions in the feed and extraction section to promote extractable Np (VI). However, in process, the Np oxidation state is strongly impacted by the presence of nitrous acid which is typically formed in nitric acid by radiolysis. The presence of nitrous acid induces the reduction of Np(VI) to Np(V).

The single stage Np redox tests were run with a 2-cm contactor housed in a hood. Two Np feed solutions were used that would bracket the range of feed conditions that were examined for the case study flowsheet using AMUSE. The O:A was kept constant and consistent with that used in the first segment of the case study flowsheet.

The tests were run in three parts. The Np feed was first introduced as formed and samples of the effluents were collected at various times. The single stage tests were started with Np (as received) added to nitric acid solution. Sodium vanadate was then added to the feed solution to ensure that all of the Np was as Np(VI) and effluents were again collected. Finally, sodium nitrite was added to the feed solution to simulate production of nitrite by radiolysis, and effluents were again collected. These tests are intended to provide a first dataset covering the expected Np behavior at different acidities. Multiple timed samples were collected to develop a profile for the extraction of neptunium by TBP as a function of time and oxidation/reduction conditions. The samples were submitted for analysis by gamma spectroscopy and liquid scintillation counting.

2.6 Lab-Scale Testing of Reference Processes: INL

L. R. Martin, Idaho National Laboratory

Experimental work to support the lab scale testing of reference processes focused on preliminary investigations to identify the behavior of important fission products such as Tc, Zr, Mo and Rh in a Co-Decontamination flowsheet (Re was used as a Tc surrogate). Two types of batch contact flowsheet tests were performed, shown in Figure 9a and Figure 9b, using the feed simulant, with and without U, and 30% TBP/kerosene.



Figure 9. a) Baseline extraction, scrub (SC), and strip (ST) flowsheet test using feed simulant, without U present. B) Extraction flowsheet with one extraction and three strip phases.

A series of tests was conducted using a simulant with metal concentrations equivalent to the estimated Co-Decontamination process feed. Flowsheet testing, including one extraction phase and three strip phases, were performed using neat simulant, sodium fluoride (NaF) inclusive simulant, and U inclusive simulant. Most of the metal ions present showed little to no extraction into 30% TBP/ kerosene with the exception of cerium (Ce), molybdenum (Mo), neodymium (Nd), ruthenium (Ru), and zirconium (Zr) which showed some extraction over background between the neat and contacted aqueous phase. The Argonne Model for Universal Solvent Extraction (AMUSE) was used to model the extraction distributions for the various metals in the feed simulant. The AMUSE model distributions for the neat

stimulant where no F or U was present, predicated considerably higher extraction distributions for Re, Ru, and Zr than were found in the experimental data.

The results of the experiments performed in this study have shown the Re surrogate for Tc to perform poorly in comparison to the AMUSE prediction for the extraction of Tc and therefore may not necessarily be a suitable surrogate. Future flowsheet tests will include Tc in order to provide more detailed results. The U distribution was also found to be slightly different than the AMUSE prediction however, this could be partially explained by low concentration levels due to a single extraction versus multiple extraction phases. Future work will require an expansion of the flowsheet tested to incorporate multiple extraction steps as this may have led to the differences observed between the AMUSE code and the experimental results.

2.7 Lab-Scale Testing of Reference Processes: ORNL

K. Felker, R. T. Jubin, S. H. Bruffey, K. K. Patton, S. M. Robinson, M. R. Chattin and J. M. Giaquinto, Oak Ridge National Laboratory

Iodine Capture Performance of Silver-Functionalized Silica Aerogel Exposed to High Levels of NO₂. One of the Reprocessing Case Studies included an advanced head-end unit operation that involved the use of high concentrations of NO₂ and elevated temperatures to remove tritium from UNF. Initial studies of this head-end process also showed that significant fractions of iodine may be volatilized during the treatment of the UNF. The treatment process also included a recycle loop for the NO₂. If the iodine is released into the vapor phase, it would be desirable to remove the iodine from the circulating NO₂ stream. One of the materials currently under evaluation for iodine removal is reduced silver-functionalized silica aerogel. The aim of this study was to determine the effects of limited exposure (1 week to 1 month) to high levels of NO₂ vapor on the iodine capture capacity of exposed reduced silver-functionalized silica aerogel.

Silver-functionalized silica aerogel was supplied by researchers at PNNL in FY 2014 for this series of tests. This series of tests was conducted using a static 75 v/v% NO₂ gas environment. These static aging studies were similar to those reported on Ag⁰Z (Jubin, 2013) but using higher concentrations of NO₂. Each sample holder was loaded with ~10 grams of silver-functionalized silica aerogel. The holders were then evacuated, and an aliquot of 100% NO₂ gas was charged into the holder, followed by dilution with zero air to yield a 75v/v% NO₂ environment. Next, the holders were pressurized slightly above atmospheric pressure and were then placed in an oven at 150°C for up to 1 month.

The aged silver-functionalized silica aerogel material was loaded with iodine under conditions similar to those described in previous studies (Jubin, 2011). For each thermogravimetric (TGA) test, the silver-functionalized silica aerogel was dried at 150°C using dry air. After drying was complete and the weight was stable, the flow of gas, containing iodine at a concentration of 56 ppm, was initiated and maintained at a 10.3 m/min superficial velocity as used in previous aerogel aging studies (Bruffey et al., 2013). The changes in weight obtained from the TGA data for 0, 1 week, and 1 month NO₂-aged silver-functionalized silica aerogel samples are shown in Figure 10. The time zero on this figure corresponds to the time at which the iodine stream was introduced to the sample. The data curves end after the 24 hour purging period. The un-aged silver-functionalized silica aerogel showed a gain of approximately 33.1% by weight. The sample aged 1 week under an atmosphere of 75% NO₂ appeared to achieve similar iodine loading based on TGA data. The sample that was aged 1 month lost approximately 8.5% of its original capacity, for a total loading of 30.3% by weight. The iodine loadings measured by neutron activation

analysis are slightly higher than the TGA results but were consistent, with only a slight decrease of ~4% in the loading following aging for 1 month.

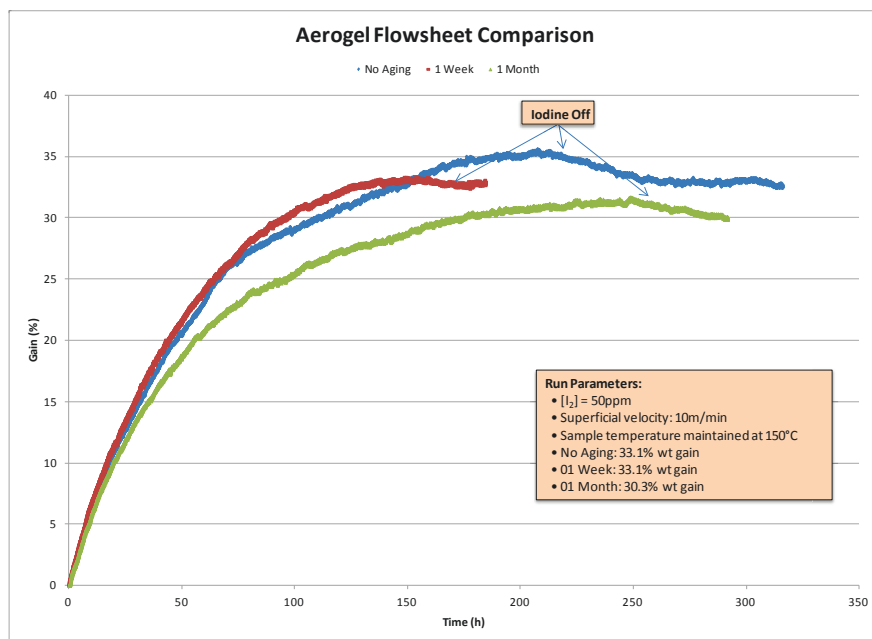


Figure 10. Iodine loading curves for 75% NO₂-aged silver-functionalized silica aerogel.

Evaluation of Tritium Content and Release from Surry-2 Fuel Cladding. Zircaloy® cladding makes up roughly 25% by mass of UNF in the United States. Treatment options for Zircaloy cladding include recycling to recover the significant cost of the zirconium and eliminate costs associated with the disposal of transuranic-contaminated Zircaloy®. If LWR fuel is reprocessed and the fuel is dissolved without tritium pretreatment, the tritium in the cladding will remain bound to the cladding. If tritium pretreatment is included in the flow sheet, some portion of the tritium in the cladding may be released along with the tritium from the fuel matrix.

Reported estimates of the percentage of tritium in the fuel rod that is found in the cladding range from 0–96%. A single sample of cladding from fuel that had undergone the tritium pretreatment operation was analyzed as part of the Coupled End-To-End (CETE) project, and no tritium was detected in the cladding. This single data point was not a definitive test, but the results warranted additional investigation since it indicated that tritium pretreatment could potentially eliminate the presence of tritium in the zirconium recycle step. The present study was undertaken to understand how tritium pretreatment at standard air tritium pretreatment conditions (480 - 600°C) affects the tritium content in the Zircaloy® cladding and the extent to which the tritium content could be reduced with modest increases in the tritium pretreatment temperature. Scoping tests are being performed to determine the tritium content of pre- and post-tritium pretreated cladding.

For the characterization of tritium content in irradiated cladding, Carbolite Combustion Tube Furnace, Model MTT 12/38/850 was used. The furnace can operate at a maximum combustion zone temperature of 1200°C and utilizes a copper metal catalyst in a separate heated zone for conversion of tritium gas to water for trapping. The sample carrier gas consisted of a 50:50 mixture of oxygen and nitrogen, and a 100% oxygen gas flow was used for the catalyst zone. Three bubblers containing ~60 mL of deionized

(DI) water each were connected in series to the outlet of the furnace. The first two bubblers were routinely sampled during the tests, and the third bubbler only sampled at the end of the test. The experimental system is shown schematically in Figure 11.

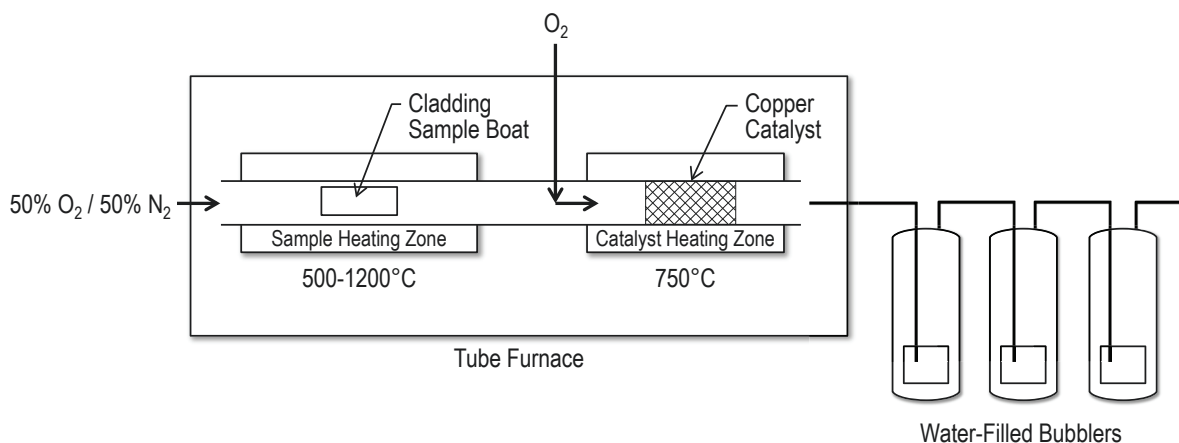


Figure 11. Schematic of experimental test system

For these experiments, a 5–6 mm wide ring of Surry-2 pressurized water reactor (PWR) cladding was cut into three equal segments (samples 1A, 1B, and 1C) by cutting the ring at radial positions (i.e., 0, 120, and 240 degrees). Sample 1A received no simulated tritium pretreatment; it was heated to 1100–1200°C to oxidize the zirconium and release all of the tritium in the cladding sample. The tritium content was measured to be ~240 $\mu\text{Ci/g}$.

Cladding samples were heated to 500°C, which is within the temperature range (480 - 600°C) expected for standard air tritium pretreatment systems, and to a slightly higher temperature (700°C) to determine the impact of tritium pretreatment on tritium release from the cladding. The tritium concentrations in the off-gas from cladding samples 1B and 1C that were exposed to simulated tritium pretreatment conditions at 500 and 700°C were 0.55 and 19.2 $\mu\text{Ci/g}$, respectively. The residual tritium released during subsequent oxidation of the cladding samples was 247.2 and 201.7 $\mu\text{Ci/g}$ for the 500 and 700°C pretreated samples, respectively. Based on the sum of the tritium released during these two heating periods, the tritium pretreatment conditions of 500 and 700°C removed ~0.2 and 9% of the tritium in the cladding leaving a significant fraction of the tritium bound in the cladding and must be considered in operations involving cladding recycle. The results are summarized in Table 1. These data are consistent with that found in the literature (Robinson and Jubin, 2013) and with ORIGEN calculations for the total tritium content of the fuel (~280 $\mu\text{Ci/g}$ cladding for Surry-2 fuel that has been out of the reactor for 33 years assuming all tritium is contained in the cladding). The tritium found in the cladding appears at the higher end of the percent expected, but the tritium content in the cladding is not uniform over the length of the rod, whereas the total tritium content predicted by ORIGEN is an average value.

Table 1. Tritium in Surry-2 cladding

Sample	Simulated tritium pretreatment condition (°C)	Tritium released during simulated tritium pretreatment (μCi/g)	Tritium in cladding sample during oxidation ¹ (μCi/g)	Total tritium recovered from cladding sample (μCi/g)	Tritium removed during simulated tritium pretreatment (%)
1B	500	0.55	247.2	247.7	0.2
1C	700	19.2	201.7	220.9	8.7

¹ Oxidation of cladding @ 1100–1200°C to release residual tritium

References

1. Bruffey, S. H., Jubin, R. T., Anderson, K. K., and Walker Jr., J. F., *Humid Aging and Iodine Loading of Silver-functionalized Aerogels*, FCRD-SWF-2013-000258, US Department of Energy Separations and Waste Forms Campaign, August 30, 2013.
2. Jubin, R. T., Letter to T. A. Todd, *Aging and Iodine Loading of Ag⁰Z in a static 2% NO₂ Environment*, ORNL/LTR-2013/351, August 30, 2013.
3. Jubin, R. T., *Report of the FY11 Activities of the Off-Gas Sigma Team*, FCR&D-SWF-2011-000306, US Department of Energy Separations and Waste Forms Campaign, August 31, 2011.
4. Robinson S. and R. Jubin, *Review of Tritium in Zircaloy Cladding from Light Water Reactor*, RCRD-SWF-2013-000288, September 2013

2.8 Lab-Scale Testing of Reference Processes: PNNL

G. J. Lumetta and A. J. Casella, Pacific Northwest National Laboratory

Separating the lanthanide fission product elements from the minor actinide elements (Am and Cm) at an industrial scale is one of the most daunting challenges to fully closing the nuclear fuel cycle.^[1-2] Achieving this separation is necessary if the minor actinide elements are to be converted to short-lived or stable isotopes in fast reactors because of the relatively large neutron cross sections of the light lanthanide elements. Nearly all methods under investigation for separating the minor actinides from the lanthanides exploit the apparent slightly softer character of the trivalent actinide ions compared to the trivalent lanthanide ions. Thus ligands containing nitrogen or sulfur donors have received considerable attention.^[1, 3-5] The ligands can be deployed in either the organic phase (as extractant) or in the aqueous phase (as an actinide-holdback reagent) in liquid-liquid extraction systems.

The Full Recycle Case Study that was performed in FY 2013, and updated in FY 2014, identified the Trivalent Actinide-Lanthanide Separations by Phosphorus-reagent Extraction from Aqueous Complexes (TALSPEAK) process^[6-7] as the primary candidate for separating the lanthanides from the minor actinides. The TALSPEAK process has previously been demonstrated at a laboratory scale to separate the minor actinides from the lanthanides.^[8] However, the Case Study also identified a variation of the TALSPEAK process for potential near-term insertion into the fuel recycle flowsheet. In this variant of TALSPEAK, the traditionally used extractant, bis(2-ethylhexyl)phosphoric acid (HDEHP; Figure 12), is replaced with 2-ethylhexylphosphonic acid mono-2-ethylhexyl ester (HEH[EHP]; Figure 12). Three key advantages of switching to the HEH[EHP] extractant were claimed: less dependence of the process performance on the aqueous solution pH, more predictable extraction behavior, and more rapid extraction kinetics.^[9] This variant of the TALSPEAK process is now referred to as *Advanced TALSPEAK*. In FY 2013, work was conducted at PNNL to characterize the process chemistry relevant to the Advanced

TALSPEAK concept so as to further evaluate whether this system should replace the conventional TALSPEAK process in the FCRD Program's full recycle flowsheet. This work was extended into FY 2014, when single-stage 2-cm contactor tests were performed to determine the effective distribution ratios for Am and the lanthanides in this prototypic contacting equipment.

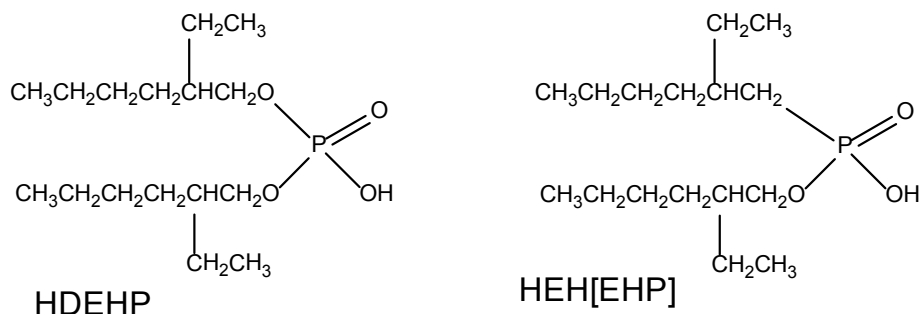


Figure 12. Chemical structures of the TALSPEAK (HDEHP) and Advanced TALSPEAK (HEH[EHP]) extractants.

Process Concept. The Advanced TALSPEAK system operates by extracting the lanthanide ions into an aliphatic hydrocarbon phase containing HEH[EHP]. A polyaminocarboxylate ligand is added to the aqueous phase to suppress the extraction of Am and Cm. In this case, the soft amine donor groups in the polyaminocarboxylate ligand preferentially bind the softer actinide ions, keeping them in the aqueous phase. Batch distribution measurements conducted in FY 2013 led to the choice of N-(2-hydroxyethyl)ethylenediamine-N,N',N'-triacetic acid (HEDTA; Figure 13) as the preferred polyaminocarboxylate ligand to use as the actinide-holdback reagent in the Advanced TALSPEAK system. Citric acid is also added to the aqueous phase to control the solution pH (Figure 13).

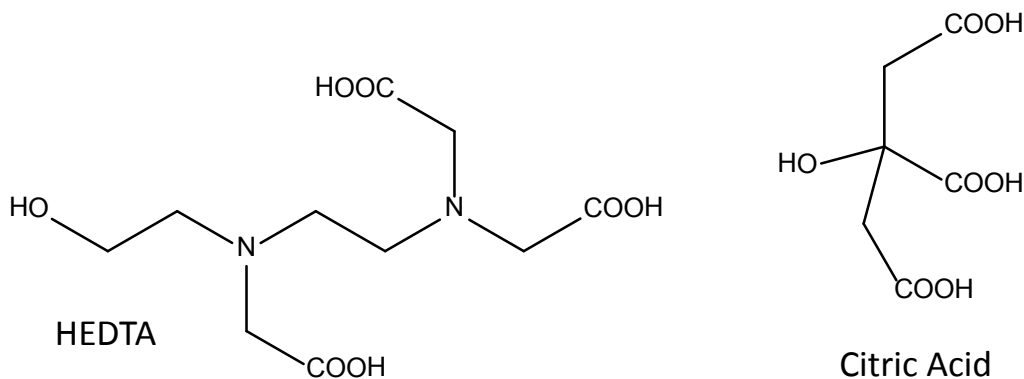


Figure 13. Chemical structures of the aqueous-phase complexant and buffers used in the Advanced TALSPEAK system.

The objective of this work is to generate the data required for designing and testing the Advanced TALSPEAK flowsheet. Batch distribution measurements conducted in FY 2013 indicated the feasibility of the concept from a thermodynamic point of view. In FY 2014, a set of experiments was performed using a single 2-cm centrifugal contactor to determine the effective distribution ratios for Am and selected lanthanide elements under dynamic flow conditions.

Accomplishments. Both batch kinetic experiments and a single-stage flow experiment were conducted with a 241Am-spiked feed containing La, Ce, Pr, Nd, Sm, Eu, and Gd (15 mmol/L total lanthanides). The aqueous feed solution also contained 0.125 mol/L HEDTA plus 0.2 mol/L citrate, and was adjusted to pH 3.1. Figure 14 presents the batch D values obtained for 241Am and the lanthanides as a function of time.

The results show that under the vortex mixing conditions used, equilibrium was achieved for all the investigated lanthanides and ^{241}Am within 5 minutes. As desired, ^{241}Am had a much lower D value than the lanthanides, and its equilibrium D value was determined to be 0.472 ± 0.007 . At equilibrium, the minimum separation factor (SF) achieved was defined by the extraction behavior of Nd, with the $\text{SF}_{\text{Nd}/\text{Am}} = 18.4 \pm 0.9$. Although the kinetic batch extraction experiment revealed that equilibrium was achieved after 5 minutes of vortex mixing for all the elements studied, for process application it is essential to know what the effective D values are in the contacting equipment. This will depend on the extent of mixing achieved in the contacting equipment as well as the residence time. In this work, a 2-cm centrifugal contactor was investigated as a prototypic contacting device that might be employed for the advanced TALSPEAK system.

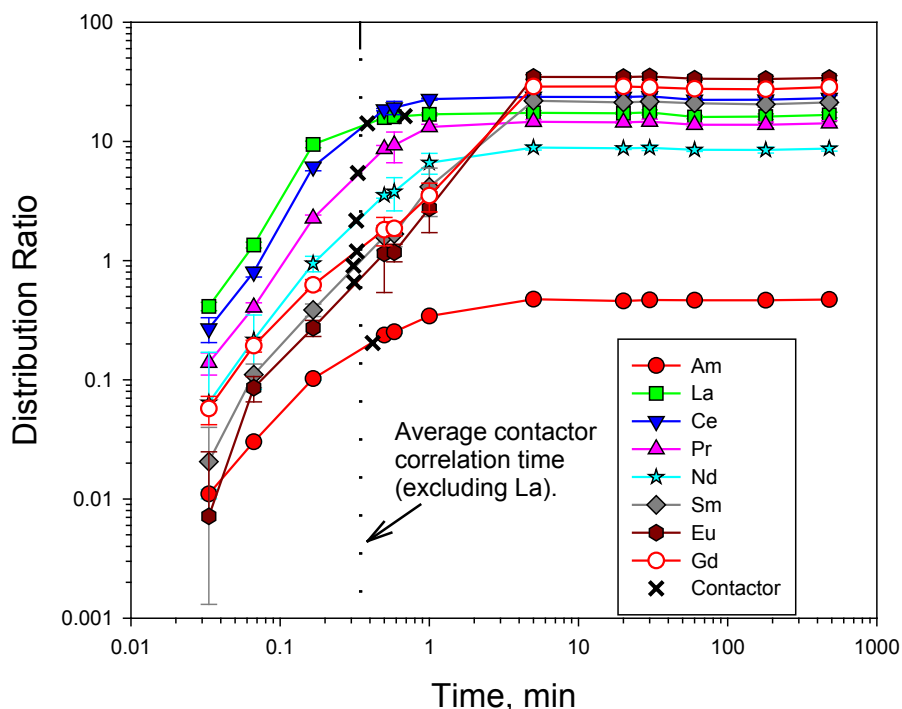


Figure 14. Overlay of the batch extraction results of lanthanides and ^{241}Am with the data obtained during the dynamic flow extraction. The times for the flow data were obtained from interpolating the measured contactor D -values between the kinetic data points.

The radioactive flow experiment was performed with an average aqueous flow rate of 10.2 ± 1.1 mL/min and an average organic flow rate of 9.55 ± 0.10 mL/min. The operational compatibility of the advanced TALSPEAK system was demonstrated through clean separation of the phases and the absence of emulsions in either exit stream. The ^{241}Am D values were nearly identical for all 15 continuous samples taken during the experiment, with the average effective D value being 0.203 ± 0.001 . Likewise, the lanthanide concentrations were also consistent among all samples measured, indicating the system was at steady state throughout the sampling period of the test. Table 2 lists the D values for ^{241}Am and the lanthanides measured during the contactor run. The D values were relatively low, especially those for the heavier lanthanide elements, some of which are less than 1. This resulted in a minimum SF of 3.24 ± 0.33 (defined by the Eu/Am SF), which is about 6-times less than the minimum SF obtained in batch mode ($\text{SF}_{\text{Nd}/\text{Am}} = 18.4 \pm 0.9$).

Table 2. <i>D</i> values of lanthanides and ²⁴¹Am and minimum SF in the dynamic flow extraction.	
Element	D-Value
La	16.3 ± 0.6
Ce	14.2 ± 0.6
Pr	5.43 ± 0.24
Nd	2.17 ± 0.12
Sm	0.904 ± 0.077
Eu	0.659 ± 0.064
Gd	1.20 ± 0.08
²⁴¹ Am	0.203 ± 0.001
Min SF	3.24 ± 0.33

Based on the results of this study, alterations to the advanced TALSPEAK system should be explored for extraction improvements. To assess the effectiveness of modifications to the process chemistry, without having to perform actual contactor runs, a correlation was made between the batch and flow systems. The vortex mixing time that yields extraction performance equivalent to the 2-cm contactor was determined by interpolating the measured *D* values obtained in the contactor run between the kinetic data points (Figure 14). With the exception of La, the results for the lanthanides tested and ²⁴¹Am were relatively consistent, resulting in an average correlated vortex time 21 seconds (if the La data is excluded). Note that this value is specific to the technique used and not a general correlation.

Conclusions. In this work, we initiated a study of the process chemistry related to the advanced TALSPEAK system. A solvent formulation consisting of 1.0 mol/L HEH[EHP] in *n*-dodecane, and an aqueous phase consisting of HEDTA in a 0.2 mol/L citrate buffer, were chosen for further process development. From an equilibrium standpoint, this system is robust with respect to slight changes in pH or the concentrations of HEDTA, citrate, or HEH[EHP]. The advanced TALSPEAK system appears to be compatible with centrifugal contactors in terms of its hydraulic behavior. The process should easily operate in the pH range of 3 to 4, although slow extraction kinetics is still a concern for the heavier lanthanides Sm, Eu, and Gd, as revealed in the single-stage contactor experiment. Further development of the process chemistry is needed to overcome the kinetic issues. Alternatively, other types of contacting equipment (e.g., mixer-settlers) could be considered that offer longer residence times.

References

1. Hudson, M. J.; Harwood, L. M.; Laventine, D. M.; Lewis, F. W. "Use of Soft Heterocyclic N-Donor Ligands to Separate Actinides and Lanthanides," *Inorganic Chemistry*, 2013, 52, 3414-3428.
2. Todd, T. A. "Separations Research for Advanced Nuclear Fuel Cycles," *Nuclear Energy and the Environment*; Wai, C. M.; Mincher, B. J., Eds; American Chemical Society: Washington, DC, 2010, 13-18.
3. Ekberg, C.; Fermvik, A.; Retegan, T.; Skarnemark, G.; Foreman, M. R. S.; Hudson, M. J.; Englund, S.; Nilsson, M., "An overview and historical look back at the solvent extraction using nitrogen donor ligands to extract and separate An(III) from Ln(III)," *Radiochimica Acta*, 2008, 96, 225-233.
4. Wang, X.; Zhu, Y.; Jiao, R. "Separation of Am from Macro Amount of Lanthanides by a Countercurrent Multistage Extraction with Purified Cyanex 301 and TBP," *Solvent Extraction and Ion Exchange*, 2001, 19, 1007-1015.
5. Law, J. D.; Peterman, D. R.; Todd, T. A.; Tillotson, R. D. "Separation of trivalent actinides from lanthanides in an acetate buffer solution using Cyanex 301," *Radiochimica Acta*, 2006, 94, 261-266.
6. Weaver, B.; Kappelmann, F. A. "Preferential Extraction of Lanthanides Over Trivalent Actinides by Monoacidic Organophosphates from Carboxylic Acids and From Mixtures of Carboxylic Acids and Aminopolyacetic Acids," *Journal of Inorganic and Nuclear Chemistry*, 1968, 30, 263-272.
7. Nilsson, M.; Nash, K.L., "A Review of the Development and Operational Characteristics of the TALSPEAK Process," *Solvent Extraction and Ion Exchange*, 2007, 665-701.

8. Regalbuto, M. C. "Alternative separation and extraction: UREX+ processes for actinide and targeted fission product recovery," *Advanced Separation Techniques for Nuclear Fuel Reprocessing and Radioactive Waste Treatment*, Nash, K. L.; Lumetta, G. J., Eds., Oxford: Woodhead Publishing, 2011, 176-200.
9. Braley, J. C.; Grimes, T. S.; Nash, K. L. "Alternatives to HDEHP and DTPA for Simplified TALSPEAK Separations," *Industrial & Engineering Chemistry Research* 2012, 51, 629-638.

2.9 Define and Document Reference Flowsheet

J. Law, Idaho National Laboratory; J. D. Vienna, Pacific Northwest National Laboratory

A team of experts from Argonne National Laboratory (ANL), Idaho National Laboratory (INL), Oak Ridge National Laboratory (ORNL), Pacific Northwest National Laboratory (PNNL), Savannah River National Laboratory (SRNL), the Department of Energy, Nuclear Energy (DOE-NE), AREVA and EnergySolutions were assembled in FY 2013 to perform a case study evaluation of full recycle technologies for both the processing of LWR UNF as well as fast reactor UNF in the full recycle option. This effort focused on the identification of the case study processes and the initial preparation of material balance flowsheets for the identified technologies. In identifying the case study flowsheets, it was decided that two cases would be developed: one which identifies the flowsheet as currently developed and another near-term target flowsheet which identifies the flowsheet as envisioned within two years, pending the results of ongoing research. In FY 2014 the team revisited this effort and updated this document based upon results of research which occurred in FY 2014. Changes to the case study or near-term target case flowsheets were detailed in Report FCRD-SWF-2013-000380, Revision 1 (Law et al. 2014). Specifically, the following revisions were made: 1) Tritium pretreatment with NO₂ was chosen as the sole near-term target technology as compared to FY 2013 which included both NO₂ and O₂, 2) The electrochemical separations mass balance write-up was expanded to include significant work performed in FY 2014, 3) the waste treatment and disposal sections for aqueous and electrochemical separations were modified significantly based upon the FY 2014 analysis detailed in the Closed Fuel Cycle Waste Treatment Strategy report, FCRD-SWF-2014-000212, 4) mass balance assumptions were updated in all areas based upon the results of recent research, and 5) a detailed review by Chris Phillips, EnergySolutions, was performed and comments incorporated.

The case study focus is homogeneous recycle of the U/TRU resulting from the aqueous processing of LWR UNF as feed for metal fuel fabrication. The metal fuel is utilized in a sodium cooled fast reactor and the used fast reactor fuel processed using electrochemical separations. The recovered U/TRU from electrochemical separations is recycled to fuel fabrication and the fast reactor. Waste streams from the aqueous and electrochemical processing are treated and prepared for disposition. Off-gas from the separations and waste processing are also treated. The document presents, in detail, the technologies chosen by the team for the case study flowsheet and near-term target case flowsheet. The technologies are described and assumptions as to the behavior of actinides, fission products and other elements of interest are documented to support development of the mass balance. In addition, unknowns, areas for development and current research status are detailed.

In conjunction with documentation of the flowsheet technologies, mass balances have been created. Much of the focus in FY 2013 was on developing the mass balances for the used LWR fuel processing. In FY 2014, modeling efforts focused upon the electrochemical processing flowsheets.

Development of the case study flowsheet will allow for objective comparison of technologies currently being developed by the MRWFD Campaign as well as future technology developments, to assess their benefits and potential improvements relative to this full recycle flowsheet. Ultimately, this effort will provide benefits in terms of understanding the interfaces between specific processes both upstream and downstream, will aid in identifying knowledge gaps and areas for process improvements, will serve as a tool for comparison of new technologies, and will identify potential regulatory issues for UNF recycling.

Closed Fuel Cycle Waste Treatment Strategy. A study was performed to evaluate the waste management approaches for nuclear fuel cycle facilities in comparison to the objectives of implementing an advanced fuel cycle in the U.S. under current legal, regulatory and logistical constructs. The study rests heavily on the Global Nuclear Energy Partnership (GNEP) *Integrated Waste Management Strategy* (IWMS) (Gombert et al. 2008) as a general strategy and associated *Waste Treatment Baseline Study* (WTBS) (Gombert et al. 2007). The tenets of the IWMS are equally valid to the current waste management study. However, the flowsheet details have changed significantly from those considered under GNEP. In addition, significant additional waste management technology development has occurred since the GNEP waste management studies were performed. This study updates the information found in the WTBS, summarizes the results of more recent technology development efforts, and describes waste management approaches as they apply to both the nominal case study and near-term target reprocessing flowsheets (Law et al. 2014). Many of the waste management technologies discussed also apply to other potential flowsheets that involve reprocessing. These applications are discussed where the data are more readily available; however, mass balances are available only from the flowsheets by Law et al. (2014).

The report summarizes the waste arising from aqueous reprocessing of a typical light-water reactor (LWR) fuel to separate actinides for use in fabricating metal sodium fast reactor (SFR) fuel and from electrochemical reprocessing of the metal SFR fuel to separate actinides for recycle back into the SFR in the form of metal fuel. The primary streams considered and the recommended waste forms include:

- Tritium separated from either a low volume gas stream or a high volume water stream. The recommended waste form is low-water cement in high integrity containers (HICs).
- Iodine-129 separated from off-gas streams in aqueous processing. There are a range of potentially suitable waste forms. As a reference case, a glass composite material (GCM) formed by the encapsulation of the silver Mordenite (AgZ) getter material in a low-temperature glass is assumed. A number of alternatives with distinct advantages are also considered including a fused silica waste form with encapsulated nano-sized AgI crystals.
- Carbon-14 separated from LWR fuel treatment off-gases and immobilized as a CaCO_3 in a cement waste form.
- Krypton-85 separated from LWR and SFR fuel treatment off-gases and stored as a compressed gas.
- An aqueous reprocessing HLW raffinate waste which is immobilized by the vitrification process in one of three forms: a single phase borosilicate glass, a borosilicate based glass ceramic, or a multi-phased crystalline synthetic rock (SynRoc).
- A undissolved solids (UDS) fraction from aqueous reprocessing of LWR fuel that is either included in the borosilicate HLW glass or is immobilized in the form of a metal alloy in the case of glass ceramics or SynRoc.

**Material Recovery and Waste Form Development
2014 Accomplishments Report**

- Zirconium-based LWR fuel cladding hulls and stainless steel fuel assembly hardware that are washed and super-compacted for disposal or as an alternative with high promise the purification and reuse (or disposal as low-level waste, LLW) of Zr by reactive gas separations.
- Electrochemical process salt HLW which is incorporated into a glass bonded Sodalite waste form known as the ceramic waste form (CWF).
- Electrochemical process UDS and SS cladding hulls which are melted into an iron based alloy waste form.

Mass and volume estimates for each of the recommended waste forms based on the source terms from the mass balances given by Law et al. (2014) are reported. The resulting waste form masses and volumes are summarized in Table 3.

Table 3. Summary of Projected Waste Form Masses and Volumes

Stream	Waste form	Mass, kg/tU	Vol, m ³ /y	Comment
Tritium				
TPT off-gas	low water cement	0.07	0.035	water:cement ratio of 0.3
High volume water	low water cement	16 700	8770	water:cement ratio of 0.3
Optimized water	low water cement	1000	526	water:cement ratio of 0.3
Isotope enriched	low water cement	16.7	8.77	water:cement ratio of 0.3
Iodine				
AgZ	glass composite material	130	29.5	
AgAero	fused silica-AgI	2.93	0.975	
Krypton	Low pressure gas	0.646	3.7×10 ⁻³	50 atm
Krypton	High pressure gas	0.646	1.1×10 ⁻³	163 atm
Krypton	Zeolite	0.646	2.8×10 ⁻³	HIP
Krypton	Metal matrix	0.646	7.8×10 ⁻⁴	Cu matrix
Carbon	Cement	68	35.8	CaCO ₃ :cement ratio of 0.3
High level waste				
LNFP+TMFP+UDS+Tc	Borosilicate glass	401	154	5 y cooled fuel
LNFP+TMFP+UDS+Tc	Borosilicate glass	302	116	50 y cooled fuel
LNFP+TMFP	Glass ceramics	214	70	5 y cooled fuel
LNFP+TMFP	Glass ceramics	76	25	50 y cooled fuel
LNFP+TMFP	SynRoc	173	38	
UDS+Tc	e-metal	9.71	0.81	
UDS+Tc	Fe-metal	19.4	2.43	
Hulls and Hardware				
Hulls + Hardware	Supercompacted	301	67.6	66% volume
Hardware only	Supercompacted	47	8.9	66% volume
Zr recycle	Recycled			wastes TBD

In addition to the above listed primary waste streams, a range of secondary process wastes are generated by aqueous reprocessing of LWR fuel, metal SFR fuel fabrication, and electrochemical reprocessing of SFR fuel. These secondary wastes have been summarized and volumes estimated by type and classification.

The important waste management data gaps and research needs have been summarized for each primary waste stream and selected waste process. A draft report – Vienna et al. 2014, *Closed Fuel Cycle Waste Treatment Strategy*, FCRD-SWF-2014-000212, Rev. A – was submitted for program review. A final report will be issued during the first quarter of fiscal year 2015.

References

1. Gombert, D., R. Counce, A. Cozzi, J. V. Crum, W. L. Ebert, C. M. Jantzen, J. Jerden, R. Jubin, M. D. Kaminski, V. Maio, J. C. Marra, T. M. Nenoff, R. D. Scheele, H. D. Smith, B. Spencer, D. M. Strachan, and J. D. Vienna, *Global Nuclear Energy Partnership Integrated Waste Management Strategy Waste Treatment Baseline Study*, GNEP-WAST-AI-RT-2007-000324, Idaho National Laboratory, 2007.
2. Gombert, D., J. Carter, A. Cozzi, R. Jones, G. Matthern, M. Nutt, S. Priebe, and K. B. Sorenson, “*Global Nuclear Energy Partnership Integrated Waste Management Strategy*,” GNEP-WAST-WAST-AI-RT-2008-000214, Idaho National Laboratory, 2008.
3. Law, J. D., N. R. Soelberg, T. A. Todd, J. Tripp, C. Pereira, M. A. Williamson, W. L. Ebert, R. T. Jubin, B. A. Moyer, J. D. Vienna, G. J. Lumetta, J. V. Crum, T. S. Rudisill, J. Bresee, C. Phillips, B. Willis, P. Murray, and S. Bader, *Separation and Waste Form Campaign Full Recycle Case Study*, FCRD-SWF-2013-000380, Rev. 1, Idaho National Laboratory, 2014.

Publications

1. Law, J. D., N. R. Soelberg, T. A. Todd, J. Tripp, C. Pereira, M. A. Williamson, W. L. Ebert, R. T. Jubin, B. A. Moyer, J. D. Vienna, G. J. Lumetta, J. V. Crum, T. S. Rudisill, J. Bresee, C. Phillips, B. Willis, P. Murray, and S. Bader, *Separation and Waste Form Campaign Full Recycle Case Study*, FCRD-SWF-2013-000380, Rev. 1, Idaho National Laboratory, 2014.

This page left intentionally blank

SIGMA TEAM FOR MINOR ATINIDES

SECTION 3

3. SIGMA TEAM FOR MINOR ACTINIDES

B. A. Moyer, Oak Ridge National Laboratory

Sigma Team for Minor Actinide Separations is developing more robust and simplified approaches for separating minor actinides to enable future fuel cycles that transmute minor actinides for improved resource and waste management. There is a large international effort in nearly every fuel cycle country working on this difficult chemical separation and the FCRD program is making significant progress on the development of cost-effective methods of separating the minor actinides from used fuel.

Highlights of the Sigma Team for Minor Actinides accomplishments in FY 2014 are provided in this section as distilled from the annual reports of individual principal investigators. See these reports, listed at the bottom of this chapter, for a more complete account of research progress.

3.1 Successful Demonstration of Tandem Americium Oxidation and Solvent Extraction Using Process Equipment

B. J. Mincher, J. D. Law, T. G. Garn, M. Greenhalgh, N. C. Schmitt, V. Rutledge, Idaho National Laboratory

A major accomplishment of the Sigma Team during FY 2014 was a radiochemical bench test demonstrating the tandem oxidation of Am(III) to Am(VI) using sodium bismuthate and subsequent solvent extraction [Mincher, 2014; Mincher, et al., 2014a]. Based upon batch contact results, flowsheet design, and a previous cold test [Mincher, et al., 2013], a radiochemical test bed was successfully designed, built, and operated in a radiological fume hood at the Central Facilities Area at INL. Because of the reduction of Am(VI) by stainless steel in previous coupon tests, a special tantalum-coated contactor was employed to prevent Am(VI) reduction as well as corrosion under the aggressive oxidizing conditions. In the test, an $^{243}\text{Am}/^{139}\text{Ce}$ -spiked raffinate simulant feed was oxidized with sodium bismuthate powder in a stirred beaker, filtered through a Teflon filter, and fed directly into a custom-built CINC 5-cm centrifugal contactor. The centrifugal contactor and filtration system employed in this test is shown in Figure 15. The solvent used was diamylamylphosphonate (DAAP) in dodecane [Mincher, et al., 2014b] with three contacting stages: extraction, Am stripping, and Ce stripping. Since Ce(III) in the feed is oxidized to extractable Ce(IV) by sodium bismuthate, a Ce strip step is needed, which in batch tests is easily accomplished with dilute hydrogen peroxide [Mincher, et al., 2013]. Sixty-three percent extraction of the Am in the feed was obtained in the extraction stage, the expected recovery based on a prior batch contact with the same feed solution and assuming 100% stage efficiency.

This result demonstrates for the first time that Am(VI) can be extracted using process equipment, considered a major risk in the development of this concept given the unstable nature of Am(VI). We attribute this desired result to the choice of inert materials of construction, the direct filtration of the feed into the contactor, and the short residence time in the contactor. In the two stripping contactors, however, the performance did not match the expectations from batch tests. Although Am(VI) was expected to be easily reduced and stripped based on batch contacts, the short residence time apparently made stripping ineffective, equivalent to an effective distribution ratio D_{Am} of 3.5 vs the value of <0.4 obtained in the batch experiments. This finding may be fortuitous in that it indicates that the lifetime of Am(VI) under the dynamic filtration and contacting conditions may permit multiple extraction and scrubbing stages in the flowsheet. The increased recovery afforded by extra stages could thus reduce the need for one or more repeated oxidation cycles on the raffinate [Mincher, et al., 2013], which would be a major improvement in the implementation of this concept. Cerium stripping using H_2O_2 was also inefficient, in spite of the

success of that strip during batch cold testing. This is again attributed to short residence time of the contact. However, selective stripping should still be possible, given either longer residence times in contact with the organic phase or use of more aggressive reductants in the strip solutions. Many options for stripping Am and Ce exist, with high likelihood of developing a practical solvent cycle. Overall, the implications of this successful hot test are far reaching while indicating the need for further research efforts in the future.



Figure 15. Radiochemical hood showing the three-stage centrifugal contactor test bed, simulant feed reservoir, and bismuthate filter. Note: The system was photographed prior to introducing radioactivity, and therefore there are no Contamination Area postings on the hood.

3.2 Catalyzed Oxidation of Am(III) to Am(VI) Using Ozone

G. S. Goff, L. Seaman, G. D. Jarvinen, and W. Runde, Los Alamos National Laboratory

A highly promising chemical oxidation of Am(III) to Am(VI) has been identified by using ozone as an oxidant together with Ag(I) as a catalyst [Goff, et al., 2014]. Major advantages of this method include effectiveness at moderately high nitric acid concentrations, practically negligible secondary waste, use of inexpensive oxidant with proven industrial technology, and no complications involving particulate solids. Upon further development, this avenue of research has the potential to make separations of MAs viable based on redox manipulation of the americium oxidation state. Progress on use of the high oxidation states of Am to effect its separation from lanthanides has so far relied on use of sodium bismuthate and peroxydisulfate as oxidants. While these reagents have allowed the demonstration of separations involving Am(V) and Am(VI) over the past several years, their use involves considerable drawbacks. In the case of sodium bismuthate, the oxidant is a solid that must be filtered before subsequent separations, and the significant amounts of bismuth that are dissolved can interfere with certain downstream separations as well as add secondary waste to the aqueous stream. In the case of peroxydisulfate, the sulfate produced poses unwanted complications for downstream vitrification processing to produce a final waste form. Both oxidants present kinetic issues, and the effectiveness of peroxydisulfate is poor at >1 M HNO_3 . All of these disadvantages practically vanish with use of ozone with a small concentration of

Ag(I) catalyst, taking note that Ag is a fission product and likely will in any case be present at minor concentration after the initial co-decontamination step.

Insight into the properties of the catalyzed ozonation of Am(III) and the stability of oxidized species was gained in FY 2014 toward developing an optimal Am(VI) containing feed for subsequent separation. It was shown that Ag(I) functions as an effective catalyst up to 8 M HNO₃, quantitative yields of Am(VI) being obtained at 3 M HNO₃. Oxidation rates appear to be controlled by mass transfer of ozone into solution, and Am(IV) and Am(V) are not detectable as intermediate species in the oxidation step. Oxidation yield and stability of Ag(II), the oxidized form of the catalyst, increase with increasing nitric acid, and its autoreduction follows second-order kinetics, thought to indicate a rate-determining disproportionation to Ag(I) and Ag(III). Since the stability of Am(VI) decreases with increasing nitric acid concentration, an optimum nitric acid concentration is indicated, which will be investigated in FY 2015. Figure 16 shows that Am(VI) continues to grow in for a time after ozone sparging is stopped in 1 M HNO₃, and Am(VI) subsequently disappears with initial ingrowth of Am(V) according to first-order kinetics. The increased staying power of Ag(II) at high nitric acid concentrations can be exploited to provide a long-lasting holding oxidant for Am(VI). For example, it was shown that Ag(II) can stabilize Am(VI) for up to 48 hours in 6 and 8 M HNO₃. Once the Ag(II) is consumed, the Am(VI) undergoes autoreduction as shown in Figure 16.

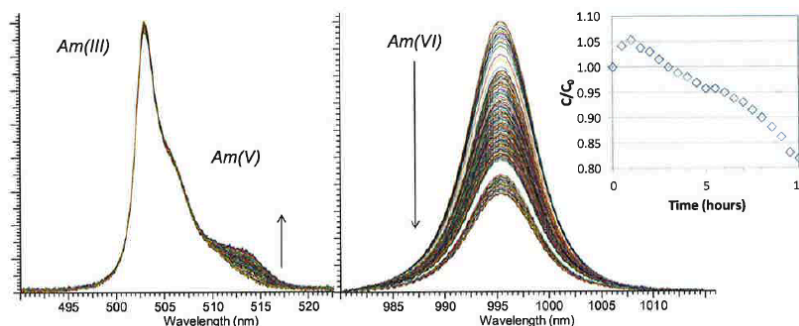


Figure 16. Stability of Am(VI) in 10 mM AgNO₃/1 M HNO₃ after ozonation. Left: Residual Am(III) with ingrowth of Am(V) as the initial reduction product of Am(VI). Right: Decrease of Am(VI) concentration over time.

3.3 Electrochemical Oxidation of Americium

C. Dares, and T. J. Meyer (UNC-CH), B. J. Mincher, Idaho National Laboratory

The first electrolytic oxidation of americium in a noncomplexing aqueous solution has been demonstrated [Dares, et al., 2014]. This milestone result provides the first evidence that an electrochemical approach to generating the higher oxidation states of Am in nitric acid media may be possible, potentially enabling subsequent separations. An attractive feature of electrochemistry is the ability to manipulate redox states without chemical additions, which can minimize secondary waste. Challenges lie especially in understanding and controlling the molecular redox processes that occur at the electrode surface. Owing to the high oxidation potentials employed, the surface must be passive to parasitic oxidation of water, which is thermodynamically favorable and would otherwise waste energy, generate gasses, and obscure the process of interest.

Promising results have been obtained with a high surface-area, fluoride-doped tin oxide electrode coated with nanoparticles of tin-doped indium oxide (*n*ITO). A key element of this system is derivatization of the oxide surface with a surface-bound terpyridine ligand (Figure 17) for binding of the actinide at the surface under the hypothesis that such binding facilitates electron transfer to the electrode. At an anodic potential

of 1.8 V vs. Ag/AgCl (~0.8 V below the Am(IV/III) redox couple), a 0.42 mM solution of Am(III) in 0.1 M nitric acid and 0.95 M sodium nitrate, approximately 50% of the Am(III) was oxidized to Am(V) over the course of 1 hour as observed by electronic spectroscopic measurements (Figure 18). This two-electron oxidation of Am(III) is thought to support the hypothesis of facilitated electron transfer by coordination of Am(III) to the surface-bound terpyridine ligand. Our initial results point to the value of future systematic investigation at a variety of electrode surfaces derivatized with surface-bound ligands capable of coordinating americium in different oxidation states. The aim of future study would be to establish conditions that lead to electrochemical oxidation of Am(III) to Am(V) or Am(VI) with subsequent separation from the waste stream. Factors such as relative affinities and binding strengths of Am(III) (and higher valent ions) compared to the non-redox active lanthanides will be assessed to find conditions where competitive binding of Ln(III) does not completely inhibit binding and selective oxidation of Am.

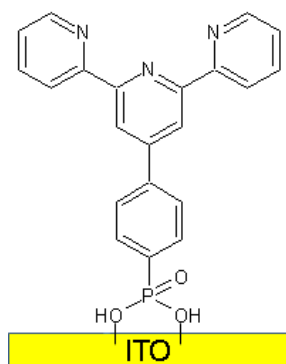


Figure 17. A terpyridine ligand bound to an indium tin oxide electrode surface via a phosphonic acid linker.

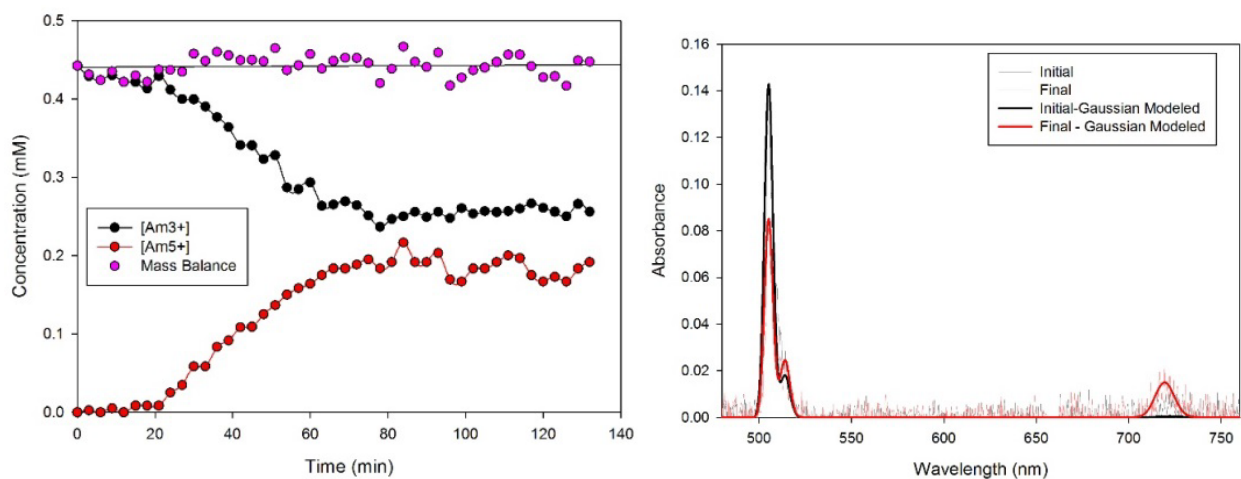


Figure 18. Left: Concentration of Am species in solution as measured by visible spectroscopy over time during a controlled-potential electrolysis at 1.8 V vs. Ag/AgCl using a ligand-modified high-surface-area working electrode, a Pt foil counter, and a Ag/AgCl wire as a reference electrode. The aqueous electrolyte was 0.1 M nitric acid and 0.95 M sodium nitrate. The working- and counter-electrode areas were separated by a fine glass frit. Right: Initial and final electronic spectra measured in a 1 cm path-length cuvette and modeled with Gaussian functions.

3.4 ALSEP Process Development for An/Ln Separation

G. J. Lumetta, Pacific Northwest National Laboratory, A. V. Gelis, Argonne National Laboratory

Significant progress has been made to mature the Actinide-Lanthanide SEparation (ALSEP) process concept [Gelis and Lumetta, 2014] to a degree that will allow a bench-scale test in engineering equipment within the next two years. ALSEP combines an acidic extractant with a neutral chelating extractant (Figure 19) to yield a single process for recovering the trivalent MA elements Am and Cm from acidic high-level waste raffinate. The raffinate is assumed to be generated by an initial co-decontamination step that removes the bulk of the U, Pu, and Np, as defined in a recent case study [Law, 2013]. This single process has the potential to replace two separate processes previously required to achieve this separation, thus significantly simplifying a closed fuel-cycle. In the past year, we have made significant progress in developing the process chemistry of the ALSEP system and have initiated dynamic testing using centrifugal contactors. Proof-of-concept batch tests and contactor results together indicate the feasibility of the basic system while revealing issues that will require dedicated efforts in FY 2015. Highlights of the development are provided below.

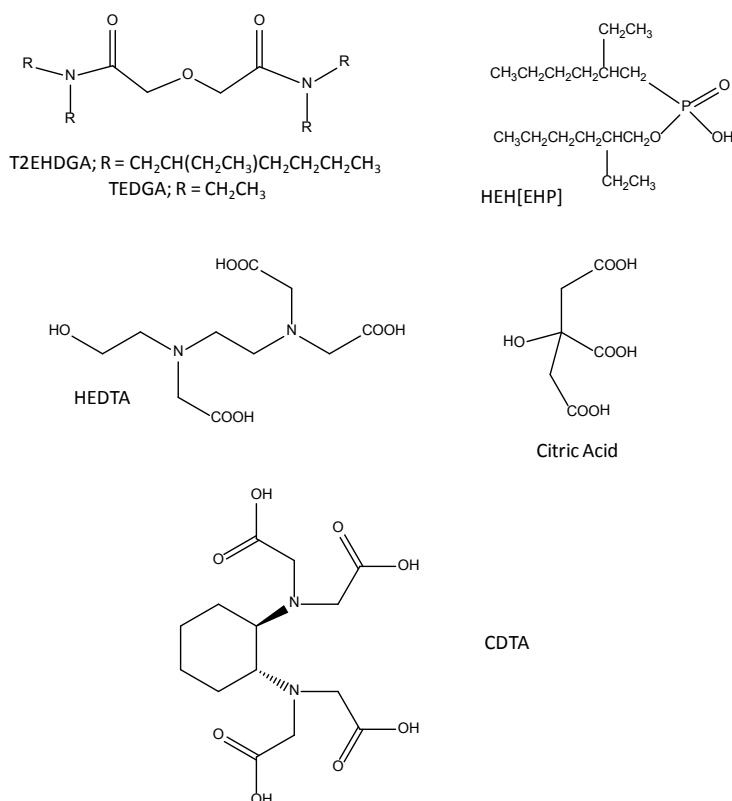


Figure 19. Component chemicals used in FY 2014 testing of ALSEP.

ALSEP chemistry combines a bifunctional neutral extractant with an acidic extractant in dodecane. The neutral extractant serves to co-extract the trivalent actinides and lanthanides from nitric acid (HNO₃) solutions, while the acidic extractant serves to hold the trivalent lanthanides in the organic phase while the actinides are selectively stripped into a carboxylate-buffered solution containing a polyaminocarboxylate ligand. Recent research has explored the effectiveness of combinations of various candidate extractants, complexants, and buffers [Gelis and Lumetta, 2014; Lumetta, et al., 2014a; Braley, et al., 2013; Lumetta, et al., 2013; Tkac, et al., 2012; Lumetta, et al., 2011; Lumetta, et al., 2010], and related literature has been

reviewed [Lumetta, et al., 2010]. This body of work has led to a focus on the set of system components shown in Figure 19. Their use and function will be described further below.

3.5 ALSEP Batch Testing and Proof of Concept

G. J. Lumetta, T. G. Levitskaia, B. M. Rapko, C. M. Niver, and M. R. Smoot (PNNL)

A proof-of-principle experiment successfully demonstrated Am separation from lanthanides and fission products but indicated the need to further investigate certain behavior, especially regarding fission products [Lumetta, et al., 2014b]. The experiment involved performing a series of batch contacts, including: 1) extraction, 2) HNO₃ scrub, 3) citrate scrub (to remove Mo from the solvent), 4) Am strip, and 5) lanthanide strip. The feed consisted of 2.20 M HNO₃ with the lanthanides La–Gd, Y, Zr, Mo, Fe, and Ru at mM concentrations representative of co-decontamination raffinate. To suppress Zr extraction, *trans*-1,2-diaminocyclohexane-*N,N,N',N'*-tetraacetic acid (CDTA) monohydrate was added to the feed solution at a concentration of 0.05 mol/L. The adjusted feed solution was then spiked with ²⁴¹Am and the batch contacts performed in order. As expected based on preliminary batch extraction survey [Lumetta, et al., 2013], the light lanthanides were not efficiently extracted in the extraction step, which is regarded as advantageous, whereas the heavier lanthanides were strongly extracted. Americium was extracted, but the distribution ratio D_{Am} was only 1.7, which can be improved by increasing the HNO₃ concentration in the feed. Despite the addition of CDTA to the feed, Zr was extracted into the organic phase during the extraction step. The mass distribution suggests that the Zr remained in the organic phase throughout the experiment because only ~12% was recovered across all the aqueous phases. All of the Zr that was recovered was found in the *N,N,N',N'*-tetraethylglycolamide lanthanide strip solutions. Also as expected, Mo was efficiently extracted from the feed into the ALSEP solvent. The citrate scrub effectively removed Mo from the solvent, but ~8% of the Mo ended up in the Am product. The Mo/Am separation could presumably be improved by optimizing the citrate scrub under countercurrent flow conditions, but also can be dealt with using additional stages. With the exception of Zr, the mass recoveries for all the elements examined were good, ranging from 96 to 102%.

Extraction and stripping of Am was found not to be affected significantly by using as-received or purified HEH[EHP]. Extraction distribution ratios of Am and Ln–Gd under the two conditions were almost superimposable, though re-equilibrating loaded solvent with starting nitric acid did show some differences, possibly reflecting impurity or kinetic effects. Stripping of Am from the loaded ALSEP solvent into 0.125 mol/L HEDTA/0.2 M citrate also was investigated using both purified and as-received HEH[EHP]. As shown in Figure 20, little difference is seen between the purified and as-received solvents in the MA stripping regime.

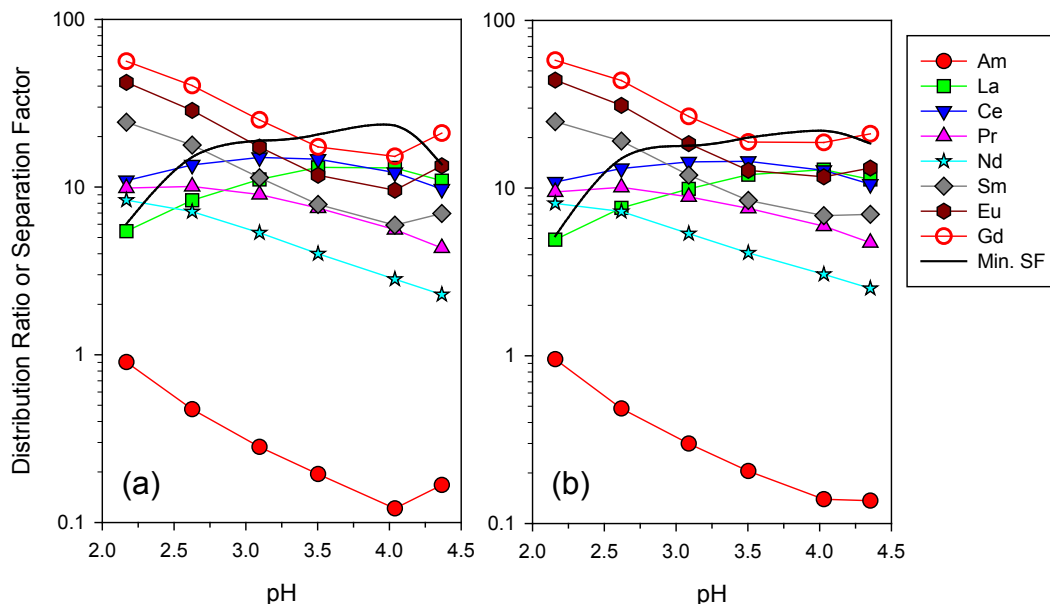


Figure 20. Distribution ratios as a function of pH for the back-extraction of various elements from the loaded ALSEP solvent into aqueous 0.125 mol/L HEDTA + 0.2 mol/L citrate; a) as-received HEH[EHP] used, b) purified HEH[EHP] used; contacting method: 60-min vortex mixing.

Inconsistent behavior was noted with Zr and Ru in separate batch tests. A prior experiment conducted with CDTA showed that the extraction of Zr(IV) from HNO_3 (0.5 to 4.5 mol/L) can be completely suppressed by adding 50 mmol/L CDTA to the feed, while the distribution ratios for the lanthanide elements are little affected by the presence of CDTA. The lack of Zr suppression in the proof-of-principle experiment might be due to inconsistent histories of the Zr-containing stock solutions used in the different experiments, resulting in different Zr speciation at the time of extraction. The behavior of ruthenium(III) (Ru) was also found to be inconsistent in the presence of CDTA. In the absence of CDTA, Ru D values are <0.1 for HNO_3 concentrations 0.6 to 4.4 mol/L HNO_3 . However, in one experiment with 50 mmol/L CDTA present, the Ru D values were in the hundreds in the range 2.5 to 4.5 mol/L HNO_3 . On the other hand, in the proof-of-principle experiment, the Ru D value was only 0.03 when CDTA was added. These discrepancies will be examined in FY 2015.

3.6 First Contactor Testing of ALSEP

A. V. Gelis and M. A. Brown, Argonne National Laboratory

The first tests of ALSEP chemistry in engineering contacting equipment were conducted in FY 2014, and like the proof-of-principle batch testing, results gave both encouragement and indications of the need for further work [Gelis and Brown, 2014]. Assuming that the chemical issues noted above are successfully resolved, obtaining good hydraulic and stage efficiency in contacting equipment then would permit the design of a bench-scale flowsheet demonstration. Toward this end, single-stage contactor tests were performed using a 2-cm centrifugal contactor designed and built at ANL. On the positive side, extraction of Am appears to be readily adaptable to centrifugal contactors as shown in Figure 21. No kinetic issues were identified in comparing distribution ratios obtained at equilibrium with effective distribution ratios obtained at a relatively high contactor flow rate.

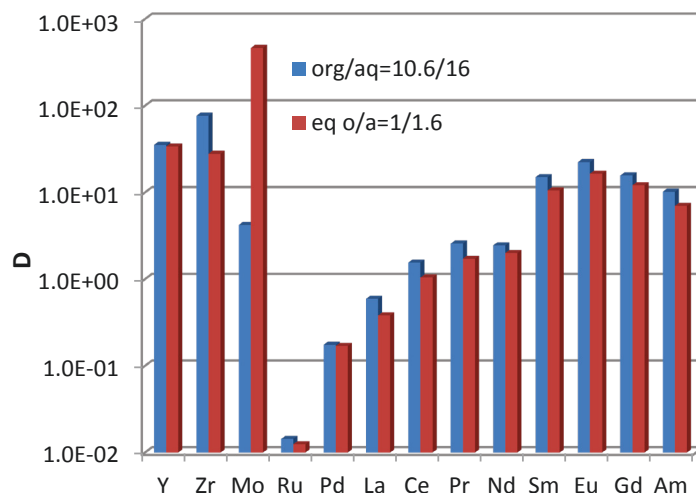


Figure 21. Fission product, lanthanide, and ^{241}Am extraction from 3 HNO_3 with 50mM T2EHDGA and 1 M HEH[EHP] in *n*-dodecane in a 2-cm centrifugal contactor. Red: equilibrium batch distribution ratios at an O:A ratio of 1:1.6. Blue: effective distribution ratios at contactor flow rates 10.6 mL/min organic and 16 mL/min aqueous.

Stripping performance using the 2-cm contactor indicated kinetic limitations. A solvent mixture of 0.75 M HEH[EHP] with 0.05 M *N,N,N',N'*-tetrakis(2-ethylhexyl)diglycolamide (T2EHDGA) in *n*-dodecane was contacted with equal volumes of a simulated PUREX raffinate solution plus Am/Eu or Am/Pm spikes in a separatory funnel. The loaded solvent was then contacted with equal volume of a 0.5 M ammonium citrate solution at pH 3.5 and allowed to equilibrate overnight. Over 60% of the Mo was stripped in the single citrate scrub. Most of the Ln, Am, Fe, Y, and Zr remained in the solvent. Using the loaded solvent and an aqueous matrix of 0.49 M ammonium citrate with 0.025 M DTPA (pH after the extraction is 3.17), effective separation factors were below 10 and thus not satisfactory. However, runs with 0.125 M HEDTA/0.2 M ammonium citrate solution as a stripping reagent were more promising. Results suggest that if the flow rate is decreased below 6 mL/min, a separation factor of 10 can be achieved. Increasing the temperature should increase the separation factors as well.

3.7 Aqueous Complexes for Americium-Curium Separation

M. P. Jensen, R. Chiarizia, Argonne National Laboratory

Although separating Am from Cm will be de-emphasized as a Sigma Team goal in FY 2015, studies of sterically constrained complexants have led to a feasible approach to a selective strip of Am from Cm in an ALSEP type system [Jensen and Chiarizia, 2014]. This approach offers the major advantage that a separate unit operation does not have to be devoted to an Am-Cm separation should it be desired, but rather, the ALSEP chemistry can be modified to deliver a Cm-free product of Am, possibly without even having to add additional stages. Separating Cm from other minor actinides may be desirable for advanced nuclear fuel cycles involving actinide partitioning and transmutation because the reduced radiation would simplify fuel fabrication and reduce the buildup of transcurium actinides in subsequent transmutation cycles [Pillon, 2003]. However, the very similar chemistries of Am and Cm make their *efficient* separation quite difficult. As described in a recent publication [Jensen, et al., 2014], we are exploring a different way to separate Am and Cm using sterically constrained ligands that amplify the very small

thermodynamic differences between Am^{3+} and Cm^{3+} complexes that arise from the slightly different radii of these two actinide ions. Some of the complexants being examined are shown in Figure 22.

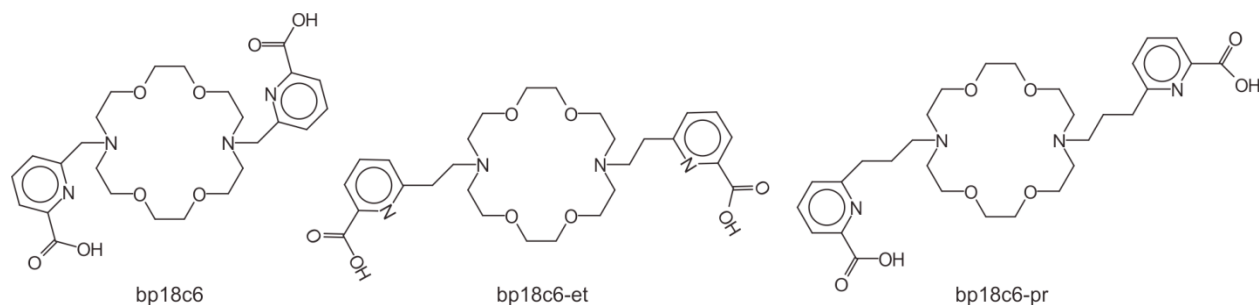


Figure 22. Structures of candidate sterically constrained macrocyclic ligands under study: *N,N'*-bis[(6-carboxy-2-pyridyl)methyl]-4,13-diaza-18-crown-6 (bp18c6) and two new derivatives with longer picolinic acid arms.

In FY 2014 we devised a way to implement an americium-selective strip in an ALSEP framework. Key to this strategy is the replacement of the complexant used in ALSEP stripping with bp18c6. In FY 2014 we overcame several obstacles to deploying bp18c6, showing that an americium-selective strip in a modified ALSEP solvent is feasible (Figure 23). First, a process solvent containing 0.05 M TEHDGA and 0.3 M HEH[EHP] in dodecane was shown to work well with 0.05 M bp18c6 plus lactate buffer in the aqueous phase. Second, the light lanthanides can be separated from Am in the loading stage, as may be seen in Figure 23a. Americium can then be separated from Cm and the heavier lanthanides using bp18c6 in the stripping stage (Figure 23b). In FY 2015, efforts will proceed to investigate the synthesis and selectivity of alternative complexants, seeking to understand the roles of steric strain and soft-donor effects and the possibility of improving upon the promising performance so far achieved.

3.8 Fundamental Chemistry of TALSPEAK-Like Systems

K. L. Nash, Washington State University

This investigation has advanced the fundamental science of TALSPEAK-like separations of the MAs from fission product lanthanides [Nash, 2014a], thereby enabling the development of Advanced TALSPEAK as well as ALSEP. TALSPEAK-like separations are those systems based on the use of actinide-selective aqueous complexants like DTPA. As recently reviewed [Nash, 2014b], it has been demonstrated that conventional TALSPEAK (based on lactate buffers, HDEHP, and DTPA) is characterized by complex interactions that reduce predictability of system performance as well as give rise to an impractical steep pH dependence. Insights developed in the WSU investigations (and complementary NEUP studies) have led to the proposed Advanced TALSPEAK system based on the phosphonate (HEH[EHP]) analog to TALSPEAK extractant HDEHP matched to a weaker holdback reagent and potentially a different buffer. The Advanced TALSPEAK concept and the introduction of HEH[EHP] led to the ALSEP combined process concept (under development at PNNL and ANL). At WSU, current research has been focusing on 1) alternative buffers (specifically malonate) for Advanced TALSPEAK, 2) the synthesis, characterization and demonstration of dipicolinate derivatives as alternatives to conventional aminopolycarboxylate holdback reagents, and 3) a mixed extractant system based on equimolar mixtures of the commercially available extractants Cyanex 923 and HEH[EHP] (PC-88A, Ionquest 801, aka HEH[EHP]) combined with a glycine buffer and various actinide selective holdback reagents.

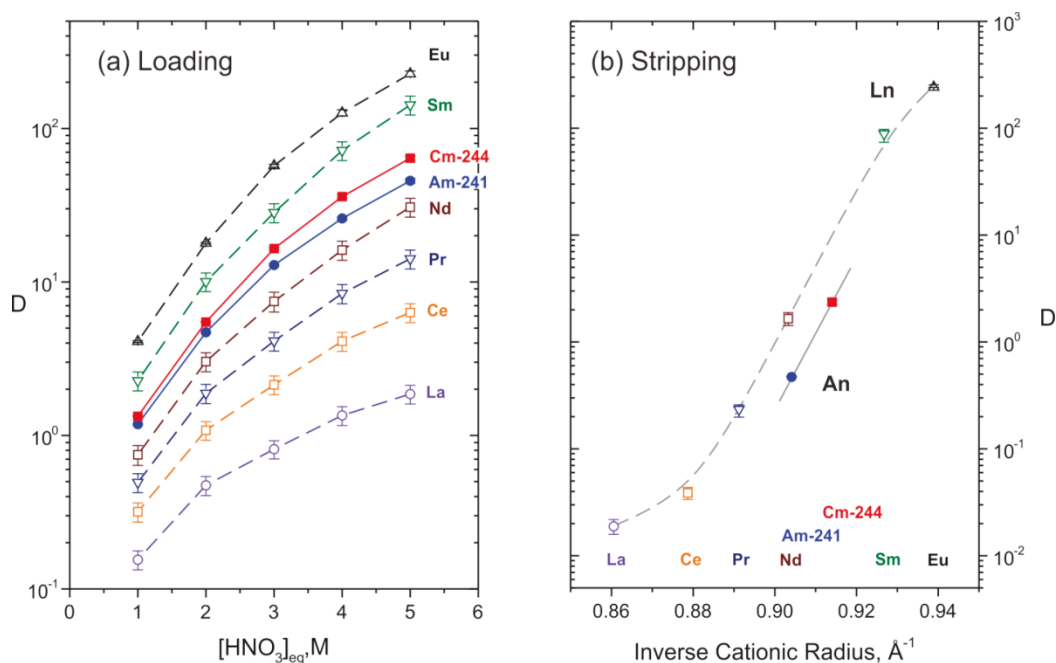


Figure 23. (a) Distribution ratios of Ln, Am, and Cm for loading of modified ALSEP solvent, 0.05 M TEHDGA/0.3 M HEDH[EHP] in dodecane from nitric acid. (b) Stripping stage distribution ratios for the modified ALSEP solvent contacted with 0.05 M bp18c6/0.4 M lactate at pH 3 show good separation of Am from Cm and lanthanides heavier than Pr.

A recent advance in FY 2014 has been the finding that an alternative buffer, malonate, may prove advantageous in TALSPEAK-like systems. Though Advanced TALSPEAK development continues to focus on citrate or lactate as preferred buffer media, malonate is of interest due to its high solubility, its lower pK_a as compared with lactate (which could enable TALSPEAK chemistry in a lower pH range), and its weaker complexing strength relative to citrate (which could improve the relative effectiveness of the actinide-selective complexant such as HEDTA). An investigation of the basic extraction chemistry of the malonate/HEDTA/HEH[EHP]-dodecane based system has established that this system could produce acceptable Ln/Am separation factors at pH 2.5 with rapid extraction kinetics and a flat separation vs. pH profile (Figure 24). Furthermore, Am/Eu separation factors increase with increasing [HEDTA]. HEDTA does not have an adverse effect on extraction kinetics; vortex-mixed samples reach extraction equilibrium within 2 minutes (or less) contact time under the conditions listed in Figure 24 at 0.5 M malonate and pH 2.6. Mixed Ln(Mal)(HEDTA) complexes are in evidence; spectrophotometric investigations conducted with Sergey Sinkov at PNNL provide new thermodynamic data describing Am and Nd complexes with HEDTA and malonate. The principal issue with this system is that La³⁺ is relatively poorly extracted, possibly resulting in some La contamination of the Am product. Separation of Am from strongly neutron absorbing Nd, Sm, Eu, and Gd is significantly better. A manuscript describing these recently verified results is in preparation.

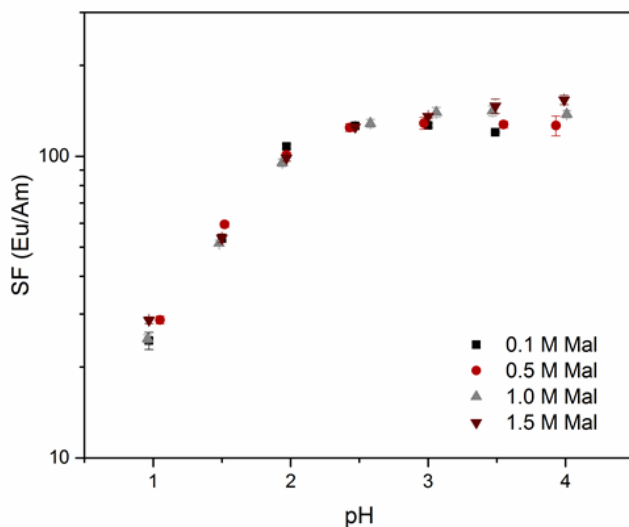


Figure 24. Advanced TALSPEAK from malonate buffer media with 0.02 M HEDTA. Organic phase: 0.2 M HEH(EHP) in *n*-dodecane.

3.9 Mixed-Donor Extractants

B. P. Hay, A. M. Panagopoulos, L. H. Delmau, V. Bryantsev, and B. A. Moyer, Oak Ridge National Laboratory

Synthesis and testing have confirmed that a preorganized analog of picolinamide (PA) results in an unprecedented factor of 10^8 increase in trivalent f-block metal extraction efficiency over a conventional picolinamide [Hay and Bryantsev, 2014]. The focus of this work is on mixed N,O-donor ligands formed by the addition of amide groups to N-heteroaromatic compounds, such as PAs. Compared to the polyazine N-donor ligands, N,O-donor ligands can offer an advantage of higher binding affinities and extractabilities, because the presence of amide oxygen donors provides good affinity toward f-elements atoms and reduces the basicity of N-heteroatoms. However, virtually all PAs reported to date have shown very weak or no extraction of Ln(III) or An(III) from aqueous nitric acid solutions, likely related to their poor preorganization, as the pyridyl and carbonyl groups are oriented *anti* to each other in the most stable conformation of the free ligands (Figure 25). This led to our hypothesis that preorganization of PAs by locking them in a conformation that is more favorable for binding could significantly boost their extractive power toward trivalent Ln/An.

To test our hypothesis, we measured under identical conditions the distribution ratios for Am(III) and Eu(III) between aqueous solutions and 1,2-dichloroethane solutions of **1a** or **2a** (Figure 25). Plots of D values vs ligand concentrations on a log-log scale are linear with slopes near 2, suggesting a 2:1 ligand:metal ion stoichiometry for the extracted complexes. At 0.05 M, the less organized ligand **1a** weakly extracts Am^{3+} with a measured D_{Am} of 0.00059, whereas the preorganized ligand **2a** strongly extracts Am^{3+} with a measured D_{Am} of 77,400, an increase of 1.3×10^8 ; at 0.1 M ligand the measured enhancement is 8.2×10^7 . The observed 10^8 -fold increase in extraction efficiency from the non-organized ligand **1a** to the preorganized ligand **2a** is unparalleled and remarkable considering the minimal structural difference between the two ligands. The average Am/Eu separation factor ($D_{\text{Am}}/D_{\text{Eu}}$) exhibited by ligand **1a** is 2.9 and by ligand **2a** is 13.2. Further improvements in Ln/An extraction efficiency and selectivity by similar ligands should be possible considering that the complementarity of **2a** for trivalent f-block metal ions is far from optimal.

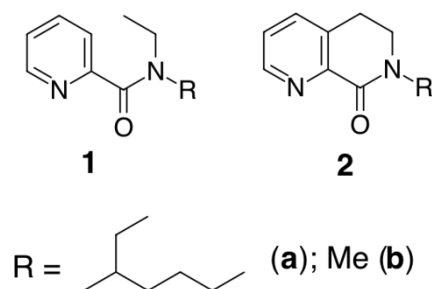
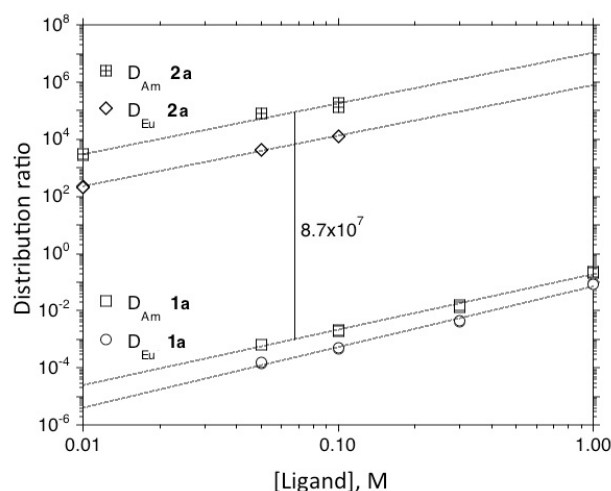


Figure 25. Plots of the distribution ratios for Am(III) and Eu(III) vs ligand concentration for 1a and 2a. Distribution measurements were made after contacting the organic phases (1,2-dichloromethane with variable concentration of ligand) with the aqueous phases (7 M LiNO₃, 10⁻⁴ M HNO₃) at 1:1 v/v phase ratios at 25 °C.

3.10 Separation of Minor Actinides from Trivalent Lanthanides Using Bis-triazinyl Pyridine Derivatives

L. H. Delmau, Oak Ridge National Laboratory; K. D. Richards and K. N. Tevepaugh, ORNL/Tennessee University; J. D. Carrick and D. D. Ensor, Tennessee Technological University

A promising baseline solvent system employing a bistriazinylpyridine type N-donor extractant has been chosen for development [Delmau, et al., 2014]. It exhibits excellent selectivity for Am(III) vs Ln(III), good Am(III) distribution ratios, good stability to prolonged contact with nitric acid, and rapid kinetics. Generally speaking, selective actinide extraction (SANEX) offers an attractive alternative to TALSPEAK-like systems, because it avoids the extraction of the lanthanides and necessity for a selective stripping strategy using complexants. It therefore entails lower total loading of the solvent and is conceptually simpler. To accomplish this result, attention worldwide has focused on soft-donor extractants employing S- and N-donor ligands. Both S- and N-donor families have encountered difficulties with stability and weak extraction at high nitric acid concentration. However, members of the extended family of bistriazinyl-pyridines (BTP), -bipyridines (BTBP), and -phenanthrolines (BTPhen) have exhibited good extraction at high nitric acid concentration, and certain alkyl substituents such as that derived from camphor (Figure 26) yield good stability. The aim of this project has been to identify an optimum extractant structure and diluent that lead to selective extraction of trivalent Am and Cm together and overall process-suitable performance. In FY 2014, the focus was on testing a range of bistriazinyl extractants and choosing a baseline solvent system for further development.

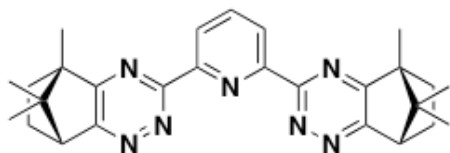


Figure 26. Camphor-BTP

The proposed baseline solvent comprises 50 mM of CA-BTP in the fluorinated diluent FS-13 (trifluoromethylphenylsulfone). The particular derivative of BTP based on camphor type substituents is relatively economical, synthetically accessible, and robust. The diluent is polar and provides relatively good solubility. In Figure 27 is shown the extraction of Am(III) from nitric acid yielding Am/Eu separation factors in excess of 10^2 . Extraction D values for Am(III) and Am/Eu selectivity remain good at 1–2 M HNO_3 even in the presence of a great excess of lanthanides. In addition to the variation of the acid concentration, the dependence on the concentration of ligand was also determined, indicating that a mixture of 1:2 and 1:3 complexes forms in the organic phase. On vortexing, equilibrium is reached in 1 minute, which is encouraging, as extraction kinetics are widely considered a potential issue with this type of compound. Extraction D values for Am(III) and Am/Eu selectivity from 1 M HNO_3 remain constant for three months, indicating promising stability. A potential question regarding the effect of the various isomers of CA-BTP was addressed by synthesizing and testing the different isomers. It was found that the effect of the isomer structure on extraction was somewhat variable but minor overall. Thus, mixed isomers can be used without preference for any given isomer.

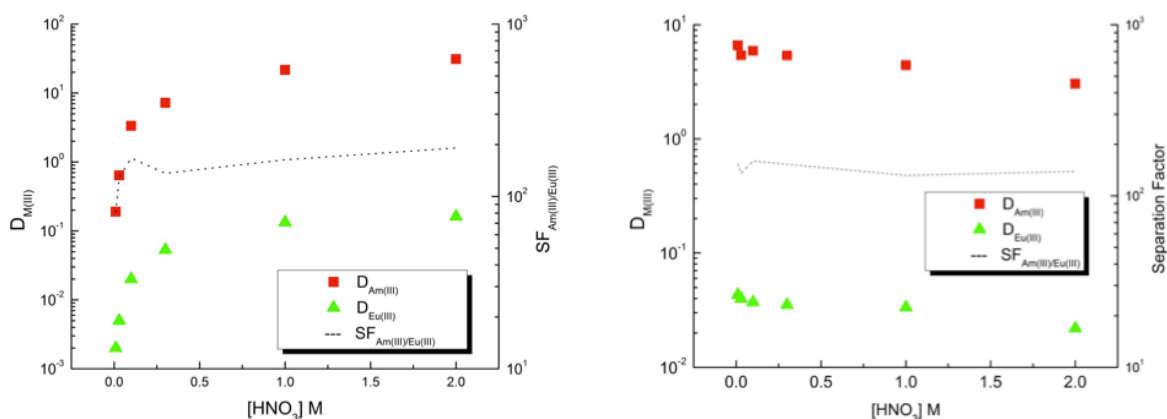


Figure 27. Extraction of Am(III) and Eu(III) from nitric acid using 50 mM CA-BTP in FS-13. O:A = 1:1, $T = 25^\circ\text{C}$. Left: 0.1 mM Ln $\text{Eu}(\text{NO}_3)_3$. Right: 0.2 M Ln (La, Nd, Ce, Eu)(NO_3)₃.

3.11 Dithiophosphinic Acid Extractants for Minor Actinide Extraction

D. R. Peterman, P. R. Zalupski, J. R. Klaen, R. G. McDowell, and J. D. Law, Idaho National Laboratory

Progress was made toward developing a solvent employing soft-donor dithiophosphinic acid (DPAH) extractants for SANEX type separation of MAs from nitric acid solution [Peterman, et al., 2014]. During the current fiscal year, a new diluent, trifluoromethylphenyl sulfone (FS-13), was adopted, and the synergistic interaction between the DPAH and several organophosphorus reagents was confirmed. The strategy of employing soft-donor extractants is based upon the proposed differences in the extent of covalent bonding occurring within the 5f-orbitals for the actinides, relative to the 4f-orbitals of the lanthanides [Nash, 2006]. DPAH compounds have attracted considerable attention in the past two decades because of their extraordinary selectivity for An(III) vs Ln(III). Particular challenges in the development of these compounds have arisen in their poor stability and weak extraction strength at >0.1 M HNO_3 . Results in this work point to significant improvements in addressing such challenges.

Continuous-variation experiments confirmed synergistic interactions between the DPAH and organophosphorus reagents in the extraction of Am(III). Three organophosphorus synergists were tested: TOPO, butyl bis(2,4,4-trimethylpentyl)phosphinate, and dibutyl butylphosphonate. For a synergistic solvent extraction system, a plot of the distribution ratio versus the mole fraction of a component present in the mixture at constant total concentration will exhibit a maximum at the greatest synergistic effect upon the extraction system. The continuous-variation experiments were performed using FS-13 as the diluent and an aqueous phase composition of 0.1 M HNO₃. An example continuous-variation experiment performed using a solvent containing TOPO and bis-(o,o-trifluoromethylphenyl)dithiophosphinic acid is shown in Figure 28. The maximum in the D_{Am} plot vs mole fraction of TOPO demonstrates that a large synergistic extraction mechanism is operative. Similar results were obtained when using BuCy272 or DBBP as the synergist.

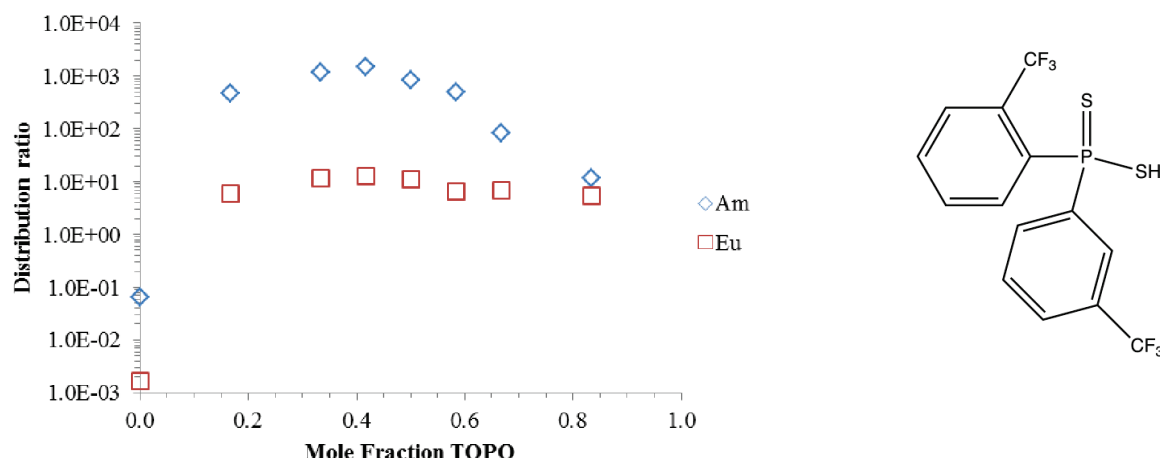


Figure 28. Continuous-variation plot of Am(III) (open diamonds) and Eu(III) (open squares) distribution ratios for TOPO and bis-(o,o-trifluoromethylphenyl)dithiophosphinic acid dissolved in FS-13. Aqueous phase: 0.1 M HNO₃.

Improved stability of DPAH solvents can be obtained by adding a reductive stabilizer to the aqueous phase. A solution containing 0.5 M bis-(o,o-trifluoromethylphenyl)dithiophosphinic acid and 0.1 M TOPO in FS-13 was contacted with 0.5 M HNO₃ containing 0.005 M hydrazine. Samples of the aqueous and organic phases were removed periodically for determination of Am and Eu distribution ratios and ³¹P NMR analysis. No statistical decrease in distribution ratios was detected over 6 weeks. By ³¹P NMR it was possible to detect approximately 1% degradation of the DPAH to the disulfide oxidative coupling product, which has no effect on extraction at such low levels. Gamma radiolysis experiments are in progress. Initial tests conducted without the hydrazine stabilizer indicated degradation of Am extraction at about 20 kGy and precipitation at 100 kGy. ³¹P NMR analysis indicated degradation of both TOPO and the DPAH compound, the chief radiolysis product of the latter being the disulfide. Future efforts will continue to examine the question of stability and synergism toward more effective extraction from nitric acid.

Publications

1. Brown, M. A.; Kropf, A. J.; Paulenova, A.; Gelis, A. V., *Aqueous Complexation of Citrate with Neodymium(III) and Americium(III): A Study by Potentiometry, Absorption Spectrophotometry, Microcalorimetry, and XAFS*, *Dalton Transactions*, 43, 2014, 6446–6454.
2. Carrick, J. D.; Tai, S.; Williams, N. J., “Synthesis of Bis-1,2,4-triazines via Telescoped Condensation of [1,10]-Phenanthroline-2,9-dicarbonitrile with Aromatic 1,2-Dicarbonyls,” *Journal of Heterocyclic Chemistry*, 2014, in press.

3. Hay, B. P.; Panagopoulos, A. M.; Delmau, L. H.; Custelcean, R.; Moyer, B. A.; Watson, L. A., "Ligand Preorganization Leads to 108-fold Increase in Extraction Efficiency of Trivalent f-block Metal Ions by Lipophilic Picolinamides," Submitted.
4. Gelis, A. V.; Lumetta, G. J., "Actinide Lanthanide Separation Process—ALSEP," *Industrial & Engineering Chemistry Research*, 53, 2014, 1624–1631.
5. Grimes, T. S.; Nash, K. L., "Acid Dissociation Constants and Rare Earth Stability Constants for DTPA," *Journal of Solution Chemistry*, 43(2), 2014, 298–313.
6. Jensen, M. P.; Chiarizia, R.; Shkrob, I. A.; Ulicki, J. S.; Spindler, B. D.; Murphy, D. J.; Hossain, M.; Roca-Sabio, A.; Platas-Iglesias, C.; de Blas, A.; Rodríguez-Blas, "T. aqueous complexes for efficient size-based separation of americium from curium," *Inorganic Chemistry*, 53(12), 2014, 6003–6012.
7. Law, J.; Mincher, B.; Garn, T.; Greenhalgh, M.; Schmitt, N.; Rutledge, V., "Development and Testing of an Americium/Lanthanide Separation Flowsheet Using Sodium Bismuthate, In *Proceedings of ICAPP*, Charlotte, NC, Apr. 4–6, 2014, American Nuclear Society, La Grange Park, IL, 2014; Paper 14040.
8. Lumetta, G. J.; Gelis, A. V.; Carter, J. C.; Niver, C. M.; Smoot, M. R. "The actinide-lanthanide separation process," *Solvent Extraction and Ion Exchange*, 32(4), 2014, 333–347. DOI:10.1080/07366299.2014.895638.
9. Lumetta, G. J.; Levitskia, T. G.; Rapko, B. M.; Carter, J. C.; Niver, C. M.; Gelis, A. V., "Development of the Actinide-Lanthanide Separation (ALSEP) Process." In *Proceedings of the 20th International Solvent Extraction Conference*, Würzburg, Germany, Sept. 7–11, 2014; DECHEMA, Gesellschaft für Chemische Technik und Biotechnologie e.V., Frankfurt am Main, Germany, 2014; Paper No. 8709, 557–562.
10. Marie, C.; Krahn, E. O.; Nash, K. L. "Probing Ligand Exchange Kinetics in Actinide/Lanthanide Solvent Extraction Systems using NMR Spectrometry," In *Proceedings of the 20th International Solvent Extraction Conference*, Würzburg, Germany, Sept. 7–11, 2014; DECHEMA, Gesellschaft für Chemische Technik und Biotechnologie e.V., Frankfurt am Main, Germany, 2014; Paper No. 4850.
11. Mincher, B. J.; Schmitt, N. C.; Tillotson, R. D.; Elias, G.; White, B. M.; Law, J. D. "Characterizing Diamylamylphosphonate (DAAP) as an Americium Ligand for Nuclear Fuel Cycle Applications," *Solvent Extraction and Ion Exchange*, 32, 2014, 153–166.
12. Mincher, B. J.; Schmitt, N. C.; Grimes, T. S. "The persistence of Am(VI) in nitric acid solution," *Solvent Extraction and Ion Exchange*, submitted.
13. Moyer, B. A.; Lumetta, G. L.; Mincher, B. J., "Recent Advances in the USA in Minor Actinide Separation." in *Reprocessing and Recycling of Spent Nuclear Fuels*, Oxford: Woodhead Publishing, 2014 (In press).
14. Nash, K. L. "The chemistry of TALSPEAK: A review of the science," *Solvent Extraction and Ion Exchange*, 2014, accepted.
15. Nash, K. L.; Heathman, C., "New Dipicolinic Acid Derivatives for Actinide-Lanthanide Separations." In *Proceedings of the 20th International Solvent Extraction Conference*, Würzburg, Germany, Sept. 7–11, 2014; DECHEMA, Gesellschaft für Chemische Technik und Biotechnologie e.V., Frankfurt am Main, Germany, 2014; Paper No. 8947.
16. Sinkov, S. I.; Lumetta, G. J. "Americium(III) oxidation by copper(III) periodate in nitric acid solution as compared with the action of Bi(V) compounds of sodium, lithium, and potassium," *Radiochimica Acta*, submitted.

17. Tai, S.; Marchi, S. V.; Carrick, J. D., "Efficient preparation of pyridinyl-1,2,4-triazines via telescoped condensation with diversely functionalized 1,2-dicarbonyls," *Journal of Heterocyclic Chemistry*, 2014, submitted.
18. Tevepaugh, K. N.; Coonce, J.; Delmau, L. H.; Carrick, J.; Ensor, D. D. "Chromatographic separation of americium from europium using Bis-2,6-(5,6,7,8-tetrahydro-5,9,9-trimethyl-5,8-methano-1,2,4-benzotriazin-3-yl)pyridine," *Solvent Extraction and Ion Exchange*, 2014, submitted.

Reports

1. Dares, C. and Meyer, T. J. *Strategic Plan for Am Oxidation*. FCR&D-SWF-2014-000422, Idaho National Laboratory, August 25, 2014.
2. Delmau, L. H., Tevepaugh, K. N., Richards, K., Carrick, J., Ensor, D. D. *Trivalent Actinide – Lanthanide Separation using Bis Triazinyl Pyridine Derivatives*, FCRD-SWF-2014-000225, Oak Ridge National Laboratory, August 2014.
3. Gelis, A. V. and Brown, M. A. *ALSEP Year-End Report*, FCRD-SWF-2014-000216, Argonne National Laboratory, September 2014.
4. Gelis, A. V., Pereira, C., Lumetta, G. J. *AMUSE Model of a Conceptual Actinide-Lanthanide Separation (ALSEP) Flowsheet*, FCRD-SWF-2014-000027 (Limited Distribution), Pacific Northwest National Laboratory, 2014.
5. Goff, G. S., Seaman, L., Jarvinen, G. D., Runde, W. *Sigma Team for Minor Actinide Separations: LANL FY2014 Annual Report*, FCRD-SWF-2014-000221, Los Alamos National Laboratory, September 19, 2014.
6. Hay, B. P., Bryantsev, V. *Molecular Modeling and Synthesis of Sequestering Agents for An(III)/Ln(III) Partitioning*, FCRD-SWF-2014-000228, Oak Ridge National Laboratory, August 2014.
7. Hobbs, D. T., Shehee, T. C. *Experimental Findings on Minor Actinide and Lanthanide Separations Using Ion Exchange*, FCRD-SWF-2014-000230 (SRNL-STI-2014-00398), Savannah River National Laboratory, September 12, 2014.
8. Jensen, M. P., Chiarizia, R., *Feasibility of Americium-Curium Separation by Sterically Constrained Complexes*, FCRD-SWF-2014-000213, Argonne National Laboratory, September 30, 2014.
9. Lumetta, G. J., Levitskaia, T. G., Rapko, B. M., Sinkov, S. I., Niver, C. M., Smoot, M. R. *Sigma Team for Minor Actinide Separation: PNNL FY 2014 Summary Report*, FCRD-SWF-2014-000229, Pacific Northwest National Laboratory, September 2014.
10. Mincher, B. J., Tillotson, R., Law, J. D., Garn, T., Schmitt, N. *Sodium Bismuthate Process: Oxidation Test Bed Setup and Hot Testing*, FCR&D-SWF-2014-000218, Idaho National Laboratory, September 30, 2014.
11. Mincher, B. J. *Am(VI) Partitioning Studies: FY 2014 Final Report*, FCR&D-SWF-2014-000630, Idaho National Laboratory, September 30, 2014.
12. Moyer, B. A. *Sigma Team for Minor Actinide Separations FY2014 Accomplishments and Directions*, FCRD-SWF-2014-000223, Oak Ridge National Laboratory, September 30, 2014.
13. Nash, K. L. *Fundamental Studies for Improving TALSPEAK-Type Separations*, FCRD-SWF-2014-00224, Washington State University, August 26, 2014.
14. Peterman, D. R., Zalupski, P. R., Klaehn, J. R., McDowell, R. G., Law, J. D. *FY-2014 Summary Report—Minor Actinide Separations Using INL DPAH Extractants*, FCRD-SWF-2014-000615, Idaho National Laboratory, September 29, 2014.

Material Recovery and Waste Form Development
2014 Accomplishments Report

15. Peterman, D. R. *Identification of Process Suitable Diluent*, FCRD-SWF-2014-00423, Idaho National Laboratory, January 16, 2014.
16. Peterman, D. R., Zalupski, P. R., Klaehn, J. R. *Minor Actinide Separation Using INL DPAH and Synergist*, FCRD-SWF-2014-000219, Idaho National Laboratory, August 1, 2014.
17. Peterman, D. R., Zalupski, P. R., Klaehn, J. R., Law, J. D. *Flowsheet for Minor Actinide Separation Using INL DPAH Extractants – OUO*, FCRD-SWF-2014-000220, Idaho National Laboratory, August 28, 2014.
18. Zalupski, P., McDowell, R., Peterman, D. *Distribution Behavior of Soft Metal in INL DPAH Solvent*, FCRD-SWF-2014-00424, Idaho National Laboratory, July 21, 2014.

SIGMA TEAM FOR OFF-GAS

SECTION 4

4. SIGMA TEAM FOR OFF-GAS CAPTURE AND IMMOBILIZATION

B. Jubin, Oak Ridge National Laboratory

The Off-Gas Sigma Team was formed in fiscal year 2010 (FY 2010) to bring together multidisciplinary teams from across the DOE complex and academia that would work collaboratively to solve the technical challenges and to develop the scientific basis for the capture and immobilization of air-borne effluents from used fuel treatment processes so that regulatory requirements could be met. The overarching goal of the team is to develop effective methods to capture and immobilize iodine-129, carbon-14, krypton-85, and tritium released from fuel treatment processes to enable a range of advanced fuel cycle options in the U.S. General Sigma Team objectives include:

- Develop materials and processes for capturing iodine, tritium, krypton, and carbon for effective implementation across likely used fuel treatment processes.
- Development of fundamental understanding of the generation, capture, and immobilization radionuclides from used fuel treatment process off-gas to gain confidence in their performance and allow for new solutions to be developed as fuel treatment processes are better defined.
- Develop waste forms and processes to manage off-gas waste streams in an effective manner.
- Design and demonstrate the effectiveness of integrated off-gas treatment systems for likely fuel treatment processes.

Five major thrust areas were included in the activities for FY 2014: i) iodine capture, ii) iodine immobilization, iii) tritium separations from head-end off-gas deploying a tritium pretreatment process, iv) krypton separations and storage, and v) integrated off-gas treatment system development. Highlights from these activities are summarized below and described in detail in the associated technical reports generated for each task at each contributing laboratory.

4.1 Control of Tritium/Iodine Coadsorption onto Ag0Z and 3A MS

B. B. Spencer, S. H. Bruffey, J. F. Walker, Jr. and R. T. Jubin, Oak Ridge National Laboratory

The Off-Gas Sigma Team has been investigating the implementation of fixed bed adsorbers using reduced silver mordenite (Ag0Z) and type 3A molecular sieve (3AMS) beds to sequester iodine and water (tritium), respectively. The segregation of iodine from tritium is necessary to avoid elevating low-level tritium waste to high level waste. Laboratory tests conducted over fiscal years 2012–2013 showed that Ag0Z absorbs iodine up to ~13% by weight depending on process conditions while also adsorbing water from humidified feed streams to a concentration of about 1 wt% water at 150°C. The 3AMS adsorbs water to a concentration of around 20 wt% at 25°C, and was also shown that adsorption of water is accompanied by limited co-adsorption of iodine (about 0.5 wt%) under conditions expected in the effluent streams from used nuclear fuel processing operations (e.g., oxidative pretreatment or nitric acid dissolution steps).¹

Regeneration of the 3AMS is achieved by heating the sorbent to temperatures not exceeding 270°C, causing the water to desorb into a low volume carrier gas stream. The co-adsorbed iodine is mostly released with the water, providing no opportunity to separate the water and iodine using this sorbent. Tests showed that the heating of Ag0Z that contains both iodine and water up to 230°C released the water that was adsorbed, but a small fraction of iodine (thought to be physisorbed) was also released with the water.¹

An off-gas processing sequence was proposed that could separate the iodine and water sequestered with these sorbents. It involves placing the heated ($\sim 150^{\circ}\text{C}$) Ag^0Z sorbent upstream of the 3AMS. Breakthrough of water occurs in the Ag^0Z column far earlier than does the iodine breakthrough, thus the iodine-free, moisture-laden stream is subsequently treated with a 3AMS column to recover the water. When iodine breakthrough occurs at the Ag^0Z column, a second Ag^0Z column is placed on-line that accepts the process off-gas. In practice, the first Ag^0Z column would be heated and purged at a low-flow-rate and the effluent would be routed to the second Ag^0Z column along with the process off-gas. This would permit the first column to expel the water it had sorbed and any iodine that escapes with the water would be adsorbed in the second Ag^0Z column. Columns of 3AMS would be rotated as required to collect the water present in the Ag^0Z effluent stream. In concept, no iodine reaches the 3AMS columns [1]. The fundamental concept for such a design is illustrated in Figure 29.

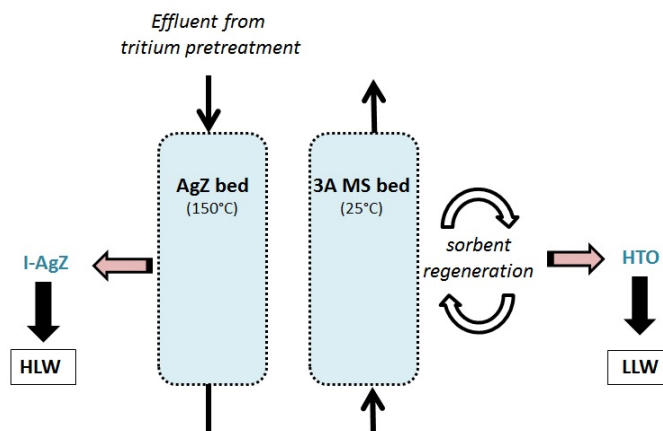


Figure 29. Segregation of iodine and tritium through the use of sorbent beds

Integrated co-adsorption tests were completed to determine the effectiveness of the proposed processing sequence in recovering and segregating iodine and water (tritium) from off-gas streams. Loading tests have been performed to verify the breakthrough time of both water and iodine from the Ag^0Z . At operating temperatures of about 130°C to 150°C , these tests showed Ag^0Z sorbs up to 8 wt% iodine and 2 wt% water, with water breakthrough occurring much earlier than iodine breakthrough. All tests imply that the iodine is sorbed onto a moisture saturated media.

The width of the measureable mass transfer zone (MTZ) for iodine sorption on Ag^0Z was shown to be ~ 6.5 in. Use of an Ag^0Z guard column permitted detection of breakthrough from the primary Ag^0Z column, while protecting the downstream 3AMS column from collecting iodine. In some tests it was evident that very low concentrations of iodine escaped the Ag^0Z column due to the wide MTZ, and a short guard column (about $1\frac{1}{2}$ inch) was insufficient to protect the 3AMS. In an integrated test using a longer guard column (about 5 inch), neutron activation analysis of the downstream 3AMS following a loading and regeneration cycle was unable to detect the presence of iodine. The results successfully demonstrated that iodine can be sequestered in the Ag^0Z while the water is collected free of iodine in the 3AMS column [2].

Tests were also performed to measure desorption of iodine from the Ag^0Z by changing the synthetic off-gas stream to a dry, iodine-free feed. Desorption began at a temperature of 150°C , the same temperature as loading. The temperature was increased stepwise at irregular intervals to 180°C , 210°C , and 380°C . Upon each temperature increase the rate of iodine release from the Ag^0Z bed increased substantially. The cumulative iodine release at about 180 hr and a temperature of 380°C was over 50% of the amount sorbed

and was still increasing when the test was terminated [2]. The large amounts of iodine released from the Ag^0Z at elevated temperature is reason for concern for high temperature processes that might be used to manufacture a waste form using this material.

References

1. B. B. Spencer, S. H. Bruffey, J. F. Walker, Jr., K. K. Anderson, and R. T. Jubin, *Iodine and Water Co-adsorption on Deep Beds of 3AMS and AgZ*, FCRD-SWF-2013-000329, also ORNL/LTR-2013/439, Oak Ridge National Laboratory, September 2013.
2. B. B. Spencer, S. H. Bruffey, J. F. Walker, Jr., and R. T. Jubin, *Integrated Iodine and Water Co-adsorption Tests*, FCRD-SWF-2014-000034, also ORNL/LTR-2014/472, Oak Ridge National Laboratory, September 2014.

4.2 Effects of Aging Conditions on Iodine Adsorption

S. H. Bruffey, K. K. Patton, R. T. Jubin and J. Matyáš, Oak Ridge National Laboratory, *Pacific Northwest National Laboratory*

A series of tests have exposed both iodine sorbents of interest (Ag^0Z and Ag^0 -aerogel) to progressively more complex simulated off-gas streams. These tests, lasting up to 6 months, examine the effects of long-term exposure, or aging, on the performance of the sorbent. To date, Ag^0Z and Ag^0 -aerogel have each been exposed to a dry air stream, a humid air stream, and an NO_2 environment. Ag^0Z has also been exposed to NO. Upon completion of the aging study, the sorbent is tested to evaluate the deleterious effects of long-term exposure to the selected component on the sorbent's ability to remove iodine from a dry air stream. The ability of iodine-loaded Ag^0Z to retain iodine during extended exposure to these streams has also been examined. The results of all aging tests completed are summarized in Table 4.

Table 4. Aging studies completed at ORNL

Test Matrix			I_2 Capacity or Retention	
Aging environment	Ag^0Z	Ag^0 -Aerogel	Ag^0Z	Ag^0 -Aerogel
Dry air	✓	✓	-40%	-22%
Moist air	✓	✓	-60%	-22%
2% NO_2^a	✓	✓	-30%	-15%
1% NO	✓	□	-78%	—
I_2 pre-loaded; aged in dry air	✓	□	Iodine retained	—
I_2 pre-loaded; aged in 2% NO_2	✓	□	Iodine retained	—

In FY 2014, the long-term effects of both NO and NO_2 exposure on the iodine capture performance of Ag^0Z was determined. Ag^0Z was exposed to a 2% NO_2 environment for up to 4 months. This resulted in a 29% decrease in iodine capacity. Exposure to a 1% flowing NO stream degraded the sorbent more severely; a 78% decrease in iodine capacity was observed after 1 month of aging.

In addition to aging of Ag^0Z , the aging of iodine loaded silver mordenite ($\text{I-Ag}^0\text{Z}$) upon exposure to NO_2 was examined. This type of study will provide insight into the ability of the sorbent to retain iodine following capture despite degradation by the potentially corrosive off-gas stream. It was found that 4 months of exposure to a 2% NO_2 environment did not result in any loss of iodine from the sorbent as shown in Table 4.

In FY 2012 and -13, Ag^0 -functionalized aerogel demonstrated good stability and sorption performance after extended aging in dry or humid air. Exposure to these conditions over a period of 6 months resulted in a decrease of iodine sorption capacity of only 22 relative percent as noted in Table 4[1,2]. In FY 2014, testing continued on Ag^0 -functionalized silica aerogel exposed to dry air containing 2% NO_2 . The iodine loading capacity of the sorbent decreased from 33 to 28 wt% after 4 months, a loss of 15 relative percent [3].

References

1. Bruffey S. H., Anderson K. K., Jubin R. T. and Walker J. F. Jr., *Aging and Iodine Loading of Silver-functionalized Aerogels*, FCRD-SWF-2012-000256, August 31, 2012.
2. Bruffey S. H., Anderson K. K., Walker J. F. Jr., and Jubin R. T., *Humid Aging and Iodine Loading of Silver-Functionalized Aerogels*, FCRD-SWF-2013-000258. August 30, 2013.
3. Jubin R.T., Bruffey S.H., Patton K.K., “Humid Aging and Iodine Loading of Silver-Functionalized Aerogels,” FCRD-SWF-2014-000594, September 2014.
4. Bruffey, S. H., Jubin, R. T., Anderson, K. K., and J. F. Walker, Jr., “Aging and Iodine Loading of Ag^0Z in a static 2% NO_2 Environment,” ORNL/LTR-2013/351, U.S. Department of Energy Separations and Waste Forms Campaign, August 2013.
5. Bruffey, S. H., Jubin, R. T., Anderson, K. K., and J. F. Walker, Jr., “Aging and Iodine Loading of Ag^0Z in a static 2% NO_2 Environment,” ORNL/LTR-2013/351, U.S. Department of Energy Separations and Waste Forms Campaign, August 2013.

4.3 Determining the Mechanisms of Methyl Iodide Adsorption on Ag^0Z through Deep Bed Testing

T. M. Nenoff, Sandia National Laboratories; N. Soelberg, Idaho National Laboratory

Silver mordenite (AgZ) was identified in the 1970's for its potential as iodine sorbent, reacting with molecular iodine (I_2) to form AgI . However the mechanisms for the capture of organoiodine, such as CH_3I , are not well understood. Deep bed CH_3I adsorption tests were performed at the INL to support sorbent, adsorption, and waste form studies at PNNL, ORNL, and Sandia National Laboratory (SNL). The deep bed test system (Figure 30) is designed to emulate an actual fixed sorbent bed and enable measurements at different bed depths for determining capture efficiencies, sorbent capacities, CH_3I adsorption process reactions and reaction byproducts, and mass transfer zone depths. Tests have established detection limits, developed procedures for sample analysis with minimal analytical interferences, and show that CH_3I reacts when in contact with the Ag^0Z sorbent [1].

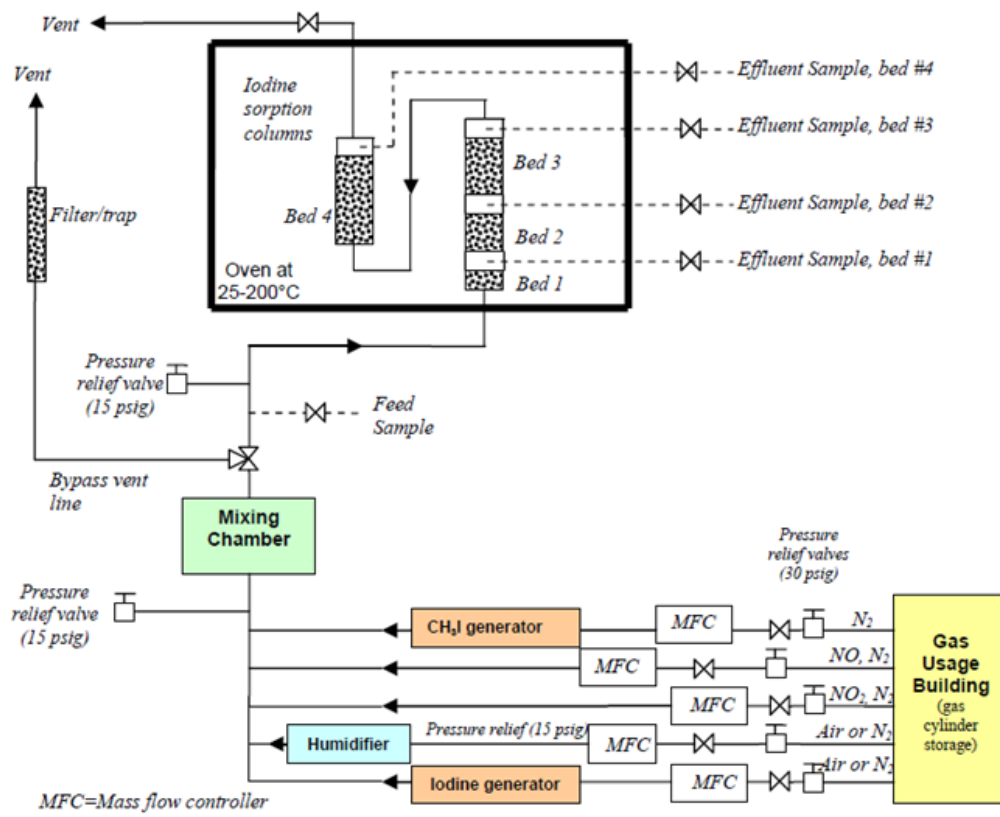


Figure 30. Deep bed adsorption test system

CH₃I decontamination factors observed during deep bed testing exceeded 1,000 across the 8 inch total bed depth for a gas stream containing 57ppm CH₃I, ~800 ppm NO and NO₂ and 1.8 vol% H₂O vapor and a superficial velocity of 4.3 m/min. The CH₃I mass transfer zone (MTZ, or depth of the bed where adsorption reactions occur) was estimated at 4-8 inches, deeper than MTZs estimated for I₂ adsorption from dry air on AgZ. Other gas constituents (such as NO_x and H₂O) can affect the CH₃I reactions, resulting in variations in the speciation of uncaptured iodine exiting iodine-laden sorbent beds (both dimethyl ether (C₂H₆O) and nitromethane (CH₃NO₂) have been observed).

Chemical analysis of the effluent gas stream in concert with in-depth characterization of the recovered sorbent was used to elucidate the mechanism for CH₃I decomposition by AgZ. Post sorption results indicate that the capture of iodine CH₃I by AgZ proceeds via a series of catalytic and sorption processes. Specifically, the formation of alkoxy species on the zeolite surface, such as surface methoxy species (SMS, Al–O(Me)–Si), is known to be a key intermediate in a number of important catalytic processes. The SMS, formed by addition of the methyl halides, can react with a number of different molecules in the stream to form various hydrocarbon products. For example, SMS reacts with water to form methanol, and methanol to form dimethyl ether (DME) in each case regenerating the acid site. The SMS can react with NO_x to form methyl nitrite leaving a basic site. Reaction with O₂, and oxidation of the SMS produces CO and CO₂ [2].

Based on the species observed downstream from the CH₃I adsorption over the AgZ, the TGA/DSC–MS of the iodine loaded AgI–MOR, and the structural analyses, we postulate the following reactions occur in the process of capturing the iodine from the complex input stream of CH₃I, H₂O, NO, NO₂ and air [3]. The mechanism is illustrated in Figure 31. First, CH₃I is cleaved to form an iodine species and a SMS at

the low operating temperature of the adsorption process, 150°C. Second, the iodine reacts with the Ag to form AgI nanoparticles inside the zeolite pore. Third, the SMS react with NO_x to form methyl nitrite or with water to form methanol, which can further react with other SMS to form dimethyl ether. Methanol, dimethyl ether and methyl nitrite are seen downstream of the adsorption column.

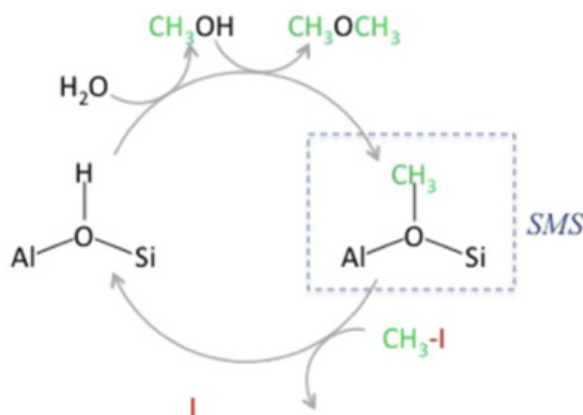


Figure 31. A schematic portraying the dual catalytic CH₃I decomposition and I confinement reaction pathway over the Ag⁺Z zeolite framework (-Si-O(-H)-Al-). The SMS unit is identified. Note: the fate of the charge balancing proton is not fully elucidated.

References

1. Soelberg, N. and T. Watson, *Phase I Methyl Iodide Deep-Bed Adsorption Tests*, INL/EXT-14-32917, August 22, 2014.
2. Y. Jiang, M. Hunger, W. Wang, *Journal of the American Chemical Society*, 128, 2006, 11679–11692.
3. T. M. Nenoff, M. A. Rodriguez, Sandia National Laboratories, N. R. Soelberg, Idaho National Laboratory, K. W. Chapman, Advanced Photon Source, Argonne National Laboratory, FCRD-SWF-2014-000471, DOE/NE-Fuel Cycle R&D Separations Working Group, M4FT-14SN0312041, “Determine Mechanism of CH₃I Capture in AgZ,” August 16, 2014.

Publications

1. T. M. Nenoff, M. A. Rodriguez, N. Soelberg, K. W. Chapman, *Microporous and Mesoporous Materials*, 2014, <http://dx.doi.org/10.1016/j.micromeso.2014.04.041>

4.4 Improved Xe/Kr capacity and selectivity in advanced materials

P. K. Thallapally, Pacific Northwest National Laboratory

In an effort to improve the separation of Xe and Kr using solid sorbents, a new class of materials called porous organic cage compounds (CC3) were explored in collaboration with the University of Liverpool, UK. The CC3 cage compound can be synthesized *via* condensation of 1,3,5-triformylbenzene and R,R-1,2-diaminocyclohexane. The organic cage molecule, CC3 (Figure 32), had an internal cavity that was precisely the right size for Xe. In the crystalline state, the cage consolidated to give a robust 3-dimensional pore structure. To evaluate CC3 for separations of noble gases at low concentrations in air, breakthrough measurements were obtained using an adsorption column with a diameter of 7.7 mm and 39.0 mm of length packed with CC3 crystals. When a mixture of Xe (400 ppm) and Kr (40 ppm) balanced

with simulated air was passed through this column, the Xe component was retained for more than 15 minutes, even at a flow rate of 0.67 L/s, twice the volumetric flow rate used in experiments with the previously tested sorbent Ni/DOBDC metal organic framework (MOF). By contrast, Kr and the other components (N₂, O₂, and CO₂) broke through almost immediately. Under these conditions, CC3 adsorbs twice (11 mmol kg⁻¹) as much Xe as the leading MOF, Ni/DOBDC (4.8 mmol kg⁻¹). In addition, the Xe/Kr selectivity for CC3 under these conditions is almost three times higher than for Ni/DOBDC: 20.4 versus 7.3. Selectivity and capacity are often seen as a trade-off. Here, CC3 showed significant improvement in both of these key parameters with respect to the leading Ni/DOBDC MOF material.

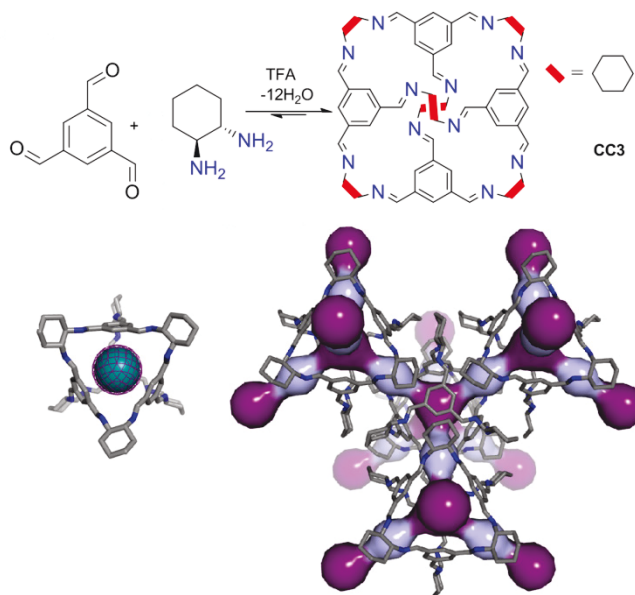


Figure 32. New porous organic cage molecule (CC3) with 2X and 3X improved capacity and selectivity compared to NiDOBDC MOF. The perfect size to accommodate a single xenon atom (cyan sphere). Two pore cavities exist in the 3D pore structure, a cage cavity inside the molecule itself (dark purple) and a window cavity between adjacent cage windows (light purple).

Publications

1. Chen, e. a., Riess, P. S., Chong, S. Y., Holden, D., Jelfs, K. E., Hasell, T., Little, M. A., Kewley, A., Briggs, M. E., Stephenson, A., Thomas, M., Armstrong, J. A., Bell, J., Busto, J., Noel, R., Liu, J., Strachan, D. M., Thallapally, P. K., Cooper, A. I., "Separation of rare gases and chiral molecules by selective binding in porous organic cages." *Nature Materials*, 2014, 1-7.
2. Liu, J., C. A. Fernandez, P. F. Martin, P. K. Thallapally and D. M. Strachan, "A Two-Column Method for the Separation of Kr and Xe from Process Off-Gases." *Industrial & Engineering Chemistry Research*, 53(32), 2014, 12893-12899.
3. Liu, J., D. M. Strachan and P. K. Thallapally, "Enhanced noble gas adsorption in Ag@MOF-74Ni." *Chemical Communications*, 50(4), 2014, 466-468.
4. Liu, J., P. K. Thallapally and D. Strachan, "Metal-Organic Frameworks for Removal of Xe and Kr from Nuclear Fuel Reprocessing Plants," *Langmuir*, 28(31), 2012, 11584-11589
5. Soelberg, N. R., T. G. Garn, M. R. Greenhalgh, J. D. Law, R. Jubin, D. M. Strachan and P. K. Thallapally, "Radioactive Iodine and Krypton Control for Nuclear Fuel Reprocessing Facilities." *Science and Technology of Nuclear Installations*, 2013.

6. Thallapally, P. K., J. W. Grate and R. K. Motkuri (2012). “Facile xenon capture and release at room temperature using a metal-organic framework: A comparison with activated charcoal,” *Chemical Communications*, 48(3), 347-349.
7. Fernandez, C. A., J. Liu, P. K. Thallapally and D. M. Strachan, “Switching Kr/Xe Selectivity with Temperature in a Metal-Organic Framework,” *Journal of the American Chemical Society* 134(22), 2012, 9046-9049.

4.5 Behavior of Radioactive Semivolatile Species during Nuclear Fuel Reprocessing

R. T. Jubin, D. M. Strachan, G. Ilas, B. B. Spencer, and N. R. Soelberg[†] Oak Ridge National Laboratory, *Pacific Northwest National Laboratory (Retired) and [†]Idaho National Laboratory*

In nuclear fuel reprocessing, various radioactive elements enter the gas phase across a range of unit operations found in the reprocessing facility. Jubin et al. reported on the evolution pathways and required removal of four radionuclides known to be volatile, ¹⁴C, ³H, ¹²⁹I, and ⁸⁵Kr [1-2]. There is, however, another group of elements with reaction products that, if formed, would be expected to be at least somewhat volatile, or semivolatile, under certain conditions and need to be removed from the off-gas streams. The term *semivolatile* does not appear to be concisely defined in the literature.

In this study, the term *semivolatile* is used to identify inorganic and organometallic species that are gaseous at ambient conditions within a reprocessing facility or have sufficiently high vapor pressures to report to the vapor phase above process liquids. Generally, the metal elements are not volatile and only become volatile when they react with other elements to form compounds that are volatile.

In this study, an effort was made to determine which, if any, of 24 potentially semivolatile radionuclides could be released from a reprocessing plant and, if so, what would be the likely quantities released.

A study has been performed to determine if radionuclides present in used fuel, which are or can form compounds known to be semivolatile during used fuel reprocessing, need to be captured along with volatile radionuclides in reprocessing facility off-gas systems to ensure compliance to Environmental Protection Agency (EPA) and Nuclear Regulatory Commission (NRC) regulations. This is a follow-on study to the volatile radionuclide evaluations previously reported [1-2].

This study was performed in several steps.

- A list of isotopes present in used nuclear fuel (UNF) was generated with the ORIGEN and SCALE codes [3-4].
- A list of possible semivolatile compounds containing these isotopes was developed based on a literature search and knowledge of the chemical processes in typical aqueous processing of UNF, assuming initially that all elements (isotopes) that can form volatile species through chemical reaction do form those volatile species. Electrochemical UNF reprocessing was not included in the scope of this study.
- This long list of possible radionuclides was shortened by considering only isotopes with half-lives greater than 91 days, since isotopes with half-lives shorter than 91 days would decay to negligible levels (by a factor of 9.5×10^{-7}) if UNF is not reprocessed for at least 5 years after removal from the reactor. The list contracted to 47 isotopes.

- This list of isotopes was further trimmed by calculating the dose from each to a maximum exposed individual (MEI) with the US EPA airborne radiological dispersion and risk assessment code CAP-88^{5,6} to yield a shorter list shown in Table 5 containing 17 isotopes. Control of the elements on this list needs to be considered because they could require high decontamination factors (DFs, the ratio of the uncontrolled and controlled emission) to meet a reasonable fraction of the regulated release.

Because the chemistry of an element dictates the method by which a DF is achieved, the list of isotopes in Table 5 can be shortened by only considering the largest required DF for the isotopes for that element (shown in bold in Table 5); for example, the DF for cesium is dictated by ¹³⁷Cs at 4.9×10^9 . There are three elements with required DF values < 10 (< 90% removal): cadmium, palladium, and tellurium. It is also important to note that the DF values are based on the total amount of that isotope in the used fuel. Thus, it would require the ~71% of the Pd in the fuel to be volatilized and released to the environment (i.e., a DF=1.4) to yield a dose of 0.025 mRem to the MEI.

Based on the DFs shown in Table 5 Cs, Ru, Sb, and Tc have the greatest potential for requiring additional control on releases. However, upon closer examination and past experience, none of these elements form sufficiently volatile compounds, in the context of the current reprocessing facility operations, to be of regulatory concern from an emission standpoint based on volatility alone. And with current or proposed use of scrubbers and particulate filtration technology, neither are particulate forms an emission concern.

Table 5. Maximum required DFs for the semi-volatile isotopes with the potential to yield 0.025 mRem to the MEI.

Isotope	Required maximum DF	Isotope	Required maximum DF
^{110m} Ag	2370	¹²⁵ Sb	9.56×10^6
¹⁰⁹ Cd	6.36	⁷⁹ Se	524
¹³⁴ Cs	9.56×10^8	^{119m} Sn	58.8
¹³⁵ Cs	2160	^{121m} Sn	7600
¹³⁷ Cs	4.92×10^9	¹²³ Sn	63.2
¹⁰⁷ Pd	1.4	⁹⁸ Tc	1.3
¹⁰² Rh	15.2	⁹⁹ Tc	9.44×10^4
^{102m} Rh	8920	^{127m} Te	3.08
¹⁰⁶ Ru	3.04×10^7		

References

1. Jubin, R, N. Soelberg, D. Strachan, and G. Ilas, 2012a, *Fuel Age Impacts on Gaseous Fission Product Capture During Separations*. FCRD-SWF-2012-000089, PNNL-22550, Oak Ridge National Laboratory.
2. Jubin, R. T., N. R. Soelberg, D. M. Strachan, and G. Ilas, 2012b, *Position Paper on Practicable Performance Criteria for the Removal Efficiency of Volatile Radionuclides*, FCRD-SWF-2012-000091, Oak Ridge National Laboratory.
3. Gauld, I. C., G. Radulescu, G. Ilas, B. D. Murphy, M. L. Williams, and D. Wiarda, 2011, "Isotopic Depletion and Decay Methods and Analysis Capabilities of SCALE," *Nuclear Technology* 174(2), 169-195.
4. ORNL, 2009, *SCALE: A Modular Code System for Performing Standardized Computer Analyses for Licensing Evaluations (Version 6)*, ORNL/TM 2005/39 Vols. I - III, Oak Ridge National Laboratory.
5. Rosnick, R., 1992, *CAP-88 (Clean Air Act Assessment Package-1988)*. US Environmental Protection Agency, Washington, DC.

6. Rosnick, R, 2007, *CAP88-PC Version 3.0 User Guide*, Environmental Protection Agency, Washington, DC.

4.6 Optimization Studies on GCM for Iodine Waste Forms

T. M. Nenoff, P. V. Brady, C. Mowry, T. J. Garino, Sandia National Laboratories

A primary thrust of the Off-Gas Sigma team is to understand the durability and materials processability of the low temperature sintering Bi-Si oxide Glass Composite Material (GCM)¹. In FY 2014 the effects of a number of synthesis variables to assess their effects on the durability of the Sandia GCM waste form were investigated. A Single Pass Flow Through (SPFT)² test was used to determine variables that might affect the rate at which iodine and silver are released from the waste form, and therefore its durability. The results of these studies are briefly summarized below and complement ongoing GCM waste forms studies for iodine.³⁻⁹

- **AgI-Z weight percent levels:** SPFT testing indicates that GCM fabricated with 22 and 25% AgI-Z releases of Ag and I at the same low rates as 15% AgI-Z GCM, and by the same mechanism. Iodine and Ag release is controlled by the low solubility of an amorphous, hydrated silver iodide, not by the surface-controlled dissolution of I₂-loaded Ag-Mordenite.
- **AgI-Z particle size:** The AgI-Z particle size in a GCM waste form was determined to have no effect on iodine or silver release because, as expected, both are limited by the low solubility of AgI. The higher effluent portion of Ag relative to I suggests that Ag leaching from the waste form controls equilibrium levels of iodine.
- **Organic iodine source and retention:** Durability results for the GCM fabricated with AgI-Z produced through exposure to an off-gas stream containing gaseous water, CH₃I, NO and NO₂ indicate releases of Ag and I at the same low rates as I₂-loaded AgI-Z GCM, and by the same mechanism. Evaluations were performed on how the iodine adsorbed from CH₃-I is retained during waste form production. Thermal data of the loaded mordenite indicates that at 225 °C, there is a release of iodine, NO, CO and CO₂. There is no evidence of AgI loss (melting point 556 °C) up to 600°C.
- **Silver Addition and Sintering Atmosphere:** The minimum amount of silver flake required to prevent loss of I₂ during sintering in air was determined to be 1.1 wt% Ag (studies utilized AgI-MOR with 8.7wt% I). The final GCM composition prior to sintering was 20 wt% AgI-Z, 1.1 wt% Ag, and 80 wt% Bi-Si oxide glass. Alternatively, heating the AgI-Z in inert atmosphere instead of air allowed for densified GCM formation without I₂ loss, and no necessity for the addition of Ag. Heating rate, iodine loading levels and atmosphere are the important variables that determine AgI migration and results suggest that AgI may be completely incorporated into the mordenite structure by the 550°C sintering temperature.

Provisional Patents

1. Tina M. Nenoff, Dorina F. Sava Gallis, Karena W. Chapman, Peter J. Chupas, “*System and method for the capture and storage of waste*,” 10/23/2013.
2. Tina M. Nenoff, Dorina F. Sava Gallis, Terry J. Garino, “*Densified waste form and method for forming*,” 11/15/2013.

References

1. Garino, T. J.; Nenoff, T. M.; Krumhansl, J. L.; Rademacher, D. “Low-Temperature Sintering Bi- Si- Zn Oxide Glasses For Use in Either Glass Composite Materials or Core/Shell ¹²⁹I Waste Forms,” *Journal of the American Ceramic Society*, 2011, 94(8), 2412-2419.
2. ASTM, “Standard Practice for Measurement of the Glass Dissolution Rate Using the Single-Pass Flow- Through Test Method,” Accessed 11/08/2012.
3. Nenoff, T. M.; Brady, P. V.; Garino, T. J.; Mowry, C. D. “Determination of Baseline Iodine Waste Form Performance Characteristics,” FCRD-SWF-2012-000172, SAND 2012-6892C, 2012.
4. Nenoff, T. M.; Brady, P. V.; Mowry, C. D. “Effect of pH and Temperature on AgI-Mordenite and Bi-Si Glass Dissolution” FCRD-SWF- 2013-000098, SAND 2013-1205P, 2013.
5. Nenoff, T. M.; Brady, P. V.; Garino, T. J.; Mowry, C. D. “SPFT Testing of Optimized Weight Loadings of AgI-Z in GCM,” FCRD-SWF-2013-000215, SAND 2013-5763P, 2013.
6. Nenoff, T. M.; Brady, P. V.; Garino, T. J.; Mowry, C. D. “Study of Variable I₂ Loadings in Ag-MOR in Sandia Low Temperature Bi-Si Glass Composite Material (GCM) Waste Form,” FCRD-SWF-2013-000232, SAND 2013-7437 P, 2013.
7. Nenoff, T. M.; Brady, P. V.; Garino, T. J.; Mowry, C. D. “Effect of Particle Size on Iodine Loaded Ag-MOR on Final GCM Waste Form,” FCRD-SWF-2014-000472, SAND 2014- 4846P, 2014.
8. Nenoff, T. M., Rodriguez, M. A., Soelberg, N., Chapman, K. A., “Silver-mordenite for radiological gas capture from complex streams: Dual catalytic CH₃I decomposition and I confinement,” *Microporous and Mesoporous Materials*, 2014, in press (Invited, *special issue cluster for Thomas Bein*), DOI: 10.1016/j.micromeso.2014.04.041
9. Chapman, K; Chupas, P.; Nenoff, T. M. “Radioactive Iodine Capture in Silver-Loaded Zeolites Through Nanoscale Silver Iodide Formation” *Journal of the American Chemical Society*, 2010, 132(26), 8897–8899.

4.7 Consolidation of Iodine-Loaded Silver Sorbents

J. Matyáš, Pacific Northwest National Laboratory; S. H. Bruffey, R. T. Jubin, Oak Ridge National Laboratory

Consolidation of both iodine-loaded Ag₀Z and iodine-loaded Ag₀-functionalized silica aerogel powders into a waste form by hot isostatic pressing (HIPing) was investigated.

HIPing of Ag₀Z samples was conducted at ORNL. Samples were pressed with temperatures ranging from 525 to 1100°C and pressures ranging from 100 to 300MPa. Additionally, a number of samples were of varied composition, including iodine as either NaI, AgI, or AgI-MOR, and mordenite as pure sodium mordenite, Ag-mordenite, or an engineered form of mordenite. These samples were analyzed by X-ray diffraction (XRD) and scanning electron microscopy (SEM)-EDS. It was found that in all cases, the material was transformed into an amorphous phase with AgI clusters present throughout. Leaching studies will be conducted in FY15 to determine the ability of these pressed amorphous pellets to retain iodine.

HIPing of Ag₀-functionalized silica aerogel powders was conducted at PNNL by pressing the material at 1200°C for 30 min under 207 MPa. This resulted in a fully dense silica-based waste form of 3.3 g/cm³ apparent density containing ~22 mass% of iodine. The distribution of individual elements (Ag, I, and Si) and morphology of particles are shown in Figure 33. Iodine was retained in the form of nano- and micro-inclusions of AgI (white particles) dispersed in the silica matrix (dark grey areas).

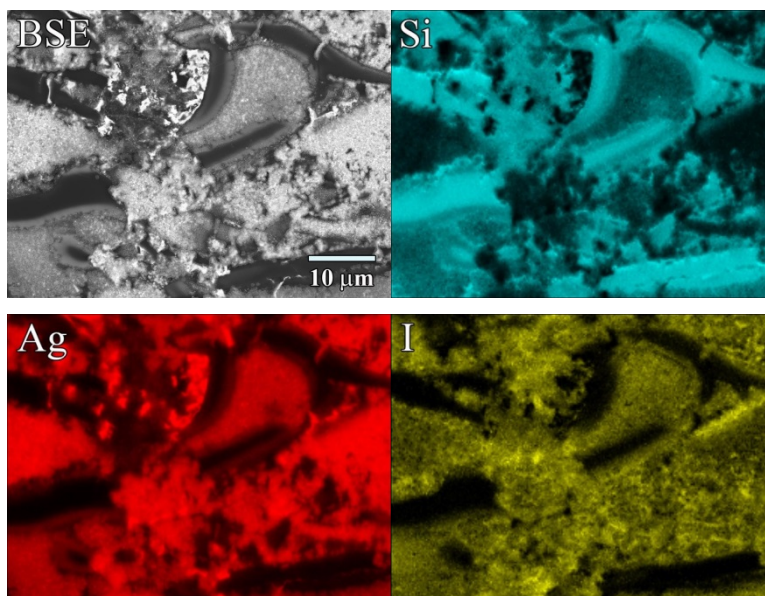


Figure 33. Elemental dot map of the HIP-consolidated iodine-loaded Ag^0 -functionalized silica aerogel

4.8 Silver-Functionalized Silica Aerogel for Iodine Adsorption and Immobilization

J. Matyáš, A.V. Walter, and J.A. Rice, Pacific Northwest National Laboratory

In FY 2012 and -13, Ag^0 -functionalized aerogel demonstrated good stability and sorption performance after extended aging in dry or humid air. Exposure to these conditions over a period of 6 months resulted in a decrease of iodine sorption capacity of only 22 relative percent [1-2]. In FY 2014, testing continued on Ag^0 -functionalized silica aerogel exposed to dry air containing 2% NO_2 . The iodine loading capacity of the sorbent decreased from 33 to 28 wt% after 4 months, a loss of 15 relative percent [3].

A large quantity of Ag^0 -functionalized silica aerogel was synthesized with the bench-scale apparatus developed in FY 2013. A total of 500 g of granules bigger than 0.85 mm with a bulk density $\sim 500 \text{ kg/m}^3$ was delivered to Oak Ridge National Laboratory⁴ and Idaho National Laboratory⁵ for testing.

A characterization study was performed on the intermediate product of chemical functionalization (thiol-aerogel) and Ag^0 -functionalized silica aerogel. Analysis of the thiol-aerogel with ^{29}Si -NMR revealed a high population density of silanes ($\sim 5.3 \text{ silanes/nm}^2$) and its favorable speciation within a monolayer, indicating an excellent environment to achieve a high number density of uniformly distributed Ag^0 nanoparticles ($< 10 \text{ nm}$). Analysis of the surface of iodine-loaded thiol- and Ag^0 -functionalized silica aerogels with X-ray photoelectron spectroscopy revealed that thiol-aerogel can capture iodine in two forms: I_2S_2 and a yet unknown iodine compound. However, Ag^0 -functionalized silica aerogel captures iodine only in the form of AgI . Other components (S, C, Si) do not seem to contribute to iodine capture.

Iodine-loaded Ag^0 -functionalized silica aerogel powders were consolidated into a waste form. Hot isostatic pressing (HIP) of this material at 1200°C for 30 min under 207 MPa resulted in a fully dense silica-based waste form of 3.3 g/cm^3 apparent density containing $\sim 22 \text{ mass\%}$ of iodine.⁶ The distribution of individual elements (Ag, I, and Si) and morphology of particles are shown in Figure 33 (above). Iodine was retained in the form of nano- and micro-inclusions of AgI (white particles) dispersed in the silica matrix (dark grey areas).

References

1. Bruffey S. H., Anderson K.K., Jubin R. T. and Walker J. F. Jr., *Aging and Iodine Loading of Silver-functionalized Aerogels*, FCRG-SWF-2012-000256, August 31, 2012.
2. Bruffey S. H., Anderson K. K., Walker J. F. Jr., and Jubin R. T., *Humid Aging and Iodine Loading of Silver-Functionalized Aerogels*, FCRG-SWF-2013-000258, August 30, 2013.
3. Jubin R. T., Bruffey S. H., Patton K. K., *Humid Aging and Iodine Loading of Silver-Functionalized Aerogels*, FCRG-SWF-2014-000594, September, 2014.
4. Matyáš J., *Production of Ag0-functionalized silica aerogel for testing at ORNL*, FCRD-SWF-2014-000463, December 18, 2014.
5. Matyáš J. *Production of Ag0-functionalized silica aerogel for testing at INL*, FCRD-SWF-2014-000468, February 26, 2014.
6. Matyáš J. and Walters A. V., *Consolidation of iodine-loaded Ag0-functionalized silica aerogel with HUP, HIP, and SPS*, draft 2104, Pacific Northwest National Laboratory.

4.9 Results of Economic Evaluation of MOFs for Kr Capture

J. E. Cabe, M. D. Bearden, D. R. Brown, P. K. Thallapally, D. M. Strachan, Pacific Northwest National Laboratory

An economic evaluation was performed for two processes that can be used to separate Xe and Kr from the off-gases from the reprocessing UNF. Both processes were configured for continuous operations and the compressed gas storage of the separated Xe and Kr. The latter process, storage, was assumed to be the same for both processes and, therefore, the estimates for actual immobilization process were not included. However, both separations processes were configured for an output consistent with compressed gas storage. Because the physical state of the output product to the immobilization process was different, there were minor cost differences for this step in the overall process.

The first configuration is based on conventional cryogenic distillation. This process is based on commercial processes and had been the subject of previous evaluations (Mellinger et al 1984). The process utilizes low temperature and high pressure distillation columns to separate the low-temperature constituents of air according to differences in boiling point. Before separating Xe and Kr, the NO_x and other contaminants in the process off-gas must be removed. Additionally, because radiolysis of the O₂ causes the formation of O₃, most of the O₂ must also be removed. The cryogenic distillation process results in relatively high purity Kr gas that can be stored in pressurized vessels for storage or disposal.

The second process configuration to be compared, utilizes experimental results from tests on Ni/DOBDC MOF in packed columns to separate Kr from process off-gas. The MOF unit operation can be conducted at a lower pressure and at a higher temperature (-40 °C¹) than the cryogenic process, giving the MOF-based process an economic advantage. For continuous operation, the process feed gas is envisioned to use two sets of two sorption beds: one set of beds operates while the second is regenerated by vacuum swing. The adsorbed Xe and Kr is recovered from their respective beds, compressed, and provided to the immobilization process. In the MOF-based process, the primary components of the feed gas, nitrogen and oxygen and the contaminants (NO_x, CO₂, etc.), pass through the beds un-adsorbed to the plant stack. In

¹ This experimental temperature was an artifact of the experimental apparatus; higher temperatures may be possible, but because the experiments from which the data were used in this evaluation were obtained at this temperature, -40 °C was used as well.

this process, no O₃ is generated since no liquid O₂ is present and any trace quantities of O₃ would pass through the MOF sorbent.

A summary of the results from the economic study are shown in Table 6. These results indicate that there is an economic advantage to the use of MOF-based processes for the removal of Kr from reprocessing off-gas streams. These results indicated that a MOF-based process was cost competitive despite the concern over the projected high materials costs.

At equivalent flow rates and off-gas composition, the Ni-DOBDC MOF process metrics indicate that improvements can be realized in regard to capital outlay, annual operating costs, and improved environmental release profiles with potentially high decontamination factors. Additional process refinement, integrative studies, and advances in MOF production cost knowledge would serve to further refine this initial comparative evaluation. Further research and modeling addressing definitive cost estimates for MOF production should be completed to appropriately understand the true cost of manufacturing. As the assumption with the highest level of uncertainty in this analysis, a definitive cost of manufacturing would enable a full life cycle cost analysis for MOF based processes, as well as comparative technologies. Similarly, further research on MOFs and related porous materials is required to improve the adsorption capacity and selectivity of Kr from process off-gases. Obtaining better capacities and selectivities would further reduce the cost per kg to remove Kr. Clearly, research is needed on the number of sorption and desorption cycles before capacity degradation requires MOF replacement and the total amount of radiation that can be tolerated before degradation forces bed replacement.

Table 6. Comparative Criteria for MOF and Cryogenic Process Evaluations

Process	Decontamination Factor	Total Project Capital (\$10 ⁶)	Proposed Annual Consumables ^A (\$)
Cryogenic Distillation	67	8.77	267 000 ^A
MOF Adsorption	100 ^B	8.42	78 000

Notes:

^A Includes compressor/pump utility loads adjusted to capacity factor and \$0.10/kWh, and annual consumables (hydrogen for cryogenic and MOF for the adsorbent process).

^B The MOF DF is theoretical and neither measured nor calculated. The model assumed complete adsorption based on experimental data and performance criteria established in bench scale testing.

References

1. Mellinger, P. J., L. W. Brackenbush, J. E. Tanner, and E. S. Gilbert. *Krypton-85 Health Risk Assessment for a Nuclear Fuel Reprocessing Plant*, 1984, PNL-5209, Pacific Northwest Laboratory.

This page left intentionally blank

FUNDAMENTAL SCIENCE AND METHODS / M&S

SECTION 5

5. FUNDAMENTAL SCIENCE AND METHODS DEVELOPMENT / MODELING AND SIMULATION

The Fundamental Science and Methods Development / Modeling and Simulation (S&M)/ (M&S) team are utilizing new tools and research methods to understand the fundamental properties of extraction systems. These fundamental properties are the basis for understanding any separation process from a science-based approach rather than an empirical approach, which has been the typical approach used in the past. A greater understanding of the fundamental properties (such as thermodynamics, kinetics, effects of radiation on chemistry) will enable the development of more robust processes and also support future models that allow for a predictive capability of process performance.

5.1 Contactor Modeling

K. Wardle, Argonne National Laboratory

This project as funded in FY 2014 under the ‘Contactor Modeling’ work package represents the combination of computational and experimental efforts aimed at liquid–liquid contactors that were funded separately in FY 2012 and combined into a single effort in FY 2013. The significant successes produced by this effort include:

Products

- **MultiphaseEulerFoam** – Hybrid multiphase CFD solver which combines the Eulerian–Eulerian multi-fluid method with VOF sharp interface capturing on selected phase pairs. A description of the solver is given in Wardle and Weller (2013) (Figure 34a). Additionally, the solver has been released as part of the open-source CFD toolkit OpenFOAM since version 2.0 and is available for download at www.openfoam.org. The solver is currently available to, and in use by researchers worldwide.
- **MultiphaseEulerFlexFoam** – This is an expanded version of multiphaseEulerFoam which includes dispersed phase droplet size prediction (as described in Wardle (2013)) along with the enhancements noted in Section 2 of the project’s year-end report.
- **3D Printable ANL-2cm centrifugal contactor** – As part of the 3D printing investigations conducted during the current fiscal year, a redesign of the ANL-2cm housing (and rotor) was undertaken to improve the design for optimum 3D printing (reduction of materials and faster, more reliable prints) (Figure 34c). While additional testing is needed to understand materials compatibility issues for plastic prints (e.g. potential effects from possible plasticizer leaching), this redesign may facilitate a significant reduction in fabrication cost and also open the possibility for many novel design features—a few of which have already been realized. The redesigned contactor housing has also successfully been 3D printed in alloy 15-5 stainless steel using the direct metal laser sintering (DMLS) process.
- **Novel, laser-free droplet imaging system** – As described in year-end reports from the previous two FYs, a novel lighting and imaging setup was assembled for in situ imaging of liquid-liquid dispersion in an annular centrifugal contactor (Figure 34b). This setup employs a high-power, short pulse (500 ns) strobe for synchronized lighting and a long-range, telecentric microscope lens (K1 CentriMax) coupled with a high-resolution DSLR camera for imaging. Images from this

setup are featured on the lens manufacturer's website² and have also been highlighted in the *Argonne Now* magazine (Spring 2014, page 3)³.

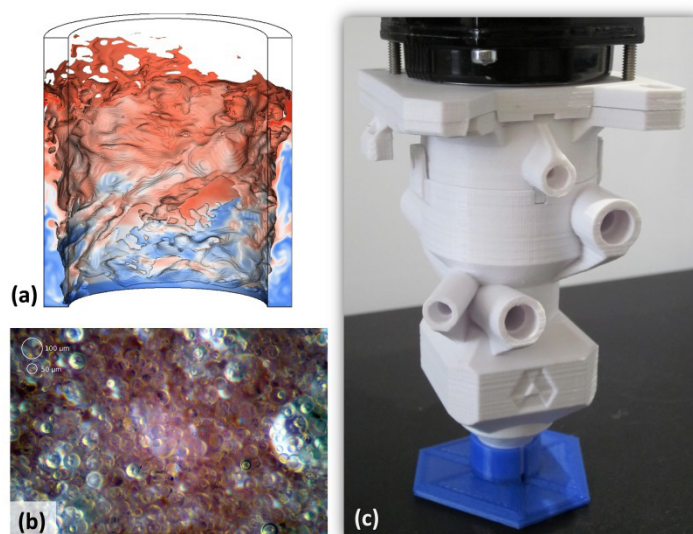


Figure 34. (a) Snapshot from multiphase CFD simulation using multiphaseEulerFoam (Wardle & Weller 2013). (b) Image of a liquid-liquid dispersion taken *in situ* in an operating centrifugal contactor. (c) Redesigned and 3D printed ANL-2cm centrifugal contactor.

The above listing provides a good picture of the productivity of this project with the broad insights gained through simulation and experiment culminating in a patentable advancement of centrifugal contactor technology having direct application to the needs of the FCT program (i.e. extending mixing residence time).

Patents

1. “Extended Residence Time Centrifugal Contactor Design Modification and Centrifugal Contactor Vane Plate Valving Apparatus for Extending Mixing Zone Residence Time” (application submitted 30 September 2014, no. 14/501,898)

This patent comprises several centrifugal contactor design modifications which can provide a greater than two-fold increase in mixing zone residence time and improve equipment performance for kinetically limited extraction processes (e.g. TALSPEAK, ALSEP).

Publications

1. Wardle, K. E., Weller, H. G., 2013. Hybrid multiphase CFD solver for coupled dispersed/ segregated flows in liquid-liquid extraction. *Int. J. Chem. Eng.* 2013, 128936
2. Wardle, K. E., 2013. Hybrid multiphase CFD simulation for liquid-liquid interfacial area prediction in annular centrifugal contactors. In: *Proceedings of Global 2013*. p. 7650
3. Wardle, K. E., Lee, T., 2013. Finite element lattice boltzmann simulations of free surface flow in a concentric cylinder. *Computers & Mathematics with Applications*, 65, 230–238

² http://www.infinity-usa.com/Products.aspx?pg=Model_K1-CentriMax

³ <http://www.anl.gov/downloads/argonne-now-magazine-summer-2014>

4. Vedantam, S., Wardle, K. E., Tamhane, T. V., Ranade, V. V., Joshi, J. B., 2012. CFD simulation of annular centrifugal extractors. *Int. J. Chem. Eng.* 2012, 759397 (invited review article)
5. Gandhir, A., Wardle, K. E., 2012. CFD analysis of fluid flow above the upper weir of an annular centrifugal contactor. *Sep. Sci. Technol.* 47, 1–10
6. Wardle, K. E., 2011. Open-source CFD simulations of liquid–liquid flow in the annular centrifugal contactor. *Sep. Sci. Technol.* 46, 2409–2417

5.2 Fundamental Radiation Chemistry

B. J. Mincher, Idaho National Laboratory

The diglycolamides (DGAs) are finding increasing attention for applications in fuel cycle separations. The octyl derivative *N,N,N',N'*-tetraoctyldiglycolamide (TODGA, Figure 35a) has received detailed study for its applications at the back end of the nuclear fuel cycle in European work, while the branched-chain TODGA derivative *N,N,N',N'*-tetra-2-ethylhexyldiglycolamide (T(EH)DGA, Figure 35b) has been promoted as an alternative with less affinity for fission product complexation in the USA program. The radiolytic stability of these DGAs is of obvious potential concern. Among the few previous studies, Sugo et al. reported a decrease in TODGA concentration with dose, with the rate being slower for neat TODGA than for TODGA in dodecane [1]. This so-called “sensitization effect,” in which dodecane increased the rate of TODGA decomposition was attributed to electron transfer reactions with dodecane radical cations [2]. These are produced by the direct ionization of dodecane during radiolysis and will react with any species having a higher ionization potential, including the DGA. The presence of nitric acid during irradiation was reported to have little effect on the rate of TODGA radiolysis. Only one study has previously examined T(EH)DGA radiolysis [3].

To confirm and expand upon these few published reports, a collaborative effort between the radiation chemistry program at INL and partners at Forschungszentrum Juelich was established. The Juelich partners have long-term experience studying TODGA as a fuel cycle solvent extraction ligand, and have previously examined the effects of TODGA irradiation on metal distribution ratios. In the current work, solutions of TODGA and T(EH)DGA in *n*-dodecane were subjected to γ -irradiation in the presence and absence of an acidic aqueous phase. These solutions were then analyzed using UHPLC-ESI-MS (Ultra-High Performance Liquid Chromatography- Electrospray Ionization- Mass Spectrometry) to determine the rates of radiolytic decay of the two extractants, as well as to identify radiolysis products.

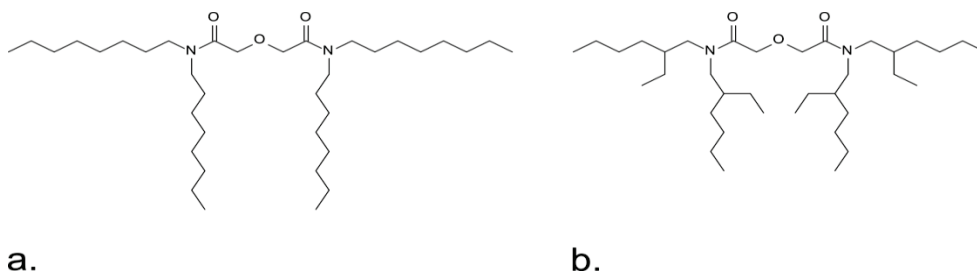


Figure 35. Structures of the two diglycolamides studied here: a. *N,N,N',N'*-tetraoctyldiglycolamide (TODGA) and b. *N,N,N',N'*-tetra-2-ethylhexyldiglycolamide (T(EH)DGA).

Both DGAs were found to decrease in an exponential fashion (Figure 36) with increasing dose at the same rate and were not influenced by the presence or absence of an acidic aqueous phase. Since the

degradation rate was the same even in the absence of the aqueous phase, this is consistent with a reaction with the dodecane radical cation.

Therefore, techniques were developed to observe and measure the kinetics of the reaction of TODGA with the dodecane radical cation, taking advantage of a long-term existing INL collaboration with California State University Long Beach, and using a fast electron pulse radiolysis system at Brookhaven National Laboratory. This is the first rate constant ever reported for the dodecane radical cation: $k_1 = (9.72 \pm 1.10) \times 10^9 \text{ M}^{-1} \text{ s}^{-1}$. This is a fast reaction, and further implicates the cation as being the important species in DGA radiolysis.

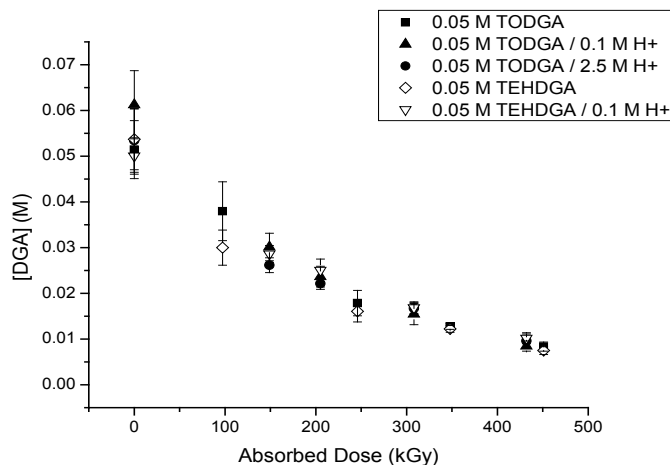


Figure 36. DGA concentration vs. absorbed dose. The solid squares are 0.05 M TODGA, the open diamonds are 0.05 M T(EH)DGA, the solid upward-facing triangles are 0.05 M TODGA contacted with 0.1 M HNO₃, the open inverted triangles are 0.05 M T(EH)DGA contacted with 0.1 M HNO₃, and the solid circles are 0.05 M TODGA contacted with 2.5 M HNO₃.

A number of radiolysis products were also identified by UHPLC-ESI-MS, and are consistent with those previously identified for these two compounds using GC-MS [1,2,3]. The identity of these radiolysis products suggests that the bonds most vulnerable to radiolytic attack are those in the diglycolamide center of these molecules, and not on the side-chains. The major products of these reactions retain the ability to form multidentate coordination complexes with metal cations, so radiolysis reactions may not immediately play a large role in influencing distribution ratios or separation factors.

This collaborative program between INL, Juelich, Cal State, and Brookhaven has already produced a manuscript under review with *Solvent Extraction and Ion Exchange*, and will continue. Upcoming work will include the measurement of the radical cation rate constant for reactions with T(EH)DGA, and octyl(phenyl)-N,N-diisobutylcarbonylmethyl-phosphine oxide (CMPO). The CMPO comparison will be instructive since the acidic aqueous phase was previously found to protect CMPO, [4] in contrast to the DGAs. Two new DGAs recently proposed by Juelich will also be examined for radiation stability.

References

1. Sugo, Y.; Sasaki, Y.; Tachimori, S., "Studies on hydrolysis and radiolysis of N,N,N',N'-tetraoctyl-3-oxapentane-I,5-diamide." *Radiochimica Acta*, 90, 2002, 161-165.

2. Sugo, Y.; Izumi, Y.; Yoshida, Y.; Nishijima, S.; Sasaki, Y.; Kimura, T.; Sekine, T.; Kudo, H., "Influence of diluent on radiolysis of amides in organic solution." *Radiat. Phys. Chem.* 76, 2007, 794-800.
3. Sharma, J. N.; Ruhela, R.; Singh, K. K.; Kumar, M.; Janardhanan, C.; Achutan, P. V.; Monaohar, S.; Wattal, P. K.; Suri, A. K., "Studies on hydrolysis and radiolysis of tetra(2-ethylhexyl)diglycolamide (TENDGA)/isodecyl alcohol/n-dodecane solvent system." *Radiochimica Acta*, 98, 2010, 485-491.
4. Mincher, B. J.; Mezyk, S. P.; Elias, G.; Groenewold, G. S.; Riddle, C. L.; Olson, L. G. "The radiation chemistry of CMPO: Part 1. Gamma radiolysis." *Solv. Ext. Ion Exch.*, 31, 2013, 715-730.

5.3 Separation Process Thermodynamics and Kinetics: Development of Microfluidic Devices for Solvent Extraction Studies and Radioanalytical Applications

Artem V. Gelis, Cari A. Launier, Argonne National Laboratory

A second-generation plug-based microfluidic system was developed and tested. This system uses flowing plugs (droplets) in microfluidic channels to determine absolute interfacial mass transfer rate constants. Unlike conventional macro-scale systems, measurements are done under conditions of both rapid mixing and controlled interfacial area with the generation of very little waste. While the first generation system was custom laser machined, the second generation system is modular and composed entirely of commercially available components. The design changes make the microfluidic system more robust, since failed components can be replaced individually, and more versatile, since it can process a wider range of solutions and flow rates. Improvements were also made to the experimental protocol to facilitate more rapid screening of a variety of reprocessing solvent extraction schemes. The improved system was utilized to determine the pseudo-first order rate constants for interfacial transfer of lanthanides and americium under various ALSEP process conditions. The following observations have been made regarding Ln and Am stripping kinetics:

- For DTPA/citrate solutions, the Am and Ln forward- and back-extraction rates decrease drastically as the pH increases
- HEDTA/citrate solution provides somewhat higher extraction rates than a DTPA/citrate solution at the same pH, although the equilibrium separation factors are less than the ones for the DTPA system.
- The highest Ln/Am separation factors at equilibrium for tested solutions are achieved with a DTPA/citrate solution at pH 4, which possesses the slowest Ln and Am extraction rates.

The measured absolute interfacial mass transfer constants for back extraction of selected lanthanides and americium are presented in Figure 37. Figure 38 shows the time-dependent separation factors for one of the two most problematic pairs--neodymium/americium.

These results will allow for optimizing ALSEP back-extraction kinetics thus improving the overall process effectiveness.

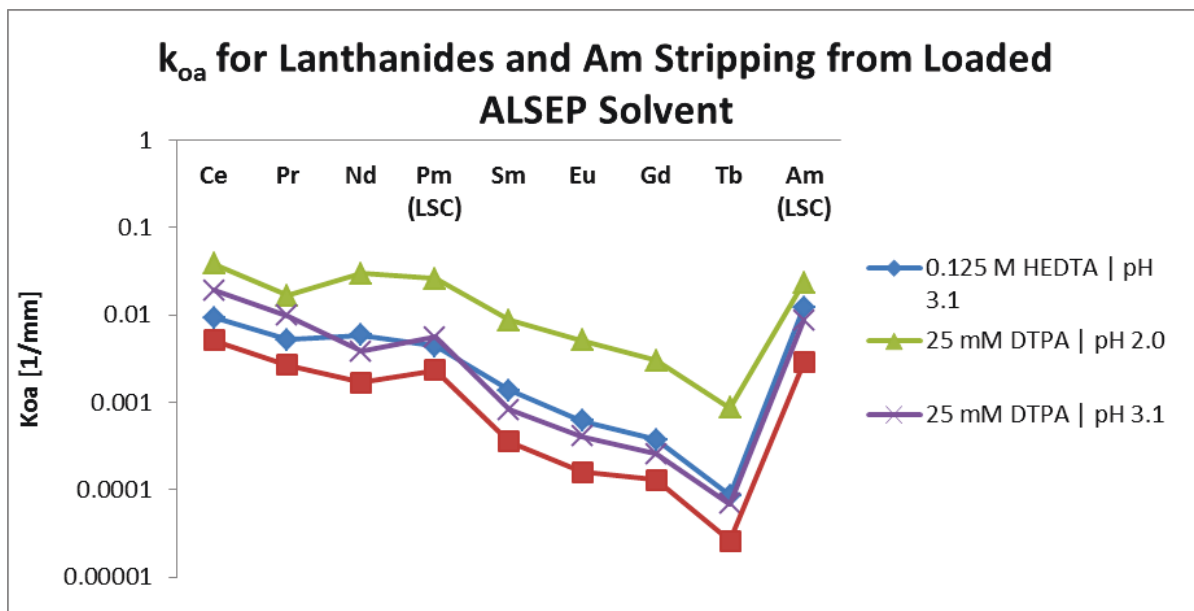


Figure 37. Absolute organic to aqueous interfacial mass transfer constants.

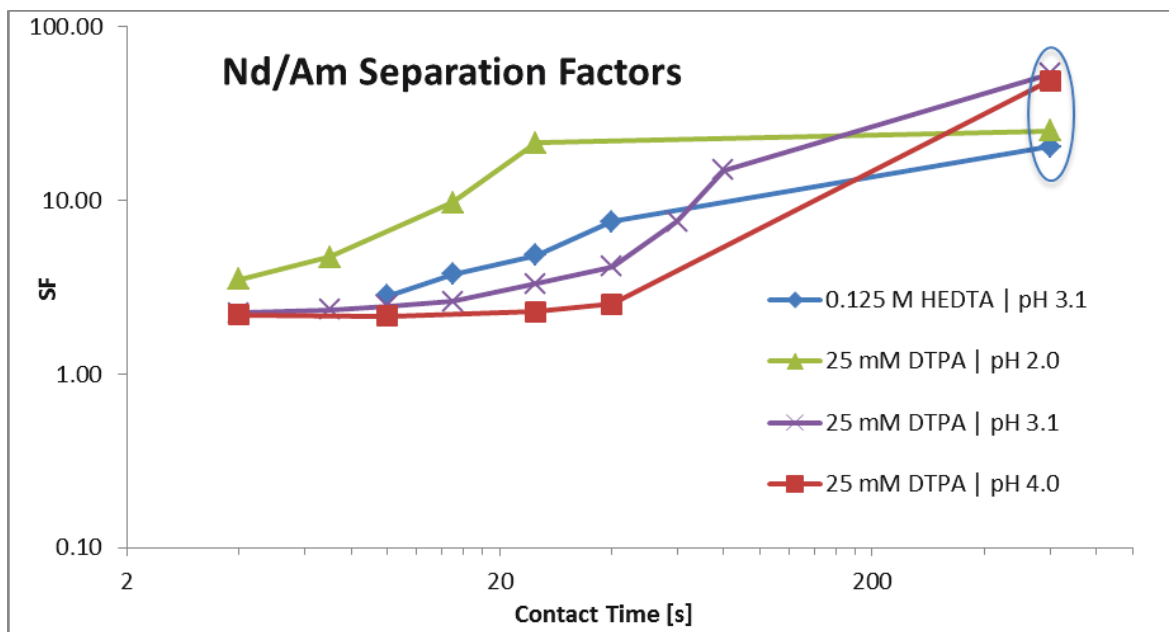


Figure 38. Neodymium/Americium separation factor dependency on aqueous phase, pH and contact time.

5.4 Thermodynamics and Kinetics of Advanced Separations Systems

L. R. Martin, Idaho National Laboratory

The Thermodynamics and Kinetics of Advanced Separations Systems program has continued its integrated multi-national laboratory team approach to understanding the fundamental science behind actinide/lanthanide partitioning in FY 2014. The INL-led team of LBNL, SRNL, and ANL has continued to use its collective expertise to combine theory and experimental measurements to gain insight into understanding these separations systems.

At the heart of every liquid-liquid distribution for metal ion separations is selective complex formation in aqueous and/or organic media. Although thermodynamics drives the complex formation, these parameters give no information about the mechanism by which these reactions take place. To determine such information, reaction kinetics need to be studied. The existing flowsheet case studies offer very different approaches to the separation of the actinide elements. In particular, the co-extraction of actinides (COEX) [1] type systems for used fuel separations require investigations into the behavior of oxidized transuranic materials. By studying the chemistry of neptunium researchers have a window into what might occur with Am(V) and Am(VI) in such systems. In addition, with the ability to study U(VI), Np(VI) and Pu(VI), predictive trends may become apparent across the actinide series.

In FY 2014 INL began investigating electrochemically produced Np(V) binding kinetics with AAIII using stopped-flow spectrophotometry and UV-visible absorption spectroscopy, building on the last reported data from some 15 years ago [2,3]. Further, these investigations were expanded to incorporate Np(VI) to begin exploring the differences in behavior of these two actinyl cations in solution.

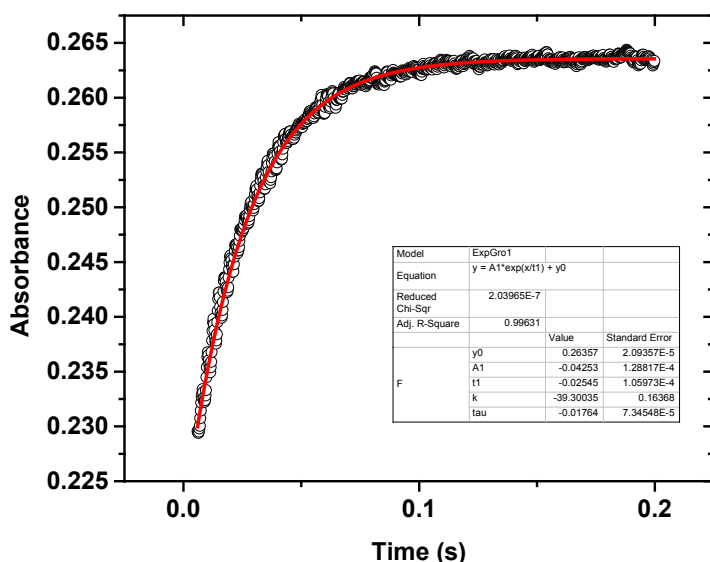


Figure 39. Sample absorption growth kinetics trace from the stopped flow spectrophotometer measuring the rate of reaction of Np(V) with AAIII at 650 nm. [Np] = 5×10^{-5} M, [AAIII] = 1×10^{-5} M I = 0.1 M, pH= 4.0, T = $21 \pm 1^\circ\text{C}$. Open circles represent the measured data the red line represents the fit.

The binding kinetics of a chromotropic acid, Arsenazo III, to Np(V) and Np(VI) was studied under mildly acidic conditions using stopped flow spectrophotometry. For both Np(V) and Np(VI) reactions, the

absorbance vs time plots were fitted with the simple first order rate law under second order conditions. This is indicative of the rate determining step for the reaction being intramolecular in nature. In the Np(V) system increasing the pH was seen to significantly increase the rate of reaction, however increasing the ionic strength and AAIII concentration led to a decrease in the reaction kinetics.

The Np(VI) system studied displayed slower binding kinetics than that of the Np(V) reaction at pH 4. This may be due to a weaker complex formation between the Np(VI) and AAIII however further study would be required to confirm this hypothesis. The relative rates analysis between the Np(VI) measured here and U(VI) system reported in prior literature [2,3] demonstrated that the U(VI) system is ~30 times faster. It is not clear from the experiments performed if the acetate buffer is interfering with the complexation in the Np(VI) system.

The results presented here begin to identify that the metal-complex stability observed in actinyl systems may be related to the rate of formation of the metal-complex. Further there may be significant differences in the binding kinetics for one valence state across the actinide series. Future experiments are planned to assess these trends for the actinide series, with a more extensive study of ionic strength, pH and acetate dependencies. In addition to these studies, rates of reaction will be measured as a function of temperature to determine the activation energy and entropy of these systems.

In addition to the kinetic work, preliminary experiments were performed in support of determining the thermodynamic parameters for the ALSEP process.⁴ The ALSEP process is a mixed extractant system comprised of a cation exchanger 2-ethylhexyl-phosphonic acid mono-2-ethylhexyl ester (HEH[EHP]) and a neutral solvating extractant N,N,N',N'-tetraoctyldiglycolamide (TODGA). The extractant combination produces complex organic phase chemistry that is challenging for traditional measurement techniques. To neutralize the complexity, temperature dependent solvent extraction experiments were conducted with neat TODGA and scaled down concentrations of the ALSEP formulation to determine the enthalpies of extraction for the two conditions. A full set of thermodynamic data for Eu, Am, and Cm extraction by TODGA from 3.0 M HNO₃ is reported. These data are compared to previous extraction results from a 1.0 M HNO₃ aqueous medium, and a short discussion of the mixed HEH[EHP]/TODGA system results is offered.

The thermodynamic parameters for the extraction of Eu, Am, and Cm by TODGA from 3.0 M HNO₃ were determined for the first time and are shown in Figure 40 and Table 7. The comparison to 1.0 M ionic strength data showed the TODGA extraction at 3.0 M behaved similarly. Temperature dependent extractions for a mixed TODGA/HEH[EHP] system showed increased distribution ratios for Eu and Am compared to the neat TODGA system. This may suggest that the HEH[EHP] is enhancing the extraction from the 3.0 M system through some extractant interaction with the TODGA to create a new extractant molecule complex. However, the heats of extraction for this system were lower than the neat TODGA system.

Table 8. A good first step has been taken toward addressing the thermodynamics behind this complex extractant system.

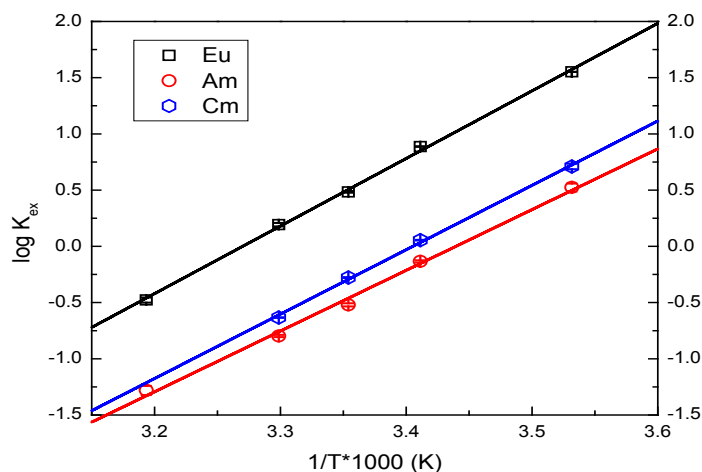


Figure 40. Temperature dependence for the extraction of Eu, Cm, Am by TODGA. Organic phase: 0.0035 M TODGA in dodecane. Aqueous phase: 3.0 M HNO₃.

Table 7. Complete set of thermodynamic parameters for Eu, Cm, Am extraction with TODGA from 3.0 M HNO₃. The thermodynamic data reported in Ref. 4 for Am extraction with TODGA from 1.0 M HNO₃ is shown for comparison.

	log K _{ex}	ΔG (kJ/mol)	ΔH (kJ/mol)	ΔS (kJ/mol)	
Eu	9.60 ± 0.01	-54.8 ± 0.1	-115.1 ± 2.4	-202.2 ± 4.3	p.w.
Cm	8.70 ± 0.01	-49.7 ± 0.1	-110.0 ± 2.9	-201.2 ± 5.4	p.w.
Am	8.47 ± 0.01	-48.4 ± 0.1	-103.4 ± 4.0	-186.6 ± 7.1	p.w.
Am	9.4	-27.9	-47.6	-66.1	Ref. 5

Table 8. Heats of extraction for Eu and Am extraction by 0.0035 M TODGA/0.0053 M HEH[EHP]. The extractant ratios were scaled down to reflect the original ALSEP formulation.

	ΔH (kJ/mole)
Eu	-91.34 ± 1.5
Am	-73.88 ± 4.3

References

1. Drain, F. Emin, J. L.; Vinoche, R.; Baron, P., COEX process: cross-breeding between innovation and industrial experience. *Proceedings from Waste Management 2008*, Tucson, AZ, USA, 2008.
2. Fugate, G. A.; Nash, K. L.; Sullivan, J. C., *Radiochim Acta.*, 1997, 79, 161.
3. Fugate, G. A.; Fell-Jenkins, J. F.; Sullivan, J. C.; Nash, K. L., *Radiochim Acta.*, 1996, 73, 67-72.

4. Gelis, A. V.; Lumetta, G.; Actinide Lanthanide Separation Process-ALSEP. *Industrial & Engineering Chemistry Research*, 2014, 53, 1624.
5. Ansari, S. A.; Pathak, P. N.; Husain, M.; Prasad, A. K.; Parmar, V. S.; Machanda, V. K. *Radiochimica Acta*, 2006, 94, 307-312.

Publications

1. Travis S. Grimes, Peter R. Zalupski and Leigh R. Martin, Features of the Thermodynamics of Trivalent Lanthanide/Actinide Distribution Reactions by Tri-n-Octylphosphine Oxide and Bis(2-EthylHexyl) Phosphoric Acid, Accepted, *Journal of Physical Chemistry B* (2014).
2. Travis S. Grimes, Richard D. Tillotson and Leigh R. Martin, Trivalent Lanthanide/Actinide Separation Using Aqueous-Modified TALSPEAK Chemistry, *Solvent Extraction and Ion Exchange*, 32(4), 2014, 378-390.

5.5 Thermodynamics and Kinetics

L. Rao, Lawrence Berkeley National Laboratory

In FY 2014, thermodynamic studies were completed on the effect of temperature on the protonation and complexation of HEDTA with lanthanides to support the development of the modified TALSPEAK process that utilizes a combination of HEDTA/HEH[EHP] and affords a better pH dependency and a faster extraction kinetics than the conventional TALSPEAK [1,2]. The data help to evaluate the effectiveness of the separation process when the operation envelope (e.g., temperature) varies and, eventually, will help to achieve a better control of the separation process based on the HEDTA/HEH[EHP] combination.

Besides the experimental studies, the manuscript on the complexation of Cm(III) with DTPA has been submitted to Inorganic Chemistry for publication and is under review at present.

The protonation constants of HEDTA at 25°C and 70°C were determined by potentiometry and are listed in Table 9.

Table 9. Thermodynamic parameters for the protonation of HEDTA. $I = 1.0 \text{ M NaClO}_4$ and $\log \beta_{H,M}$ represents the protonation constants in molarity.

Reaction	$t, ^\circ\text{C}$	$\log \beta_{H,M}$	$\Delta H, \text{kJ}\cdot\text{mol}^{-1}$
$\text{H}^+ + \text{L}^{3-} = \text{HL}^{2-}$	25	9.14 ± 0.01	-27.8 ± 0.02
	40	8.94 ± 0.01	
	55	8.69 ± 0.01	
	70	8.56 ± 0.01	
$2\text{H}^+ + \text{L}^{3-} = \text{H}_2\text{L}^-$	25	14.66 ± 0.01	-49.3 ± 0.02
	40	14.34 ± 0.01	
	55	13.97 ± 0.02	
	70	13.81 ± 0.02	
$3\text{H}^+ + \text{L}^{3-} = \text{H}_3\text{L}$	25	17.20 ± 0.01	-46.5 ± 0.03
	40	16.95 ± 0.02	
	55	16.62 ± 0.02	
	70	16.54 ± 0.03	

Data of the calorimetric titrations for the protonation of HEDTA are shown in Figure 41. The observed reaction heat (“partial” or stepwise Q) is a function of a number of parameters, including the concentrations of reactants (C_H , C_L), the protonation constants ($\log\beta_H$) and the enthalpy of protonation of the ligand (ΔH). Using the stoichiometric concentrations of the reactants and the protonation constants measured by potentiometry measured in this work, the enthalpies for the protonation reaction of HEDTA at 25°C are calculated from the calorimetric titration data, and are presented in Table 8.

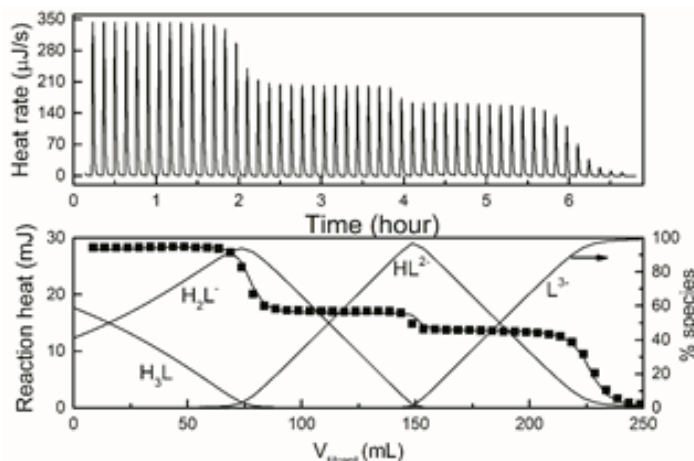


Figure 41. Calorimetric titrations of the protonation of HEDTA, $I = 1 \text{ mol/L NaClO}_4$, $t = 25^\circ\text{C}$. (Top) a representative thermogram. (Bottom) A plot of Q_{partial} vs. the volume of titrant, Symbols of the bottom: ■ - experimental Q , lines – fit. Initial cup solutions: HEDTA, C_H°/C_L° (mmol/L) = 29.88/9.96; titrant: 99.83mmol/L NaOH, 5.0 μL /addition.

With the protonation constants measured at different temperatures, it is possible to evaluate the change of speciation of HEDTA at different acidity ($-\log[H^+]$ from 2 to 12). Figure 42 compares the speciation of the ligand (in the absence of metal ions) at 25°C and 70°C. Small but definite differences for all species between the two temperatures can be observed. For example, at higher temperature, there is less H_2L^- species and more H_3L and L^{3-} species. In brief, the protonation of HEDTA generally becomes weaker at higher temperatures. Such changes in the speciation would certainly affect the speciation of An(III) and Ln(III) in the modified TALSPEAK system. The significance of the effect will be evaluated in conjunction with the stability constants of the An(III)/Ln(III) complexes with HEDTA at different temperatures.

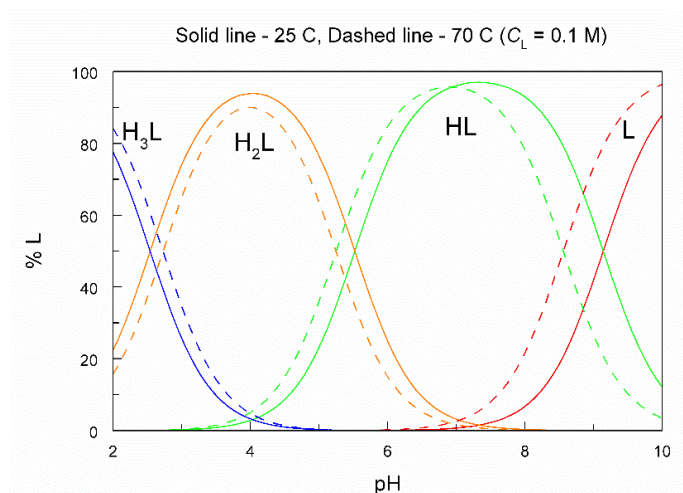


Figure 42. Speciation of HEDTA as a function of acidity ($-\log[H^+]$) at different temperatures. $I = 1 \text{ mol/L NaClO}_4$.

Potentiometric (not shown) and spectrophotometric titrations were performed to determine the stability constants of Nd(III)/HEDTA complexes at different temperatures. The calculated stability constants are shown in Table 10. It was found that it is necessary to include a species, noted as NdH_1L^- , to fit the data in the higher pH region. This species could be a ternary hydrolyzed species, $\text{Nd}(\text{OH})\text{L}^-$, or a species with the hydroxyl group in HEDTA deprotonated. Thermodynamic data alone do not allow the differentiation between these two species.

Table 10. Thermodynamic parameters for the Nd(III)/HEDTA complexes at different temperatures. $I = 1 \text{ M NaClO}_4$. $\log\beta_M$ represents the complex formation constants in molarity.

Reaction	$t, ^\circ\text{C}$	$\log\beta_M$	$\Delta H, \text{kJ}\cdot\text{mol}^{-1}$
$\text{Nd}^{3+} + \text{L}^{3-} = \text{NdL}$	25	13.29 ± 0.02	-28 ± 1
	40	13.10 ± 0.03	
	55	13.58 ± 0.02	
	70	12.96 ± 0.03	
$\text{Nd}^{3+} + \text{L}^{3-} + \text{H}_2\text{O} = \text{NdH}_1\text{L}^- + \text{H}^+$	25	3.11 ± 0.03	14 ± 2
	40	3.25 ± 0.03	
	55	3.42 ± 0.03	
	70	3.82 ± 0.04	

The enthalpy of complexation between Nd(III) and HEDTA was determined by microcalorimetry and shown in Table 10.

The fluorescence spectra and lifetime (Figure 43) of the Eu(III)/HEDTA system were measured to help understand the coordination modes of Ln(III) with HEDTA. From the lifetime, the hydration number of Eu(III) was calculated using the correlation in the literature.

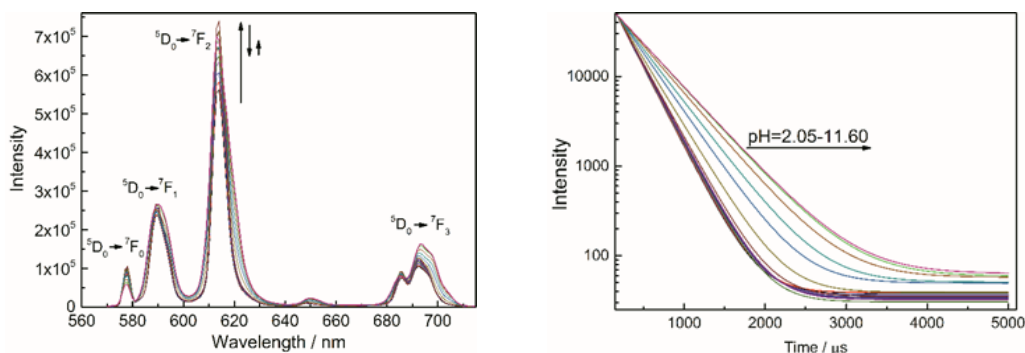


Figure 43. Fluorescence spectra (left) and lifetime (right) of Eu(III)/HEDTA at 25 °C. $I = 1 \text{ M NaClO}_4$. Excitation. 395 nm, $V^0 = 5.04 \text{ mL}$, $C_{\text{Eu}}/C_L/C_H (\text{mM}) = 36.26/37.30/80.0$. Titrant: 0.1 mM NaOH.

References

1. J.C. Braley, T.S. Grimes, K.L. Nash, "Alternatives to HDEHP and DTPA for Simplified TALSPEAK Separations," *Industrial & Engineering Chemistry Research*, 51(2), 2012, 629-638.
2. J.C. Braley, J.C. Carter., S.I. Sinkov, K.L. Nash, G.J. Lumetta, "The role of carboxylic acids in TALSQuEAK separations," *Journal of Coordination Chemistry*, 65(16), 2012, 2862-2876.

5.6 Computational and Spectroscopic Investigations of DTPA Complexes

L. E. Roy and N. J. Bridges, Savannah River National Laboratory

In FY 2014, work continued on how DTPA ligand interacts with both *f*-elements and with lactate through a combined experiment/theoretical approach within the pH window of TALSPEAK using Raman spectroscopy. The goal of this task is to understand ligand arrangement in solution and how it affects complexation within the pH window of TALSPEAK. The second task focused on scoping calculations using time-dependent density functional theory (TDDFT) to investigate the excited states and emission spectra of M-DTPA complexes. The goal here is to evaluate if TDDFT calculations of M-DTPA complexes are possible for systems with a large number of unpaired spins. Finally spin-orbit coupling calculations were performed on actinide molecules to evaluate the approach.

Raman spectroscopy studies. Quantum mechanics/molecular mechanics (QM/MM) calculations and Raman spectroscopy were used to determine how DTPA behaves in solution over a large pH range to pinpoint favorable geometric configurations before metal complexation. Calculations show that hydrogen-bonding interactions between water molecules and DTPA ligand help to position basic groups within the cavity for favorable metal complexation. The QM/MM structures were then verified using Raman spectroscopy. The calculated and experimental spectra are similar considering the number of calculated species involved. The calculated structures also support previous NMR observations on the protonation sequence of DTPA. The most significant finding is that a cavity is formed from the hydrogen-bonding interactions between the water molecule and the protonation sites on DTPA (Figure 44). In addition, hydrogen-bonding interactions occur among the water molecule and a terminal carboxylate group. The bond distances to the water molecule are ~ 1.9 Å and the angle of the protonation sites and water is $\sim 145^\circ$. This is structurally significant because it suggests that hydrogen-bonding interactions at high pH could help to facilitate the formation of a metal complex with correctly positioned basic groups within the cavity. It also supports the notion that the complex remains fairly stable throughout the pH range studied.

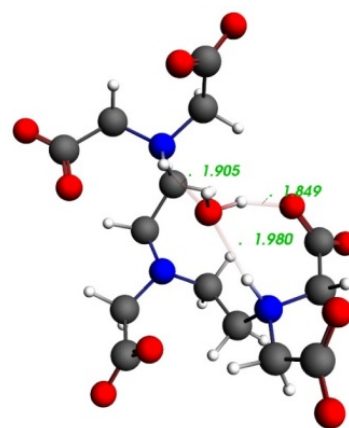


Figure 44. Structural information for the lowest energy QM/MM optimized solution with coordinating water molecules. Only structurally significant water molecules are included in the figure. The bond distances are shown in Angstroms.

Experimental Raman studies were completed on La-DTPA in aqueous media and the results were compared to the calculated spectra of $[\text{La}^{\text{III}}(\text{DTPA})\text{-H}_2\text{O}]^{2-}$ and $[\text{La}^{\text{III}}(\text{HDTPA})\text{-H}_2\text{O}]$ (Figure 45). There are very subtle but important differences between the two spectra. Firstly, the calculated peak at ~ 1750 cm^{-1} is attributed to the protonated carboxylate group. Secondly, the $[\text{La}^{\text{III}}(\text{DTPA})\text{-H}_2\text{O}]^{2-}$ peaks at ~ 900 cm^{-1} and ~ 375 cm^{-1} split into doublets upon protonation. When compared to experiment, there is a very weak intensity peak ~ 1780 cm^{-1} that correlates well with the protonated carboxylate spectrum from the pH range of 3–8. Additionally, all other peaks match well with the calculated values for $[\text{La}^{\text{III}}(\text{HDTPA})\text{-H}_2\text{O}]$. These results suggest that $[\text{La}^{\text{III}}(\text{HDTPA})\text{-H}_2\text{O}]$ is the major species within the pH range of 3 – 8. Also, the spectral changes at pH = 11 suggest that $[\text{La}^{\text{III}}(\text{DTPA})\text{-H}_2\text{O}]^{2-}$ the most prominent structure at high pH.

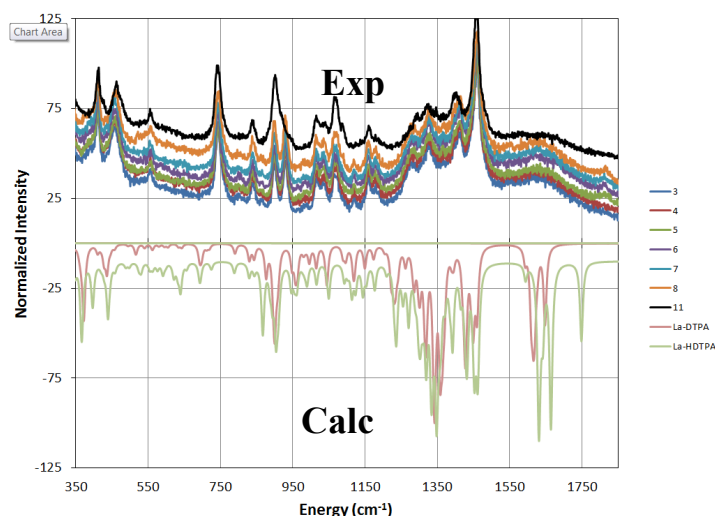


Figure 45. Comparison of experimental Raman spectra of La-DTPA solutions from pH = 3 – 8, 11 and calculated Raman spectra of $[\text{La}^{\text{III}}(\text{DTPA})\text{-H}_2\text{O}]^{2-}$ (pink) and $[\text{La}^{\text{III}}(\text{HDTPA})\text{-H}_2\text{O}]$ (green). The values were offset to show discernable differences between spectra.

Optimization calculations were also performed on DTPA-lactate system in water (Figure 46). The structures with 218 water molecules were converged using Terachem, a GPU-based quantum chemical program. Calculations show that $\text{H}_3\text{DTPA}^{2-}$ and lactic acid have no interaction among each other and therefore may be considered independent of one another in solution. With carry-over funds from this year, focus on this system will be on molecular dynamics simulations in a series of pH ranges from 3 to 8. These results should indicate the stability of the primary components within the TALSPEAK range. Once this study is complete, the results will be compared with Raman spectra for any local structure information.

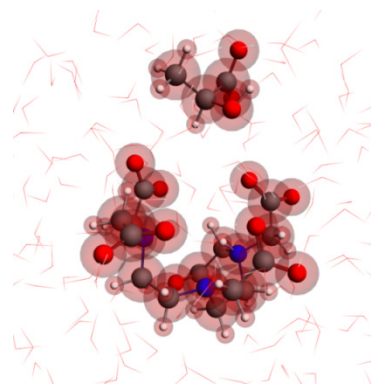


Figure 46. Optimized structure of $\text{H}_3\text{DTPA}^{2-}$ and HLac in water.

TDDFT calculations of Eu-DTPA. TDDFT has had great success in providing a theoretical description of the electronic absorption and emission spectra of large molecules with closed-shell (i.e. no unpaired spins) ground states. However, open-shell molecules (i.e. unpaired spins) have absorption spectra which are more difficult to describe with any method. TD-DFT calculations provide excellent agreement with experiment for simple excitation of radicals and first row transition elements such as Cu^{2+} , but there has been very little focus on other elements in the periodic table. There is one study calculating the transition energies for $[\text{M}(\text{dmpe})_3]^{2+}$ but the results are questionable because no calculated spectrum was provided to compare with experiment (Del Negro, *et al.*, JACS, 2012, 16494). The issue with conventional TD-DFT for unpaired spins is that the spin-flip methodology can only treat four states correctly for a doublet state (for example) leading to an unphysically large amount of spin contamination. The spectroscopy of open-shell molecules is very interesting, in particular, the lanthanides and actinides absorption and emission bands are very useful for fingerprinting and quantization of these species. Initial scoping calculations performed looked at the electronic structure of $[\text{Eu}(\text{DTPA})\text{H}_2\text{O}]^{2-}$ in hopes of evaluating the TD-DFT method for open shell f-f transitions; other M-L transitions may not be accurate based on spin contamination issues. These calculations proved to be more difficult than expected due to non-Aufbau occupation of the molecular orbitals (Figure 47). The “triply degenerate HOMOs” are in actually split by < 0.01 eV and contain

orbital occupations of 0.82, 0.73 and 0.45. Until an Aufbau occupation can be converged, TD-DFT calculations cannot be performed. However, I am very optimistic that the calculations will converge to an Aufbau orbital filling allowing TD-DFT evaluation to begin.

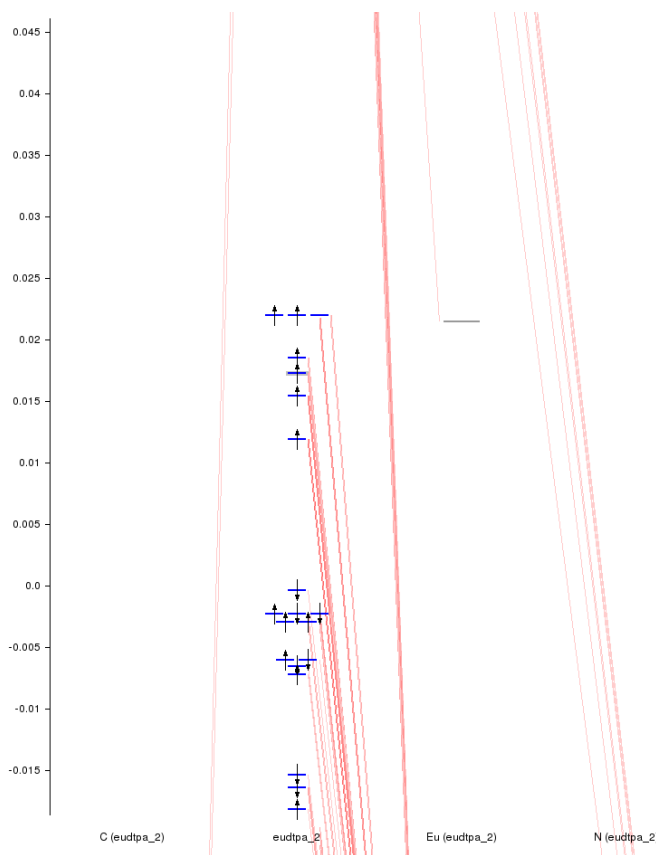


Figure 47. Molecular orbital diagram for [Eu(dtpa)(H₂O)]²⁻.

Scoping calculations on spin-orbit relativistic time dependent density functional theory calculations on actinide molecules. The X-Ray absorption structures near the ionization threshold (NEXAFS region) are closely related to the local electronic structure around the atom in which the excitation takes place and contain the most significant information on the low-lying unoccupied states of the system. The spectral structures are associated to transitions from a core orbital strongly localized on a particular atom to the unoccupied electronic states which lie near the ionization limit of this specific core state. Theoretical calculations relate each excitation energy to a virtual state whose nature (valence or Rydberg) can be defined, and yield oscillator strengths which are connected with the composition of the unoccupied orbitals, mapping in particular the dipole-allowed atomic site component of the virtual states. The fine structure around the K absorption edge has been extensively studied recently for structural determination. L-edge structures for the actinides could provide more information since the dipole transitions could directly probe the metal f content of the different unoccupied levels, and therefore detail of the f involvement into the bonding. From a theoretical point of view, a proper description of the L edge requires the inclusion of the configuration mixing and spin-orbit (SO) coupling in the calculations. TDDFT for the treatment of the core electron excitations has been able to reproduce general features of core absorption spectra (at the K edge) for simple actinide complexes. However, there is a major limit in the inability to treat SO effects in the 2p spectra of heavy elements (starting from the second row elements, such as P, S and Cl), which means that it is not possible to distinguish between the L₂ and L₃

edges. Also, SO splitting of core orbitals leads to the existence of spin-orbit partner states, which give rise to distinct structures converging to different ionization thresholds.

The purpose of these scoping calculations was to test a general method which includes both configuration mixing as well as SO coupling for description of X-ray absorption spectroscopy (XAS) spectra of actinide compounds. Initial calculations assessed the performance of DFT to calculate the electronic structure of Cm-DTPA including SO coupling with the hopes of extending the analysis to core orbital electronic transitions. Calculations of Cm-DTPA are difficult to converge when including SO effects because the electronic configuration may give non-Aufbau results. After several attempts, SO calculations did converge only to have a considerable amount of mixing from the unoccupied orbitals with the unpaired electrons of the system. Therefore an accurate assessment could not be made using M-DTPA and a simpler system was tried, namely UOCl_5^- since the calculations can be verified by K-edge XAS experiments. (Minasian *et al*, JACS, 2012, 5586). The molecule has C_{4v} symmetry and SO coupling splittings into spinors can be found in Figure 48. The calculated TDDFT spectra for the scalar and SO solutions for UOCl_5^- can be found in Figure 49. The K-edge X-Ray absorption spectrum for UOCl_5^- is characterized by three low-energy pre-edge features (< 2823 eV) involving 5f orbitals and two high energy features (> 2823 eV) involving low-lying 6d orbitals. Both spectra are in excellent agreement with experiment and provide a better representation of the experimental spectrum compared with previous TDDFT calculations. While the transition patterns from experiment remain, calculations predict a larger intensity for the Cl 1s $\rightarrow a1$ transition than orbitals of e symmetry. Also, the transitions to $b2$ and e symmetries at higher energy are shifted by ~ 2 eV. Comparing the two calculations, SO coupling and configuration mixing refines the structure such that the transition from Cl 1s \rightarrow “ $b2$ ” is more pronounced and the high energy transitions are broader and better correlate with experiment. The description of the transitions are from spinor to spinor (i.e. $e_{1/2} \rightarrow e_{1/2}, e_{3/2}$) and span contributions from the singlet and triplet/allowed and forbidden transitions within that spinor.

K-edge features provide a direct probe of M-L bond covalency by probing the transitions from the ligand into the unoccupied valence MOs. This may be combined with M $L_{2,3}$ -edge which supply a further probe of the M contribution of the unoccupied orbitals in the ligand field manifold. Based on these results vs. previous work in the area, this method could transition into studying $L_{2,3}$ -edge XAS spectra for actinide compounds and provide interpretation of the results with a fairly high degree of accuracy. The systems to be studied first would need to be small and contain 0 or 1 unpaired spins. This methodology including SO effects has not been tested for the unpaired spin case given the limitations of the software version available to us. An upgrade to software is expected to be completed this FY and the methodology can be tested for the unpaired spin case.

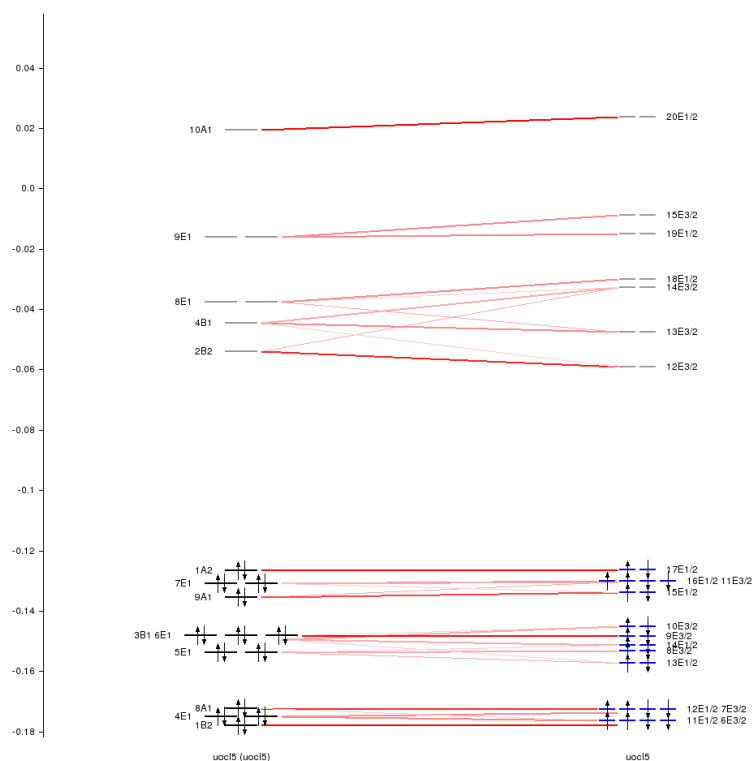


Figure 48. MO diagram and associated spin-orbit splittings of UOCl_5^- . The vertical axis is in Hartrees

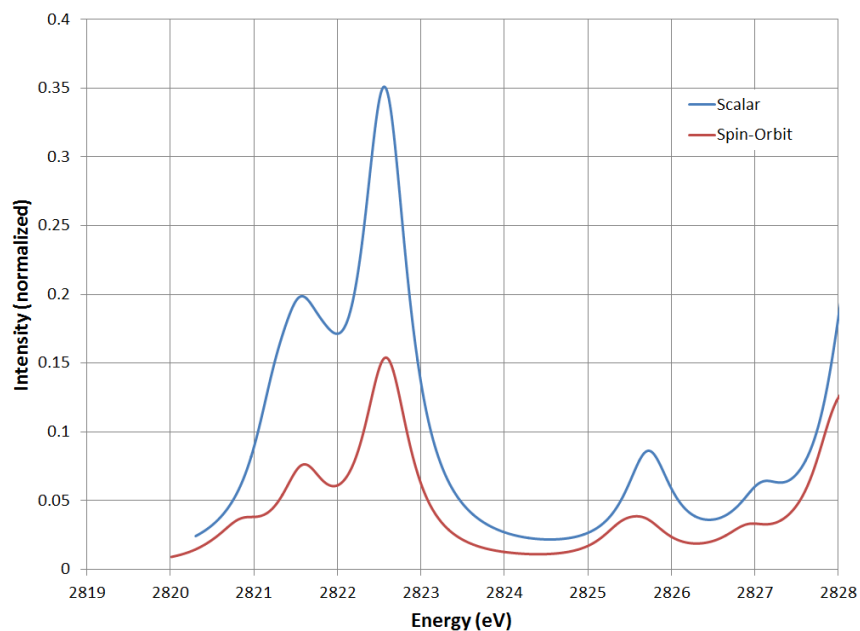


Figure 49. Calculated scalar and spin-orbit TDDFT spectra for UOCl_5^- . Values are scaled for comparison with experiment.

5.7 Non-Ideality in Solvent Extraction Systems

P. Zalupski, Idaho National Laboratory

The overarching objective of the collaborative efforts of “Non-Ideality in Solvent Extraction” FCRD project is to advance the ability of theoretical representation of solute partitioning in two-phase systems. Our efforts entail surveys of the existing theory, which, together with the established new means of experimental inquiry into basic physical chemistry of liquid mixtures, allow us to progressively represent chemistry using equations. Such mathematical description is fundamental to our goal of computational prediction of aqueous separations using models that accurately describe non-ideal behavior in the liquid phases. Non-ideal behavior in solutions always complicates accurate representation of mixtures when modeling a chemical system. A theoretical representation, i.e. model, is particularly challenging when modeling chemical systems as complex as those encountered in aqueous partitioning processes for actinide recycling from dissolved used nuclear fuel. This research effort illustrates how non-idealities obstruct accurate modeling of separations based on liquid-liquid distribution of the metal between two immiscible phases, i.e. solvent extraction. The overarching objective of the project seeks to build experimental capabilities to enable studying fundamental physical properties of solutions. Such inquiry builds thermodynamic knowledge of complex mixtures, allowing better numerical representation, and, as a result, greater accuracy of computational prediction.

Potentiometric studies for the HEDTA protonation and Eu^{3+} complexation in sodium nitrate background electrolyte pave way to Pitzer parameterization. Acid dissociation constants and europium complexation constants by HEDTA have been collected at 5 different ionic strengths controlled by sodium nitrate. The collected thermodynamic data compares well with that reported in the literature for different aqueous electrolyte media. Ionic strength dependencies for all investigated equilibria are well-defined. The thermodynamic data collected here affords an important contribution to the new task of building a thermodynamic model for the $\text{H}^+ - \text{Na}^+ - \text{Eu}^{3+} - \text{NO}_3^- - \text{citrate} - \text{HEDTA} - \text{H}_2\text{O}$ electrolyte mixture. The collected ionic strength dependencies for the metal ion complexation equilibria may now be modelled using the Pitzer ion interaction theory to build an initial theoretical description of an aqueous environment present in Advanced TALSPEAK.

Liquid-liquid distribution studies yield the ionic strength dependency pattern for the formation of europium nitrate complexes. To properly elucidate the Eu^{3+} complexation equilibrium by HEDTA the knowledge of the stability constants for the competing nitrate coordination is necessary. Liquid-liquid partitioning studies for Eu^{3+} were performed, when a non-coordinating perchlorate anion is replaced by nitrate anion in the aqueous phase. This allows studying the aqueous complexing reactions as they begin to influence the liquid-liquid partitioning of the metal ion. The application of the SIT theory to the collected stability constant trend across 6 ionic strengths clearly shows a departure from linear relationship attributed to the growing complexity of the aqueous electrolyte mixture.

The initial thermodynamic model for the aqueous phase of Advanced TALSPEAK has been constructed. The construction of the initial model for the $\text{H}^+ - \text{Na}^+ - \text{Eu}^{3+} - \text{NO}_3^- - \text{citrate} - \text{HEDTA} - \text{H}_2\text{O}$ system used the thermodynamic data available in the literature. The model factors in the non-ideal ion-ion interactions using the Pitzer ion interaction theory. The model is contained by a computer program PitzINL II. The identification of the dominating ion-ion interactions in solution has been performed using sensitivity analysis.

Non-ideal behavior of HEH[EHP] dimer is less pronounced compared to HDEHP dimer. The shift of focus onto the Advanced TALSPEAK formulation required to evaluate a less potent phase transfer reagent, HEH[EHP], to determine whether the aggregative tendencies of this reagent in aliphatic diluents

are comparable to HDEHP, or more pronounced due to a reduced acidity / enhanced basicity of the – POOH polar core. Despite the very similar solubility parameters calculated for dimeric aggregates of this reagent and HDEHP, the calculated activity coefficients reveal that the deviation from ideal behavior is less pronounced for the HEH[EHP] dimer, relative to HDEHP dimer. This observation agrees well with the physico-chemical characteristics of these investigated reagents.

5.8 Extractant Design by Covalency

*A. J. Gaunt, E. R. Batista, S. A. Kozimor, A. Olson, J. Macor, Los Alamos National Laboratory;
J. R. Klaehn and D. R. Peterman, Idaho National Laboratory*

This project aims to provide an electronic structure-to-function understanding of extractants for actinide selective separation processes. The research entails a multi-disciplinary approach that integrates chemical syntheses, structural determination, K-edge XAS, and DFT calculations. Research has evolved from determining known extractant electronic structure to a phase where the information learned can be used in a predictive capacity to design new extractants that are anticipated to be actinide selective.

Two milestones were successfully completed: (1) Develop a phosphorus K-edge XAS capability for dithiophosphinate systems; (2) Develop the new solution capability to be used on f-metal extractant complexes. In addition, substantial progress was made in the synthesis of proposed new dithiophosphinate extractant molecules.

Research in previous years had focused on probing the sulfur K-edge in dithiophosphinate extractant molecules, and uncovered clear electronic structure differences that correlate to differences in observed Am/Ln separation factors. It appeared that enhanced orbital mixing in the highly actinide-selective $[\text{S}_2\text{P}(\text{o-CF}_3\text{C}_6\text{H}_4)_2]^-$ extractant facilitates increased negative charge delocalization, and therefore provides a rational basis from which to propose new extractant designs/modifications. However, to gain acceptance of this strategy, it is necessary to demonstrate that these findings in the solid-state hold true under conditions that closely mimic separation tests. Phosphorus K-edge XAS is anticipated to allow acquisition of solution measurements in the same sulfone diluent that has been used for many Am/Ln Separation Factor determinations of CF_3 -derivatized dithiophosphinates. The P K-edge should provide equivalent electronic structure information as sulfur, and solves the problem that S atoms in sulfone would swamp the signal. Since this is a new atom type, then initial data was collected in the solid state, as was a necessary first step when previously developing the sulfur K-edge XAS technique.

Figure 50 shows the phosphorus K-edge spectra that were acquired on a range of differently substituted dithiophosphinate molecules that each exhibit different levels of actinide selectivity. The first feature of note is that the sulfur K-edge finding that the $[\text{S}_2\text{P}(\text{o-CF}_3\text{C}_6\text{H}_4)_2]^-$ extractant has a unique electronic structure is replicated. This means that probing the P K-edge in the sulfone diluent is a viable method to obtain the electronic structure information to determine if the increased orbital mixing holds true in the exact diluent that the separation factors were measured. The second feature to note is that the spectrum of a new extractant design, $[\text{S}_2\text{P}(\text{C}_{12}\text{H}_8)_2]^-$, which directly tethers together the phenyl rings (and was proposed on the basis of previous S K-edge data) is even more distinct than the $[\text{S}_2\text{P}(\text{o-CF}_3\text{C}_6\text{H}_4)_2]^-$ extractant, suggesting that K-edge XAS can indeed be a useful tool in the ligand design process.

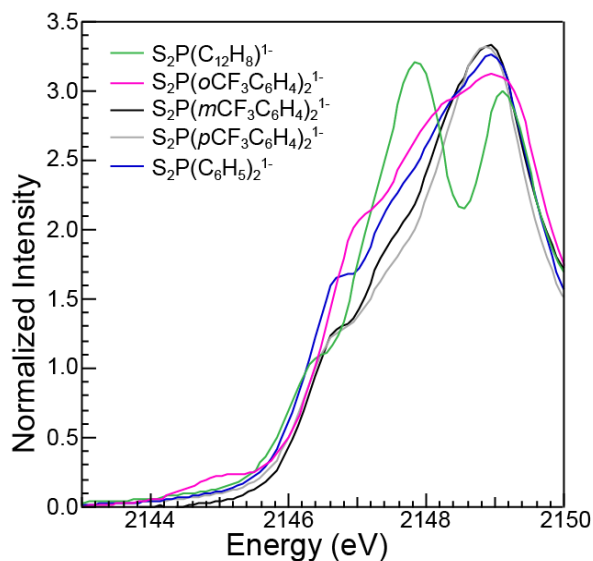


Figure 50. The P K-edge XAS data from $[\text{AsPh}_4]\text{S}_2\text{P}(\text{C}_{12}\text{H}_8)^{1-}$ (green trace), $[\text{AsPh}_4]\text{S}_2\text{P}(\text{o}-\text{CF}_3\text{C}_6\text{H}_4)_2^{1-}$ (pink trace), $[\text{AsPh}_4]\text{S}_2\text{P}(\text{m}-\text{CF}_3\text{C}_6\text{H}_4)_2^{1-}$ (black trace), $[\text{AsPh}_4]\text{S}_2\text{P}(\text{p}-\text{CF}_3\text{C}_6\text{H}_4)_2^{1-}$ (gray trace), and $[\text{AsPh}_4]\text{S}_2\text{P}(\text{C}_6\text{H}_5)_2^{1-}$ (blue trace).

The previously developed sulfur K-edge XAS solution phase capability was verified as reproducible in FY 2014 and extended to include measurements on f-metal dithiophosphinate complexes (Figure 51). Integrity of the dynamic liquid containment was also demonstrated, leading to approval from the synchrotron facility for future measurements of solutions containing radioactive actinide samples.

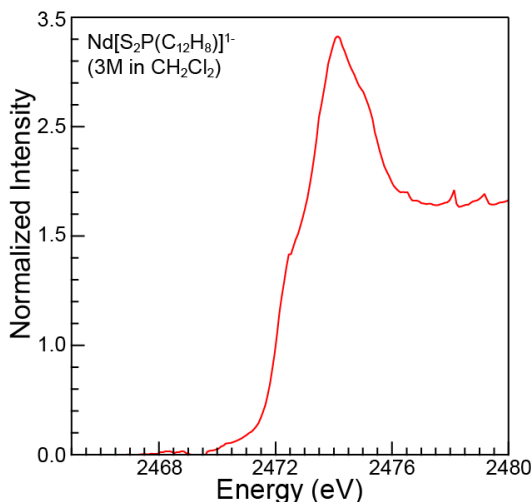


Figure 51. Solution phase S K-edge XAS spectrum from $[\text{AsPh}_4][\text{Nd}(\text{S}_2\text{PPh}_2)_4]^-$ (3 M) in CH_2Cl_2 .

An improved synthetic route to the new extractant design, $[\text{S}_2\text{P}(\text{C}_{12}\text{H}_8)_2]^-$ (**1**), was also developed in FY 2014. The tethering of the phenyl rings in fixed planar geometry is predicted to maximize orbital mixing and negative charge delocalization, which should render the molecule highly actinide selective on the basis of sulfur K-edge XAS analysis and DFT predictions. The ligand can now be isolated in gram quantities (Figure 52) and was shipped to INL for separation factor determination. Low solubility of **1** in the organic phase hampered the measurements, so the synthetic scheme was adapted to install tert-butyl groups on the phenyl rings of **1** to enhance solubility. Am/Ln separation factor measurements at INL on the tert-butyl version are pending to determine the level of actinide selectivity of **1**.

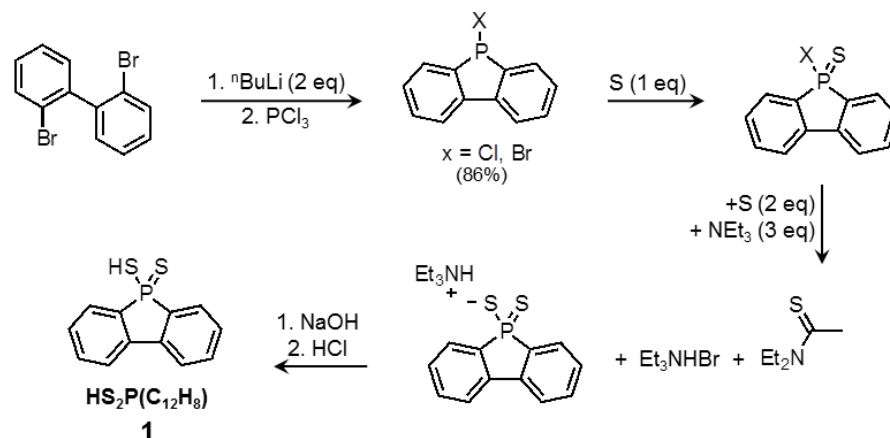


Figure 52. Optimized synthetic steps for the preparation of new extractant design 1 in gram quantities.

In summary, K-edge XAS probing of both the S and P atoms can successfully reveal electronic structure to separation-function relationships in dithiophosphinate extractants in both solid and solution-phases. The data can be utilized to propose new extractant designs that are currently being tested, and the process will be refined as we acquire XAS data under conditions that more closely mimic separations.

ADVANCED WASTE FORM CHARACTERIZATION

SECTION 6

6. ADVANCED WASTE FORM CHARACTERIZATION

Advanced Waste Form Characterization is used to develop sufficient understanding of waste form degradation behavior to predict radionuclide release over geologic timescales. This fundamental understanding is required to optimize waste form chemistry and support disposal system performance assessment.

6.1 Metal Waste Forms

W. L. Ebert, Argonne National Laboratory

An analytical model has been developed to calculate the release rates of radionuclides during the corrosion of metallic waste forms that can be used as source terms in performance assessment (PA) models conducted to support the design and qualification of potential high-level waste disposal systems. The source term model was derived from mechanistic models for key processes based on electrode kinetics and mixed potential theories, and is being parameterized using a protocol of standard electrochemical and corrosion test methods developed for that purpose. Metallic waste forms are composites formulated to incorporate and immobilize radionuclides and other constituents in waste streams within several chemically durable intermetallic and solid solution alloys. Radionuclides are released upon oxidation reactions occurring at the alloy surfaces and dissolve according to solubility limits. The model includes terms representing (1) the oxidation rate, which depends on the solution Eh and temperature, (2) the attenuating effect of passivation, which depends on the chloride concentration, and (3) the propensity of the radionuclide to dissolve, which depends on its oxidation state and the solution composition. Electrode kinetic theory provides the scientific basis for modeling the electrochemical effects of environmental variables (primarily the temperature, Eh, pH, and Cl^-) on the corrosion of each alloy that are combined with the chemical effects controlling the release of each oxidized radionuclide species to calculate the fractional release rate of each radionuclide.

The degradation model is being developed as the product of terms representing the fractional release rates of specific radionuclides on three terms: the bare surface oxidation rate, which depends on several environmental variables; attenuation of the bare surface oxidation rate by passivation, which develops as corrosion progresses and is poisoned by dissolved chloride (and other halides); and moderated by the solubility of the oxidized radionuclide. It is anticipated that the degradation model will have the generic form

$$FR(RN) = B(Eh, T, pH, Cl^-) \times P(E, Cl^-) \times D(T), \quad (4)$$

where the fractional release of a radionuclide RN depends on the oxidation of the waste form through the B and P terms and the oxidation state of each RN through the D term. The B term quantifies effects of the surface potential Eh that is established by redox-reactions with the solution, temperature T , pH, and chemical effects of dissolved chloride Cl^- on the bare surface corrosion properties. The P term is an attenuation function that quantifies effects of the formation of corrosion layers and possible passivation that occurs over time and changes the corrosion potential E . The oxidation rate of the waste form that is predicted based on electrochemical theory (through the B and P terms) is combined with the radionuclide release behavior measured in the test solution to include the propensity of the radionuclide to dissolve based on its oxidation state at the potential used in the experiment. The effects of the environmental variables and passivation on the oxidation kinetics are taken into account analytically using a model having an underlying scientific basis that provides confidence in the long-term predictions. The release behaviors of individual radionuclides from several constituent phases are measured directly to empirically

account for the effects of the oxidation state and corrosion layers through the D term. This semi-empirical equation can be used to calculate radionuclide release rates into solution over long times.

An electrochemical test procedure was developed to determine the dependencies of the B , P , and D terms on key environmental factors and measure model parameter values for a range of alloy and solution compositions. The procedure tracks the corrosion current under potentiostatic conditions for about a month and is interrupted periodically to measure electrochemical characteristics of the evolving surface (e.g., daily) and the release of radionuclides into solution (e.g., weekly). This is sufficient time for a stable surface layer to form and corrosion to proceed at a steady state rate. Long-term immersion tests are being conducted to corroborate the radionuclide release behavior. Tests are conducted under open circuit conditions and at several imposed potentials to determine the dependence of active and passive corrosion on the potential. Electrochemical measurements made periodically include a potentiodynamic sweep over a limited potential range to measure the open circuit corrosion potential, polarization resistance, and Tafel constants, and electrochemical impedance spectroscopy to characterize the electrical properties of the developing surface corrosion layer. At the end of the test, the corroded alloy surface is examined with an SEM to characterize corrosion products and identify which phases were active during the test. Tests are being conducted in acidic, neutral, and alkaline solution with and without added NaCl, in a range of NaCl brines, in solutions exposed to air or purged with argon or reagent gas (2% H_2 in He), and in solutions with added H_2O_2 to represent radiolysis products. Tests are being conducted at ANL and SRNL with several alloys made with Type 316 and HT-9 steels and various amounts of surrogate fuel wastes and trim Zr and Cr to determine the sensitivities of model parameters to the waste form composition.

Recent results for an alloy representing the Experimental Breeder Reactor (EBR)-II metal waste form reacted in acidic brine are shown as an example in Figure 53. Variations in the corrosion current in Figure 53a reflect changes in the corrosion resistance of the surface, which are quantified by a Nyquist plot of the electrochemical impedance spectroscopy (EIS) data in Figure 53b and the amounts of U and alloying constituents released at different reaction time intervals in Figure 53c. Negligible amounts of U are released beyond about 400 hours because the U-bearing phases have been dissolved from the surface, as shown by the SEM image in Figure 53d. The black areas (labeled 1) are voids where the U-bearing Fe_2Zr intermetallic has been lost (the oxide layer covering the specimen had been wiped away to reveal the underlying alloy). The darker gray areas (2) are the steel-like iron solid solution phase and the light gray areas (3) are Fe_2Zr intermetallic with low U contents. Small areas of U-rich Fe_2Zr intermetallic (4) remain unreacted. Note the pitting in the iron solid solution phase, which may be the active phase beyond 400 hours.

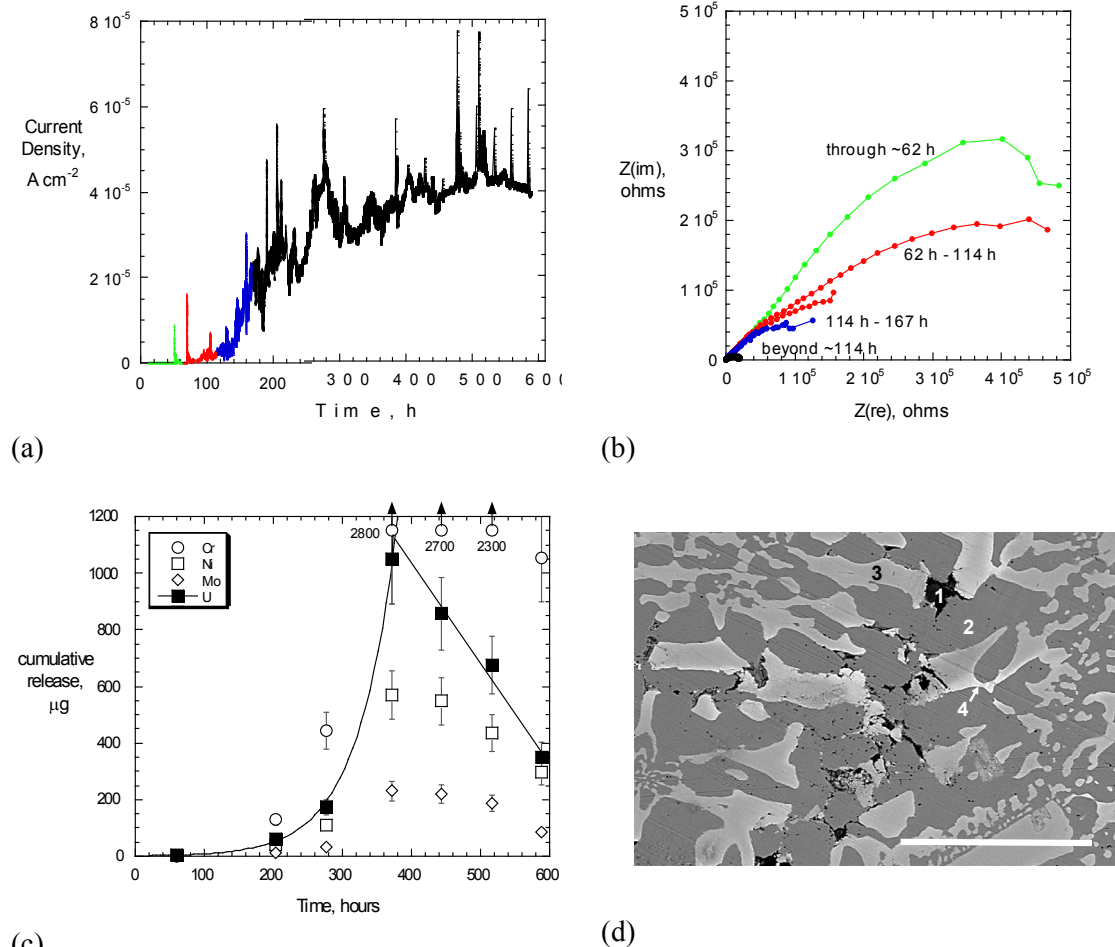


Figure 53. Results of electrochemical tests with RAW-5 showing: (a) corrosion current, (b) Nyquist plot of EIS results showing decrease in corrosion resistance, (c) cumulative releases of U and alloy constituents, and (d) SEM image showing depletion of U-bearing phases at alloy electrode surface (black voids). (scale bar = 100 μm)

Providing confidence that the model represents long-term corrosion is a major challenge. Short-term electrochemical tests were conducted with RAW-1 at an imposed potential of 700 mV to aggressively corrode the alloy phases under transpassive conditions and generate a thick corrosion layer for examination. Corrosion under these conditions provides insights into some aspects of long-term behavior. The corroded electrode was fixed in acrylic and ground to provide side-views of the specimen. Figure 54a is an optical micrograph showing the corroded surface on the left-hand side and the silver epoxy used to make the electrical connection on the right hand side. The corroded region is about 3 mm thick, with an outer layer labeled “A” and an inner layer that is labeled “B.” The uncorroded alloy is labeled C. The box drawn in Figure 54a is the region shown in the SEM photomicrograph in Figure 54b, with regions A, B, and C labeled. The cross-hairs numbered 1 through 9 locate spots that were analyzed for composition, which is discussed below. Figure 54c and Figure 54d are SEM images taken in region A and at the interface of regions B/C, respectively. The island-like features are domains of the Fe_2Mo intermetallic that remain after the surrounding phases (primarily the Fe_2Zr intermetallic) were corroded and converted to iron oxides. Note that an appreciable amount of the oxides appears to have been lost from region B during sample preparation, but many of the Fe_2Mo domains remain intact. This suggests a

contiguous framework of the Fe_2Mo intermetallic remains throughout the corroded A and B regions that is attached to the alloy in region C (both physically and electrically). Figure 54d shows the corrosion front penetrating into the alloy to be fairly flat with uniform loss of the Fe_2Zr intermetallic. That is, there is not significant penetration of the corrosion front at the phase boundaries between intermetallics and not significant pitting of the Fe_2Zr domains. (The Fe_2Zr domains are lighter contrast than the Fe_2Mo domains.)

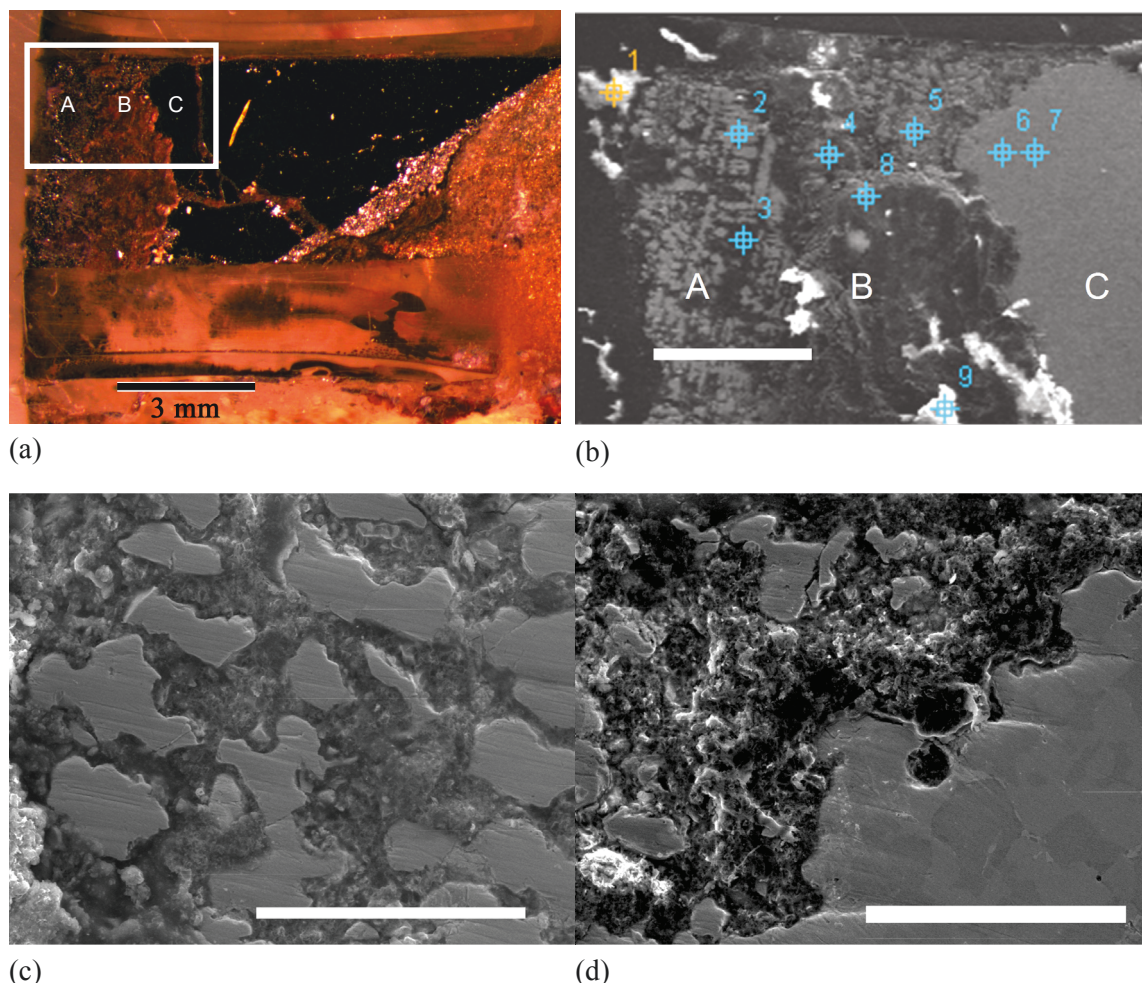


Figure 54. Images of cross sectioned RAW-1 electrode after corrosion at 700 mV: (a) Optical micrograph showing corroded layer penetrating about 3 mm and SEM images (b) showing outer layer (A), inner layer (B), and uncorroded alloy (C) (scale bar = 500 μm), (c) region of outer layer A (scale bar = 500 μm), and (d) interface of regions B/C (scale bar = 100 μm).

The compositions of several areas in the corrosion layer (e.g., at the identified spots in Figure 54b) were measured with X-ray emission spectroscopy during the SEM analysis. The compositions are consistent with the constituent phases of RAW-1 measured previously (Fortner 2012). From analysis of the bulk alloy, Fe_2Mo , Fe_2Zr , and Pd_2Zr intermetallics occupy about 52%, 32%, and 3% of the volume, and the steel-like iron solid solution occupies the remaining 13%. Spots 6 and 7 in Figure 54b are on Fe_2Zr phases in the unreacted alloy; no other Zr-rich phase was detected in Region B. Spots 1, 3, 8, and 9 have high Ru contents and may be residual material leached from the Zr-bearing intermetallics. Spots 2, 4, and 5 are on islands of Fe_2Mo intermetallic in Region B that did not dissolve under these test conditions.

The RAW-1 electrode was reacted for 9 days at 700 mV with solution sampled after 3 and 9 days. About 9.3 μg Tc was released to solution during the test. The corroded volume is estimated to be 0.0088 cm^3 , which corresponds to 0.081 g RAW-1. The alloy contains about 2.5 mass% Tc, so about 2.0 mg Tc was available in the corroded volume but only about 0.46 % of that was released to solution. This is consistent with the majority of Tc in the waste form being immobilized in the durable Fe_2Mo phases. The relationship between the extent of alloy corrosion (as measured by the corrosion current) and the release of Tc into solution is taken into account in the source term model through the D term for Tc. The stability of the Fe_2Mo phases relative to other phases (notably the Fe_2Zr phases) attenuates the release of Tc.

6.2 Oxide Waste Forms: Glass Waste Form Characterization

J. Ryan, S. Kerisit, P. Rieke, and J. Neeway, Pacific Northwest National Laboratory; W. L. Ebert, Argonne National Laboratory; C. Crawford and C. Jantzen, Savannah River National Laboratory

Borosilicate glass is being used to immobilize HLW in the United States and internationally. The release of radionuclides from borosilicate glass waste forms into the environment requires the initial degradation of the glass structure during corrosion in groundwater. Subsequent transport is determined by environmental factors including advection, sorption, precipitation, colloid formation, size filtration, etc., and is being addressed in the Used Fuel Disposition campaign. The source term for radionuclide release being addressed in the Material Recovery and Waste Form Development campaign is the product of the radionuclide inventory, the glass dissolution rate, and the glass surface area. The objective of activities in this control account is to develop the scientific data base and mechanistic understanding of glass degradation necessary to reach an international consensus on how to model the corrosion behaviors of glass waste forms over geologic time scales and calculate radionuclide source terms for a variety of relevant disposal environments.

Waste glass corrosion is conveniently illustrated by the simplified reaction progress diagram shown in Figure 55, where an overall progress variable is used to represent several parallel, sequential, and coupled reactions between glass and groundwater that result in the glass being replaced by an assemblage of thermodynamically stable secondary phases in a solution that is saturated with respect to those phases. Corrosion can be described as occurring in three stages in which different reactions or sets of reactions dominate the reaction progress and the kinetics. Stage I behavior is that experienced by glass dissolving into a dilute solution through hydrolysis and ion exchange reactions with no transport or reaction affinity limitations. This transitions to Stage II behavior, which represents the very low “residual” rate observed at long times in static conditions. The mechanisms behind this behavior are a source of the scientific non-consensus, and may include slowing effects of a decreasing reaction affinity due to increasing solution concentrations and mass transport limitations imposed by developing surface alteration layers. Stage III behavior, a marked increase in the rate of glass alteration after a period of time at the relatively low “residual” rates, is not observed in all glass compositions or all environmental conditions. Although the cause of this increased rate is uncertain, it is usually associated with the formation and rapid precipitation of silica-containing minerals typically of zeolitic mineralogy. Stage III behavior can also be transitory, meaning that the rate can accelerate and slow successively.

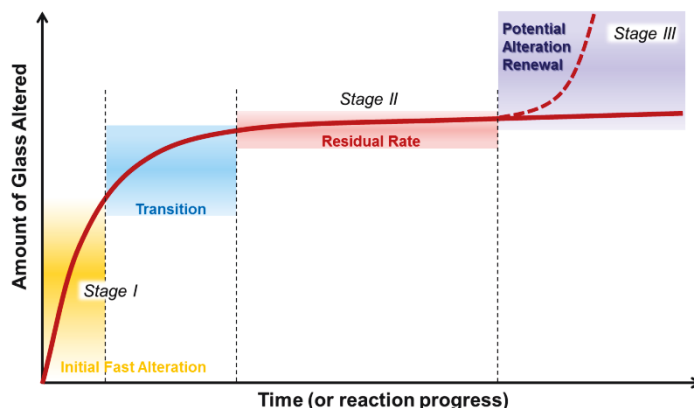


Figure 55. Schematic reaction progress plot for glass corrosion.

The primary challenges to the HLW glass degradation model are to calculate the dissolution rate in Stage II, predict if and when the system can evolve from Stage II to Stage III, and then calculate the dissolution rate in Stage III. Although Stage I is not expected to last long in the real system, Stage I experiments are necessary to parameterize some portions of the glass degradation models. The activities in this control account address the processes, kinetics, and couplings that contribute to and control corrosion within the different stages and transitions between stages. The corrosion stages addressed by work in each activity are identified in the summaries.

A detailed integrated plan for understanding these and other aspects of long-term glass behavior and developing international consensus on the glass dissolution rate law was developed in fiscal year 2011 and subjected to peer review [Ryan et al. 2012]. That plan includes experiments designed to address particular aspects of glass corrosion with modeling efforts performed at the atomic and continuum scales to help interpret the experiments, apply the results to the degradation model, and interface the degradation model with disposal system performance assessment calculations. The initial results of those collaborations have been documented in recent review papers (Gin et al. 2013, Vienna et al. 2013). A more complete review is given in the recent update on the model development (Ryan et al. 2014), which details the logical process necessary to provide a rate simple enough to insert into a broad performance assessment calculation, yet based on sound scientific bases. The detail of the document presents five mechanistic processes that have the potential to significantly impact radionuclide release at certain points in the glass corrosion timeline: dissolution, secondary phase precipitation, solid-state transport, gel transport, and the evolution of the glass-solution interphase. An overview of the mechanisms of these processes is given, including how they may be modeled and their measured impact (direct or coupled) on radionuclide release. Following the mechanistic models, the report explains how these detailed models will lead to rates that can be used within a performance assessment.

The primary tasks that remain are determining analytical forms to quantify the effects of mass transport and solution feedback over the relevant range of disposal conditions and as the contributions of different processes change as corrosion progresses. Uncertainties in quantifying mass transport stem from the effect of the solution composition on the effectiveness of the transport barrier and identification of the physical layer providing the transport resistance, and from changes in both as corrosion proceeds. Uncertainties in quantifying the solution effects include the analytical forms of the reaction affinity term that occur in concentrated solutions (negative feedback) and the presence of secondary phases (positive feedback). Experimental and modeling activities are in progress to address these factors in the glass dissolution rate law.

As mentioned in the Collaboration section, the glass corrosion efforts benefit from co-funding from DOE-EM and significant characterization support from DOE-SC. Additionally, many of the activities in this control account benefit by collaborations with NEUP-funded research being conducted at several universities in the United States. A meeting coordinating these diverse US groups was instituted in January, graciously hosted by the University of North Texas. The annual international workshop was held in May in Aachen, Germany and Mol, Belgium with our partners France (CEA, Subatech, AREVA), Belgium (SCK-CEN), U.K. (NNL, Amec, Sheffield), and Japan (Kyushu, JAEA). Our Belgian partners hosted 2 days of that workshop, including a tour of their underground HADES research facility. Additional collaborations are being initiated with researchers in other countries. These collaborations are yielding scientific advances more quickly and fostering consensus in the scientific understanding of waste glass corrosion and the development of an effective mechanistic rate law. The work completed in FY 2014 provided key structural findings and databases that will define the potential mechanisms responsible for the various stages of glass degradation. Development of a holistic model that accounts for observed glass degradation behavior continues. Summary descriptions of selected experimental and modeling results follow.

6.2.1 Examinations of Surface Alteration Layers

J. Ryan, Z. Zhu, D. Schreiber, A. Mitroshkov, Pacific Northwest National Laboratory

Working with our international partners, one of the most consistent sources of uncertainty is the interfacial region that separates the glass from the gel. This region is the solid phase contacting the pore solution, and thus it is the phase where dissolution occurs rather than the glass itself. In the model development literature, it is acknowledged that the glass itself is not the solid phase that is driving the affinity model. Instead, a pseudo-equilibrium constant is used for the dissolving solid phase, with properties generally intermediate between quartz and amorphous silica - typically of the same order as silica-rich phases such as chalcedony. It is also believed that the actual exchange of ions that provides the source term for the ion exchange diffusion profiles occurs at this region. Further, some of our international partners include the effects of a transport barrier at this interfacial region into their models, although they do not definitively identify the critical species that are affected by it.

In any case, detailed knowledge of the composition, evolution, and sensitivity to the solution composition of this interfacial region is required for a good technical basis for any performance model. Studying surface alteration layers is challenging because they develop slowly, are fragile and easily damaged by handling, and are sensitive to changes in solution chemistry. Multi-year isotope swap experiments have provided a detailed view of the interfacial region where glass corrosion is occurring and new insights to possible mass transport barriers. For example, atom-probe tomography (APT) data demonstrated the presence of two reaction areas: a very sharp interface locating the depth to which boron was released and another interface closer to the solution where the network silica have rearranged due to condensation reactions. Further toward the solution, the tests indicated that silica from solution reacted readily with the porous gel region. This year, a joint CEA/PNNL experiment, the fruit of last year's visit by scientist Stéphane Gin, used isotopic tracing to examine the formation and behavior of glass in silica-saturated conditions. The results were surprising, changing the way this interfacial layer is viewed.

In these experiments, the International Simple Glass – a six oxide borosilicate glass selected by the international nuclear glass community to improve the understanding of glass corrosion mechanisms and kinetics – was altered at 90 °C in a solution initially saturated with respect to amorphous 29SiO₂. The pH_{90°C} was fixed at 9 at the start of the experiment and raised to 11.5 after 209 d by the addition of potassium hydroxide (KOH). Isotope sensitive analytical techniques were used to analyze the solution

and altered glass samples, helping to understand the driving forces and rate limiting processes controlling long-term glass alteration. At pH 9, the corrosion rate was found to drop in an asymptotic manner and the glass slowly transformed into a uniform, homogeneous and isovolumetric amorphous alteration layer. The continuation of alteration in a silica-saturated condition confirms previous studies that concluded that silica saturation was not sufficient to halt further alteration. Further, the resultant amorphous alteration layer was not formed using silica from solution (Figure 56), instead appearing to be a relic of the glass structure with the most weakly bonded cations (Na, Ca and B) removed. These two results are critical as they are not reproduced by any of the historically used corrosion models. It is evident that another mechanism is controlling behavior at silica saturation. The characterization of this mechanism and the development of a mathematical model to describe it are two main goals for FY 2015.

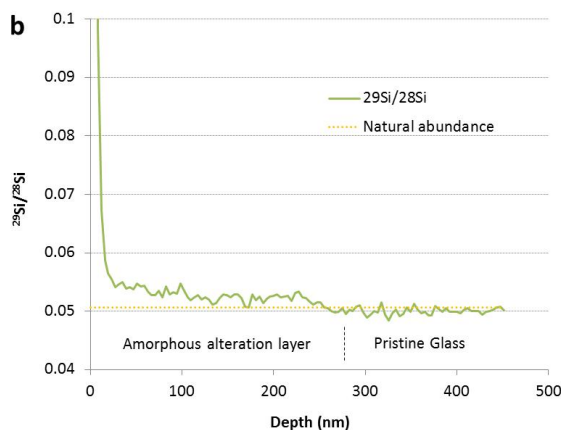


Figure 56. Plot of the silicon isotopic ratio with depth in ISG glass corroded in a ^{29}Si enriched solution. The miniscule ratio change in the amorphous alteration layer shows that only one atom in every thousand from that layer originated in the solution.

As mentioned, the experiment did not end there. After more than 200 days, the solution was artificially changed to pH 11.5, with the intent being to examine the behavior at conditions relevant to the Stage III acceleration of dissolution experienced by some samples in some conditions. At this high pH, silica (and other species) was no longer in saturation. Thus, the high solubility of glass network formers (Si, Al, Zr) triggered the rapid and complete dissolution of the glass (dissolution becomes congruent) and precipitation of amorphous and crystalline phases. Unlike at pH 9 where glass corrosion rate decreased by 3 orders of magnitude, the alteration rate at pH 11.5 was maintained at a value close to the forward rate. Quickly (although not immediately), amorphous calcium-silicate-hydrate phases and zeolites began to precipitate from solution. The delay both illustrates the importance of kinetics in crystal alteration phase precipitation as well as suggesting that zeolite formation may be a sustaining effect of Stage III behavior rather than a cause.

Additionally, the trend of developing advancements in characterization techniques was continued to enable previously difficult or impossible analyses. A journal article was submitted that presented a novel technique developed by the team that can provide accurate compositional profiles with nanometer scale depth resolution for non-flat samples. By performing NanoSIMS characterization on a wedged crater prepared using a focused ion beam (FIB) instrument, a 5-fold improvement in depth information for NanoSIMS measurements was obtained. This improvement confirmed prior results that the breakdown of the silica glass network is further from the pristine glass than a second dissolution front for boron, another

glass former, despite only ~50 nm distance between them. Also, the results show that the corrosion-induced roughness mostly exists in Si corrosion layer. This novel technique is important because many of the interfaces roughen and become irregular during corrosion, particularly once Stage III corrosion behavior is observed. The powerful atom-probe tomography technique is less useful (or unavailable) for these kinds of samples, and this NanoSIMS technique will fill the knowledge gap for these important structures. Another SIMS technique that led to a publication will enable more rapid throughput of samples as well as higher accuracy results for samples with thick alteration layers. Our NEUP partnership with the University of North Texas focused in part on understanding of why some multicomponent glasses can be characterized with atom-probe tomography while others are very problematic. With this information, minor additions to simplified waste glass compositions will enable far more accurate interfacial analyses.

6.2.2 A Novel Approach to Ion Exchange Studies

J. Neeway, S. Kerisit, J. Ryan, Pacific Northwest National Laboratory

Ion exchange is recognized as an integral, if underrepresented, mechanism influencing glass corrosion. However, due to the formation of various alteration layers in the presence of water, it is difficult to conclusively deconvolute the mechanisms of ion exchange from other processes occurring simultaneously during corrosion. In this work, an inert non-aqueous solution was used as an alkali source material to isolate ion exchange and study the solid-state diffusion of lithium. Specifically, the experiments involved contacting simulated nuclear waste glass coupons with a non-aqueous solution of ${}^6\text{LiCl}$ dissolved in dimethyl sulfoxide at 90 °C for various time periods. Two glass compositions were studied: the complex SON68 glass and a lithium-containing version of the International Simple Glass. The depth profiles of major elements in the glass coupons were measured using time-of-flight secondary ion mass spectrometry. Lithium interdiffusion coefficients, D_{Li} , were then calculated based on the measured depth profiles as shown in Figure 57. The results indicate that the penetration of ${}^6\text{Li}$ is faster in the simplified CJ-6 ($D_{6\text{Li}} \approx 4.0\text{--}8.0 \times 10^{-21} \text{ m}^2/\text{s}$) compared to the more complex SON68 ($D_{6\text{Li}} \approx 2.0\text{--}4.0 \times 10^{-21} \text{ m}^2/\text{s}$). These parameters and the diffusion formalism are being incorporated into the glass performance model complex. More complex experiments needed to extend the evaluation to hydrogen-alkali interdiffusion, which were enabled by this research into alkali-alkali interdiffusion, are scheduled for completion in FY 2015.

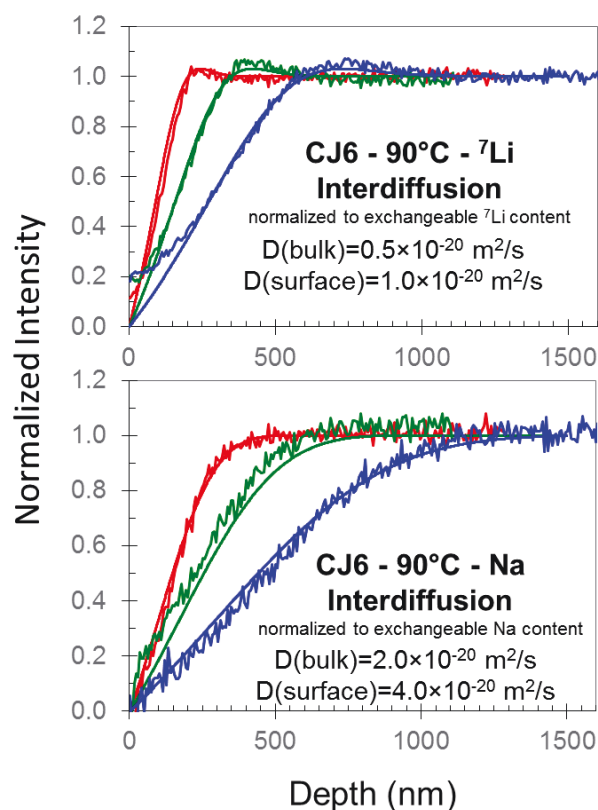


Figure 57. Interdiffusion profiles for labeled ions, including both fits (thin lines) and data (thick lines) for 10 day, 30 day, and 89 day measurements.

6.2.3 Using Monte Carlo Approaches to Model Gel Evolution

S. Kerisit, Pacific Northwest National Laboratory

The formation of the porous gel layer is an area that is generally overlooked by glass corrosion models, although some do have an empirical “retention factor” that defines how much silica is retained. Monte Carlo models have been used in the past to simulate gel formation, with mixed results. The impact of transport limitations through the porous material has not been taken into account, however. Therefore, three different models for dissolved Si diffusion in the altered layer were implemented in a Monte Carlo model and evaluated for glasses in the compositional range $(75-x)$ mol% SiO₂ $(12.5+x/2)$ mol% B₂O₃ and $(12.5+x/2)$ mol% Na₂O, where $0 \leq x \leq 20\%$, and corroded in static conditions at a surface-to-volume ratio of 1000 m⁻¹. The three models considered three transport behaviors in the gel area: instantaneous homogenization (M1), linear concentration gradients (M2), and concentration profiles determined by solving Fick’s 2nd law using a finite difference method (M3). The latter model, M3, exhibited variations in concentration profiles within the altered layer that were nonlinear and changed in shape and magnitude as corrosion progressed, in contrast to the other models. Because of this, model M3 showed that, for borosilicate glasses with a high forward dissolution rate compared to the diffusion rate, the gradual polymerization and densification of the altered layer is significantly delayed compared to models M1 and M2, better reproducing results. With these results, it is evident that certain glass compositions may require a diffusion model to be inserted in the gel layer area to reproduce corrosion behavior.

6.2.4 The Impact of Solution Composition on Stage III Acceleration

D. Strachan, J. Neeway, Pacific Northwest National Laboratory

One issue with the control of Stage III behavior by the consumption of the rate-controlling H₄SiO₄ species is the observation that concentrations of silica-bearing solution species does not significantly decrease (and may even increase), while other ions indicate an acceleration in network dissolution. To examine whether or not these two observations are compatible, the relationship between glass dissolution rates and the precipitation rate of a representative zeolitic silica-bearing alteration product, analcime [Na(AlSi₂O₆)·H₂O] was investigated using geochemical modeling. To simplify the calculations, all alteration products except analcime, gibbsite (Al(OH)₃), and amorphous silica were suppressed. Using a commonly accepted pseudo-equilibrium-constant for the glass, the glass dissolution rate was calculated using different values for the analcime precipitation rate constant and the glass dissolution rate constant. The simulations revealed the expected kinetic coupling between the formation of the zeolitic phase and glass dissolution. Depending on the relative kinetics of glass dissolution and secondary phase precipitation, corrosion was rapidly suppressed, reached a steady state, or resumed alteration at a relatively rapid rate. Additionally, in some conditions the glass dissolution rate was found to control the rate of analcime precipitation in the long term rather than vice versa. It was also shown that the total silica content in solution could increase at the same time that the glass dissolution was accelerated by the decrease in concentration of a single silicate species. This provides credence that this potential mechanism of Stage III behavior is not ruled out simply by the observation that total silica content is increasing during Stage III. The results confirm the necessity of focus on these topics reflected in the ongoing studies at ANL, PNNL, and the joint Penn State University/PNNL NEUP program.

6.2.5 Stage 3 Model and Supporting Experiments

W. Ebert, Argonne National Laboratory; C. Jantzen, C. Crawford, Savannah River National Laboratory

Recent work done in the MRWFD campaign has led to the formulation of a new conceptual model for glass dissolution that has a scientific basis and is consistent with glass corrosion observed in laboratory tests. The new model addresses the effects of alteration layers formed on the glass and secondary phase precipitation without the unnecessary and unjustified constraints that have been placed on the analytical form of the rate equation. The most important aspect of calculating the long-term dissolution rate of glass waste forms in a disposal system is taking into account the sudden increase that occurs when certain secondary phases form, which is referred to as Stage 3.

Glass is thermodynamically driven to convert to an assemblage of stable phases, but that transformation is limited by the available reaction pathways and the slow kinetics of the processes that are involved. The general kinetic pathway for transformation is (1) dissolution of glass into solution, (2) nucleation of secondary phases, and (3) coupled growth of the secondary phases from solute provided by continued glass dissolution. The second and third steps are crucial to long-term glass corrosion modeling behavior. Transformation of glass to alteration phases cannot occur until secondary phases nucleate, and then the glass dissolution rate is coupled to the growth of each secondary phase through the transfer of species that are common to both phases. The glass dissolution kinetics may be affected as each new secondary phase nucleates and grows if that phase provides a kinetically favored pathway. A secondary phase can have either an accelerating or decelerating impact on the glass dissolution rate depending on the precipitation rate. Phyllosilicate phases (clays) generally form first by in-situ transformation of the amorphous gel formed by dealkalization and hydrolysis reactions. Due to their slow growth kinetics, these phases can have a negative feedback effect that lowers the glass dissolution rate. The low rate when glass dissolution is coupled with secondary phases having a negative feedback is referred to as the residual rate. In contrast, tectosilicates (zeolites) that generally nucleate after more glass has dissolved have high precipitation rates and provide a positive feedback effect on glass dissolution. This is Stage 3.

Work to address glass dissolution in Stage 3 is in progress at ANL focused in three areas: theory to provide mechanistic basis for a Stage 3 rate law, empirical analyses of data from long-term product consistency tests (PCTs) conducted with a large number of glasses to identify and quantify the triggering conditions, and experiments designed to measure and characterize the Stage 3 rate.

In theory, the nucleation and growth of some secondary phases causes the observed increase in the glass dissolution rate. Glass dissolution and secondary phase precipitation are linked through the solution composition: dissolution of the glass provides the species needed to form the secondary phases. The same phases are generally seen to form when a wide range of glass compositions enter Stage 3, including analcime, phillipsite, and Na-chabazite. It is expected that each of these phases precipitates when the solution composition exceeds a particular solubility product constant. The evolution of the solution composition depends on the composition and dissolution rate of the glass, which depends primarily on the pH, temperature, and dissolved silica concentration. It is proposed that the solution composition be tracked as the glass dissolves to (1) determine the glass dissolution rate prior to Stage 3 and (2) determine when Stage 3 is triggered based on the solution attaining a critical composition. When that occurs, the glass dissolution rate is set at the constant Stage 3 rate.

A model for the coupled glass dissolution and secondary phase precipitation kinetics was developed based on thermodynamic and kinetic principles. At steady state, the dissolution and precipitation rates are equal and mathematically related to the kinetics and reaction affinity for each individual reaction as

$$rate_{coupled} = \frac{rate_{dissolution}^{(1)} rate_{precipitation}^{(2)}}{rate_{dissolution}^{(1)} + rate_{precipitation}^{(2)}} \left[1 - \exp\left(\frac{\Delta G^{(1)} + \Delta G^{(2)}}{RT}\right) \right], \quad (1)$$

where $rate_{coupled}$ is the steady-state rate for the coupled dissolution and precipitation reactions, which are distinguished by the superscripts (1) and (2), respectively, $rate_{dissolution}^{(1)}$ and $rate_{dissolution}^{(2)}$ are the kinetic glass dissolution and secondary phase precipitation rates, and $\Delta G^{(1)}$ and $\Delta G^{(2)}$ are Gibbs free energies driving glass dissolution and secondary phase precipitation, respectively. The dissolution rate is expressed as a negative value and the precipitation rate as a positive value by convention. Two limiting cases are of interest. When the precipitation rate is much lower than the glass dissolution rate, the coupled rate term simplifies to $rate_{precipitation}^{(2)}$. When the precipitation rate is much higher than the glass dissolution rate, the coupled forward rate term simplifies to $rate_{dissolution}^{(1)}$. Under most conditions, the rates of both reactions affect the coupled rate. A key challenge to modeling glass dissolution is that the reacting system changes as new phases are generated that affect the analytical forms and values of the kinetic and affinity terms and the values of $\Delta G^{(1)}$ and $\Delta G^{(2)}$. Additional rate and free energy terms are included to account for other secondary phases.

An important aspect of the couple kinetics is that the reaction affinity for the coupled reactions can become “arrested” because progress in the transformation of glass to a secondary phase results in equal but opposite changes to $\Delta G^{(1)}$ and $\Delta G^{(2)}$ that maintains the sum at a constant value. The model is consistent with the constant values typically measured for residual rates and Stage 3 rates (see below); these are steady-state rates for glass dissolution coupled with secondary phases that precipitate slowly (typically clays) or with secondary phases that precipitate rapidly (typically zeolites), respectively. The rates measured in experiments represent a combination of the glass dissolution rate and the precipitation rates of several secondary phases that are probably affected by the relative surface areas and mass transport processes that cannot be measured directly and changes in the assemblage of secondary phases as the reaction progresses. The steady-state rates can be measured empirically and there is no need to measure precipitation rates for individual phases that may not be known or isolatable. Experimental methods for measuring Stage 3 rates are being developed (e.g., Ebert et al. 2013). An additional study addressing the quantitation of dissolution rates for tests conducted with crushed glass was completed as a joint effort between ANL and SRNL. Most available test data showing Stage 3 behavior is from PCTs.

Another challenge in developing the radionuclide source term calculation model is when to trigger a reacting system to enter Stage 3. Exploratory analyses of test results recently compiled by SRNL in the ALTGLASS database were performed at ANL and SRNL to evaluate the possibility that a general solution composition can be identified for that purpose. Most tests documented in the ALTGLASS database were conducted as modified PCTs wherein small aliquots of test solution were removed for analysis and replaced with fresh water 10-20 times over the test duration. Many of the tests documented in ALTGLASS proceeded long enough that Stage 3 was observed, although Stage 3 behavior was not observed for all glasses. Of 160 test series that were evaluated, which included some replicate series, 120 test series entered Stage 3, 29 did not enter Stage 3, and 11 were uncertain or only showed an increase at the last sampling. All glasses are alkali boro-aluminosilicate glasses that generate similar secondary phases. It was assumed that the concentration(s) triggering Stage 3 was just slightly higher than that in solution just prior to Stage 3. The solution concentrations of Al, B, Na, and Si and the pH were plotted against the reaction time to visually determine if the reaction entered Stage 3 or not. This was based on discernible sudden increases in the releases of B and/or Na. The solution compositions for tests with

glasses that did enter Stage 3 were then compared with solution compositions from tests with other glasses that did not enter Stage 3 within the test duration.

The averages of the solution concentrations of Al, Na, and Si and the pH values in the two tests immediately before Stage 3 and the average concentrations and pH values at the two longest test durations for tests that did not enter Stage 3 were used in the comparison. These elements were selected for comparison because they are constituents in the solubility products of zeolites commonly seen to be formed in Stage 3 (namely Na-chabazite and analcime). The results for each component were plotted against the average pH value for the solutions being compared. The total amounts of alkali metals Li, Na, and K in those solutions were also compared. Figure 58 shows the total alkali metal contents in the solutions plotted against the pH. The filled symbols are for tests that entered Stage 3 and the open symbols are for tests that did not enter Stage 3; the squares are for test series conducted with 15

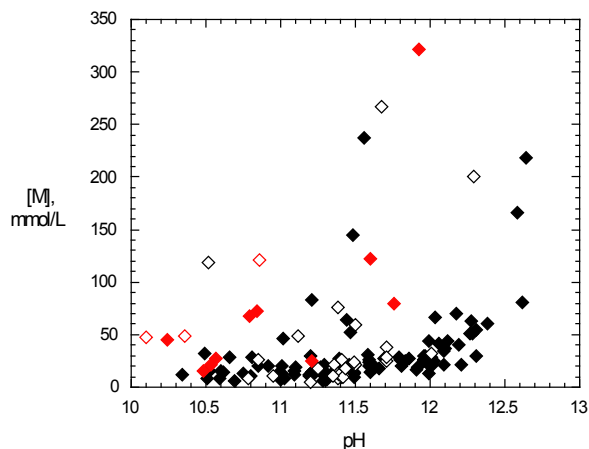


Figure 58. Total alkali metal (M) concentration vs. pH for glasses that entered Stage 3 (solid symbols) or did not enter Stage 3 (open symbols) in long-term PCTs conducted at 90 °C. Red symbols for HLW glasses and black symbols for LAW glasses.

surrogate HLW glasses and the circles are for test series 145 conducted with surrogate LAW glasses. This plot shows the total concentrations of dissolved alkali metals in the four subsets cover the same ranges and cannot be used directly to predict whether glass dissolution will enter Stage 3 or not. Plots of the Al, Na, and Si concentrations and pH values suggest these are likewise not useful for directly predicting the occurrence of Stage 3 behavior. Although the dependence on the total concentrations were compared without regard to speciation, the fact that the Stage 3 behavior cannot be distinguished over a wide range of pH values is evidence taking speciation into account will not result in discrimination. This may indicate a yet-to-be-determined aspect of secondary phase nucleation or growth triggers Stage 3.

The limited set of HLW glasses in the ALTGLASS database (10 West Valley glasses, 2 DWPF glass, EA, AFCI, and SON68) was evaluated independently at SRNL. The B concentrations from those tests are plotted separately in Figure 59 for glasses that do and do not show Stage 3 behavior. Note the very long test durations required for some glasses to enter Stage 3, the persistence of linear residual rates prior to Stage 3 and linear rates thereafter, and that all of the B was released in some tests. Hierarchical modeling was used to investigate how the {gel-leachate} interactions are controlled by the bulk glass composition and structure. Differences between the glass and solution compositions were used to define the compositions of the hydrogels. Compositional differences occurred between the hydrogels on glasses that showed Stage 3 behavior and those that did not: alkali (primarily Li) was retained in the hydrogels of glasses that resumed accelerated dissolution but not retained to any great extent in the hydrogels of glasses that did not resume accelerated dissolution. High alkali concentrations in the glass appeared to result in alkali retention in the hydrogel, which caused excess strong base to form in the leachates over time for the glasses that resumed accelerated dissolution. The excess strong base in the leachate further reacts with the hydrogel to generate the zeolite phases associated with Stage 3. Glasses without excess molar alkali did not resume accelerated leaching and generated weak acids in the leachate solution over

time. That caused the gel to age into clays instead of zeolites. Exchange reactions leading to the formation of hydrogel layers that determine if Stage 3 occurs or not were hypothesized. This approach of modeling the Stage 3 behavior will be expanded to include datasets for LAW glasses in the ALTGLASS database.

Additional PCTs were conducted at SRNL with glasses having a range of Al and Fe contents to supplement the ALTGLASS database: HM glass has high Al and low Fe, Purex glass has low Al and high Fe, and the Blend-1 and Batch-1 glasses have low Al and low Fe.

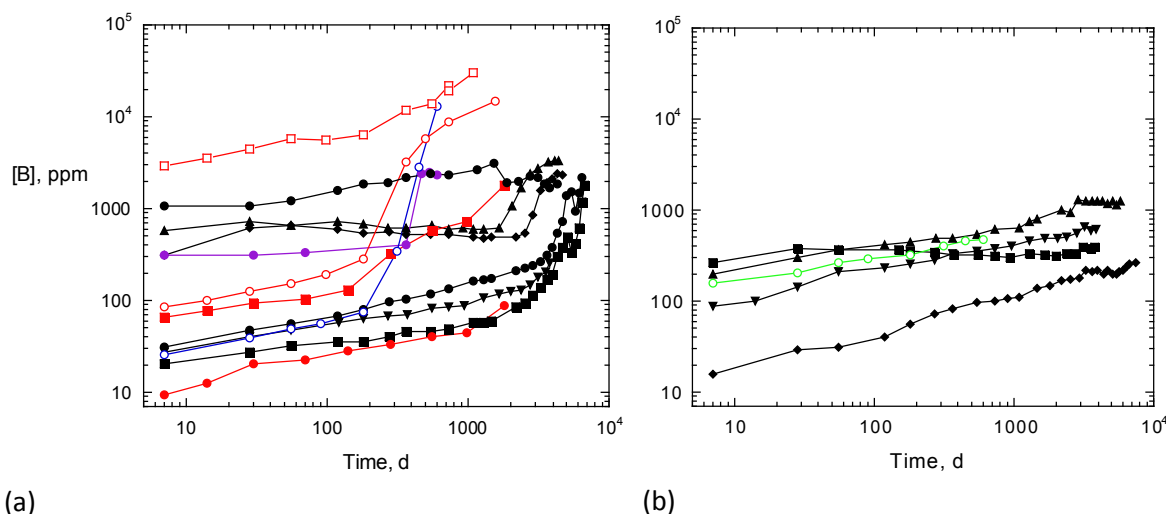


Figure 59. Boron concentrations for PCTs with glasses (a) that do show Stage III behavior and (b) that do not show Stage III behavior: WV glasses (black), DWPf glasses (red), AFCI glass (blue), and SON68 (green). Solid symbols are for PCTs at $\sim 2000 \text{ m}^{-1}$ and open symbols are for PCTs at $\sim 20,000 \text{ m}^{-1}$.

6.2.6 Stage 3 Model and Supporting Experiments (ANL and SRNL)

Recent work done in the MRWFD campaign has led to the formulation of a new conceptual model for glass dissolution that has a scientific basis and is consistent with glass corrosion observed in laboratory tests. The new model addresses the effects of alteration layers formed on the glass and secondary phase precipitation without the unnecessary and unjustified constraints that have been placed on the analytical form of the rate equation. The most important aspect of calculating the long-term dissolution rate of glass waste forms in a disposal system is taking into account the sudden increase that occurs when certain secondary phases form, which is referred to as Stage 3.

Glass is thermodynamically driven to convert to an assemblage of stable phases, but that transformation is limited by the available reaction pathways and the slow kinetics of the processes that are involved. The general kinetic pathway for transformation is (1) dissolution of glass into solution, (2) nucleation of secondary phases, and (3) coupled growth of the secondary phases from solute provided by continued glass dissolution. The second and third steps are crucial to long-term glass corrosion modeling behavior. Transformation of glass to alteration phases cannot occur until secondary phases nucleate, and then the glass dissolution rate is coupled to the growth of each secondary phase through the transfer of species that are common to both phases. The glass dissolution kinetics may be affected as each new secondary phase nucleates and grows if that phase provides a kinetically favored pathway. A secondary phase can have either an accelerating or decelerating impact on the glass dissolution rate depending on the precipitation

rate. Phyllosilicate phases (clays) generally form first by in-situ transformation of the amorphous gel formed by dealkalization and hydrolysis reactions. Due to their slow growth kinetics, these phases can have a negative feedback effect that lowers the glass dissolution rate. The low rate when glass dissolution is coupled with secondary phases having a negative feedback is referred to as the residual rate. In contrast, tectosilicates (zeolites) that generally nucleate after more glass has dissolved have high precipitation rates and provide a positive feedback effect on glass dissolution. This is Stage 3.

Work to address glass dissolution in Stage 3 is in progress at ANL focused in three areas: theory to provide mechanistic basis for a Stage 3 rate law, empirical analyses of data from long-term product consistency tests (PCTs) conducted with a large number of glasses to identify and quantify the triggering conditions, and experiments designed to measure and characterize the Stage 3 rate.

In theory, the nucleation and growth of some secondary phases causes the observed increase in the glass dissolution rate. Glass dissolution and secondary phase precipitation are linked through the solution composition: dissolution of the glass provides the species needed to form the secondary phases. The same phases are generally seen to form when a wide range of glass compositions enter Stage 3, including analcime, phillipsite, and Na-chabazite. It is expected that each of these phases precipitates when the solution composition exceeds a particular solubility product constant. The evolution of the solution composition depends on the composition and dissolution rate of the glass, which depends primarily on the pH, temperature, and dissolved silica concentration. It is proposed that the solution composition be tracked as the glass dissolves to (1) determine the glass dissolution rate prior to Stage 3 and (2) determine when Stage 3 is triggered based on the solution attaining a critical composition. When that occurs, the glass dissolution rate is set at the constant Stage 3 rate.

A model for the coupled glass dissolution and secondary phase precipitation kinetics was developed at ANL based on thermodynamic and kinetic principles. At steady state, the dissolution and precipitation rates are equal and mathematically related to the kinetics and reaction affinity for each individual reaction as

$$rate_{coupled} = \frac{rate_{dissolution}^{(1)} rate_{precipitation}^{(2)}}{rate_{dissolution}^{(1)} + rate_{precipitation}^{(2)}} \left[1 - \exp\left(\frac{\Delta G^{(1)} + \Delta G^{(2)}}{RT}\right) \right], \quad (1)$$

where $rate_{coupled}$ is the steady-state rate for the coupled dissolution and precipitation reactions, which are distinguished by the superscripts (1) and (2), respectively, $rate_{dissolution}^{(1)}$ and $rate_{dissolution}^{(2)}$ are the kinetic glass dissolution and secondary phase precipitation rates, and $\Delta G^{(1)}$ and $\Delta G^{(2)}$ are Gibbs free energies driving glass dissolution and secondary phase precipitation, respectively. The dissolution rate is expressed as a negative value and the precipitation rate as a positive value by convention. Two limiting cases are of interest. When the precipitation rate is much lower than the glass dissolution rate, the coupled rate term simplifies to $rate_{precipitation}^{(2)}$. When the precipitation rate is much higher than the glass dissolution rate, the coupled forward rate term simplifies to $rate_{dissolution}^{(1)}$. Under most conditions, the rates of both reactions affect the coupled rate. A key challenge to modeling glass dissolution is that the reacting system changes as new phases are generated that affect the analytical forms and values of the kinetic and affinity terms and the values of $\Delta G^{(1)}$ and $\Delta G^{(2)}$. Additional rate and free energy terms are included to account for other secondary phases.

An important aspect of the couple kinetics is that the reaction affinity for the coupled reactions can become “arrested” because progress in the transformation of glass to a secondary phase results in equal

but opposite changes to $\Delta G^{(1)}$ and $\Delta G^{(2)}$ that maintains the sum at a constant value. The model is consistent with the constant values typically measured for residual rates and Stage 3 rates (see below); these are steady-state rates for glass dissolution coupled with secondary phases that precipitate slowly (typically clays) or with secondary phases that precipitate rapidly (typically zeolites), respectively. The rates measured in experiments represent a combination of the glass dissolution rate and the precipitation rates of several secondary phases that are probably affected by the relative surface areas and mass transport processes that cannot be measured directly and changes in the assemblage of secondary phases as the reaction progresses. The steady-state rates can be measured empirically and there is no need to measure precipitation rates for individual phases that may not be known or isolatable. Experimental methods for measuring Stage 3 rates are being developed (e.g., Ebert et al. 2013). An additional study addressing the quantitation of dissolution rates for tests conducted with crushed glass was completed as a joint effort between ANL and SRNL. Most available test data showing Stage 3 behavior is from PCTs.

Another challenge in developing the radionuclide source term calculation model is when to trigger a reacting system to enter Stage 3. Exploratory analyses of test results recently compiled by SRNL in the ALTGLASS database were performed at ANL and SRNL to evaluate the possibility that a general solution composition can be identified for that purpose. Most tests documented in the ALTGLASS database were conducted as modified PCTs wherein small aliquots of test solution were removed for analysis and replaced with fresh water 10-20 times over the test duration. Many of the tests documented in ALTGLASS proceeded long enough that Stage 3 was observed, although Stage 3 behavior was not observed for all glasses. Of 160 test series that were evaluated, which included some replicate series, 120 test series entered Stage 3, 29 did not enter Stage 3, and 11 were uncertain or only showed an increase at the last sampling. All glasses are alkali boro-aluminosilicate glasses that generate similar secondary phases. It was assumed that the concentration(s) triggering Stage 3 was just slightly higher than that in solution just prior to Stage 3. The solution concentrations of Al, B, Na, and Si and the pH were plotted against the reaction time to visually determine if the reaction entered Stage 3 or not. This was based on discernible sudden increases in the releases of B and/or Na. The solution compositions for tests with glasses that did enter Stage 3 were then compared with solution compositions from tests with other glasses that did not enter Stage 3 within the test duration.

The averages of the solution concentrations of Al, Na, and Si and the pH values in the two tests immediately before Stage 3 and the average concentrations and pH values at the two longest test durations for tests that did not enter Stage 3 were used in the comparison. These elements were selected for comparison because they are constituents in the solubility products of zeolites commonly seen to be formed in Stage 3 (namely Na-chabazite and analcime). The results for each component were plotted

against the average pH value for the solutions being compared. The total amounts of alkali metals Li, Na, and K in those solutions were also compared. Figure 60 shows the total alkali metal contents in the solutions plotted against

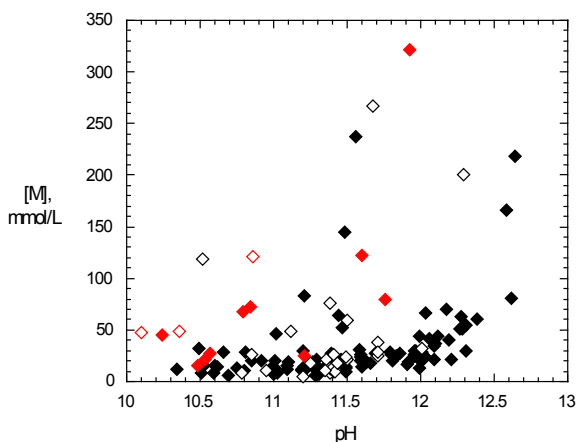


Figure 60. Total alkali metal (M) concentration vs. pH for glasses that entered Stage 3 (solid symbols) or did not enter Stage 3 (open symbols) in long-term PCTs conducted at 90 °C. Red symbols for HLW glasses and black symbols for LAW glasses.

the pH. The filled symbols are for tests that entered Stage 3 and the open symbols are for tests that did not enter Stage 3; the squares are for test series conducted with 15 surrogate HLW glasses and the circles are for test series 145 conducted with surrogate LAW glasses. This plot shows the total concentrations of dissolved alkali metals in the four subsets cover the same ranges and cannot be used directly to predict whether glass dissolution will enter Stage 3 or not. Plots of the Al, Na, and Si concentrations and pH values suggest these are likewise not useful for directly predicting the occurrence of Stage 3 behavior.

Although the dependence on the total concentrations were compared without regard to speciation, the fact that the Stage 3 behavior cannot be distinguished over a wide range of pH values is evidence that taking speciation into account will not result in discrimination. This may indicate a yet-to-be-determined aspect of secondary phase nucleation or growth triggers Stage 3.

The limited set of HLW glasses in the ALTGLASS database (10 West Valley glasses, 2 DWPF glass, EA, AFCI, and SON68) was evaluated independently at SRNL. The B concentrations from those tests are plotted separately in Figure 61 for glasses that do and do not show Stage 3 behavior. Note the very long test durations required for some glasses to enter Stage 3, the persistence of linear residual rates prior to Stage 3 and linear rates thereafter, and that all of the B was released in some tests. Hierarchical modeling was used to investigate how the {gel-leachate} interactions are controlled by the bulk glass composition and structure. Differences between the glass and solution compositions were used to define the compositions of the hydrogels. Compositional differences occurred between the hydrogels on glasses that showed Stage 3 behavior and those that did not: alkali (primarily Li) was retained in the hydrogels of glasses that resumed accelerated dissolution but not retained to any great extent in the hydrogels of glasses that did not resume accelerated dissolution. High alkali concentrations in the glass appeared to result in alkali retention in the hydrogel, which caused excess strong base to form in the leachates over time for the glasses that resumed accelerated dissolution. The excess strong base in the leachate further reacts with the hydrogel to generate the zeolite phases associated with Stage 3. Glasses without excess molar alkali did not resume accelerated leaching and generated weak acids in the leachate solution over time. That caused the gel to age into clays instead of zeolites. Exchange reactions leading to the formation of hydrogel layers that determine if Stage 3 occurs or not were hypothesized. This approach of modeling the Stage 3 behavior will be expanded to include datasets for LAW glasses in the ALTGLASS database.

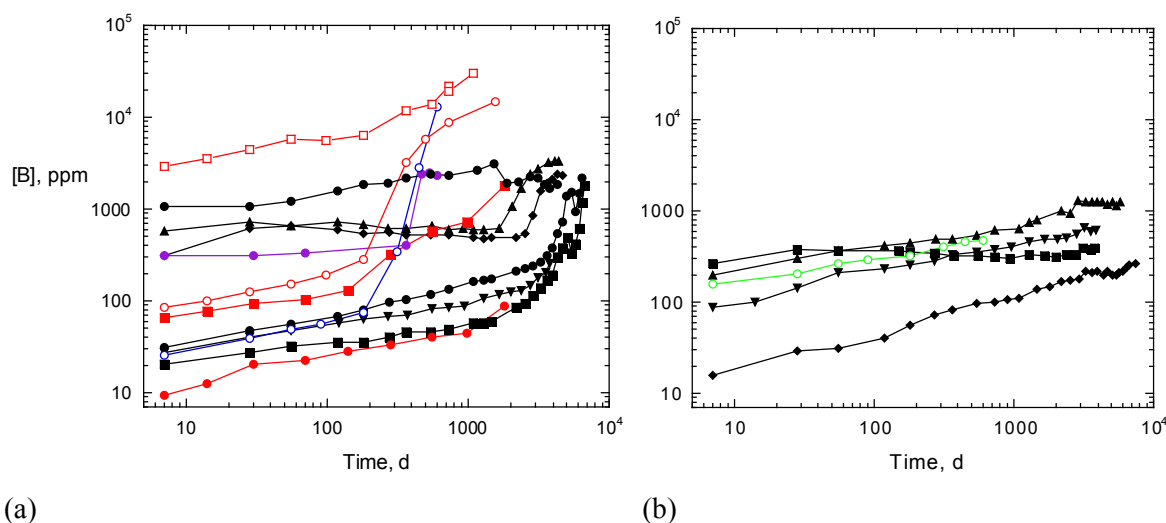


Figure 61. Boron concentrations for PCTs with glasses (a) that do show Stage III behavior and (b) that do not show Stage III behavior: WV glasses (black), DWPF glasses (red), AFCI glass (blue), and SON68 (green). Solid symbols are for PCTs at ~2000 m⁻¹ and open symbols are for PCTs at ~20,000 m⁻¹.

Additional PCTs were conducted at SRNL with glasses having a range of Al and Fe contents to supplement the ALTGLASS database: HM glass has high Al and low Fe, Purex glass has low Al and high Fe, and the Blend-1 and Batch-1 glasses have low Al and low Fe.

Static tests were conducted previously to measure Stage 3 rates using solution that was generated in PCTs and pre-equilibrated with secondary phases that had been generated in VHTs (Ebert et al. 2012). That solution was used as the leachant in a test with pristine glass specimens to characterize factors affecting the Stage 3 rate, but the test solution was only analyzed at the end of the test. The column test method allows for continuous sampling of the effluent to characterize changes in the solution composition that trigger Stage 3. A column test method is being developed to determine the range of compositions triggering the Stage 3 rate and measure the Stage 3 rate to provide values for the glass source term model. The solution in a packed column is not well-mixed and the solution chemistry changes over the length of the column. In the simplest case of plug flow, a concentration gradient exists along the length of the column but not laterally. Steady-state conditions can be attained in a column wherein the concentration will vary continuously along the length of the column, but not change over time. The concentration and glass dissolution rate at every point in the column will depend on the flow rate and the eluate concentration will depend on the column length and be the most concentrated. Therefore, Stage 3 is expected to occur first near the exit and the eluate to represent the steady state solution.

The mathematics for interpreting test results has also been developed. The concentration of component *i* at any point *L* in the column is related to the glass dissolution rate as

$$\Delta C_i = \frac{\beta_i \text{rate}_{\text{dissolution}}}{qV} L \bar{S} \quad (2)$$

where ΔC_i is the concentration accumulated in the flowing solution over the collection interval when the system is a steady state, *q* is the linear flow rate (m s⁻¹), *V* is the volume (liters) of solution in the column, \bar{S} is the average surface area per length, $\text{rate}_{\text{dissolution}}$ (mol m⁻² s⁻¹) the measured glass dissolution rate, and β_i is the mass fraction of element *i* in the glass. Solving Equation 2 for the rate coefficient gives

$$\text{rate}_{\text{dissolution}} = \frac{\Delta C_i qV}{\beta_i L \bar{S}} \quad (3)$$

A dissolution rate can be calculated for any set of test parameters based on the eluent composition using Equation 3. To obtain a rate that is characteristic of the material, the eluate must represent steady-state conditions, and that rate will be a function of the flow rate and column length (i.e., a function of the solution composition). When the solution composition triggers Stage 3, a sudden increase will occur in the steady-state eluate composition. The combined adjustments of leachant composition, column dimensions, glass particle size, and flow rate provide the experimental controls to determine the triggering solution composition(s) and measure the Stage 3 rate.

Scoping tests conducted at 70 °C with columns of various length and diameter and various size fractions of crushed glass indicated steady state was achieved within a few days at the low flow rates of interest

***Material Recovery and Waste Form Development
2014 Accomplishments Report***

(about 0.5 mL h⁻¹) and was sensitive to the dependencies included in Equation 3. A problem with outgassing in tests conducted at 90 °C was recently solved. Tests will be conducted at 90 °C in FY 2015. The Stage 3 model described above is based on the solution becoming saturated with respect to an unidentified secondary phase. Solutions having compositions similar to those measured in static tests before Stage 3 is triggered will be used as leachants in the column tests so only small concentration gradients must be generated in the column. This will keep column lengths and flow rates at practical values. Leachants with various concentrations of Na and Si and pH values will be used to determine the form of the affinity term for the glass source term model for PA.

ADVANCED WASTE FORMS AND PROCESSES

SECTION 7

7. ADVANCED WASTE FORMS AND PROCESSES

Advanced Waste Forms and Processes are necessary for the immobilization of waste streams from the advanced separation processes, including advanced aqueous and electrochemical processes. These waste forms are designed to improve the performance over current waste forms, such as borosilicate glass, over geologic time frames. Higher performance can be achieved by utilizing glass ceramic or ceramic waste forms. Any new waste form must be processed in production-scale continuous processing equipment. Ceramic containing waste forms must be processed at higher temperatures than glass waste forms; therefore standard joule-heated melters are not adequate. Investigation of cold crucible induction melters for processing advanced waste forms is in progress. The goal of this work is to significantly reduce the cost of waste treatment, storage, transportation and disposal, while improving performance.

7.1 Advanced Waste Forms (Ceramics)

J. W. Amoroso, Savannah River National Laboratory

A multi-phase ceramic waste form is being developed at the SRNL for treatment of waste streams generated by next generation reprocessing technologies for commercial spent nuclear. A multi-phase ceramic waste form tailored to incorporate all the waste components has the potential to broaden the available disposal options and to lower the storage and disposal costs associated with advanced fuel cycles. In contrast to more conventional synthesis/crystallization methods, SRNL has developed and designed multi-phase ceramic systems that crystallize upon cooling from a melt. Such *melt processed* ceramics were developed to take advantage of existing melter technology. Together, *melt processed ceramics* have the possibility to reduce the reliance on and cost of advanced barrier and processing systems. Work performed in FY 2014 focused on process optimization and melt property data assessment to support a Cold Crucible Induction Melter (CCIM) demonstration at the INL.

The waste composition that formed the basis for development and testing is provided in Table 11. Noble metals, minor actinides and Tc were not included for cost and handling reasons. Based on that recent research, two candidate compositions were down-selected for feasibility testing of melt processing multiphase titanate-based ceramics. Both nominal compositions are similar with the major difference being the stoichiometry of the targeted hollandite phase. One composition, designated *Fe-MP*, targeted a $\text{Ba}_{1.0}\text{Cs}_{0.3}\text{Fe}_{2.3}\text{Ti}_{5.7}\text{O}_{16}$ hollandite and was designed towards optimized processing. The other, designated *CAF-5%TM-MP*, targeted a $\text{Ba}_{1.0}\text{Cs}_{0.3}\text{Cr}_{1.0}\text{Al}_{0.3}\text{Fe}_{1.0}\text{Ti}_{5.7}\text{O}_{16}$ hollandite and was designed towards optimized microstructure. The two down-select compositions are listed in Table 12.

Table 11. Projected and re-normalized waste composition targeted in this study.

Group	Fuel ^a	SRNL ^b	Fuel ^c
Alkali	7.6	13.4	9.6
Alkaline Earth	8.3	12.9	10.6
Lanthanides	33.1	51.8	42.0
Actinides	4.0	-	-
Noble Metals	14.6	-	-
MoO ₃	13.7	3.4	17.4
ZrO ₂	13.7	12.1	17.4
TcO ₂	2.7	-	-
Others	2.4	6.3	3.0
Total	100	100	100

^aProjection

^bDoes not include corrosion and process products

^cRenormalized to exclude corrosion and process products

Table 12. Target Oxide Concentrations (wt. %) in Ceramic Waste Form.

Component	Fe-MP	CAF-5%TM-MP
Al ₂ O ₃	0.00	1.25
CaO	1.37	1.75
CdO	0.11	0.11
Cr ₂ O ₃	0.00	6.23
Eu ₂ O ₃	0.17	0.17
Fe ₂ O ₃	15.13	6.55
Gd ₂ O	0.16	0.16
SrO	0.97	0.96
TiO ₂	48.65	49.48
ZrO ₂	2.96	3.06
BaO	12.63	12.57
Ce ₂ O ₃	3.07	3.03
Cs ₂ O	2.85	2.81
La ₂ O ₃	1.57	1.55
MoO ₃	0.84	0.83
Nd ₂ O ₃	5.18	5.11
Pr ₂ O ₃	1.43	1.41
SeO ₂	0.08	0.08
SnO ₂	0.07	0.07
Sm ₂ O ₃	1.07	1.05
TeO ₂	0.65	0.67
Y ₂ O ₃	0.62	0.64
Rb ₂ O	0.42	0.43

The *Fe-MP* composition was based on earlier research in which Fe additions were found to greatly reduce the melting temperature of the composition. However, the reactivity of Fe in the melt resulted in a crystalline ceramic with minor amounts of undesirable phases that resulted in lower product quality. Those undesirable effects were found to be suppressed with appropriate processing controls but, nonetheless the nature of processing the high Fe compositions was unattractive.

Alternatively, a composition with Cr and only minor Al and Fe additions was shown to have superior phase assemblage but, melted at a higher temperature than if only Fe was added. In order to lower the melting temperature, the concentration of rare earth and transition metal oxides already present in projected waste, were increased. Increasing the concentration of either transition metal oxides or rare earth oxides by as little as 5 wt. % was sufficient to lower the melting temperature. The CAF-5%TM-MP composition chosen for further investigation had 5 wt. % additional transition metal oxides compared to the nominal concentration. Overall, the 5% increase in total transition metal content had negligible effect on individual component concentrations.

Melting/crystallization behavior, viscosity, electrical conductivity, and thermal analysis were performed on the two candidate compositions in preparation for processing in the CCIM [1]. The results from those experiments and the collected property data are summarized in a data package to develop an appropriate

run plan to successfully process ceramics through the CCIM. Some of the key experiments and results are presented subsequently.

To date, previous melt processing experiments were carried out by melting material in a crucible and allowing crystallization to occur upon cooling in the furnace over the course of many hours. Recently, laboratory-scale melts were poured at temperature into stainless steel molds. Digital images of the resultant pours of each down select composition are shown in Figure 62.

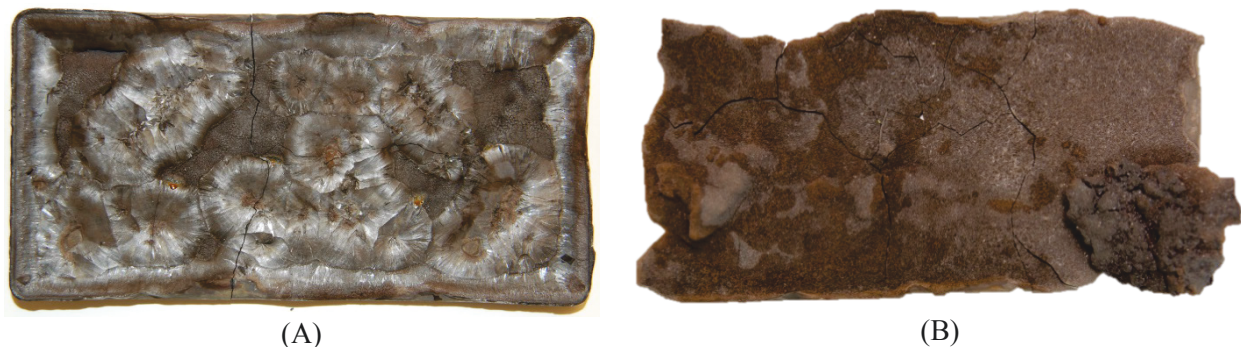


Figure 62. Digital images of pour patties from laboratory scale melting of the (A) Fe-MP and (B) CAF-5%TM-MP compositions.

Both compositions were melted at 1600°C and Figure 62 clearly shows that the Fe-MP composition poured more easily and entirely filled the mold whereas the CAF-5%TM-MP compositions crystallized sufficiently rapidly that the mold was not filled completely. Scanning electron microscopy (SEM) with elemental mapping and area analysis confirmed the overall phases formed from poured samples were similar to slower cooled samples from previous studies as shown in Figure 63. An Al-rich phase, has been found in melt processes samples and is likely due to processing in alumina crucibles at high temperatures. Although not anticipated, the Al-rich phase does not appear to significantly affect the primary phase assemblage nor is the durability expected to be negatively affected given its composition.

Density measurements on these materials are difficult to quantify given their morphology. Densities of hot-pressed samples of similar composition were approximately 4.7 – 4.9 g/cm³ which are thought to approach theoretical given typical densities of the constituent phase/structures. Measured densities for melt processed samples were measured to be approximately 4.5 – 4.8 g/cm³. This range in densities was not unexpected based on visible void space in bulk melt processed material that resulted from crystallization and grain growth during cooling.

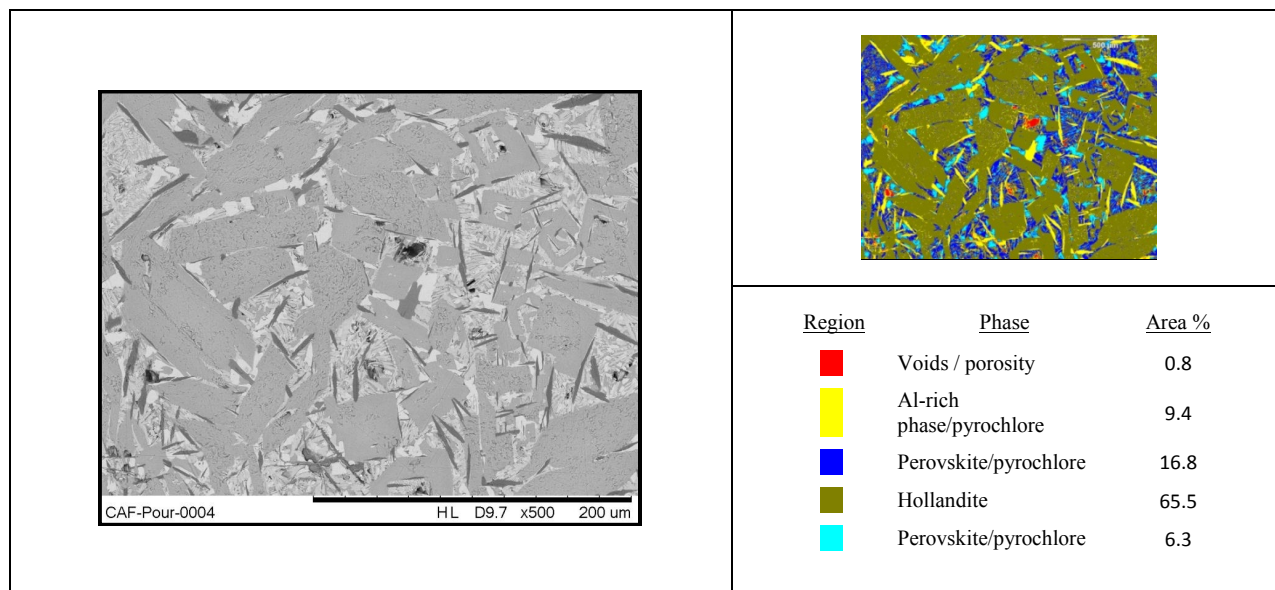


Figure 63. SEM micrograph and corresponding area map of CAF-5%TM-MP sample after cooling showing phase assemblage.

Viscosity as a function of temperature was measured for both down-selected compositions to assess the crystallization and melt behavior of the compositions at high temperatures. Figure 64 shows viscosity plotted as $\ln(\eta)$ (in Poise) versus $1/\text{temperature}$ (in K) for each composition. That data shows that rapid crystallization occurs at approximately 1375°C for the Fe-MP composition and at approximately 1405°C for the CAF-5%TM-MP composition. Examination of the viscosity curves further reinforces the melt behavior observations. The viscosity at which both sample crystallize is ~ 100 poise, or similar to that of honey. The Fe-MP composition exhibited a very narrow temperature range ($\sim 60^\circ\text{C}$) over which the viscosity transitioned from ~ 1 to ~ 100 poise. In contrast, the CAF-5%TM-MP composition exhibited a large temperature range ($\sim 200^\circ\text{C}$) over which the viscosity transitioned from ~ 1 to ~ 100 . A crystalline phase is believed to persist in equilibrium with a liquid in the CAF-5%TM-MP composition over much of the transition region. Clearly, the CAF-5%TM-MP composition presents challenges to melting compared to the Fe-MP composition. We anticipate that it will be more difficult to initiate and achieve constant flow conditions with the CAF-5%TM-MP composition compared with the Fe-MP composition. Nevertheless, although the nature of the melt-crystal composition is unknown, the viscosity behavior appeared reversible in the time span of the measurement as evidenced by the data taken upon re-heating for each composition.

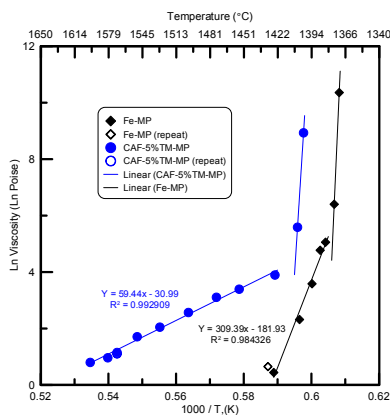


Figure 64. Viscosity relationship of (♦/◇) Fe-MP and (●/○) CAF-5%TM-MP compositions.

Material Recovery and Waste Form Development 2014 Accomplishments Report

This work package is augmented by a DOE-NEUP project that is being conducted collaboratively with Alfred University (AU). AU is performing property characterization of melt-processed material including high-temperature x-ray diffraction (HTXRD) and thermal analysis. Additionally, AU is fabricating samples with spark plasma sintering (SPS) for comparison to melt-processed samples.

In FY 2014, efforts were also made to finalize a Cooperative Research and Development Agreement (CRADA) with the Australian Nuclear Science and Technology Organization (ANSTO). The CRADA is expected to be finalized in early FY 2015 and will include exchange of data/technical information and collaborative testing to advance the chemistry and fabrication of melt processed titanate ceramics.

References

1. Amoroso, J. W. and J. C. Marra, *Ceramic Waste Form Data Package: Fuel Cycle Research and Development*, 2014, Savannah River National Laboratory: Aiken SC.

Publications

1. J. W. Amoroso and J. C. Marra, *Ceramic Waste Form Data Package: Fuel Cycle Research and Development*, US Department of Energy Report Office of Nuclear Energy Separations and Waste Forms Campaign SRNL-STI-2014-00247 (FCRD-SWF-2014-000581), Savannah River National Laboratory, 2014.
2. J. Amoroso, J. C. Marra, M. Tang, Y. Lin, F. Chen, D. Su and K. S. Brinkman, "Melt processed multiphase ceramic waste forms for nuclear waste immobilization," *Journal of Nuclear Material*, 454(1-3), 2014, 12-21.
3. M. Tang, A. Kossoy, G. Jarvinen, J. Crum, L. Turo, B. Riley, K. Brinkman, K. Fox, J. Amoroso and J. Marra, "Radiation Stability Test on Multiphase Glass Ceramic and Crystalline Ceramic Waste Forms," *Nuclear Instruments and Methods in Physics Research Section B: Beam Interactions with Materials and Atoms*, 326, 2014, 293-297.
4. J. Amoroso, J. Marra, S. D. Conradson, M. Tang and K. Brinkman, "Melt Processed Single Phase Hollandite Waste Forms for Nuclear Waste Immobilization: $\text{Ba}_{1.0}\text{Cs}_{0.3}\text{A}_{2.3}\text{Ti}_{5.7}\text{O}_{16}$; A = Cr, Fe, Al," *J. Alloys Compd.*, 584, 2014, 590-599.
5. S. Wang, M. Tang, K. S. Brinkman, and F. Chen, "Ion-irradiation Induced Reduction in $\text{Sr}_2\text{Fe}_{1.5}\text{Mo}_{0.5}\text{O}_{6-\delta}$ Perovskite," *Nuclear Instruments and Methods in Physics Research Section B*, 326, 2014, 298-302.

7.2 Summary of INL CCIM Pilot Plant Test with a Low Temperature Ceramic HLW Waste Form Surrogate –Fe-MP

T. Armstrong, R. B. Benefiel, T. Luther, V. Maio, C. Scott, Idaho National Laboratory

Cold Crucible Induction Melter Pilot Plant test using a ceramic surrogate was performed. The main goal of the test was to initiate melt, sustain melting, tap and pour at relatively low temperature ($\sim 1420^{\circ}\text{C}$) an all ceramic phase (primarily the hollandite phase of SynRoc) surrogate HLW form.

The overall test met with partial success in that a melt was initiated, but only in the lower 2-3 in. of the crucible; in a region known as the marsh. However taps and pours to create waste logs for further analysis and assess the molten flow in pans with diameters equivalent to standard disposal canisters were not achieved as expected to denote milestone success.

Preparation. The test was started with a titanium vertical 8.4-in. diameter induction wire ring bent in waves as previously done for two previous FY 2014 CCIM melts with HLW glass ceramic surrogates. The wire initiating ring was 0.08 inches thick and bent into 38 waves of amplitude 3/4 to 1 in. This particular titanium wire ring configuration provides the greatest length of induced current resistance and therefore provides heat over a greater volume of the initial cold crucible charge. The ring was placed at ~ 5.5 inches above the bottom of the crucible onto 9 Kgs of packed and tampered finely powdered- but not dusty- pre-melt oxide/carbonate surrogate (purchased from MOSCI Corporation and designated Fe-MP). Since the Fe-MP pre melted oxide surrogate (with SynRoc precursors) was only a third as dense as any previous glass and glass-ceramic HLW surrogate melted in the CCIM pilot plant, crucible loading was meticulous and required considerable tampering to ensure sufficient mass in the crucible as well as provide low porosity/high conductivity for testing. The later condition the CCIM team assumed to be a favorable one for startup. Another 4kgs of the pre-melted Fe-MP surrogate was added on top of the initiation ring for a total height of ~ 7.5 inches in the crucible. See Figure 65. Another 13 kgs of the pre melted Fe-MP surrogate was then placed in the feed hopper on the mezzanine level of the pilot plant directly above the crucible. In addition, prior to installing the drain tube for this test, it was filled with low melting phosphate glass to facilitate tapping of the CCIM. The RF generator was powered up and operated at the lowest frequency tunable (~ 1.2 MHz) to initiate a melt by first inducing a resistive joule -heated current in the titanium wire ring.



Figure 65. Pre-test fill of the Fe-MP surrogate charge into the crucible. Total crucible height is 14 in.

Melt Attempts. After loss of the initial wire ring, two more attempts to light off the Fe- MP bed were made with incrementally heavier starter rings. As the starting charge begin losing temperature with the initial wire ring—after an earlier than normal type K thermocouple centerline temperatures rise to 400°C —we were able to deploy the heavier rings by turning off the generator, entering the Faraday cage, unbolting the crucible from its main head flange, lowering the crucible, tossing in non-wire titanium rings and then centering these rings through site ports removed after the crucible was re-bolted. It appears that the first wire ring, as specified above, achieved very high temperatures very quickly as desired due to the high insulation of the packed powder Fe-MP starting bed. However, based on visible performance of the second ring as shown in the left side of Figure 66, it was assumed the relatively high carbonate salt

**Material Recovery and Waste Form Development
2014 Accomplishments Report**

content (>20%) of the Fe-MP surrogate quickly formed a small melt around the observed second heavier ring (as well as around the first wire ring) which caused a failure (break) in one or more locations of both initiator rings. The break then created a type of junction of which the low melting carbonate salts occupied. Since current is now also flowing in the very resistive salt, this junction acted as a super-heated region which quickly dissolved the ring (right side of Figure 66). The annulus of influence (conductive material which we could couple to) created by this event was not large enough to be self-sustaining with the field provided by the radio frequency (RF) generator. Worth mention is that both instrument temperature and RF generator plate current response profiles are consistent for the events described above and near identical for the first two titanium initiation rings.

For the second and heaviest starter ring (8.5 in. OD, 7.5 in. ID., 1/4 in. thick), the annulus of influence was sustainable and did not consume the ring as quickly as the first two. However this very hot annulus region of influence (created by the melting carbonate salt below the hot ring) melted its way down through the packed powder material until it fell below the direct influence of the induction coil. Once it passed the last turn of the induction coil we started to loose coupling and temperature but not before appreciable melting took place in the marsh area. Evidence of this melting at the time was based in part in quick rises in CCIM cooling water temperature and observation (even through the frozen shell) of a red melt glow between the cooling stays. If we had been able to move the coil down or the crucible up, it is the consensus of the CCIM team a full melt could have been sustained since a portion of the heaviest third ring must have rested on the top of the drain tube.

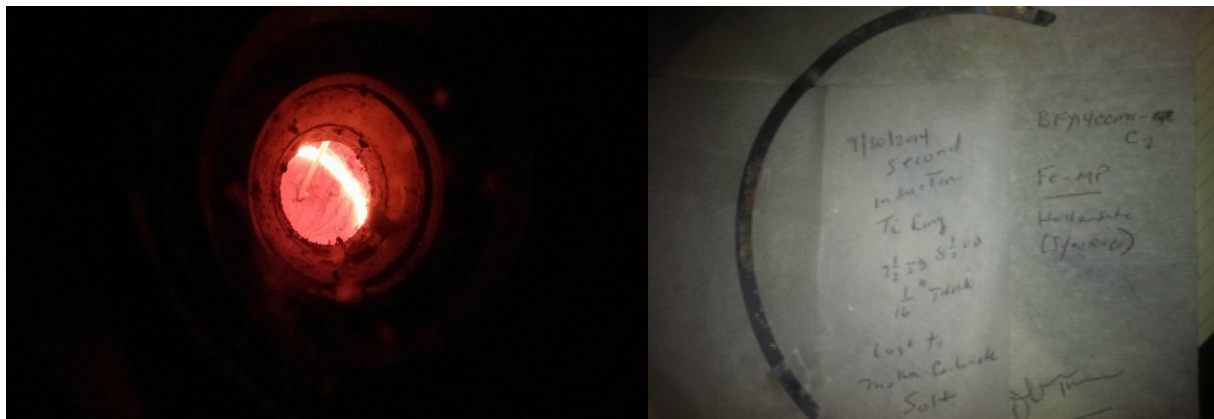


Figure 66. Right Side: As observed through the south view port, the induced glowing of the second heaviest titanium ring (8.5"OD X 7.5"ID X 1/16H) just prior to the salt junction. Unlike the last ring, the second ring was only partially insulated with ~ 200 grams of Fe-MP surrogate from the hopper, as such allowing this visual. The left side shows the remaining segment of the second ring after its dissolution and removal from the crucible.

Autopsy. On the following day, October 1, 2014, the CCIM team removed the crucible for inspection of its contents. The results of this post melt examination are described through the following three figures and their captions. Additionally the results indicate consistency with the instrument data and associated observations made during the attempted melt the previous day. No remnant of the third titanium ring was found.



Figure 67. Left Side: The bridge at the top of the bed of the partial melt after initiation with the last heaviest titanium ring. The bridge was formed as anticipated since ~1kg of Fe-MP surrogate was added to the bed as insulation after the placement of the last ring. The partially melted ~8.5" diameter core (Right Side) resided about 1 inch below the bridge. Note the complete melt of the outer surface as the ring melted down the length of the crucible.



Figure 68. Shard of cold melt removed just below the core section shown in Figure 65. The thin dark rim is consistent with high temperature melting in the annulus location of the third titanium ring. The yellow region indicates the extent of insufficient (for coupling) radial heat conduction in one location as a result of the ring being mobile. The remaining reddish area is the compacted original Fe-MP surrogate that is possibly only partially sintered



Figure 69. Four shards of melted material taken from the marsh that possess sufficient dark melt volume for follow on analysis to determine if SynRoc phase(s) were made

Path Forward. Based on the preliminary results of the attempted BFY14CCIM-C1a test, the CCIM team developed several options for path forward testing to obtain the expected milestone objectives in a prudent time frame and within budget by utilizing FY 2014 carry over dollars. Several options for this re-test were evaluated and they ranged from deploying a fixed non-inductive resistive initiation ring to starting a simple low volume glass melt at the onset to melt the hopper fed Fe-MP original surrogate until at least 99% bed turnover is achieved. However, the recommended path forward option is to place a heavy titanium ring in a 2–4-in. bed of reground Fe-MP melt placed on top of 5–7 in. of packed original Fe-MP powder surrogate. The reground bed will also contain some original powder surrogate to provide sufficient salt for melt initiation as well as keep the ring immobile.

7.3 Advanced Waste Forms-Zirconium Recycle

E.D. Collins, G.D. Del Cul, B.B. Spencer, R.D. Hunt, R.R. Brunson, and C. Ausmus, Oak Ridge National Laboratory

Process development studies are being conducted to recover, purify, and reuse the zirconium (~98.5% by mass) in UNF zirconium alloy cladding. Accomplishments in FY 2014 included non-radioactive tests and analyses to determine the effects of (1) scaling-up the chlorination process to 1 kg ZrCl_4 salt production; (2) the presence of anhydrous oxide layers of varying thickness on the cladding surface; and (3) process parameter variations (reactor temperature, Cl_2 concentration, and the presence or not of an oxide layer). In addition, further refinement of the experimental reactor and condenser design was accomplished, and an assessment of product purification needs was made.

All previous feasibility tests were made using ~15 g Zr in the cladding feed. During FY 2014, four progressively increased scale-up tests were made up to 1-kg salt production. The kg-scale salt production test exhibited the first indication of inadequate heat removal, resulting in reactor temperatures of 450-490°C. Late in the test, red-hot spots were observed on the cladding. These observations imply that heat removal capacity must be provided in the reactor design to completely remove the heat of reaction at rates commensurate with the chlorination reaction. During the process of scale-up, several reactor-condenser configurations were tested to determine the design for use in future kilogram-scale tests with actual used nuclear fuel cladding, either in the form of empty cladding hulls or segmented fuel rods. The unit for larger-scale tests is shown in Figure 70.

During a previous feasibility test on actual used nuclear fuel cladding, an incubation period of 30-45 minutes was observed in the initial dry chlorination of a ~15 g sample of a UNF cladding hull that had been previously oxidized in a dry air oxidation pretreatment prior to separation from the fuel. The incubation period was attributed to the resistance to chlorination of an oxide layer deposited on the surface of the cladding. Therefore, a study was done using ~100-gram samples of unirradiated cladding tubes to determine the effects of anhydrous oxide layers of varying thickness from ~1 to 60 μm on the chlorination reaction rate and Cl_2 utilization efficiency, and to investigate various methods of chemical pretreatment prior to chlorination to mitigate the oxide layer effects.

Dry oxidation of Zircaloy-4 cladding tubes were made in air and in NO_2 at elevated temperatures over various time intervals to deposit the anhydrous oxide layers. In general, the results indicated increasing resistance to chlorination with increased oxidation time and oxide layer thickness. While these results represent only the anhydrous oxide layers incorporated by dry oxidation, the indications will likely be similar for hydrous oxide layers deposited by irradiations in light water reactors, particularly for longer irradiated and higher burn up used fuel cladding.

Samples of cladding oxidized in air at 600°C were compared with cladding oxidized in NO_2 at 350°C. Both were compared to unoxidized cladding chlorination. The oxide layer thickness was significantly less with the NO_2 -oxidized cladding and the chlorination performance was improved in comparison to the air-oxidized cladding. These effects may have been due to the lower oxidation temperature and/or to the oxidation atmosphere. This is another reason that NO_2 oxidation is preferred.

Mitigation methods tested included: washing in concentrated nitric acid, or a nitric-oxalic acid mixture, or alkaline peroxide at temperatures at <75 C. Treatment with CCl_4 -saturated argon at 350°C was also tested. The results indicated some beneficial effects of pretreatment from nitric acid washing, better results with nitric-oxalic acid washing, and relatively greater benefits to the cladding with thicker oxide. Pretreatment with CCl_4 -saturated argon was the most effective. However, that process would require precise control

since it can also chlorinate uranium and other fuel component oxides that may be present. Of the other pretreatment methods, pre-washing with the nitric-oxalic acid mixture was most effective. This method had been suggested by consultants from Westinghouse. Optimization of that method will be worthwhile.

Tests were performed to ascertain the effect of process parameters on the chlorination rate—specifically the chlorine concentration in the feed gas and the reactor temperature. The highest rates were measured with 100% Cl_2 . Reaction rates decreased about 30% as chlorine concentration in argon decreased to 75 vol%. However and more surprising is that no significant difference in reaction rate was observed between feed gas containing 75% and 33% Cl_2 .

The reactor temperatures of 350°C and 400°C produced increased reaction rates of <20%, certainly not the doubling of reaction rate for every 10°C increase in temperature that is typical of Arrhenius law behavior. That type behavior has been observed and analyzed in a previous study^{1,2} where excess Cl_2 was present. However, in the current process, the Cl_2 feed gas is controlled and the reaction is effectively first order with respect to the concentration of zirconium in the reactor, and therefore, the potential increase in reaction rate is not realized.

Limited analyses of the test product salt (ZrCl_4) and observations of product color, have been combined with chemical thermodynamic analyses to determine likely impurity chloride species, and these analyses have been greatly supplemented by assistance from technical consultants (primarily the Shaw-Westinghouse team²) to determine likely purification needs and experimental tests. Valuable information is also available from the experimental tests and results obtained by Korean Atomic Energy Research Institute (KAERI) researchers. All of these early analyses indicate that the most likely impurities requiring further removal from the product salt are iron and niobium, plus radioactive cesium-137 and antimony-125.

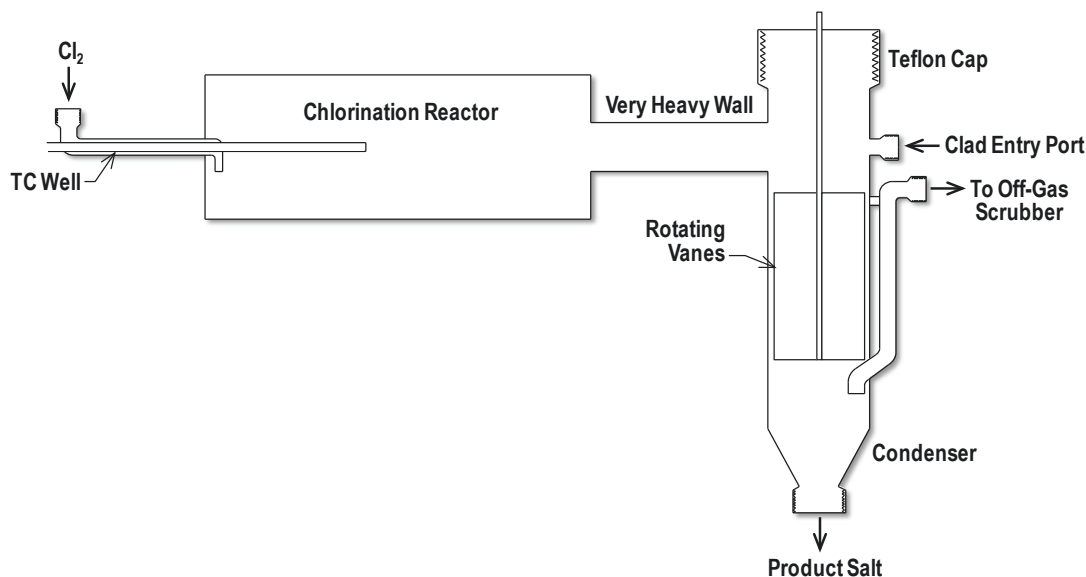


Figure 70. Chlorination Reactor

References

1. T. A. Gens, *Zircex and Modified Zirflex processes for dissolution of 8% U-91% Zr-1% H TRIGA Reactor fuel*, ORNL-3065, November 1961.

Material Recovery and Waste Form Development
2014 Accomplishments Report

2. D. F. McLaughlin and T. L. Francis, *Recycle of Zirconium from Used Nuclear Fuel Cladding: Chlorination Process Development and Design*, IDIQ Subtask 2, Westinghouse Report EPT-WZ-14-002, Rev.0, January 2014.

Publications

1. E. D. Collins, G. D. Del Cul, B. B. Spencer, R. R. Brunson, and J. A. Johnson, “Establishment of the Roadmap for Chlorination Process Development for Zirconium Recovery and Recycle,” *Proceedings of Global 2013 Conference*, American Nuclear Society, October 2013.

DOMESTIC ELECTRO- CHEMICAL SEPARATIONS

SECTION 8

8. DOMESTIC ELECTROCHEMICAL SEPARATIONS

Domestic Electrochemical (Echem) is developing technologies to enhance performance and reduce waste volumes in the treatment of fast reactor fuels. This technology is ideally suited to treatment of metallic fuels for recycle of transuranics.

8.1 Salt Waste Management Trade Study

J.D. Vienna, Pacific Northwest National Laboratory

Management of high-level waste (HLW) is a significant fraction of the used nuclear fuel reprocessing costs. Conventional wisdom suggests minimizing HLW volume will reduce this cost. However, at some point the costs of reducing volume will cease to be cost-effective. The objective of this study is to determine the relative costs of treating electrochemical salt HLW to reduce the amount of waste form. This information will ultimately guide the development of salt waste management approaches as part of the larger effort to develop electrochemical separations processes for used nuclear fuel.

Approach. Representative used metallic fuel composition and electrochemical process were selected based on the *Separation and Waste Form Campaign Full Recycle Case Study* [1]. Four salt treatment options were considered: (1) immobilize salt after TRU drawdown, (note that TRU drawdown is included in all options), (2) electrodeposit lanthanides prior to salt immobilization, (3) perform selective crystallization to concentrate fission products in salt prior to immobilization, and (4) remove cesium and strontium from salt by selective ceramic membrane prior to immobilization. The salt, thus prepared for immobilization, would be converted to a ceramic waste form (CWF) developed for immobilization of EBR-II fuel reprocessing salts [2,3]. The amount of CWF produced would be determined by the composition and mass of salt immobilized. The CWF would be stored for between 50 and 100 y in a surface facility. The cooled waste form would then be disposed of in a salt, granite, or clay deep geologic repository.

Previous detailed cost estimates for the electrochemical process, the electrochemical salt waste form fabrication, and salt waste form storage facilities were used as a baseline [4]. Differences in equipment and operations along with associated costs were then estimated for each of the processes options. Incremental disposal costs for each additional waste package were estimated using the *Secretarial Determination of the Adequacy of the Nuclear Waste Fund Fee* [5]. The amount of waste form that could be loaded into each waste package was determined based on both volume and heat limits [6]. These costs were compared to those of the baseline case (case i) to determine the relative benefit of salt treatment.

Preliminary Study Results. The study shows that some treatment approaches reduced the overall system costs while others either have no significant impact or increased cost. The most significant cost driver is the impurity concentrations in the salt before immobilization. The impurities include the chlorides of bond sodium and reactive fission products (alkali, alkaline earth, and lanthanide). Figure 71a shows the relative cost as a function of impurity content of the salt (for disposal in a salt repository). The costs are reduced until an impurity content of roughly 53 wt% after which no additional cost savings are realized. The savings seen between 22 and 53 wt% impurity (cases i and iii) are due to capital costs (41%, primarily CWF fabrication equipment/cells), operating costs (40%), and disposal costs (19%).

The cost impacts are different if disposal occurs in a clay repository due to more restrictive waste package heat limits, as shown in Figure 71b. However, the conclusion from the salt disposal results are still valid in that increasing the allowable impurity level of salt before disposal will reduce the cost up to the

roughly 50% value and not beyond. Separating out lanthanides from the salt (either with or without cesium and strontium removal) does not significantly reduce costs unless the allowable concentration of impurities increases. Removal of cesium and strontium from the salt increases overall cost.

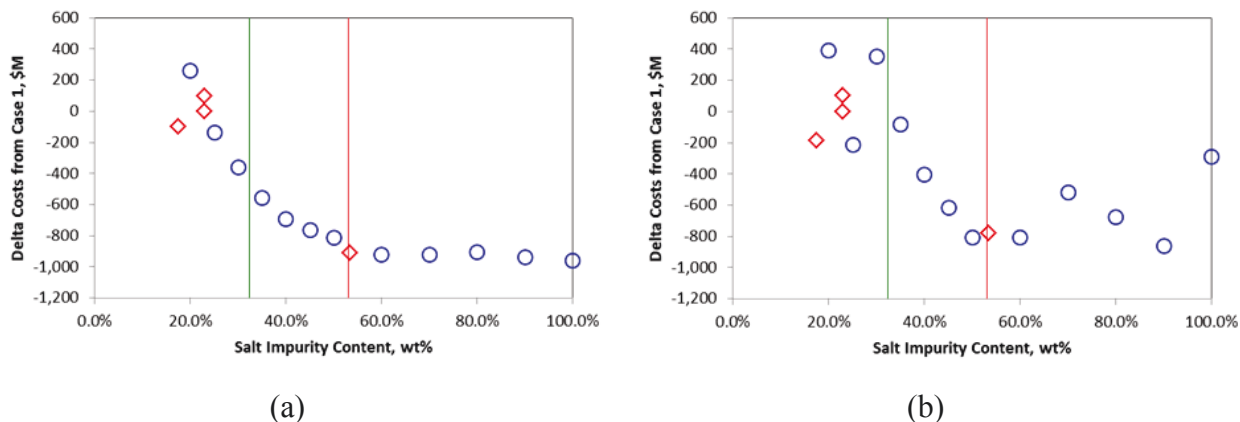


Figure 71. Difference in cost as a function of salt impurity metal chloride loading for disposal in (a) salt repository and (b) clay repository

8.1.1 Discussion and Practical Implications

The key to waste minimization is to minimize the amount of LiCl-KCl discarded during the waste process [7], i.e., increase the concentration of impurities. Increasing impurity concentrations before disposal either by using the salt longer or by purifying and recycling the salt reduces overall system cost.

Successful operation of the electrolyzer (ER) requires the disposal of impure salt and replacement with clean salt. A feed-and-bleed process would be used to maintain a nearly constant salt waste stream and ER salt impurity content. It is not currently known what determines the impurity level of ER salt before it must be immobilized. This is a very important data gap that should be addressed as soon as possible. The liquidus temperature (T_L) of salt increases with impurity content and reaches the ER operating temperature of 500 °C at 53.1 wt% impurities [8], (shown as a red line in the figure). As the currently planned ER process operates at 500 °C the 53 wt% impurity limit seems reasonable. The total lanthanide concentration may influence the lanthanide impurities in the TRU product to be used in fresh fuel. Currently, the relationship between lanthanide content in the salt and in the TRU product is unknown. It is recommended that additional work be performed to determine the tolerable impurity content in ER salt.

Initial tests have shown promise in purifying ER salt sufficient for recycle (e.g., selective crystallization [9]; precipitation and distillation [10]; ion exchange [11]). Case iii, shown as a red diamond at ~55 wt% impurity in the figure, is an estimate of the effectiveness of selective crystallization of the 22% impurity ER salt of case i. If the ER salt cannot be operated to impurity concentrations nearing 50 wt%, then we recommend pursuing methods to reduce the LiCl-KCl discarded (i.e., increase the effective impurity level of discarded salt). These techniques should focus on concentrating the primary impurities (sodium, lanthanides, alkali and alkaline earth fission products) rather than sign components.

The costs of waste management are largely dominated by the relatively inefficient process for CWF fabrication. Improvements in the efficiency of the waste form fabrication or alternative waste forms would reduce costs without changing the separations processes. Other waste forms such as solution-derived glass bonded sodalite, tellurite glass, and phosphate based waste forms have been proposed. In the second phase of this trade study, the impact of these waste forms and processes on system costs will be

evaluated. It is recommended that waste process/forms that reduce system cost be further developed and matured.

Implementing improvements in salt waste management may result in cost savings on the order of 1-5% of the total waste management costs.

References

1. Law, J.D., N.R. Soelberg, T.A. Todd, J. Tripp, C. Pereira, M.A. Williamson, W.L. Ebert, R.T. Jubin, B.A. Moyer, J.D. Vienna, G.J. Lumetta, J.V. Crum, T.S. Rudisill, J. Bresee, C. Phillips, B. Willis, P. Murray, and S. Bader. 2013. "Separation and Waste Form Campaign Full Recycle Case Study," FCRD-SWF-2013-000380, Idaho National Laboratory, Idaho Falls, ID.
2. Pereira, C., M.C. Hash, M.A. Lewis, M.K. Richmann, and J. Basco. 1999. "Incorporation of Radionuclides from the Electrometallurgical Treatment of Spent Fuel into a Ceramic Waste Form," *Scientific Basis for Nuclear Waste Management XXII*, Vol. 556, 115-120 pp. American Ceramic Society, Warrendale, PA.
3. Simpson, M.F., K.M. Goff, S.G. Johnson, K.J. Bateman, T.J. Battisti, K.L. Toews, S.M. Frank, T.L. Moschetti, T.P. O'holleran, and W. Sinkler. 2001. "A Description of the Ceramic Waste Form Production Process from the Demonstration Phase of the Electrometallurgical Treatment of EBR-II Spent Fuel," *Nuclear Technology*, 134(3):263-277.
4. Carter, J.T. and T.F. Severynse. 2010. "Electrochemical Reprocessing - Capital Cost Estimate," FCRD-SYSA-2010-000107, Savannah River National Laboratory, Aiken, SC.
5. Chu, S. 2013. "U.S. Department of Energy Nuclear Waste Fund Fee Adequacy Assessment Report," U.S. Department of Energy, Washington, D.C.
6. Hardin, E., T. Hadgu, H. Greenberg, and M. Dupont. 2012. "Parameter Uncertainty for Repository Thermal Analysis," FCRD-UFD-2012-000097, Sandia National Laboratories, Albuquerque, NM.
7. Simpson, M.F. 2013. "Projected Salt Waste Production from a Commercial Pyroprocessing Facility," *Science and Technology of Nuclear Installations*, 2013: Article 945858. <http://dx.doi.org/10.1155/2013/945858>.
8. Gutknecht, T.Y. 2012. "Thermal Analysis of Surrogate Simulated Molten Salts with Metal Chloride Impurities for Electrorefining Used Nuclear Fuel," Masters of Science, University of Idaho, Moscow, ID.
9. Williams, A.N., S. Phongikaroon, and M.F. Simpson, 2013, "Separation of CsCl from a Ternary CsCl-LiCl-KCl Salt Via a Melt Crystallization Technique for Pyroprocessing Waste Minimization," *Chemical Engineering Science*, 89:258-263. DOI: 10.1016/j.ces.2012.12.012.
10. Cho, Y.Z., T. K. Lee, H. C. Eun, J. H. Choi, I. T. Kim, G. I. Park. 2013. "Purification of used eutectic (LiCl-KCl) salt electrolyte from pyroprocessing," *Journal of Nuclear Materials* 437 (2013) 47-54.
11. Shaltry, M., S. Phongikaroon, and M.F. Simpson. 2012. "Ion Exchange Kinetics of Fission Products between Molten Salt and Zeolite-A," *Microporous and Mesoporous Materials*, 152:185-189. doi:10.1016/j.micromeso.2011.11.035.

8.2 Ion-Selective Ceramics for Mixed Waste Separations

E. D. Spoerke, Sandia National Laboratories

Pyroprocessing involves the electrochemical removal of recyclable actinides from spent nuclear fuel dissolved in eutectic LiCl-KCl molten salts. During this process, residual fission product contaminants remain dissolved in the molten salt electrolyte, potentially impacting the efficiency of electrochemical actinide separations and requiring costly disposal of the radioactive, contaminated salt. The “Ion-selective Ceramics for Mixed Waste Separations” effort is focused on developing a system to electrochemically filter such contaminants (e.g., Cs^+) from these molten salts (e.g., LiCl-KCl) using ion-selective ceramics. Not only would this process allow for recycling of the molten salts for further pyroprocessing, but it stands to significantly decrease the volume of salt to be considered for disposal. The focus of this report is to evaluate the feasibility of this concept to segregate Cs^+ from lab-scale volumes of LiCl-KCl molten salts.

The general approach developed for this process involves separating contaminated LiCl-KCl waste salt from purified LiCl-KCl molten salt with a selective ion-conducting ceramic membrane. When an electrochemical driving force is applied to the system, these engineered ion-conducting ceramics will allow Li^+ and K^+ ion transport from the contaminated salt to the purified salt, while blocking the transport of larger Cs^+ (or possibly divalent ions such as Sr^{2+}). This process will produce a volume of purified LiCl-KCl molten salt at the cathode, while concentrating contaminants in the reduced anodic salt volume. Ultimately, this contaminant-concentrated waste will be disposed of, but as a much smaller, more concentrated volume. In the interest of simplifying the technical challenges during these feasibility evaluations, the charge imbalance created by the selective cation transport through the ceramic membrane was balanced by oxidation of copper (Cu) metal at the anode and reduction of Cu^{2+} from dissolved CuCl_2 at the cell cathode. Ultimately, it is intended that copper be replaced with chlorine as the charge balancing reagent, and development of a reactor system compatible with chlorine gas at 500°C is underway.

Figure 72 shows schematically how ceramic pellets of these materials were used to demonstrate the volumetric isolation of Cs^+ from these molten salts. Ceramic pellets were assembled in 1/2-inch Swagelok® VCR fittings, sealing the interfaces of the ceramics with copper gaskets. These assemblies were placed in crucibles containing 30–50g of Cs-contaminated anodic LiCl-KCl molten salts and a copper anode (electrically-isolated from the VCR fitting). 5–7g of cathodic LiCl-KCl molten salt containing ~25 wt % CuCl_2 were placed inside the top of VCR fitting along with a copper cathodic current collector (electrically-isolated from the VCR fitting). The photograph in Figure 72 shows an assembled VCR-based reactor after a volumetric purification test.

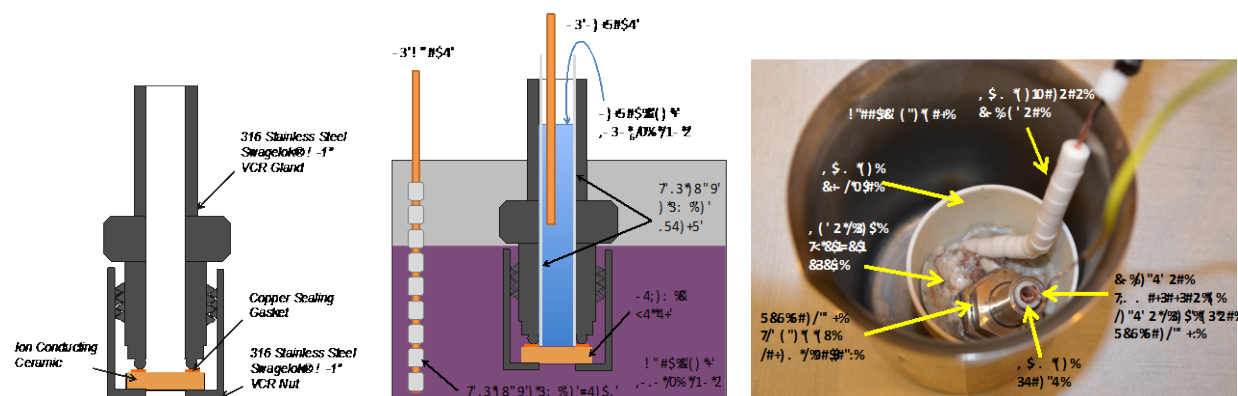


Figure 72. (Left) VCR-fitting schematic containing a ceramic pellet. (Middle) Scheme to use VCR-fitting with ceramic pellets for volumetric salt purification. (Right) Photograph of assembled VCR-device in molten salt (after cooling test device to room temperature).

The ceramic materials investigated using this system included NaSICON-type ceramics with the general structure $M_xZr_2(PO_4)_3$ and garnet-structured lithium lanthanum tantalate (LLTO) ceramics ($Li_5La_3Ta_2O_{12}$). The NaSICON-type materials evaluated include both a potassium-substituted variant of NaSICON ($KZr_2P_3O_{12}$) produced in house, as well as a commercial composition (Ceramtec, Inc.) The LLTO ceramics were synthesized in house, using a newly-developed LLTO synthesis that produced almost entirely phase pure LLTO ceramic pellets with densities exceeding 98.5% and Li^+ conductivity exceeding any previous reports for LLTO. While both NaSICON-based and LLTO ceramics were evaluated for electrochemical Cs^+ isolation from LiCl-KCl molten salt, only the LLTO samples will be discussed in detail here for conciseness.

Using the VCR-reactor configuration, a constant potential of -200mV was applied across the cell, driving ion transport through the system. Effective ion transport was evidenced both by the current measured in the system (Figure 73) as well as the macroscopic plating of copper observed at the cathode in “post-mortem” dissections of the test cells. While these observations indicate significant ion transport, elemental analyses of the anodic and cathodic molten salts “as made” and after discharge provide insight into ion-selectivity, central to effective volumetric salt-purification.

The bar graphs in Figure 73 compare the ratios of Cs:K in anodic and cathodic molten salts before and after discharge using an LLTO ceramic pellet. The ratio of Cs:K increased substantially at the anode with no significant Cs measured at the cathode (ratio was 1.64×10^{-4}). The increase in the ratio of Cs:K at the anode provides compelling evidence that K^+ was transported from the anode, while the Cs^+ was not, effectively concentrating the Cs^+ in the anodic molten salt. (Similar, corroborating data were observed for the Cs:Li ratio but are not shown for conciseness.) The notable absence of any significant Cs at the cathode is further evidence of the effective selectivity of the LLTO against Cs^+ transport. Similar results were observed using NaSICON-based ceramics, though the selectivity against Cs^+ was most pronounced with the LLTO ceramics.

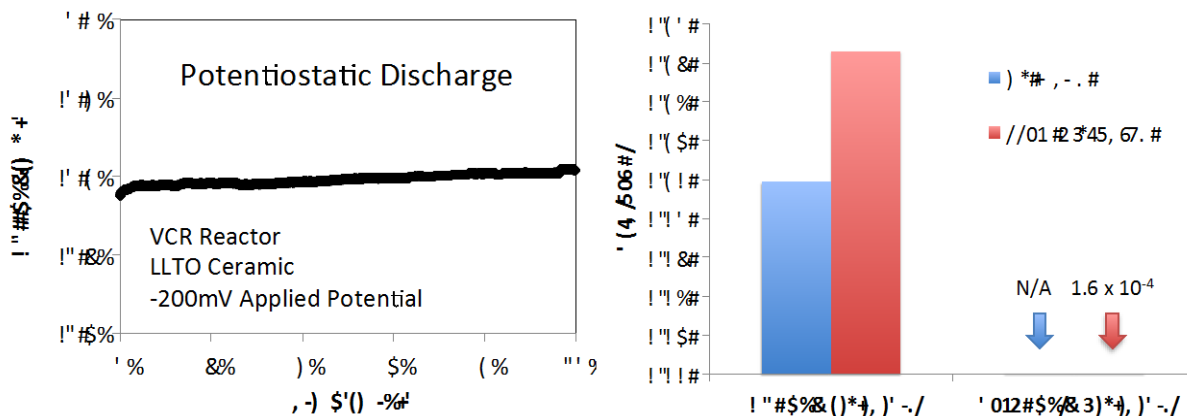


Figure 73. (Left) Potentiostatic discharge through and LLTO ceramic pellet. Constant applied potential was -200mV across the cell. Charge balance was maintained with Cu-chemistry.

These data provide compelling evidence that ion-selective ceramics can be used to segregate and concentrate Cs^+ in lab-scale volumes of contaminated LiCl/KCl molten salts. Moreover, the electrochemical nature of the approach makes it potentially compatible with existing pyroprocessing infrastructure with minimal anticipated disruption of the existing processes or waste stream development. In addition, because the consolidation and extraction of contaminants is electrochemically regulated, it is expected that the degree of contaminant concentration in waste salt could be controlled. Such control would facilitate manipulation of, for example, heat loading in waste designate for disposal.

Future studies to improve this system will involve not only more extensive characterization of the capacity and efficiency of the system, but may also involve development higher surface area ceramics, such as closed-end ceramic tubes, that would increase reaction kinetics and replace the VCR-fitting architecture. In addition, efforts should be committed to development of Cl_2 -compatible reaction vessels that would eliminate the need for additional oxidative or reductive species (such as Cu) in the system.

This page left intentionally blank



FUEL RESOURCES

SECTION 9

9. FUEL RESOURCES

S. Kung, Department of Energy

The Fuel Resources Program seeks to identify and implement actions to ensure that economic nuclear fuel resources remain available. The program will evaluate nuclear fuel resources and develop recovery technologies to enable a sustainable fuel cycle through increasing the fuel resources. Priority attention in the near term will focus on developing the technology for extraction of uranium from seawater.

9.1 Adsorbent Development, Ligand Design, Nanosynthesis, and Sorption Kinetics/Evaluation at Oak Ridge National Laboratory

C. J. Janke, T. Saito, R. T. Mayes, B. Hay, V. S. Bryantsev, C. Tsouris, S. Dai, P. F. Britt, Oak Ridge National Laboratory

The Fuel Resources Program at ORNL is divided into four subtasks: (1) adsorbent development, (2) computer-aided ligand modeling and design, (3) nanosynthesis, and (4) sorption kinetics/evaluation. Each subtask supports the overarching goal of developing advanced, high-capacity, durable adsorbents for extracting uranium from seawater at reduced cost and minimal operational and environmental risks. Marine testing of the adsorbents is carried out at PNNL's Marine Science Laboratory (MSL) located on the Olympic Peninsula in Washington State. The program benefits from collaboration with researchers from the JAEA who have supplied small quantities of their polyethylene-graft-poly (acrylic acid-co-amidoxime) adsorbent. This adsorbent is used as a benchmark and capacity target for the Fuel Resources Program.

Advanced Adsorbent Development by Radiation Induced Graft Polymerization (RIGP) focuses on increasing the adsorption capacity by increasing the surface area of the fiber adsorbents and optimizing the RIGP conditions and degree of grafting. This work built off the studies at JAEA, which focused on preparation of amidoxime-based polymers by RIGP of acrylonitrile with hydrophilic monomers on various trunk polymers. In our work, much of the effort focuses on increasing the capacity by optimizing the large number of experimental variables in the RIGP method, including the electron beam irradiation conditions, graft polymerization conditions and choice of monomers, amidoximation conditions, and alkaline conditioning variables of the grafted fibers. The resulting adsorbents are then tested for their capacity to bind uranium from seawater in marine tests at MSL/PNNL.

Ligand Design activities seek to increase the uranium adsorption capacity via the development of novel adsorbents that contain chelating sites with higher uranium binding affinity and selectivity than that exhibited in the current amidoxime-based adsorbents. A combined theoretical and experimental approach has been pursued to (1) better understand how current amidoxime-based adsorbents function; (2) identify novel chelating agents on the computer using state-of-the-art *de novo* structure-based design methods; (3) synthesize, characterize, and evaluate the performance of promising candidates in the laboratory; and (4) develop synthetic methods to allow chelate attachment to polymeric and high-surface-area materials.

Advanced Nanomaterials Synthesis activities seek to take advantage of the high surface areas of nanoporous materials ($>1,000 \text{ m}^2/\text{g}$) to generate a new class of high-capacity adsorbents that can be functionalized with ligands to selectively bind uranium. This approach toward a nanostructured alternative to polyethylene fibers focuses on two classes of material: (1) carbon-based nanostructures and (2) polymeric nanostructures. A key focus and challenge in this work is to increase grafting yields.

The **Sorption Kinetics/Evaluation** subtask seeks to understand and optimize the kinetics of the uranium adsorption. This includes understanding the mechanism of adsorption and the role of hydrophilicity, and integrating with the synthesis subtasks to develop better adsorbents.

Accomplishments

Adsorbent development has focused on two fronts: (1) RIGP and (2) controlled living polymerization via atom transfer radical polymerization (ATRP). In the RIGP task, the focus has been on developing and testing braided adsorbents. Several braided and woven fabrics were generated at Steeger USA (Inman, SC) and Philadelphia University (Philadelphia, PA). The braided adsorbents consisted of the hollow-gear polyethylene produced by Hills, Inc. (West Melbourne, FL). After irradiation at NEOBeam (Middlefield, OH), the braided and nonwoven fabrics were amidoximated and sent to MSL/PNNL for marine testing. The braided adsorbents were tested in a flume under flowing conditions to simulate oceanic deployment.

The original 38H series adsorbent has been replaced by the higher capacity AF1 series. The difference between the two series of adsorbents is that a different carboxylic acid monomer was utilized. The adsorbent has also been braided and tested under flume studies at MSL/PNNL. Figure 74 shows the change in the color of the braids over time within the flume. Figure 75 relates the time series data for several AF1 series adsorbents from column testing. In 56 days, the capacity was reported at 3.85 mg-U/g-ads. Vanadium still dominates the metals with approximately 3x the amount compared to uranium. A third series of adsorbents, AI8, based on a phosphonic acid copolymer, is currently under testing.

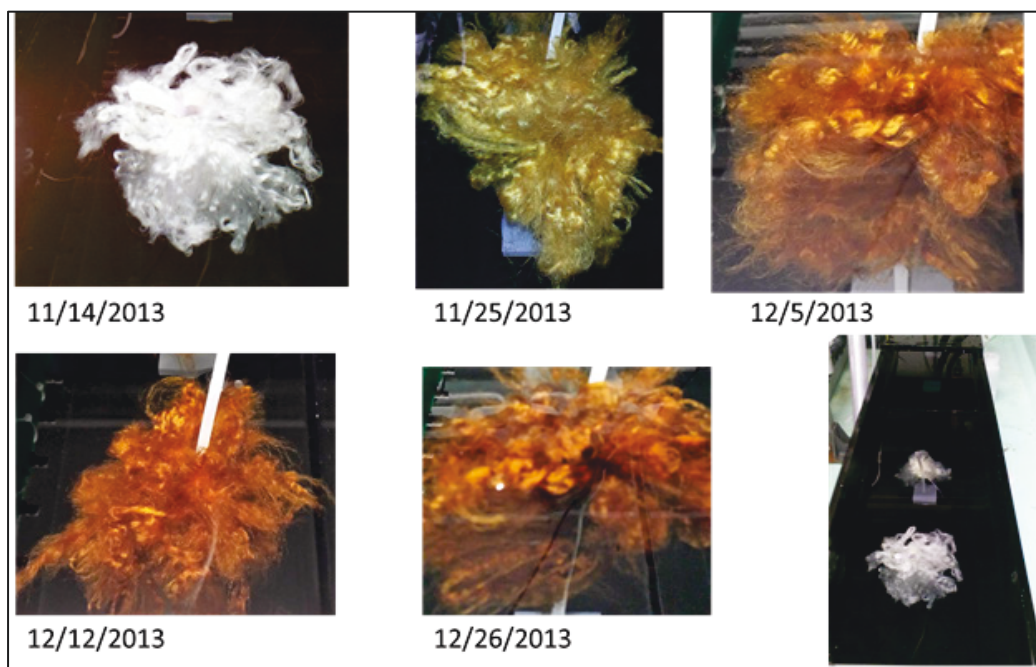


Figure 74. Flume studies of the AF1 adsorbent showing color changes over time. The flume in use is shown in the bottom right.

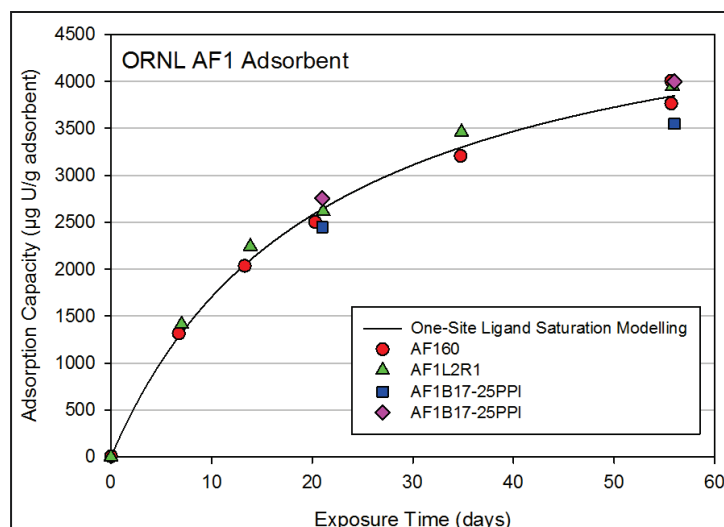


Figure 75. Time series marine testing of the AF1 series adsorbent

A second focus of the advanced adsorbent task was on a novel chemical grafting method to prepare polymeric fiber adsorbents. Although polymeric fiber adsorbents have several advantages including: (1) already proven to be deployable in seawater; (2) light weight; (3) easy to fabricate to various shapes and lengths, the RIGP method does not provide the ability to fine-tune its composition, degree of grafting (DOG), conformation, and morphology. Therefore, this task explored a novel chemical grafting technology to synthesize adsorbents for potential improvement and cost savings. The method employed is ATRP, which allows controlled radical polymerization. ATRP offers several advantages, including controllable composition and degree of polymerization (length of graft chains) and can either provide a much higher DOG or prepare the exact DOG for the best performance.

To demonstrate the capabilities of this novel approach, a hybrid method of RIGP and ATRP was first used to prepare polymeric fiber adsorbents (Figure 76A). In the hybrid method, RIGP-grafted poly(vinylbenzyl chloride) (PVBC) fibers were prepared and then PVBC initiation sites were utilized for ATRP. The RIGP-ATRP hybrid method (1) demonstrated a relatively high DOG (several thousands) of ligand-forming monomer and hydrophilic monomer; (2) showed there is a fine balance between ligand density and hydrophilicity; (3) showed that uranium adsorption kinetics in seawater was impeded due to the crowded brush structure, although it showed modest capacity; and (4) identified the importance of the conformation of graft chains. This RIGP-ATRP hybrid approach resulted in one invention disclosure and a publication (Saito et al. 2014).

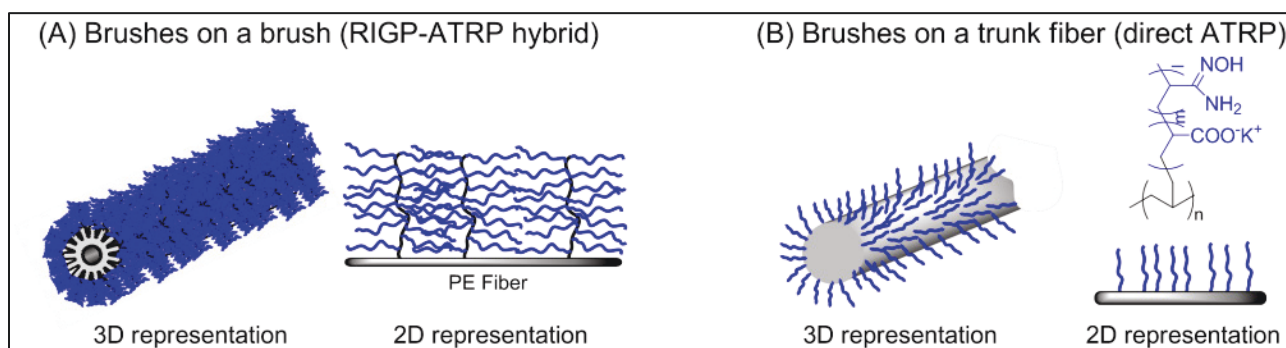


Figure 76. RIGP-ATRP hybrid method (A), direct ATRP method (B)

A second approach employed direct chemical grafting on a readily available fiber via ATRP (Figure 76B). This strategy eliminates the RIGP step, simplifying the process and reducing the cost. The experimental conditions were varied to optimize the capacity. The direct ATRP strategy successfully achieved high capacity and fast kinetics in seawater tests. The achieved capacity met M2 milestone entitled “Complete new adsorbent materials for marine testing to demonstrate 4.5 g-U/kg ads.” A recent preliminary cost analysis also showed \$553/kg uranium, which is the most cost-effective technology to-date for uranium extraction from seawater. One invention disclosure has been filed, and a manuscript is under preparation.

The Nanomaterials Synthesis subtask focuses on increasing the graft density onto carbon materials. This work utilized an oxidized PAN fiber, supplied by Toho America, and translated into a high-capacity adsorbent with capacities approaching 5 mg-U/g-adsorbent (for 35 psu seawater) in 56 days. Interestingly, at 20 days, the capacity was 80 % of the final capacity, indicating fast kinetics as well. Vanadium was the predominant metal present on the adsorbent, at nearly 7x that of uranium for this adsorbent.

The Ligand Design subtask presented the highest suggested uranyl binding ligand yet (Figure 77) using a bisamidoxime ligand. The bisamidoxime has a calculated binding affinity higher than the previously reported bis(imidedioximes). Working with the Graft Polymerization subtask, polymers were generated that allow anchoring the ligands onto a polymeric support for marine testing. “Click” chemistry is used to anchor the ligands onto the fiber. The fiber has been grafted with vinylbenzyl chloride, which is post-functionalized to the azide. The ligand has been functionalized with an alkyne. The ligand is then “clicked” onto the polymer fiber using a copper catalyst. Grafting of the new ligands is currently in progress.

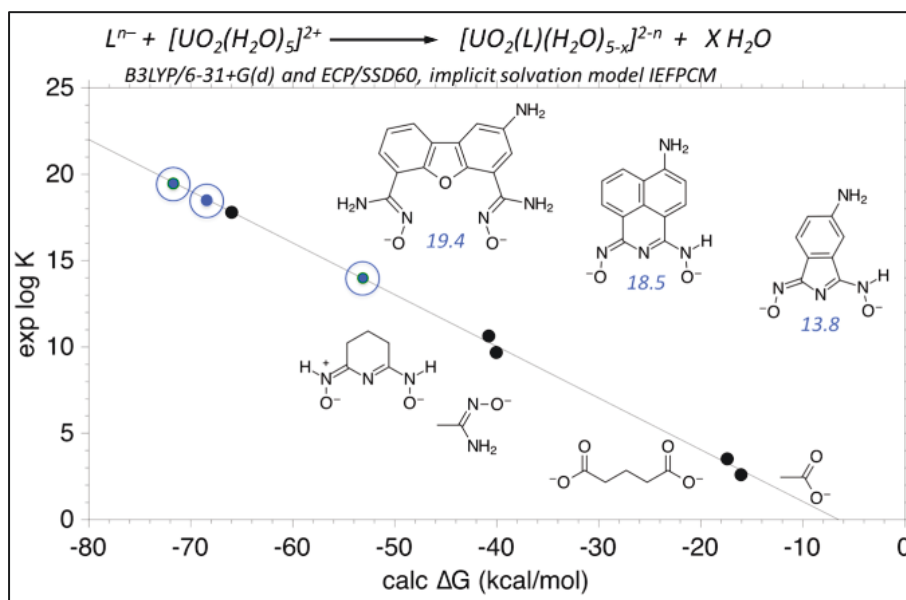


Figure 77. Calculated binding energies of some uranyl chelators.

The Kinetics/Evaluation subtask focused on (1) optimization of adsorbent conditioning parameters using a uranium screening solution, (2) influence of various parameters such as bicarbonate concentration, uranium concentration, adsorbent capacity, and presence of divalent ions and salt on uranium uptake kinetics, and (3) mechanistic modeling of the micro-scale processes that control uranium uptake. These topics are discussed in more detail below.

(1) Optimization of Adsorbent Conditioning Parameters: Alkaline conditioning of the adsorbent has been essential in preparing the adsorbent for uranium uptake. Samples of the same batch of ORNL adsorbent have been treated with KOH at various conditions and then tested with uranium screening solution. Results shown in Figure 78 demonstrate the following trend for the adsorbent performance: to $0.6\text{ M} > 0.44\text{ M} > 0.2\text{ M}$. For 0.2 M and 0.44 M KOH, 3 hours treatment is better than 2 hours, and that is better than 1 hour treatment. Also, for 0.44 M KOH, which is the concentration used by investigators at JAEA, treatment at 60°C for 3 hours is as good as treatment at 70 and 80°C for 3 hours or treatment with 0.6 M KOH for 3 hours.

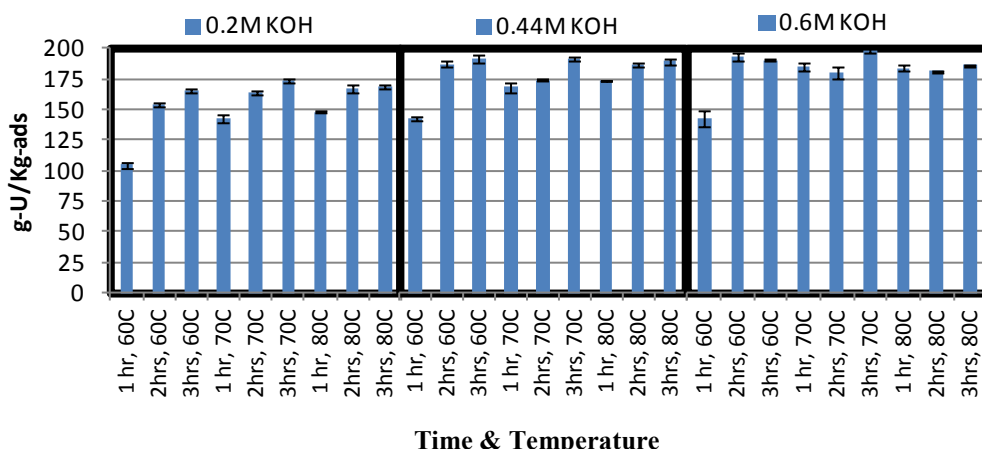


Figure 78. Performance comparison of adsorbent treated with KOH at different conditions and tested with uranium screening solution.

The performance of adsorbent treated with KOH was compared to the performance of adsorbent treated with NaOH at similar concentrations, temperature, and duration and no difference was found. This result is important because alkaline conditioning is a significant cost driver. NaOH is half the price of KOH per unit mass, therefore replacement of KOH by NaOH could lead to a reduction of cost per unit mass of uranium produced on the order of 27%. This study will continue in FY 2015, with the objective to confirm the results with seawater and quantify the impact of NaOH treatment on the adsorbent performance.

(2) Kinetic Study: The influence of various parameters including bicarbonate concentration, uranium concentration, adsorbent uranium capacity, and presence of divalent ions and salt on uranium uptake kinetics has been investigated in 5-gallon and 1-L batch experiments. Results showed that the concentration of bicarbonate ions plays an important role on uranium uptake kinetics. For example, the concentration of uranium in water in the presence of bicarbonate at the same concentration as in seawater needed 6 weeks to drop from 10 ppm to 4 ppm. In the absence of bicarbonate ions, however, it took only one day for the concentration to drop from 10 ppm to 4 ppm. This result shows that there is a strong competition between bicarbonate ions and amidoxime ligand with respect to complexation with uranyl ions. Addition of sodium chloride at the same concentration as in seawater slowed the uranium uptake by the adsorbent. Addition of sodium ortho-vanadate did not have a strong effect on uranium uptake kinetics, while addition of divalent ions of calcium and magnesium at the concentrations in seawater moderately slowed the uranium uptake rate. Finally, the use of higher uranium capacity adsorbent accelerated the uranium adsorption rate.

(3) Mechanistic Modeling of Uranium Adsorption: We have reported in the past that uranium uptake by the adsorbent is reaction limited. Our kinetic study revealed that the reason we have a reaction-limited

process is the competition of amidoxime with bicarbonate ions. In the absence of bicarbonate ions, uranium uptake by the adsorbent is not reaction limited because the competition is removed. For this case, we can use a diffusion model to describe the uranium uptake and estimate the diffusivity within the adsorbent. The estimated diffusivity from a kinetic experiment conducted without bicarbonate ions present was $7 \times 10^{-11} \text{ m}^2/\text{day}$.

Publications

1. Yue, Y.F.; Mayes, R.T.; Kim, J.; Fulvio, P.F.; Sun, X.G.; Tsouris, C.; Chen, J.; Brown, S.; Dai, S., "Seawater uranium sorbents: Preparation from a mesoporous copolymer initiator by Atom-Transfer Radical Polymerization," *Angewandte Chemie International Edition*, 52(50), 2013, 13458-13462.
2. Kim, J., Oyola, Y., Tsouris, C., Cole, C.R., Mayes, R.T., Janke, J.C., Dai, S. "Characterization of uranium uptake kinetics from seawater in batch and flow-through experiments," *Industrial & Engineering Chemistry Research*, 52, 2013, 9433-9440.
3. Yue, Y.F., Xun, X.G., Mayes, R.T., Kim, J., Fulvio, P.F., Ziao, Z.A., Brown, S., Tsouris, C., Oyola, Y., Dai, S., "Polymer-coated nanoporous carbons for trace seawater uranium adsorption," *Science China Chemistry*, 56(11), 2013, 1510-1515.
4. Kim, J., Tsouris, C., Oyola, Y., Janke, C.J., Mayes, R.T., Dai, S., Gill, G., Kuo, L.-J., Wood, J., Choe, K.-Y., Schneider, E., and Lindner, H., "Uptake of uranium from seawater by amidoxime-based polymeric adsorbent: Field experiments, modeling, and economic assessment," *Industrial & Engineering Chemistry Research*, 53, 2014, 6076-6083.
5. Saito, T., Brown, S., Chatterjee, S., Kim, J., Tsouris, C., Mayes, R., Kuo, L.-J., Gill, G., Oyola, Y., Janke, C.J., and Dai, S., "Uranium Recovery from Seawater: Development of Fiber Adsorbents Prepared via Atom-Transfer Radical Polymerization," *Journal of Materials Chemistry A*, 2, 2014, 14674-14681.
6. Sun, X., Tian, G., Xu, C., Rao, L., Vukovic, S., Kang, S. O., Hay, B. P. "Quantifying the binding strength for U(VI) with phthalimidedioxime in comparison with glutarimidedioxime." *Dalton Transactions*, 43(2), 2014, 551-557. (Vukovic and Rao are co-corresponding authors)
7. Pan, H.B., Liao, W.S., Wai, C.M., Oyola, Y., Janke, C.J., Tian, G.X., Rao, L.F., *Dalton Transactions*, 43(28), 2014, 10713-10718.

Patents

1. Janke, C.J., Dai, S., Oyola, Y. "Fiber-based adsorbents having high adsorption capacities for recovering dissolved metals and methods thereof," U.S. Patent Number: 8,722,757, issued May 13, 2014.

Invention Disclosures

1. Dai, Sheng, Yue, Yanfeng, Mayes, Richard. "Nanoporous polymer composites for heavy metal extraction and/or remediation." UT-Battelle Invention Disclosure 201303112.
2. Mayes, Richard T., Górka, Joanna, Dai, Sheng. "Preparation of carbon fiber-based adsorbents for uranium recovery from seawater by surface initiated ARGET ATRP." UT-Battelle Invention Disclosure 201403304.
3. Saito, T., Brown, S., Dai, S. "Fast and Efficient Uranium Adsorbents Prepared via Controlled Radical Polymerization" UT-Battelle Invention Disclosure 201403369.

9.2 Thermodynamic, Kinetic, Coordination and Structure Characterization at the Lawrence Berkeley National Laboratory

L. Rao, Lawrence Berkeley National Laboratory

In FY 2014, three major tasks were performed, including (1) thermodynamic studies of the interaction between Ca(II)/Mg(II) and the triscarbonato uranyl species; (2) thermodynamic studies of the interactions between Ca(II)/Mg(II) and glutarimidedioxime; and (3) preliminary investigation of the binding strength of vanadium with glutarimidedioxime and evaluation of the competition between U(VI) and V(V) for binding amidoxime ligands.

The data on the interactions of Ca(II)/Mg(II) with $\text{UO}_2(\text{CO}_3)_3^{4-}$ are of particular importance, because they show that the dominant U(VI) species under seawater conditions is not the anionic $\text{Ca}_2\text{UO}_2(\text{CO}_3)_3^{4-}$ species suggested by the previous literature, but the neutral complex, $\text{Ca}_2\text{UO}_2(\text{CO}_3)_3(\text{aq})$ (~ 60%). The results have important implications in the design of effective sorbents to extract uranium from seawater.

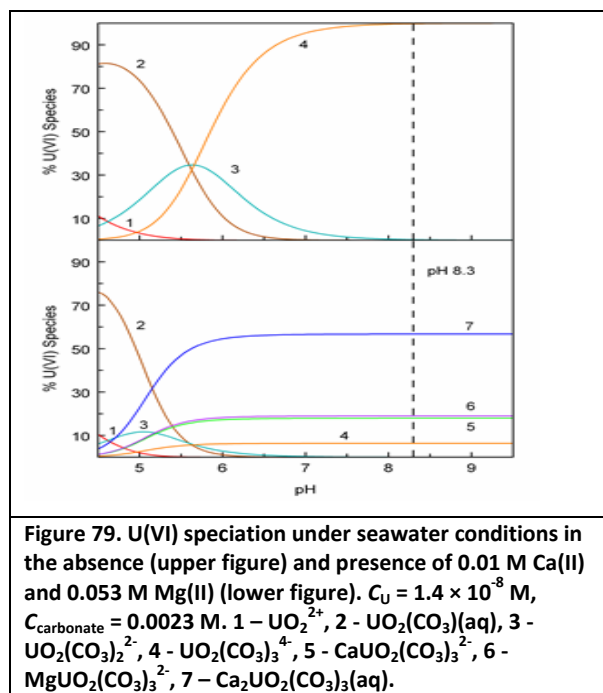
Table 13. Equilibrium constants and enthalpy of Ca/Mg complexation with $\text{UO}_2(\text{CO}_3)_3^{4-}$.

Reaction	$\log \beta \pm \sigma$			$\Delta H \pm \sigma$, kJ/M
	$I = 0 \text{ M}$	$I = 0.1 \text{ M NaCl}$	$I = 0.5 \text{ M NaCl}$	
$\text{Ca}^{2+} + \text{UO}_2(\text{CO}_3)_3^{4-} = \text{CaUO}_2(\text{CO}_3)_3^{2-}$	5.15 ± 0.06	3.42 ± 0.06	2.43 ± 0.10	$-(8 \pm 6)$
$2\text{Ca}^{2+} + \text{UO}_2(\text{CO}_3)_3^{4-} = \text{Ca}_2\text{UO}_2(\text{CO}_3)_3(\text{aq})$	9.00 ± 0.06	6.42 ± 0.06	4.96 ± 0.10	$-(8 \pm 7)$
$\text{Mg}^{2+} + \text{UO}_2(\text{CO}_3)_3^{4-} = \text{MgUO}_2(\text{CO}_3)_3^{2-}$	4.41 ± 0.06	2.69 ± 0.06	1.77 ± 0.10	

Stability constants and enthalpy of complexation: The stability constants of the complexation between Ca(II)/Mg(II) and $\text{UO}_2(\text{CO}_3)_3^{4-}$ were determined by Ca(II) selective electrode potentiometry and spectrophotometry, respectively [1]. The enthalpy of complexation for Ca(II)/ $\text{UO}_2(\text{CO}_3)_3^{4-}$ was determined by microcalorimetry. The obtained data are shown in Table 13.

Speciation of U(VI) under seawater conditions:

Though the complexation between Ca/Mg and $\text{UO}_2(\text{CO}_3)_3^{4-}$ is fairly weak, the speciation of U(VI) in seawater could be affected due to the high concentrations of Ca and Mg relative to U(VI) in seawater ($[\text{Ca(II)}] = 0.01 \text{ M}$, $[\text{Mg(II)}] = 0.053 \text{ M}$, and $[\text{U(VI)}] = 1.4 \times 10^{-8} \text{ M}$). Consequently, neglecting the formation of Ca/Mg complexes with $\text{UO}_2(\text{CO}_3)_3^{4-}$ could probably lead to erroneous speciation of U(VI) under seawater conditions. As shown in Figure 79, when pH is above 6, the aqueous chemistry of U(VI) in the presence of Ca(II) (0.01 M) and Mg(II) (0.053 M) is dominated by the formation of the $\text{M}_n\text{UO}_2(\text{CO}_3)_3^{2(2-n)-}$ ($\text{M} = \text{Ca}$ or Mg , and $n = 1$ or 2) complexes. In particular, at the seawater pH (8.2), $\text{Ca}_2\text{UO}_2(\text{CO}_3)_3(\text{aq})$ accounts for 58% of the total uranium in solution, $\text{CaUO}_2(\text{CO}_3)_3^{2-}$ and $\text{MgUO}_2(\text{CO}_3)_3^{2-}$ 18% each, and $\text{UO}_2(\text{CO}_3)_3^{4-}$ only 6%. In contrast, more than 97% of U(VI) would exist as $\text{UO}_2(\text{CO}_3)_3^{4-}$ if



the formation of Ca/Mg complexes with $\text{UO}_2(\text{CO}_3)_3^{4-}$ was neglected, as shown in the upper speciation diagram of Figure 79 [2]. Understanding the speciation of U(VI) under seawater conditions is of great significance in the development of strategies for the extraction of uranium from seawater. Since the dominant species of U(VI) is the neutral complex, $\text{Ca}_2\text{UO}_2(\text{CO}_3)_3(\text{aq})$, instead of the highly negatively charged $\text{UO}_2(\text{CO}_3)_3^{4-}$ as previously believed, the sorbents must be able to interact with $\text{Ca}_2\text{UO}_2(\text{CO}_3)_3(\text{aq})$ effectively to achieve efficient collection [2].

Table 14. Stability constants of calcium, magnesium, and uranium complexes with glutarimidedioxime (denoted as H_2L in the table)

Reaction	Log β	ΔH , kJ/M	ΔS , J/M/K
$\text{Ca}^{2+} + \text{L}^{2-} \rightarrow \text{Ca}(\text{L})$	2.44 ± 0.02	10.5 ± 4	82 ± 13
$\text{UO}_2^{2+} + \text{L}^{2-} \rightarrow \text{UO}_2(\text{L})$	17.8 ± 1.1		
$\text{Ca}^{2+} + \text{H}^+ + \text{L}^{2-} \rightarrow \text{Ca}(\text{HL})^+$	14.56 ± 0.02	-30.3 ± 4	117 ± 13
$\text{Mg}^{2+} + \text{H}^+ + \text{L}^{2-} \rightarrow \text{Mg}(\text{HL})^+$	14.40 ± 0.04		
$\text{UO}_2^{2+} + \text{H}^+ + \text{L}^{2-} \rightarrow \text{UO}_2(\text{HL})^+$	22.7 ± 1.3		
$\text{Ca}^{2+} + \text{H}^+ + 2\text{L}^{2-} \rightarrow \text{Ca}(\text{HA})(\text{L})^-$	17.27 ± 0.06	-29.9 ± 0.7	230 ± 3
$\text{Mg}^{2+} + \text{H}^+ + 2\text{L}^{2-} \rightarrow \text{Mg}(\text{HA})(\text{L})^-$	18.56 ± 0.15		
$\text{UO}_2^{2+} + \text{H}^+ + 2\text{L}^{2-} \rightarrow \text{UO}_2(\text{HA})(\text{L})^-$	36.8 ± 2.1		

Interactions between Ca(II)/Mg(II) and glutarimide-dioxime. Potentiometric and calorimetric titrations were performed to determine the stability constants of Ca(II) and Mg(II)/complexes with glutarimide-dioxime and the enthalpy of complexation. It was found that the complexation of Ca(II) and Mg(II) with glutarimide-dioxime is significantly weaker than those of U(VI), as shown in Table 14.

Interactions between vanadium(V) and glutarimide-dioxime. Potentiometric titrations were performed to evaluate the binding interactions of V(V) with glutarimide-dioxime. The tentative stability constants of V(V)/glutarimide-dioxime complexes are listed in Table 15, in comparison with those of U(VI).

Table 15. Comparison of the stability constants of V(V) and U(VI) complexes with glutarimide-dioxime (denoted as H_2L in the table)

Overall Reaction	Log β
$\text{VO}_2^+ + \text{L}^{2-} \rightarrow \text{VO}_2(\text{L})^-$	(~26-27)
$\text{UO}_2^{2+} + \text{L}^{2-} \rightarrow \text{UO}_2(\text{L})$	17.8 ± 1.1
$\text{VO}_2^+ + \text{H}^+ + \text{L}^{2-} \rightarrow \text{VO}_2(\text{HL})$	31.56 ± 0.06
$\text{UO}_2^{2+} + \text{H}^+ + \text{L}^{2-} \rightarrow \text{UO}_2(\text{HL})^+$	22.7 ± 1.3
$\text{VO}_2^+ + 2\text{H}^+ + 2\text{L}^{2-} \rightarrow \text{VO}_2(\text{HL})_2^-$	54.96 ± 0.04
$\text{UO}_2^{2+} + 2\text{H}^+ + 2\text{L}^{2-} \rightarrow \text{UO}_2(\text{HL})_2$	43.0 ± 1.1
$\text{VO}_2^+ + \text{H}^+ + 2\text{L}^{2-} \rightarrow \text{VO}_2(\text{HL})(\text{L})^{2-}$	48.52 ± 0.06
$\text{UO}_2^{2+} + \text{H}^+ + 2\text{L}^{2-} \rightarrow \text{UO}_2(\text{HL})(\text{L})^-$	36.8 ± 2.1
$\text{VO}_2^+ + 2\text{L}^{2-} \rightarrow \text{VO}_2(\text{L})_2^{3-}$	38.24 ± 0.07
$\text{UO}_2^{2+} + 2\text{L}^{2-} \rightarrow \text{UO}_2(\text{L})_2^{2-}$	36.0 ± 1.1

The stability constants for the vanadium complexes with glutarimide-dioxime are at least 8 orders of magnitude stronger than the analogous uranyl complexes as indicated in Table 14. Furthermore, as indicated by the potentiometric data, vanadium forms complexes with glutarimide-dioxime over a large range of pH values, which may complicate the efforts to remove vanadium from the polymeric fibers that are being developed to sequester uranium.

References

1. Gans, P., Sabatini, A., and Vacca, A., "Investigation of equilibria in solution. Determination of equilibrium constants with the HYPERQUAD suite of programs," *Talanta*, 43(10), 1996, 1739-1753.
2. Endrizzi, F., and Rao, L., "Formation of Ca^{2+} and Mg^{2+} complexes with $(\text{UO}_2)(\text{CO}_3)_3^{4-}$ in aqueous solution: Effect on the speciation of U(VI) and its extraction from marine environments," *Chemistry: A European Journal*, in press.

Publications

1. Pan, H-B., Liao, W., Wai, C. M., Oyola, Y., Janke, C., Tian, G., and Rao, L., "Carbonate- H_2O_2 leaching for sequestering uranium from seawater," *Dalton Transactions*, 43(28), 2014, 10653–11078.
2. Sun, X., Tian, G., Xu, C., Rao, L., Vukovic, S., Kang, S. O., and Hay, B. P., "Quantifying the binding strength of U(VI) with phthalimidedioxime in comparison with glutarimidedioxime: Implications in the extraction of U(VI) from seawater with amidoxime-based sorbents," *Dalton Transactions*, 43(2), 2014, 551-557.
3. Sun, X., Xu, C., Tian, G., and Rao, L., "Complexation of glutarimidedioxime with Fe(III), Cu(II), Pb(II), and Ni(II), the competing ions for the sequestration of U(VI) from seawater," *Dalton Transactions*, 42, 2013, 14621-14627.

9.3 Adsorbent Characterization, Durability, Toxicity, and Deployment Studies at the Pacific Northwest National Laboratory

G. A. Gill, L. J. Kuo, J. R. Wood, J.E. Strivens, M. E. Cobb, G. Bonheyo, R. T. Jeters, J. Park, T. P. Khangaonkar, S. R. Addleman, M. G. Warner, and S. M. Peterson, Pacific Northwest National Laboratory

The uranium from seawater program at the MSL/PNNL has five subtask areas: (1) Determination of Adsorbent Capacity and Adsorption Rate; (2) Adsorbent Characterization; (3) Biofouling and Toxicity Testing; (4) Material Durability; and (5) Marine Deployment Assessment. The effort at PNNL began in FY 2012 and is being conducted in coordination with ORNL, LBNL, University partners (City University of New York, University of Alabama, and the University of Maryland), and an international collaboration with Japan and China. PNNL receives uranium adsorbent materials developed by program participants and conducts independent testing with natural seawater at realistic marine conditions.

Determination of Adsorbent Capacity and Adsorption Rate. In FY 2014, the major focus of this task was characterizing adsorbent capacity and adsorption rate for the new

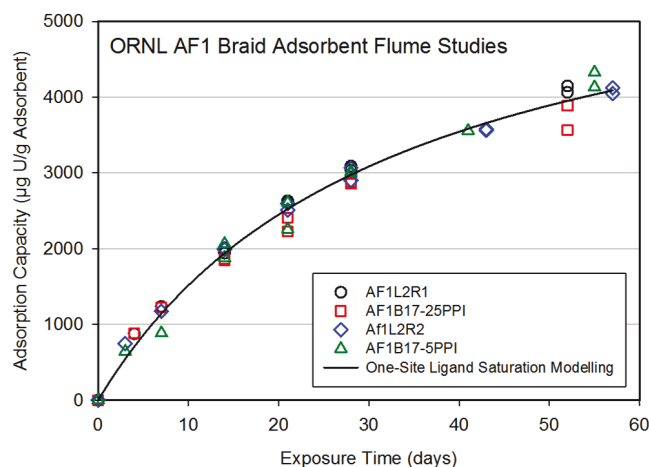


Figure 80. Time-series measurements of uranium adsorption capacity determined using flume exposure studies for 4 different formulations of the amidoxime-based adsorbent AF1 produced by ORNL. Data have been normalized to a salinity of 35 psu.

formulation of the amidoxime-based adsorbent produced by ORNL referred to as AF1. MSL received this adsorbent in braided form and conducted tests of adsorption capacity and adsorption rate using both column studies and also using the new flume developed this year for testing of braided material. Column studies were conducted using sample “snips” cut off the braided material.

The results obtained for four different formulations of the AF1 adsorbent determined using both column and flume exposure methods are shown in Figure 80. The two different exposure methods yielded very similar results for adsorption capacity (see Table 16), providing confidence in the testing methods. The ORNL AF1 adsorbent has about a 17% higher adsorbent capacity at 56 days of exposure than the previous ORNL 38H adsorbent investigated last year.

Adsorbent Characterization. A major characterization effort in FY 2014 was the assessment of the effect of temperature on adsorbent capacity. Time-series experiments under controlled laboratory conditions were conducted with three separate formulations of the ORNL amidoxime-based polymeric adsorbent (38H, AF1 and AI8) to assess the impact of adsorption capacity due to temperature. Experiments were conducted by loading the adsorbent into columns and exposing the fibers to filtered ambient seawater at several different temperatures, representative of conditions typically found in the coastal ocean (8-32 °C). Adsorption kinetics and adsorption capacity ($\mu\text{g U/g adsorbent}$) were assessed using time series determinations of uranium adsorption and one-site ligand saturation modelling.

Table 16. Comparison of 56-day adsorption capacity ($\mu\text{g U/g adsorbent}$)¹ for the ORNL AF1 adsorbent determined using both column and flume exposure methods

Adsorbent	Column	Flume ²
AF1L2R2	3950	4300 \pm 190
AF1B17-25PPI	3840	3800 \pm 330
AF1L2R2	4000	4200 \pm 180
AF1B17-5PPI	3950	4230 \pm 470

¹Normalized to a salinity of 35 psu

²Predicted using one-site ligand saturation modelling

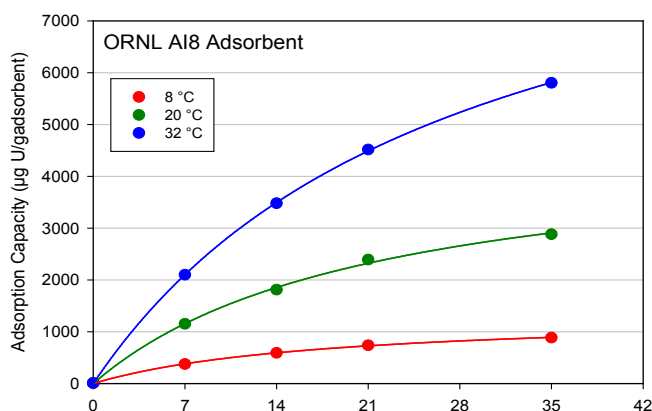


Figure 81. Time series measurements of adsorbent capacity are shown for three different temperatures with the ORNL adsorbent AI8. Lines drawn through the data points were generated with a one-site ligand saturation model. Data were normalized to a salinity of 35 psu.

All three adsorbents showed higher adsorption capacities as a function of temperature. Illustrated in Figure 81 are the time series measurements of adsorption capacity for the AI8 adsorbent, which had the highest temperature response. In all three experiments, a strong, fairly linear, relationship was observed between temperature and adsorption capacity; as the temperature increased, so did the adsorption capacity (see Figure 82).

However, the three adsorbent formulations showed different temperature responses. For the ORNL 38H, AF160 and AI8 adsorbents, the adsorbent capacity increased 40, 180, and 205 $\mu\text{g U/g adsorbent}/1^\circ\text{C}$, respectively (see Figure 82). These results illustrate quite clearly that

warmer waters increase the adsorption capacity performance of the adsorbent, and quite markedly. To illustrate, deploying the AI8 adsorbent in 32 °C seawater, compared to 20 °C seawater, results in a 200 % increase in adsorption capacity (from 2880 to 5800 $\mu\text{g U/g adsorbent}$) after 35 days of exposure.

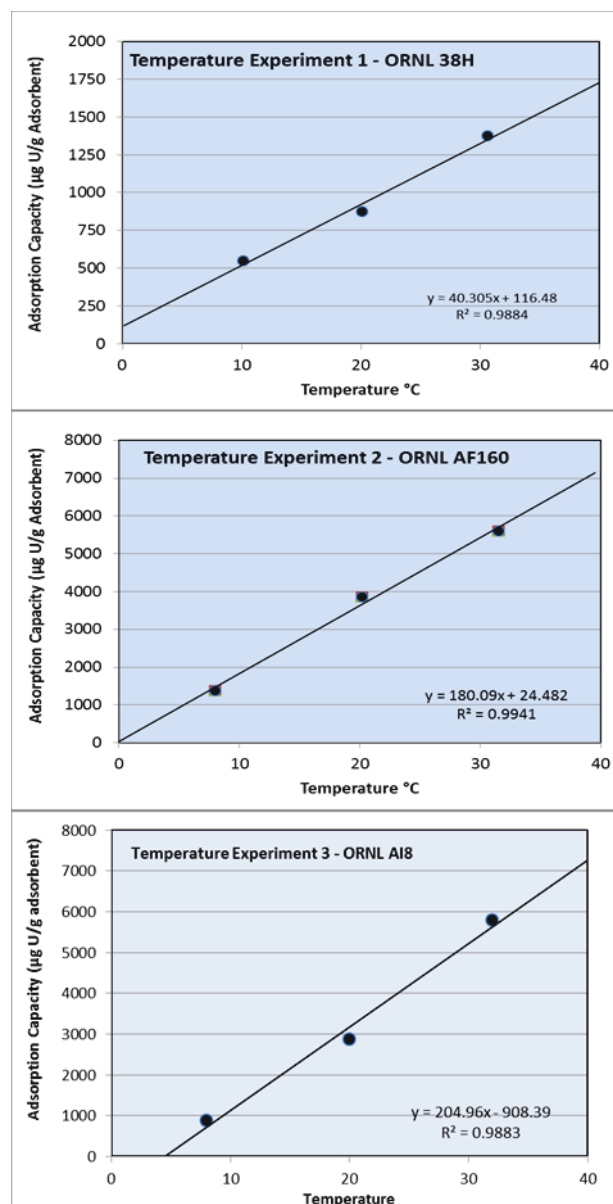


Figure 82. Temperature dependence on adsorption capacity. For experiments 1 and 2, the adsorption capacity represents 56 days of exposure. The data points for experiment 3 represent 35 days of exposure. The 32 degree point capacity for experiment 2 was taken from a separate biofouling experiment run concurrently with the temperature experiment. Data were normalized to a salinity of 35 psu.

All three temperature experiments further suggest that the rate of adsorbent saturation is also affected by temperature, the warmer the water, the slower the saturation kinetics (see Table 17). The one value that does not fit the trend well is the 20°C value for the 38H adsorbent. However, notice that the standard deviation on determination is larger than the other determinations. Hence, the trend may still be one of increasing half-saturation time with temperature. An alternative explanation is that the half-saturation times are a function of adsorption capacity. As adsorption capacity increases, the half-saturation times increase proportionally.

The ORNL AF1 adsorbent material was characterized for its ability to sequester a range of other elements (see Table 18). It is clear that the AF1 amidoxime-based adsorbent material is not element specific. The bulk of the adsorption sites are occupied by the major doubly charged cations in seawater. Uranium only occupies about 0.6% of the total adsorption sites.

Table 17. Effect of temperature on adsorbent kinetics for three adsorbent materials. Values in the table represent the half-saturation time in days

Adsorbent	8 °C	20 °C	32 °C
38H	12.9± 3.3	10.5± 4.5	15.4
AF1	15.7± 1.6	22.6± 2.3	
AI8	17.7± 1.0	21.3± 2.2	27.7± 0.6

Table 18. ORNL AF1 adsorbent characterization – elemental specificity

Element	Adsorption Capacity ($\mu\text{mol g adsorbent}$)	mol %
Mg	1000	37
Ca	590	22
Na	708	26
V	293	11
Fe	34.9	1.3
Zn	24.3	.89
K	20.5	.75
U	16.6	.61
Cu	16.3	.60
Ni	8.37	.31
Sr	2.25	.083
Ti	2.45	.090
Cr	0.631	.023
Co	0.520	.019
Mn	0.431	.016
Mo	0.119	.004
Sum	2718	1000

Biofouling and Toxicity Testing. The authors conducted a literature review to determine whether deployment of a farm of adsorbent material to mine uranium from seawater that resulted in significant removal of uranium from seawater would result in any adverse impacts on marine organisms. The review could find no published documents that would suggest that uranium removal might be adverse to marine life.

The ORNL fiber AF1L2R2 was fouled with the benthic diatom *Navicula incerta* (UTEX 2044) and then exposed to filtered seawater for 42 days to test the effect of fouling on uranium adsorption capacity. Preliminary results suggest that adsorption capacity was approximately 15% less compared to the non-fouled control.

The toxicity of uranium adsorbent materials and seawater effluent from uranium uptake columns was evaluated at multiple concentrations using the Microtox test in order to determine if these materials have any toxic effects on marine organisms. The microtox test is utilized by the

Environmental Technology Verification Program (ETV) for detecting toxicity in drinking water and by the EPA for toxicity testing of aquatic sediments. The test uses a marine organism to test toxicity. Five out of 10 sorbent materials showed toxicity (defined as an EC50), but only when the concentration of adsorbent was taken to unrealistic concentration levels. All seawater effluent samples from 47 different uranium extraction columns showed no toxic effects.

Material Durability. PNNL and Dr. Chien Wai of the University of Idaho collaborated in FY 2014 to assess the ability of bicarbonate solutions to selectively remove uranium from amidoxime-based adsorbent materials that were exposed to seawater. Initial results suggest that 3M bicarbonate can selectively remove uranium from amidoxime-based adsorbent material exposed to seawater for 56 days with greater than 90% efficiency. The bicarbonate extraction medium did not remove Fe, V, Cu, Ni and other trace elements from the adsorbent. Experiments are underway to assess how efficient the process is with multiple exposure/stripping cycles.

Marine Deployment Assessment. A major task that began in FY 2013 and concluded in FY 2014 was an assessment of the impact of the deployment of a braided adsorbent farm on hydrodynamic flow. There was concern that the farm would disrupt normal ocean currents and biogeochemical processes resulting in harm to the marine ecosystem. A hydrodynamic model of the coastal Washington coast was developed in which a braided farm consistent to that described in the literature was inserted. The impact on flow was believed to be minor, less than a 10% reduction in current flow would result at the braid density used in the literature. Additional work has suggested that biogeochemical processes such as dissolved oxygen saturation would also be only minimally impacted (< 0.3%). Late in FY 2014, the hydrodynamic model was extended to the coastal region off the Washington coast such that simulations with coastal conditions could be conducted (see Figure 83).

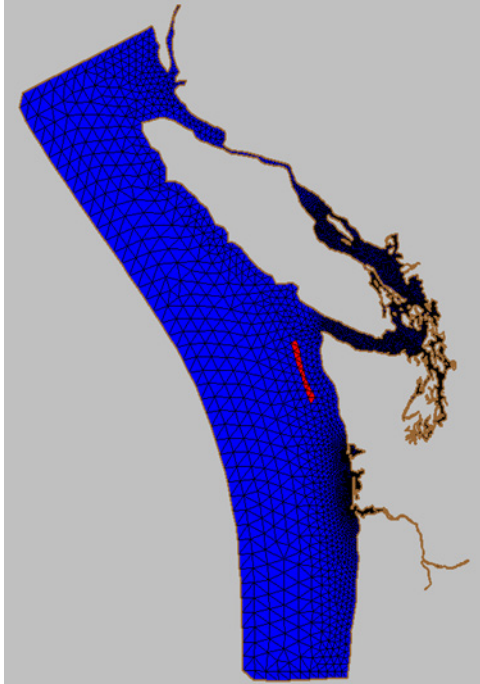


Figure 83. Model domain of the unstructured grid hydrodynamic model (FVCOM) adapted to the Coastal Waters off Washington State.

APPENDIX: ACRONYMS

Appendix: Acronyms

3AMS	3A molecular sieve
A&AC	Advisory and Assistance Contract
ACSEPT	<u>A</u> ctinide re <u>C</u> ycling by <u>S</u> E <u>P</u> ara <u>T</u> ion
AFCI	Advanced Fuel Cycle Initiative
ALSEP	Actinide-Lanthanide Separation
ALTGLASS	Accelerated Leach Testing of GLASS
AMUSE	Argonne Model of Universal Solvent Extraction
ANL	Argonne National Laboratory
APT	atom-probe tomography
ASTM	American Society for Testing and Materials
ATRP	atom transfer radical polymerization
BCNECAP	China–United States Bilateral Civil Nuclear Energy Cooperation Action Plan
CCIM	Cold Crucible Induction Melter
CEA	Commissariat à l'Énergie Atomique (France)
CETE	Coupled End-To-End
CFD	Computational Fluid Dynamics
COEX	co-extraction of actinides
CRIEPI	Central Research Institute of the Electric Power Industry
CNWG	Civil Nuclear Working Group
CWF	ceramic waste form
DFT	Density Functional Theory
DMLS	direct metal laser sintering
DOE	U.S. Department of Energy
-EM	Office of Environmental Management
-NE	Office of Nuclear Energy
-SC	Office of Science
EBR	Experimental Breeder Reactor
EIS	electrochemical impedance spectroscopy
EPA	Environmental Protection Agency
ER	electrorefiner
EU	European Union
EXAFS	Extended X-Ray Absorption Fine Structure
FCRD	Fuel Cycle Research and Development

FCT	Fuel Cycle Technologies
FIB	focused ion beam
FP	fission products
FY	fiscal year
FTIRS	Fourier transform infrared spectroscopy
GCM	glass composite material
GNEP	Global Nuclear Energy Partnership
HIC	high integrity container
HEU	high enriched uranium
HIP	hot isostatic pressing
HLW	high-level waste
HTXRD	high-temperature x-ray diffraction
HUP	hot uniaxial pressing
IWMS	<i>Integrated Waste Management Strategy</i>
IAEA	International Atomic Energy Agency
ICP-MS	Inductively Coupled Plasma-Mass Spectrometry
ICP-OES	Inductively Coupled Plasma-Optical Emission Spectroscopy
IDIQ	indefinite delivery/indefinite quality
INL	Idaho National Laboratory
JAEA	Japan Atomic Energy Agency
JNFL	Japan Nuclear Fuel Limited
LBNL	Lawrence Berkeley National Laboratory
LEU	low enriched uranium
LWR	light-water reactor
M&S	modeling and simulation
MEI	maximum exposed individual
MOF	metal-organic-framework
MOU	Memorandum of Understanding
MSL	Marine Science Laboratory
MTU	metric ton of uranium
MTZ	mass transfer zone
NEUP	Nuclear Energy University Programs
NMA	Nuclear Material Accountability
NNL	National Nuclear Laboratory (UK)
NTD	National Technical Director

**Material Recovery and Waste Form Development
2014 Accomplishments Report**

ORNL	Oak Ridge National Laboratory
PA	performance assessment
PCT	product consistency test
PI	Principal Investigator
PNNL	Pacific Northwest National Laboratory
PSU	Pennsylvania State University
PUREX	plutonium uranium reduction extraction
PWR	pressurized water reactor
QM/MM	quantum mechanics/molecular mechanics
R&D	research and development
RF	radio frequency
RIGP	radiation-induced graft polymerization
RT	retention time
SACSESS	<u>S</u> afety of <u>A</u> ctinide <u>S</u> eparation <u>P</u> roce <u>S</u> Ses
S&M	Science and Methods
SANEX	selective actinide extraction
SEM	scanning electron microscopy
SF	separation factor
SF Eu/Am	separation factor for europium from americium
SFR	sodium fast reactor
SNL	Sandia National Laboratory
SNM	special nuclear materials
SPFT	single pass flow through
SPS	spark plasma sintering
SRNL	Savannah River National Laboratory
SynRoc	synthetic rock
TALSPEAK	Trivalent Actinide - Lanthanide Separation by Phosphorous reagent Extraction from Aqueous Komplexes
TDDFT	time-dependent density functional theory
TGA	thermogravimetric
TRU	transuranic
TRUEX	transuranic extraction
UDS	undissolved solids
UK	United Kingdom
UNF	used nuclear fuel

UNT	University of North Texas
UREX+	Uranium Extraction Plus
US	United States
UV-vis	ultraviolet-Visible
UV-vis-NIR	ultraviolet-visible near-infrared
WSU	Washington State University
WTBS	Waste Treatment Baseline Study
XAS	X-ray absorption spectroscopy
XRD	X-ray diffraction

Chemical Compounds

ADU	ammonium diuranate
Ag ⁰ Z	silver substituted mordenite
AgA	silver nitrate impregnated alumina
AgS	silver nitrate impregnated silica
AgZ	silver exchanged mordenite
AgZ-PAN	silver exchanged mordenite in an engineered form sorbent
BP18C6	<i>N,N'</i> -bis[(6-carboxy-2-pyridyl)methyl]-4,13-diaza-18-crown-6
CMPO	octyl(phenyl)-N,N-diisobutylcarbonoylmethyl-phosphine oxide
DAAP	diamylamylphosphonate
DGA	diglycolamides
DMSO	dimethyl sulfoxide
DPA	dipicolinic acid
DPAH	dithiophosphinic acid
DTPA	diethylenetriamine- <i>N,N,N',N'',N'''</i> -pentaacetic acid
EDTA	ethylenediaminetetraacetic acid
H ₂	hydrogen
H ₂ MEHP	mono-(2-ethylhexyl) phosphoric acid
H ₂ O	water
H ₂ O ₂	peroxide
H ₄ SiO ₄	orthosilic acid
HDBP	di- <i>n</i> -butyl phosphoric acid
HDEHP	bis-(2-ethylhexyl) phosphoric acid
HEDHP	di(2-ethylhexyl) phosphoric acid
HEDTA	<i>N</i> -(2-hydroxyethyl)ethylenediamine- <i>N,N',N'</i> -triacetic acid
HEH[EHP]	2-ethylhexylphosphonic acid mono-2-ethylhexyl ester
HMDPA	hydroxymethyl-DPA
HNO ₃	nitric acid
KOH	potassium hydroxide
KSICON	KZr ₂ P ₃ O ₁₂
K-TSP	HK ₃ Ti ₄ O ₄ (SiO ₄) ₃ ·4H ₂ O
LA	lactic acid
LBLTO	Li ₆ BaLa ₂ Ta ₂ O ₁₂
LLTO	structured lithium lanthanum tantalate
mor-DPA	4-morpholino- DPA

mPIP-DPA	4-methyl-piperidiny-DPA
NaSICON	Na Super Ion CONductor: $\text{NaZr}_2\text{P}_3\text{O}_{12}$
NO_2	nitrogen dioxide
O_2	oxygen
PAN	polyacrylonitrile
QDPA	quaternary methyl ammonium-DPA
SFM	perovskite structured $\text{Sr}_2\text{Fe}_{1.5}\text{Mo}_{0.5}\text{O}_{6-\delta}$
TBP	tributyl phosphate
TcO_4^-	pertechnetate anion
TEDGA	tetraethyl diglycolamide
TODGA	tetraoctyldiglycolamide
TOPO	tri- <i>n</i> -octylphosphine oxide
UOX	uranium oxide (fuel)
$\alpha\text{-Fe}_2\text{O}_3$	hematite
$\alpha\text{-FeOOH}$	goethite
vC-CO ₂	deprotonated lactate
vC-COOH	protonated lactic acid